

國立臺灣大學工學院應用力學研究所



碩士論文

Institute of Applied Mechanics

College of Engineering

National Taiwan University

Master Thesis

拉福波於聲子晶體之波傳現象研究與應用

A Study of Love Waves in a Phononic Structure

劉庭瑋

Ting-Wei Liu

指導教授：吳政忠 教授

Advisor: Tsung-Tsong Wu, Professor

中華民國 102 年 12 月

December 2013

國立臺灣大學碩士學位論文
口試委員會審定書

拉福波於聲子晶體之波傳現象研究與應用

A Study of Love Waves in a Phononic Structure

本論文係劉庭瑋君（學號：R00543020）在國立臺灣大學應用力學研究所完成之碩士學位論文，於民國 102 年 12 月 10 日承下列考試委員審查通過及口試及格，特此證明

口試委員：

吳政忠 吳政忠
(指導教授)

陳永裕 陳永裕

孫嘉宏 孫嘉宏

所 長

張家歐 張家歐

誌謝



能完成這篇論文，首先要感謝恩師 吳政忠教授的教導與鼓勵。在超聲波實驗室研究期間，吳老師細心不倦地在研究上之困難給予指導。同時老師對於學生的信任與容錯，也培養了學生獨立思考、勇於嘗試的研究態度。此外，吳老師於日常言談中展現出對學生關心社會國家大事的期許，更讓學生在碩士期間獲益良多，在此謹向吳老師獻上由衷的感激。

承蒙大同大學 陳永裕教授 長庚大學 孫嘉宏教授於百忙之中撥冗擔任學生的論文口試委員。對於本論文的不吝指正，以及許多精闢見解及寶貴意見，使本論文更臻完備，在此表達誠摯的感謝。

在研究期間感謝 327 夥伴們平日之照顧與協助。感謝嘉宏、永裕學長及偉姍學姊在研究期間不厭其煩的幫助與指導。彥廷、智偉、山松以及峻偉、家浩、純劭學長們在研究上的指導，夢禎、駱爺平常的陪伴、切磋、打氣與鼓勵，以及學弟妹儒璋、思伶、泰成、東柏、辰峰、佩玲的關心與支持。與實驗室夥伴相處的點點滴滴，使我的碩士班生涯精采而豐富，這份情誼我會永遠珍惜而銘記於心。

在日本東北大學交換的半個年頭，最要感謝的就是育菁老師以及燿全學長，除了實驗上大力幫助以及政治上的庇護之外，育菁老師提供宿舍使我有棲身之所，燿全學長更打點我的吃喝玩樂和食衣住行，此恩實在難報！另外實驗上也感謝佑莨學長協助入門帶練。也感謝實驗室開放的環境，小野研、田中（秀、徹）研、羽根研的成員們，忍受我一再的使用英文叨擾，大家不厭其煩的指導，容忍一 MEMS 素人的搗亂及破壞。

另外也感謝所有的留學生及非留學生夥伴們（礙於篇幅無法逐一列出）的照顧，在玩樂中讓我又找回實驗挫折所損失的能量，也使我在人生地不熟的異鄉有個溫暖的避風港，非常高興認識大家，使我在仙台度過充實又燦爛的半年，寫下人生中精采的一頁。

感謝我的母親 洪錦華女士、父親 劉兆宏先生和哥哥庭碩對我的鼓勵與支持，細心提攜我長大至今，給我無微不至的關懷，使我能更放心而努力學習。

最後感謝上帝賜給我對真理的渴望以及好奇心，使我在研究的路上樂此不疲。

謹將此論文獻給他們。

中文摘要



聲子晶體泛指材料性質或幾何形狀週期排列之彈性結構。近二十年，由於聲子晶體具有特殊波傳效應，如完全頻隙、負折射、聲波聚焦等，已引起相當多學者的興趣與投入。由於壓電晶圓較難進行精密蝕刻，目前文獻大都以矽基聲子晶體元件為主，但矽不具壓電特性，須將氧化鋅或氮化鋁等壓電薄膜鍍於叉指電極部分以激發表面波或板波，元件插入損失較高

另一方面，在層狀介質的表面波研究中，除了偏振方向與波傳矢狀平面(sagittal plane)平行的雷利表面波外，亦存在有偏振方向與矢狀平面垂直的拉福波(Love wave)。拉福波存在於表面鍍上橫波波速小於基底材料橫波波速材料之層狀半無限域結構，大部分波的能量局限於表面的薄層中，形成一理想的橫波波導。在壓電晶體表面亦存在各類偏振方向與矢狀平面垂直的水平剪切式表面聲波，其發生原理與拉福波相似，可歸類為廣義拉福波。此類聲波常具有較雷利波為高的機電耦合係數及波速，因此廣泛用於高頻、寬頻濾波器用途。

基於拉福波之特性，如能於不易蝕刻的壓電基板鍍上一具聲子晶體結構之薄層，除具有高激發效率之波源外，亦可經由聲子晶體之頻隙特性製做高效能之濾波器或感測器。有鑒於此，本文提出具聲子晶體薄鍍層於壓電基材上之結構，使用有限元素法搭配布洛赫理論(Bloch theorem)，分析此類結構之頻散特性，證實此類結構具有拉福波的可傳頻帶及頻隙，並藉由複數波數頻散關係進一步分析頻隙內聲波之衰減現象。此外，本文也探討頻隙內聲波由均勻介質進入聲子晶體介面之反射、透射及散射現象，並設計一聲子晶體共振器結構。

實驗部分則是以奈米機電系統製程，利用電子束微影系統產生次微米級之叉指電極及聲子晶體圖案，並以反應離子蝕刻法製作出聲子晶體結構。使用斜叉指電極激發及接收寬頻聲波驗證聲子晶體之頻溝，發現在頻溝處有超過 40 分貝之插入損失，且其頻率範圍與理論之預測相當吻合。而設計於 1.25 GHz 之共振器也實現，並具有約 400 之 Q 值。

關鍵字：聲子晶體、拉福波、奈米機電系統製程、共振器

ABSTRACT



A phononic crystal (PC) is a structure whose mechanical properties are periodically arranged. 2-D PCs started to attract great attentions two decades ago. A lot of concern has been focused on their acoustic reflecting phenomenon due to the band gap. However the PC can also be an acoustic conductor, which its conductance is determined by the band structure. Novel properties such as negative refraction or acoustic lensing effect can be achieved with PCs.

Among the many applications, in the area of ultra-high frequency (UHF) acoustic wave devices, complete or partial band gap of air/silicon PC was utilized as the reflective gratings to reduce the devices' size. In those devices, a piezoelectric thin film has to be deposited on the silicon substrate to generate acoustic waves for silicon is non-piezoelectric. Although the fabrication process of the silicon based phononic device has the CMOS compatible advantage, the insertion loss of such a device is high relatively. The other more straightforward way of making a phononic acoustic wave device is to construct periodically micro-holes directly on a piezoelectric substrate. Although the electro-acoustic conversion is higher, it suffered from the anisotropic nature of lithium niobate that lead to a complicated fabrication process.

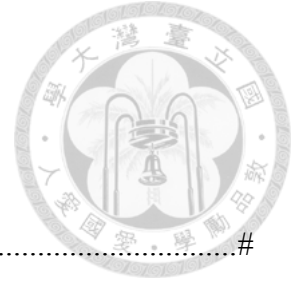
On the other hand, SH-type SAWs have several advantages compared to conventional Rayleigh-type SAWs. For example SH-type SAWs possess larger piezoelectricity than Rayleigh-type SAWs on the same substrate material. Also they are faster than Rayleigh-type SAWs therefore desirable for high frequency applications. And in liquids, SH-type SAWs lose less energy than Rayleigh-type SAWs do due to their polarization, also they are sensitive to surface loadings, so they are desirable for (bio-) sensing appli-

cations. Love wave, being one of the SH-type SAWs, shares similar physical characteristics with other SH-type SAWs. Investigating the propagating of Love waves in PCs will expand the PC applications to SH-type SAWs that have bright outlook.

In this study, we investigate Love waves propagating in a piezoelectric substrate coated with a phononic guiding layer. The phononic layer is consisted of a thin layer with periodic machined holes. It is worth noting that the thin phononic layer can be non-piezoelectric which makes the fabrication process relatively simple. And since most energy is trapped in the guiding layer it may serve as efficient reflective gratings in Love wave devices. The method proposed in this study is suitable for other SH-type SAWs also.

Keywords: Phononic crystal, Love wave, NEMS, Resonator

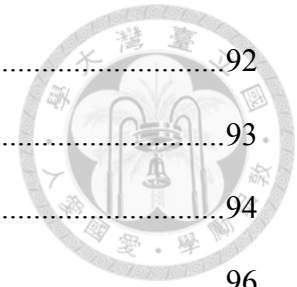
CONTENTS



口試委員會審定書	#
誌謝	i
中文摘要	ii
ABSTRACT	iii
CONTENTS	v
LIST OF FIGURES	viii
LIST OF TABLES.....	xiv
Chapter 1 Introduction	15
1.1 Motivation.....	15
1.2 Literature Review.....	17
1.3 Contents of the Chapters	18
Chapter 2 Love Wave Dispersions of a Phononic SiO₂/Quartz Layered Structure	19
2.1 The Mathematical Model of Acoustic Waves in Piezoelectric solids	20
2.1.1 Piezoelectric acoustic wave equations.....	20
2.1.2 Coordinate transformation for material constants	22
2.1.3 Materials	23
2.2 Waves in periodic structures	25
2.2.1 Direct and reciprocal lattices	25
2.2.2 Bloch's theorem.....	28
2.3 Love wave dispersion of a layered half-space	29
2.3.1 Numerical methods.....	30
2.3.2 Determination of the SiO ₂ film thickness.....	34

2.4	Love wave dispersion in a SiO ₂ /IDT/quartz structure	36
2.4.1	Background.....	36
2.4.2	Dispersion relation.....	37
2.4.3	Frequency-pitch relation.....	38
2.5	Love wave dispersion in phononic layered structures	38
2.5.1	Geometries.....	38
2.5.2	M-Y- Γ -X-M- Γ band structures	39
2.5.3	More on the Γ -X band structures.....	43
Chapter 3 Design of a One-port Resonator.....		65
3.1	Design parameters of a one-port resonator	65
3.2	Reflection on the PC border.....	66
3.3	Optimization for the delay distance	68
3.4	Resonator evaluation.....	69
3.5	Experiment setup.....	70
Chapter 4 Fabrications		83
4.1	Brief of EB lithography.....	83
4.1.1	Why EB lithography.....	84
4.1.2	Anti-charging.....	84
4.1.3	Dose determination and the proximity effect.....	84
4.2	Making the alignment marks for EB lithography	86
4.2.1	Background.....	86
4.2.2	Process and parameters.....	87
4.3	Fabrication of the aluminum IDT	90
4.4	Fabrication of the aluminum wire.....	90
4.4.1	Background.....	90

4.4.2	Process and parameters.....	92
4.5	Deposition of SiO ₂ film	93
4.6	Revealing of the contact pad.....	94
4.7	Fabrication of the PC structure	96
Chapter 5	Experiment Results	131
5.1	Transmission of PCs	131
5.1.1	SFIT without PC —verification of SFIT designs.....	131
5.1.2	SFIT with PC.....	133
5.2	One-port resonator	133
Chapter 6	Conclusions and Future Works.....	150
6.1	Conclusions.....	150
6.2	Future works	151
Appendix	Determination of the Elastic Stiffness of the PECVD SiO₂	152
REFERENCE	163



LIST OF FIGURES



Fig. 2.1 The specimen axes.	48
Fig. 2.2 Euler angles of the three rotations of the coordinate system, where (X, Y, Z) stand for the crystal axes while (x, y, z) stand for the specimen axes.	48
Fig. 2.3 ST-cut and 90°-z-rotated ST cut.	49
Fig 2.4 The bases of the direct and reciprocal lattices and the unit cells of a 2-D lattice.	50
Fig 2.5 The Wigner-Seitz cell and the 1 st Brillouin zone of a 2-D square lattice.	50
Fig 2.6 Love wave dispersion (thick red lines) obtained by a thickness-fixed (10 <i>h</i>) plate model (left) and a thickness-varying (1.6 <i>l</i>) model (right). The blue dashed line and the purple dot-dashed line indicate the SH bulk wave of the substrate (90ST quartz) and the S wave velocity of the guiding layer (CVD SiO ₂), respectively.	51
Fig 2.7 Determination of the SH component.	52
Fig 2.8 Slowness of the bulk waves in 90°-rotated ST-cut quartz along its <i>xy</i> -plane.	52
Fig 2.9 Love modes selecting.	53
Fig 2.10 (Quasi-) Love waves' dispersions along 0° (upper), 45° (mid) and 90° (lower) off the <i>x</i> -axis.	54
Fig 2.11 Electromechanical coupling coefficient.	55
Fig 2.12 Penetration depth of the Love waves.	55
Fig 2.13 DOE of the Love waves.	55
Fig 2.14 Love wave dispersion of the SiO ₂ /IDT/quartz structure, with SiO ₂ thickness = 0.9 μm, IDT aluminum thickness = 100nm, IDT pitch = 3 μm.	56
Fig 2.15 Two resonant modes on the lower (a) and the upper (b) edge of the stop band.	56
Fig 2.16 The admittance of the IDT consists of infinite pairs around the two modes.	56

Fig 2.17 The relation of the excited frequency vs. IDT pitch of the SiO ₂ /IDT/quartz, with SiO ₂ thickness = 0.9 μm, IDT aluminum thickness = 100nm, IDT pitch = 3 μm.	57
Fig 2.18 A schematic drawing of the phononic SiO ₂ /quartz layered structure	58
Fig 2.19 The unit cell of the phononic SiO ₂ /quartz layered structure	58
Fig 2.20 The sound lines.....	59
Fig 2.21 (unfiltered) calculated band structures of phononic crystals with (a) $r/a = 0.1$, (b) $r/a = 0.2$, (c) $r/a = 0.4$	60
Fig 2.22 the color marked band structures of phononic crystals with (a) $r/a = 0.1$, (b) $r/a = 0.2$, (c) $r/a = 0.4$	61
Fig 2.23 (a) Dispersion of a homogeneous medium. (b) Dispersion of a periodic structure with vanishingly small modulation (empty lattice). (c) Dispersion of a periodic structure, mode coupling happens when two modes are close and not orthogonal.....	62
Fig 2.24 Unfiltered dispersion data of PCs with $r/a = 0.1$ (left) and 0.2 (right).	63
Fig 2.25 Colorized dispersion data of PCs with $r/a = 0.1$ (left) and 0.2 (right).	63
Fig 2.26 The complex band structure of the PC with $r/a = 0.2$	64
Fig 3.1 A schematic drawing of the layout of the one-port resonator	73
Fig 3.2 Geometry of the FEM simulation investigating PC reflection.....	73
Fig 3.3 interfered displacement amplitude	74
Fig 3.4 A schematic drawing shows the reflection at the effective plane	74
Fig 3.5 Interfered amplitude vs. d /wavelength with different a	75
Fig 3.6 interfered displacement amplitude at different depth.....	75
Fig 3.7 Reflection simulation on 3 rows of PC. (a), (c): destructive interference. (b), (d): constructive interference. (a), (b): colors indicate the y -displacement in linear	

scale. (c), (d): colors indicate the y -displacement in log scale.....	76
Fig 3.8 Reflection simulation on 5 rows of PC. (a), (c): destructive interference. (b), (d): constructive interference. (a), (b): colors indicate the y -displacement in linear scale. (c), (d): colors indicate the y -displacement in log scale.....	76
Fig 3.9 Reflection simulation on 5 rows of PC. (a), (c): destructive interference. (b), (d): constructive interference. (a), (b): colors indicate the y -displacement in linear scale. (c), (d): colors indicate the y -displacement in log scale.....	77
Fig 3.10 Geometry of the FEM simulation.....	78
Fig 3.11 interfered displacement amplitude (with mechanical loading effect of IDT) ...	78
Fig 3.12 Geometry of the FEM simulation (resonator).....	79
Fig 3.13 Resonant displacement amplitude (with mechanical loading effect of IDT)....	79
Fig 3.14 Simulated admittance of the resonator	80
Fig 3.15 Transverse displacement amplitude at resonance	80
Fig 3.16 Mechanical power flux at resonance.....	81
Fig 3.17 Mechanical power flux on the model boundary at resonance.....	81
Fig 3.18 Experiment setup of PC transmission experiment.	82
Fig. 4.1 A schematic picture of the device (not to scale)	99
Fig. 4.2 A section view of the device (not to scale)	100
Fig. 4.3 The layout design	101
Fig. 4.4 Fabrications of the alignment mark.....	102
Fig. 4.5 Fabrications of the IDT	103
Fig. 4.6 Fabrications of the wire (i).....	104
Fig. 4.7 Fabrications of the wire (ii).....	105
Fig. 4.8 Fabrications of the contact pad window (i).....	106
Fig. 4.9 Fabrications of the contact pad window (ii).....	107

Fig. 4.10 Fabrications of the PC structure	108
Fig. 4.11 A schematic drawing of the electron charging effect.....	109
Fig. 4.12 The writing strategy of a Gaussian vector scan lithography system [56]	110
Fig. 4.13 Back-scattering electrons expose the resist as well. [56]	111
Fig. 4.14 Simulation of the proximity effect	112
Fig. 4.15 Developed patterns without (upper) and with (lower) coating of ESpacer....	113
Fig. 4.16 Circle size changing due to proximity effect.	114
Fig. 4.17 A wafer mark after fabrication of IDT (Al remains on scanned area)	114
Fig. 4.18 The chip mark becomes unusable.	115
Fig. 4.19 SEM images of a developed alignment mark pattern	116
Fig. 4.20 SEM images of a developed IDT pattern	117
Fig. 4.21 Microscope pictures of fabricated IDTs.....	118
Fig. 4.22 A variety of Au-Al intermetallic	119
Fig. 4.23 A Pt/Al contact pad was damaged during buffered HF wet etching.....	120
Fig. 4.24 Problems in wet etching	121
Fig. 4.25 Development is carried out in a 23°C water bath.	122
Fig. 4.26 The EB evaporator	123
Fig. 4.27 The strategy of scanning a mark (upper) and the detected signals (lower)....	124
Fig. 4.28 The P-TEOS CVD system.....	125
Fig. 4.29 The ellipsometer	126
Fig. 4.30 The RIE system	127
Fig. 4.31 PC patterns being written by the EB lithography system.....	128
Fig. 4.32 a SEM image of the PC structure	128
Fig. 4.33 more SEM images of the PC structure	129
Fig. 4.34 Complex index of refraction ($n + i\kappa$) of P-TEOS SiO ₂ vs. wavelength.....	130

Fig 5.1 VNA Agilent E5071C	136
Fig 5.2 Cascade Microtech probes with the platform.....	136
Fig 5.3 Impulse response of SFIT #2 on ST-cut quartz.....	137
Fig 5.4 Original and gated signal in frequency domain.	137
Fig 5.5 Impulse response of SFIT #2 on 90°-rotated ST-cut quartz.	138
Fig 5.6 Original and gated signal of SFIT/90°-rotated ST-cut quartz in frequency domain.....	138
Fig 5.7 Impulse response of SiO ₂ /SFIT #1/90°-rotated ST-cut quartz.....	139
Fig 5.8 Original and gated signal of SiO ₂ /SFIT #1/90°-rotated ST-cut quartz in frequency domain.....	139
Fig 5.9 Impulse response of SiO ₂ /SFIT #2/90°-rotated ST-cut quartz.....	140
Fig 5.10 Original and gated signal of SiO ₂ /SFIT #2/90°-rotated ST-cut quartz in frequency domain.....	140
Fig 5.11 Impulse response of SFIT #1 with 10 rows of PC	141
Fig 5.12 Frequency response of SFIT #1 with 10 rows of PC	141
Fig 5.13 Impulse response of SFIT #2 with 10 rows of PC	142
Fig 5.14 Frequency response of SFIT #2 with 10 rows of PC	142
Fig 5.15 Impulse response of SFIT #1 with 15 rows of PC	143
Fig 5.16 Frequency response of SFIT #1 with 15 rows of PC	143
Fig 5.17 Impulse response of SFIT #2 with 15 rows of PC	144
Fig 5.18 Frequency response of SFIT #2 with 15 rows of PC	144
Fig 5.19 Impulse response of SFIT #1 with 20 rows of PC	145
Fig 5.20 Frequency response of SFIT #1 with 20 rows of PC	145
Fig 5.21 Impulse response of SFIT #2 with 20 rows of PC	146
Fig 5.22 Frequency response of SFIT #2 with 20 rows of PC	146

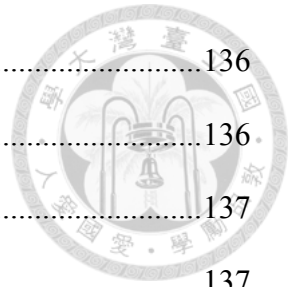
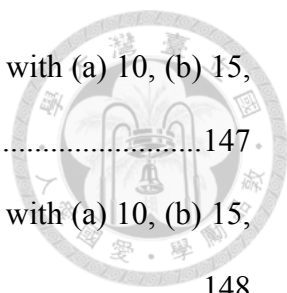


Fig 5.23 Admittance signals of resonators containing 10.5 IDT pairs with (a) 10, (b) 15, (c) 20 rows PC as reflectors	147
Fig 5.24 Admittance signals of resonators containing 30.5 IDT pairs with (a) 10, (b) 15, (c) 20 rows PC as reflectors	148
Fig 5.25 Admittance signals of resonators containing 30.5 IDT pairs with (a) 10, (b) 15, (c) 20 rows PC as reflectors	149



LIST OF TABLES



Table 2.1 Material properties of <i>a</i> -quartz w.r.t. crystal axes	44
Table 2.2 Material properties of ST-cut quartz w.r.t. specimen axes	45
Table 2.3 Material Properties of 90°-rotated ST-cut quartz w.r.t. specimen axes	46
Table 2.4 Material properties of the PECVD SiO ₂ and aluminum.	47
Table 3.1 SFIT parameters.....	72
Table 3.2 IDTs for resonators.	72
Table 4.1 Dependence of required dose on some factors	98



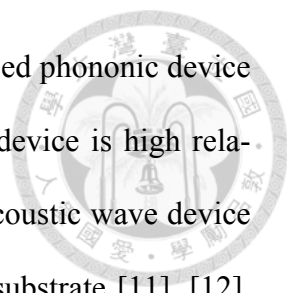
Chapter 1

Introduction

1.1 Motivation

A phononic crystal (PC) is a periodic elastic structure comprised of two or more elastic materials which differ in mechanical properties, or, with periodic geometry. And the resultant acoustic dispersion exhibits a band nature analogous to the electronic band structure in the solid. Examples of one-dimensional (1-D) PCs are the metal strip or grooved grating structures that are widely used in surface acoustic wave (SAW) devices. 2-D PCs have attracted great attentions in the past two decades. A lot of concern has been focused on their acoustic reflecting phenomenon in the frequency band gap. However the PC can also be an acoustic conductor, which its conductance is determined by the band structure. Novel properties such as negative refraction or acoustic lensing effect can be achieved with PCs [1]-[5].

Among the many applications, in the area of ultra-high frequency (UHF) acoustic wave devices, complete or partial band gaps of air/silicon PC were utilized as the reflective gratings to reduce the devices' size [7]-[10]. In those devices, a piezoelectric thin film has to be deposited on the silicon substrate to generate acoustic waves for silicon is



non-piezoelectric. Although the fabrication process of the silicon based phononic device has the CMOS compatible advantage, the insertion loss of such a device is high relatively. The other more straightforward way of making a phononic acoustic wave device is to construct periodically micro-holes directly on a piezoelectric substrate [11], [12]. Although the electro-acoustic conversion is higher than that of the piezoelectric film type device mentioned previously, it suffered from the anisotropic nature of lithium niobate that lead to a complicated fabrication process.

On the other hand, SH-type SAWs have several advantages compared to conventional Rayleigh-type SAWs. For example sometimes SH-type SAWs possess larger piezoelectricity than Rayleigh-type SAWs do on the same substrate material. Also they are faster than Rayleigh-type SAWs therefore desirable for high frequency applications. And in liquids, SH-type SAWs lose less energy than Rayleigh-type SAWs do due to their polarization, also they are sensitive to surface loadings, so they are desirable for (bio-) sensing applications. Love wave, being one of the SH-type SAWs, shares similar physical characteristics with other SH-type SAWs. Investigating the propagating of Love waves in PCs will expand the PC applications to SH-type SAWs that have bright outlook.

In this study, we investigate Love waves propagating in a piezoelectric substrate coated with a phononic guiding layer. The phononic layer is consisted of a thin layer with periodic machined holes. It is worth noting that the thin phononic layer can be amorphous material which makes the fabrication process relatively simple. And since most energy is trapped in the guiding layer it may serve as efficient reflective gratings in Love wave devices. The method proposed in this study is suitable for other SH-type SAWs also.

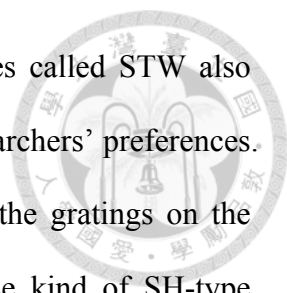


1.2 Literature Review

In 1911, A. E. H. Love published his treatise about a study of shear surface wave that particles move perpendicular to the sagittal plane of wave propagation [13]. This wave, which is called Love wave, exists when the half space is covered with a guiding layer of material with lower bulk shear wave velocity. Although pure SH-type SAWs do not exist on the half-space of an ordinary solid, in the late 1960s a pure SH-SAW was discovered to exist on some piezoelectric solids and is called the “Bleustein-Gulyaev-Shimizu wave (BGS wave)” [14], [15]. A similar but not pure SH-type “leaky SAW (LSAW),” exist in some piezoelectric solids. These SH-type SAWs are being widely used for practical SAW devices for their advantages mentioned before [16]. In 1977, Lewis demonstrated that the surface skimming bulk wave (SSBW) can exist on some piezoelectric substrate and can be used as an alternative to a SAW for a device [17]. And it is reported that the SSBW could be transformed to a “Love wave” by depositing thick electrodes on the substrate.

The research of PCs launched at the beginning of 1990s [18]. The studies of acoustic wave propagation in PCs can be classified according to the bulk acoustic wave [19]-[21], surface acoustic wave [22]-[25], and Lamb wave [26]-[29]. To analyze band structures of PCs, there are several methods exist such as the plane wave expansion (PWE) method [19], the finite difference time domain (FDTD) method [28], multiple scattering theory (MST) [30] and the finite element method (FEM).

As for SH-type SAWs in 1-D periodic structure, Auld *et al.* first proposed the formation of periodic corrugations on substrate surface of quartz to trap SSBW or LSAW and is called the “surface transverse wave (STW).” [31] The stop band of the structure was also studied. As well as corrugations, heavy or thick metal strips can also trap the



SSBW or LSAW with similar slowing mechanism. It is sometimes called STW also [32], or Love wave [33], or grating modes [34], depends on the researchers' preferences. There are also structures proposed with a guiding layer covering the gratings on the substrate [35]. A lot of application devices were made with these kind of SH-type SAWs and most of them are resonators or resonator based filters [33]-[37] since the waves concentrate near the surface only with the periodic structures, and are likely resonant in the periodic structure for the strong periodic modulation.

In this study we investigate the ordinary Love wave that is formed by SSBW trapped by a slower guiding layer deposited on the substrate. And we study the phononic crystal that is consisted of a 2-D periodic structure (micro-machined hole array) on the guiding layer. Both numerical and experimental investigations were conducted. The partial band gap was calculated and verified. We further utilized the reflection phenomenon to design and fabricate one-port Love wave resonators.

1.3 Contents of the Chapters

There are six chapters in this thesis. Chapter 1 is the introduction, with the research motivation and literature review. In Chapter 2 we show the method to calculate propagating eigenmodes in piezoelectric substrate covered with a phononic guiding layer, with a detailed discussion of their band structures. Chapter 3 is the design method of the one-port Love wave resonator. Also the physics of Love wave incident to the PC is studied. Chapter 4 is the fabrications of the experiment devices. The process of how the devices were made are shown in detail. Chapter 5 shows the experiment results with discussion. And Chapter 6 is the conclusions and future works.



Chapter 2

Love Wave Dispersions of a Phononic

SiO₂/Quartz Layered Structure

In this chapter, the numerical methods for calculating the Love wave dispersions in three different structures are proposed. They are (1) CVD SiO₂/quartz layered piezoelectric half space, (2) CVD SiO₂/aluminum electrodes grating/quartz structure, with consideration of the electrodes' mechanical loading effect, which is a 1-D periodic structure, and (3) phononic SiO₂/quartz, a 2-D periodic structure.

First the governing equations of the “quasi-static” approximated model of piezoelectric solid are derived, and then the theory of waves in periodic structure is introduced. After we have the governing equations and boundary conditions the finite element method is employed to solve the differential equations to find the dispersion relation of the 3 structures.

2.1 The Mathematical Model of Acoustic Waves in Piezoelectric solids



2.1.1 Piezoelectric acoustic wave equations

The mechanical system and the electrical system of the piezoelectric solid are coupled together in their constitutive relations. Meanwhile, Newton's 2nd law of motion

$$\nabla \cdot \mathbf{T} + \mathbf{X} = \rho \frac{\partial^2 \mathbf{u}}{\partial t^2}, \quad (2.1)$$

and the Maxwell equations

$$\nabla \cdot \mathbf{D} = \rho_f \quad (2.2)$$

$$\nabla \cdot \mathbf{B} = 0 \quad (2.3)$$

$$\nabla \times \mathbf{E} = -\frac{\partial \mathbf{B}}{\partial t} \quad (2.4)$$

$$\nabla \times \mathbf{H} = \mathbf{J}_f + \frac{\partial \mathbf{D}}{\partial t} \quad (2.5)$$

are still satisfied, where \mathbf{T} , \mathbf{X} , and \mathbf{u} are the Cauchy stress tensor, the body force density vector, and the displacement vector, respectively, while \mathbf{D} , \mathbf{B} , \mathbf{E} , \mathbf{H} , ρ_f , and \mathbf{J}_f are the electric displacement field, the magnetic flux density, the electric field, the magnetic field strength, the free charge density, and the free current density, respectively. To simplify the mathematical model, some fair assumptions are made as the following.

Body forces such as gravity are ignored ($\mathbf{X} = 0$). The piezoelectric material is assumed to be dielectric, i.e., no free charge or free current exist ($\rho_f = 0$, $\mathbf{J}_f = 0$). And the “quasi-static” approximation is introduced, that is, the electric field and the magnetic field are assumed to be static ($\frac{\partial \mathbf{B}}{\partial t} = 0$, $\frac{\partial \mathbf{D}}{\partial t} = 0$). For the reason that we are focusing on

the “quasi-acoustic waves,” and the frequencies of the “quasi-electromagnetic waves”

are much higher under the same wavenumber so that the electromagnetic field can be assumed to be static. Therefore the electric field and the magnetic field become decoupled; moreover, the magnetic field is decoupled from the piezoelectric system. Thus the governing equations of the piezoelectric solid are reduced to the following two equations (with indicial notation)

$$T_{ij,j} = \rho \ddot{u}_i, \quad (2.6)$$

$$D_{i,i} = 0, \quad (2.7)$$

with the constitutive equations which couple the two systems together:

$$T_{ij} = c_{ijkl}^E S_{kl} - e_{kij} E_k, \quad (2.8)$$

$$D_i = e_{ikl} S_{kl} + \epsilon_{ij}^S E_j, \quad (2.9)$$

where S_{kl} is the strain tensor satisfying $S_{kl} = \frac{1}{2}(u_{k,l} + u_{l,k})$, while c_{ijkl}^E , ϵ_{ij}^S , and e_{kij} represent the elastic stiffness tensor under a constant electric field, the permittivity tensor with a constant strain, and the piezoelectric coupling tensor, respectively. Substituting equations (2.8) and (2.9) into equations (2.6) and (2.7), with the electric field-potential relation $E_i = -\phi_{,i}$, and the strain-displacement relation $S_{kl} = \frac{1}{2}(u_{k,l} + u_{l,k})$, we obtain the governing equations of piezoelectricity with variables u and ϕ ,

$$\left(c_{ijkl}^E u_{k,l} + e_{kij} \phi_{,k} \right)_{,j} = \rho \ddot{u}_i, \quad (2.10)$$

$$\left(e_{ikl} u_{k,l} - \epsilon_{ij}^S \phi_{,j} \right)_{,k} = 0. \quad (2.11)$$

In the case of time harmonic motion (when calculating propagating eigenmodes or simulating the frequency response of a device), the displacement vector and the electric

potential can be represented as

$$\mathbf{u}(x, y, z, t) = \hat{\mathbf{u}}(x, y, z)e^{i\omega t}, \quad (2.12)$$

$$\phi(x, y, z, t) = \hat{\phi}(x, y, z)e^{i\omega t}, \quad (2.13)$$

where ω is the angular frequency. Hence equations (2.10) and (2.11) can be rewritten as

$$\left(c_{ijkl}^E \hat{u}_{k,l} + e_{kij} \hat{\phi}_{,k} \right)_{,j} = -\rho \omega^2 \hat{u}_i, \quad (2.14)$$

$$\left(e_{ikl} \hat{u}_{k,l} - \epsilon_{ij}^S \hat{\phi}_{,j} \right)_{,k} = 0. \quad (2.15)$$

With proper boundary conditions (BCs), the solutions of u and ϕ can be found. In this thesis, the rest jobs of solving the differential equations are leaved to a commercial finite element method (FEM) software COMSOL Multiphysics.

2.1.2 Coordinate transformation for material constants

All piezoelectric materials are anisotropic; their properties depend on the frame of reference, i.e., the crystal cut and the orientation of wave propagation, so they should be first correctly obtained. Usually the material properties with respect to (w.r.t.) the crystal axes (denoted by X, Y, Z , defined by crystal symmetry) are found in books. As for some commonly used material with specific crystal cuts such as ST-cut quartz, 128°-YX lithium niobate, the material properties can also be found in literatures. However with different definitions of the specimen axes, they are easily confused and misused. In this thesis, the specimen axes (x, y, z) are defined as follows. The axis normal to the substrate's top surface is defined as the z -axis, with the wave propagating direction defined as the x -axis, the y -axis is then obtained by the right-hand rule, as shown in Fig. 2.1. According to Euler's rotation theorem, any rotation can be decomposed into three successive rotations with three angles (Φ, Θ, Ψ), w.r.t. the axes in a certain order. However the decomposition is not unique and is order-dependent. In the thesis the



Z-X'-Z'' convention is adopted, that is, the specimen axes is rotated from the crystal axes first with an angle Φ w.r.t. the Z-axis, then rotated with an angle Θ w.r.t. the current x-axis (the X'-axis), and finally rotated with an angle Ψ w.r.t. the current z-axis (the Z''-axis). Namely, a rotation rule (ZXtlt) $\Phi/\Theta/\Psi$ following IEEE standard on piezoelectricity [39], is applied, with the plate length direction coincident with the wave propagating orientation.

Let V_i and V'_j denote the components of a vector \mathbf{V} w.r.t. the crystal coordinates and the specimen coordinates respectively, there exist a transformation rule between V_i and V'_j ,

$$V'_i = \beta_{ij} V_j, \quad (2.16)$$

where β_{ij} can be expressed in the matrix form as

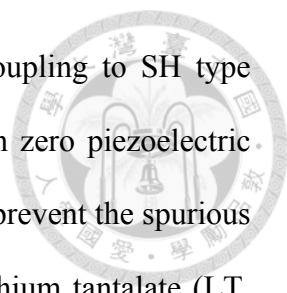
$$\left(\beta_{ij} \right) = \begin{pmatrix} \cos \Psi & \sin \Psi & 0 \\ -\sin \Psi & \cos \Psi & 0 \\ 0 & 0 & 1 \end{pmatrix} \begin{pmatrix} 1 & 0 & 0 \\ 0 & \cos \Theta & \sin \Theta \\ 0 & -\sin \Theta & \cos \Theta \end{pmatrix} \begin{pmatrix} \cos \Phi & \sin \Phi & 0 \\ -\sin \Phi & \cos \Phi & 0 \\ 0 & 0 & 1 \end{pmatrix}. \quad (2.17)$$

Similarly, the permittivity, the piezoelectric coupling tensor, and the elastic stiffness tensor, which are tensors of order 2, 3, and 4, respectively, have the transformation rules as

$$\begin{aligned} \varepsilon'_{ij} &= \beta_{ik} \beta_{jl} \varepsilon_{kl}, \\ e'_{ijk} &= \beta_{ip} \beta_{jq} \beta_{kr} e_{pqr}, \\ c'_{ijkl} &= \beta_{ip} \beta_{jq} \beta_{kr} \beta_{ls} c_{pqrs}. \end{aligned} \quad (2.18)$$

2.1.3 Materials

To support Love wave propagation, it is important choosing the material combination of the layered half-space structure. First the SH wave velocity in a virtual unbounded medium of the layer material must be slower than that of the substrate material, for it is the condition of existence of Love waves. [40], [41] Second, the substrate mate-



rial (with specific crystal cut) should have strong piezoelectric coupling to SH type wave (SH bulk wave, SSBW, SH LSAW, or BGS wave), but with zero piezoelectric coupling to Rayleigh modes or other (P or SV) bulk wave modes to prevent the spurious response. Several crystal cuts of lithium niobate (LN, LiNbO_3), lithium tantalate (LT, LiTaO_3) and quartz are found desirable for such requirements. [42] Eventually, 90° -z-rotated ST-cut quartz (henceforth 90ST quartz) was chosen for there is a fast (5000m/s) SSBW on it and ST-cut quartz is commercially available with a lower price than LT or LN. But there is a disadvantage that is the poor piezoelectric coupling of quartz. On the other hand, the layer material was chosen to be amorphous silicon dioxide (SiO_2 , silica henceforth), which is the most frequently used dielectric material in integrated circuit (IC) manufacturing hence the deposition and etching techniques for silica are well developed. In this study the silica was deposited by plasma enhanced chemical vapor deposition (PECVD) method. Its shear wave velocity is estimated to be 3438 m/s.

The elastic constants of quartz used in this study were from [43], with the kind suggestion from Prof. Yook-Kong Yong. The properties of quartz with respect to its crystal axes are listed in **Table 2.1**. The ST-cut quartz, in words of wafer manufacturers, is a singly rotated ($42^\circ 45'$ along X-axis) Y-cut quartz and the corresponding Euler angles (defined in the previous subsection) are $(\Phi, \Theta, \Psi) = (0, 132^\circ 45', 0)$. As for the “ 90° -z-rotated ST-cut quartz,” it is physically no difference from a ST-cut quartz substrate, but with the wave propagation direction parallel to the y-axis of ST-cut quartz, and perpendicular to the X-axis of quartz (or the x-axis of ST-cut quartz). So actually we demand ST-cut quartz wafer from the supplier, and make a 90° -rotated layout. The Euler angles of 90ST quartz are $(\Phi, \Theta, \Psi) = (0, 132^\circ 45', 90^\circ)$. The properties of ST-cut

quartz and 90°-rotated ST-cut quartz w.r.t. their specimen axes are detailed in **Table 2.2** and **Table 2.3**, respectively. It can be seen that the difference between them is that the components related to axes x or y are exchanged. ST-cut quartz is usually used as a Rayleigh wave device, while on a 90ST quartz SH type SSBW can be generated but Rayleigh wave is decoupled with the applied electric field from the interdigital transducer (IDT). A schematic drawing is shown in Fig. 2.3.

The amorphous silica layer in this study is deposited by a plasma-enhanced chemical vapor deposition (PECVD) method, which is described in Chapter 4. The elastic properties are listed in **Table 2.4**, where the elastic stiffness constants were obtained by a SAW method. By measuring the Love wave and Rayleigh wave velocities on the silica film/quartz substrate, the two elastic constants can be obtained. The method is detailed in the Appendix . It shows a significant difference from the bulk SiO₂ (fused quartz).

2.2 Waves in periodic structures

2.2.1 Direct and reciprocal lattices

Considering a 1-D, 2-D or 3D lattice, a basis $\{a\}$, $\{\mathbf{a}_1, \mathbf{a}_2\}$ or $\{\mathbf{a}_1, \mathbf{a}_2, \mathbf{a}_3\}$ can be chosen by selecting a lattice point as the origin, and the nearest points define the basis vector, such that the vector coordinate of any lattice points can be given by linear combinations of the basis with integer coefficients. Note that the basis is not unique. A 2-D case is shown in Fig 2.4, where $\{\mathbf{a}_1, \mathbf{a}_2\}$ or $\{\mathbf{a}'_1, \mathbf{a}'_2\}$ both can be the basis but here the grid lines are drawn w.r.t $\{\mathbf{a}_1, \mathbf{a}_2\}$.

A “primitive unit cell” can be used to represent the lattice, as it is the smallest period of the lattice. Various primitive unit cells can be chosen but the Wigner-Seitz cell is

the most common and maybe the most useful unit cell. The Wigner-Seitz cell can be chosen by constructing a domain (an interval, a polygon, or a polyhedron stand for 1-D, 2-D or 3-D lattices, respectively) about a lattice point. The boundaries (end points, borderlines or faces) of the cell are points, lines or planes that are perpendicular bisectors of the lines joining the origin with neighboring lattice points [44]. A Wigner-Seitz cell in the 2-D case is shown schematically in Fig 2.4.

Until here the discussion is about the lattice defined by $\{a\}$, $\{\mathbf{a}_1, \mathbf{a}_2\}$ or $\{\mathbf{a}_1, \mathbf{a}_2, \mathbf{a}_3\}$ basis. We refer to it as the *direct lattice*. For each lattice we may define a *reciprocal lattice* that has basis $\{\mathbf{b}\}$, $\{\mathbf{b}_1, \mathbf{b}_2\}$ or $\{\mathbf{b}_1, \mathbf{b}_2, \mathbf{b}_3\}$ given by the equation

$$\mathbf{a}_i \cdot \mathbf{b}_j = 2\pi\delta_{ij}, \quad (2.19)$$

where δ_{ij} is the Kronecker delta symbol, defined by

$$\delta_{ij} = \begin{cases} 1, & i = j \\ 0, & i \neq j \end{cases}. \quad (2.20)$$

In other words, \mathbf{b}_1 is perpendicular to \mathbf{a}_1 but has reciprocal components on $\mathbf{a}_2, \mathbf{a}_3$ (with a scaling factor $(2\pi)^{-1}$). To find the basis of the reciprocal lattice, we first build two 2×2 (3×3) matrices containing the Cartesian components of the bases $\{\mathbf{a}_1, \mathbf{a}_2\}$ and $\{\mathbf{b}_1, \mathbf{b}_2\}$ ($\{\mathbf{a}_1, \mathbf{a}_2, \mathbf{a}_3\}$ and $\{\mathbf{b}_1, \mathbf{b}_2, \mathbf{b}_3\}$), as, in the 2-D case,

$$\mathbf{A} = \begin{pmatrix} \mathbf{a}_1^T \\ \mathbf{a}_2^T \end{pmatrix} = \begin{pmatrix} \mathbf{a}_{1x} & \mathbf{a}_{1y} \\ \mathbf{a}_{2x} & \mathbf{a}_{2y} \end{pmatrix}, \quad (2.21)$$

$$\mathbf{B} = \begin{pmatrix} \mathbf{b}_1 & \mathbf{b}_2 \end{pmatrix} = \begin{pmatrix} \mathbf{b}_{1x} & \mathbf{b}_{2x} \\ \mathbf{b}_{1y} & \mathbf{b}_{2y} \end{pmatrix},$$

or in the 3-D case,

$$\mathbf{A} = \begin{pmatrix} \mathbf{a}_1^T \\ \mathbf{a}_2^T \\ \mathbf{a}_3^T \end{pmatrix} = \begin{pmatrix} \mathbf{a}_{1x} & \mathbf{a}_{1y} & \mathbf{a}_{1z} \\ \mathbf{a}_{2x} & \mathbf{a}_{2y} & \mathbf{a}_{2z} \\ \mathbf{a}_{3x} & \mathbf{a}_{3y} & \mathbf{a}_{3z} \end{pmatrix},$$

$$\mathbf{B} = \left(\mathbf{b}_1 \parallel \mathbf{b}_2 \parallel \mathbf{b}_3 \right) = \begin{pmatrix} \mathbf{b}_{1x} & \mathbf{b}_{2x} & \mathbf{b}_{3x} \\ \mathbf{b}_{1y} & \mathbf{b}_{2y} & \mathbf{b}_{3y} \\ \mathbf{b}_{1z} & \mathbf{b}_{2z} & \mathbf{b}_{3z} \end{pmatrix}.$$



(2.22)

So equation (2.19) can be rewritten as

$$\mathbf{A} \cdot \mathbf{B} = 2\pi\mathbf{I}, \quad (2.23)$$

Where \mathbf{I} is the identity matrix, therefore it follows that

$$\mathbf{B} = 2\pi\mathbf{A}^{-1}. \quad (2.24)$$

Hence the basis of the reciprocal lattice is obtained from a given direct lattice. And the

reciprocal lattice in 1-D case can be simply represented as $b = \frac{2\pi}{a}$.

The wave vector (\mathbf{k}) for a wave propagating in the direct lattice is drawn in the reciprocal lattice. The direct lattice gives the periodicity of the medium (\mathbf{x} -space), while the reciprocal lattice gives the periodicity of the frequency of the waves propagating through the medium (\mathbf{k} -space) [44].

Since the reciprocal lattice shows the periodicity in \mathbf{k} -space, just like the direct lattice in \mathbf{x} -space, a primitive unit cell can be found to describe the whole reciprocal lattice. That is the first Brillouin zone, obtained by constructing a Wigner-Seitz zone in the reciprocal lattice. It is worth noting that discontinuous frequency spectrum often occurs on the boundary of the first Brillouin zone that can be realized as Bragg's reflection condition

$$\mathbf{k} \cdot \mathbf{a} = n\pi, \quad (2.25)$$

where n is an integer. Or the level repulsion due to coupling with diffracted waves.

Fig 2.5 shows the direct lattice and the reciprocal lattice of a 2-D square lattice, as

well as the Wigner-Seitz cell of the direct lattice and the first Brillouin zone in the reciprocal lattice. Some special points Γ , X, M, and Y, on the boundary of the Brillouin zone are labeled. And the *irreducible Brillouin zone* is the first Brillouin zone reduced by all of the symmetries of the lattice. The irreducible Brillouin zone of a square lattice consists of points in the space, is the triangular gridded by the three points Γ , X, and M. But if we consider lattices containing anisotropic materials, the irreducible Brillouin zones may be different. In this study the lattice is constructed on a 90ST quartz substrate, the $(\bar{1}1)$ and (11) rows of the square lattice are no longer lines of mirror symmetry while rows (10) and (01) still remain, therefore the irreducible Brillouin zone should be the square surrounded by the four points Γ , X, M, and Y.

2.2.2 Bloch's theorem

The special form of the solutions of differential equations with periodic coefficients is given by Bloch's theorem. It dates back to 1883, Floquet [45] first showed that the solutions of a 1-variable $n \times n$ system of linear differential equations with the coefficients being a piecewise continuous periodic function with period a

$$\begin{cases} \boldsymbol{\Psi}'(x) = \mathbf{A}(x)\boldsymbol{\Psi}(x), & x \in \mathbb{R} \\ \mathbf{A}(x+a) = \mathbf{A}(x), \end{cases} \quad (2.26)$$

have the form

$$\begin{cases} \boldsymbol{\Psi}_k(x) = e^{ikx}\boldsymbol{\eta}_k(x), \\ \boldsymbol{\eta}_k(x+a) = \boldsymbol{\eta}_k(x), \end{cases} \quad (2.27)$$

where $\boldsymbol{\eta}_k$ is a periodic function with period a . This result can be extended and applied to higher order differential equations by reducing the equation(s) to first order equations with increasing the dimension of the system. It is known as Floquet's theorem. And in

1929, Bloch generalized the theorem for three dimensions in his work on the electron in a crystal [46]. We adopt his result and we have that the eigenmodes of a wave equation in a periodic medium (1-D, 2-D, or 3-D) may be written as the product of a plane wave function $e^{i\mathbf{k}\cdot\mathbf{x}}$ and a periodic function $\boldsymbol{\eta}(\mathbf{x})$ that has the same periodicity as the medium, that is,

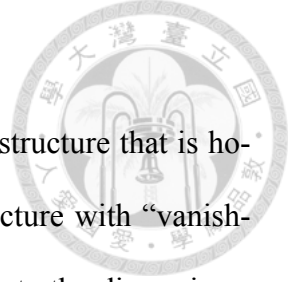
$$\begin{cases} \boldsymbol{\Psi}_{\mathbf{k}}(\mathbf{x}) = e^{i\mathbf{k}\cdot\mathbf{x}}\boldsymbol{\eta}_{\mathbf{k}}(\mathbf{x}), \\ \boldsymbol{\eta}_{\mathbf{k}}(\mathbf{x} + \mathbf{T}) = \boldsymbol{\eta}_{\mathbf{k}}(\mathbf{x}), \end{cases} \quad (2.28)$$

where \mathbf{T} is the translation vector of the crystal that is a linear combination of the basis vectors of the direct lattice with integer coefficients. We can also define \mathbf{G} as the translation vector in the reciprocal lattice.

Applying the Bloch's theorem we obtain the boundary conditions of a Wigner-Seitz cell. Then we search the eigenmodes with wave vectors \mathbf{k} 's located in the irreducible Brillouin zone, then the Bloch waves can be completely characterized. We make the dispersion relation (the ω - \mathbf{k} relation, where ω is the eigenfrequency) plotted with \mathbf{k} varying along the boundary of the irreducible Brillouin zone, which is call the *band structure*, adopted from the terminology of solid state physics. The frequency bands that contain no propagating modes in the band structure are called the *band gaps*, in which no wave can propagate in the periodic structure.

2.3 Love wave dispersion of a layered half-space

In this section we conduct the calculation of the acoustic dispersion relation of the layered structure comprises a silica film deposited on a 90ST quartz substrate. It was accomplished by applying the Bloch's theorem and the finite element method (FEM). And a proper thickness of the silica film is proposed for the experiment devices.



2.3.1 Numerical methods

We are considering the Love wave propagating on the layered structure that is homogeneous along the x - y plane. But if we treat it as a periodic structure with “vanishingly small variation,” the Bloch’s theorem can be applied to calculate the dispersions. Since the structure is actually homogeneous, the choice of the unit cell size can be whatever we like. Let the cell have a length a on the x -direction (i.e., have a “period” a), and a piezoelectric acoustic wave with wavenumber k is propagating through this 1-D “lattice,” then the Bloch wave function can be represented as

$$\begin{cases} \boldsymbol{\Psi}_k(x) = e^{ikx} \boldsymbol{\eta}_k(x), \\ \boldsymbol{\eta}_k(x+a) = \boldsymbol{\eta}_k(x), \end{cases} \quad (2.29)$$

or

$$\boldsymbol{\Psi}_k(x+a) = \boldsymbol{\Psi}_k(x) \cdot e^{ika}. \quad (2.30)$$

Where here $\boldsymbol{\Psi}_k$ can be the displacement field, velocity field, strain field, stress field, electric potential, electric displacement, etc. Therefore we can write down the boundary conditions of this cell with the dependent variable \mathbf{u} and ϕ

$$\begin{cases} \mathbf{u}_+ = \mathbf{u}_- \cdot e^{ika}, \\ \phi_+ = \phi_- \cdot e^{ika}, \end{cases} \quad (2.31)$$

where the subscription + and – stand for the properties on the right and left boundaries of the cell respectively. This is sometimes called Floquet periodicity. Generally a continuous condition requires constraints on both the displacement and traction (electric potential and electric displacement) on the identity pair boundaries. But since we know $\boldsymbol{\eta}_k(x)$ in equation (2.29) for \mathbf{u} and ϕ are smooth functions, we set the constraint order of boundary conditions (2.31) to be 2 as the quadratic Lagrangian element is used in the FEM. Therefore the traction and electric displacement also satisfying condition (2.29)

for they are just results of linear operation on \mathbf{u} and ϕ . Thus they are automatically constrained similar to boundary conditions (2.31). And with the governing equations of the domain (2.14), (2.15), the dispersion relation can be obtain by finding the eigenfrequency ω with varying the wavenumber k .

It is expected that all the dispersion information $k \in (0, \infty)$ is completely determined in the irreducible Brillouin zone that is a finite interval $k \in [0, \pi/a]$. As a result we see the dispersion curves fold back when they touch the boundary of the irreducible Brillouin zone. It is a natural result for e^{ika} is a periodic function of k with period $2\pi/a$, and there is no difference in velocity between the right- or left-propagating waves. So we have a dispersion that is periodic and even function of wavenumber k . We may also consider the boundary conditions (2.31) as “wave propagating boundary conditions” that a wave with wavenumber k propagating through a medium with a length a , experiences a phase shift ka , so the wave function on the right boundary is that on the left boundary being multiplied by e^{ika} . Consider propagating waves with wavenumber $k + \frac{2n\pi}{a}$, or $-k + \frac{(2n-1)\pi}{a}$, where n is an integer, the boundary conditions of them are all identical to (2.31) for the periodicity and of the exponential function.

We would like to postpone the folding on the boundary of the irreducible Brillouin zone to make the dispersion curve look simpler. It can be achieved by selecting a smaller unit cell, therefore the irreducible Brillouin zone, which is a unit cell in the reciprocal lattice, becomes larger, and the folding is postponed.

Ideally the model is a layered half-space, that is, the substrate is infinite deep along $-z$ -direction. However we cannot build a model with infinite depth in FEM calculation. Also the perfect matching layer (PML), and some absorption or low reflecting boundaries are not suitable in the eigenfrequency analysis. Therefore instead, a fi-

nite-depth model is used with the bottom boundary set to be fixed ($\mathbf{u} = 0$) and zero charged ($D_z = 0$). As a result, we are actually calculating the dispersion of a “plate.” But the SAW behavior can be found on the plate as the wavelength becomes much smaller than the plate thickness, or $kh_{\text{substrate}} \gg 1$. [47] Thus, if the thickness of the model’s substrate is thick enough, we can still obtain the SAW dispersion with such model. Being a surface wave, the Love wave has a displacement field in the substrate exponentially vanishing along the $-z$ -direction as

$$\begin{cases} u_y = A e^{bz} e^{ik(x - c_{\text{Love}}t)}, \\ b = k \left[1 - \left(\frac{c_{\text{Love}}}{c_{\text{SH}, 90\text{ST}}} \right)^2 \right]^{\frac{1}{2}}. \end{cases} \quad (2.32)$$

[40] We can see the vanishing factor b depends on both wave number k and the phase velocity of the Love wave c_{Love} . And the phase velocity c_{Love} always sets off from the substrate’s shear wave velocity $c_{\text{SH}, 90\text{ST}}$, and approaches to the shear wave velocity of the film material $c_{\text{S}, \text{silica}}$ as k increasing. A thickness-varying (with k) model and a fixed thickness model are employed to calculate the dispersion of the Love wave, and they show similar results (Fig 2.6) after mode selection (described in the next paragraph). Considering the penetration depth of Love waves is not only wavelength dependent (check “ b ” in equation (2.32)), and the thickness-varying model requires huge computation in the small k region which we do not really concern, so henceforth fixed thickness models with sufficient thickness are used instead of the thickness-varying models.

To pick out the modes standing for Love waves among numerous plate modes in the dispersion relation calculated by the finite-depth model, two conditions are set for mode selecting. We first define the depth of energy (DOE) as

$$\text{DOE} = \frac{\iiint_{\text{unit cell}} \frac{1}{2} T_{ij} S_{ij}^* (-z) dx dy dz}{\iiint_{\text{unit cell}} \frac{1}{2} T_{ij} S_{ij}^* dx dy dz}, \quad (2.33)$$



which is the depth of the strain-energy-weighted centroid of the unit cell. The star symbol “*” indicates the complex conjugate value of the calculated mode shape. Since the stress and strain are always in phase, the amplitude of the strain energy can be expressed as $\frac{1}{2} |T_{ij} S_{ij}| = \frac{1}{2} T_{ij} S_{ij}^*$. By setting a threshold of DOE (for example 0.2λ), the SAW modes whose energy concentrate near the free surface filters through. The selected SAW modes contain generalized Rayleigh waves (particle motion parallel to the sagittal plane), Love waves (particle motion perpendicular to the sagittal plane), and modes lie somewhere in between. We make a threshold of polarization to execute a dichotomy between them. First the displacement component normal to the sagittal plane (i.e. the shear horizontal component) of a wave with the propagation vector lies on the xy -plane can be expressed as

$$u_{\text{SH}} = -u_x \sin \theta + u_y \cos \theta \quad (2.34)$$

where θ represents the angle between the wave vector and the x -axis. (See Fig 2.8.) Then we define a value called ratio of transverse polarization (ROT) as

$$\text{ROT} = \frac{\iiint_{\text{unit cell}} u_{\text{SH}} u_{\text{SH}}^* dx dy dz}{\iiint_{\text{unit cell}} u_x u_x^* + u_y u_y^* + u_z u_z^* dx dy dz}. \quad (2.35)$$

It is a ratio of the norm of the component perpendicular to the sagittal plane, to the total displacement amplitude. When the value is greater than 0.5 it means the perpendicular-to-the-sagittal-plane component is greater than the parallel one, and is classified as the (quasi-) Love wave. On the contrary if the ROT is less than 0.5, the mode will be

classified as the (quasi-) Rayleigh wave.

From the quasi-SH wave slowness of the xy -plane of 90° -rotated ST-cut quartz (Fig 2.8) we found the velocities in all directions are higher than the S wave velocity of the guiding layer material, so we may think non-leaky quasi-Love waves will exist in all directions. But however we found leaky behavior on the directions off the x -axis. This is due to the fact that the quasi-SH wave is the fast shear wave (faster than the quasi-SV wave), and the quasi-Love wave, in order to satisfy the free boundary condition on the surface and the continuity condition between quartz and SiO_2 , the polarization is NOT coincident to the quasi-SH wave. Having a component on the slower quasi-SV wave and being faster than quasi-SV wave, it becomes leaky, energy leaks into the substrate in the form of quasi-SV wave. Only when the wave vector is parallel to the x -axis, a ROT value of 1 is obtained and the non-leaky pure-SH Love wave exists. This is due to the existence of a pure-SH bulk wave of quartz in this direction, the polarization of the pure-SH Love wave is then orthogonal to that of the quasi-SV wave, so there is no mode conversion and therefore no attenuation. We also found that the quasi-SH wave slowness of the 90° -rotated ST-cut quartz is extremely similar to the slowness of the SH LSAW (but the LSAW is slightly slower), and the attenuation of the LSAW also becomes zero when the propagation direction is parallel to the x -axis (pure-SH). [48] These results show that various types of SH SAWs can be considered as SH bulk waves trapped by some slow mechanism near the surface. Fig 2.10 shows the dispersion of Love waves along 0° (x -axis), 45° and 90° (y -axis) of the layered structure.

2.3.2 Determination of the SiO_2 film thickness

As we will further design a resonator, we have to determine a proper thickness for the guiding layer which affects the performance significantly. The first thing we con-

cern about is the electromechanical coupling coefficient. It influence the insertion loss and the bandwidth when the resonator is applied as a filter component. On the other hand, since the reflector of the resonator is the phononic crystal comprises structure modulations on the top layer only, considering the Q factor of the resonator, we want the penetration depth of the Love wave to be shallower to reduce the energy scattered into the substrate on the border of the PC reflector. Unfortunately we will find the two things conflicting, so a compromise is reached and a thickness is proposed.

Electromechanical coupling coefficient

The electromechanical coupling coefficient of the Love wave is also dispersive, it depends on the ratio of the guiding layer thickness to the wavelength. We use an approximate formula to estimate the electromechanical coupling coefficient: [49]

$$K^2 \cong 2 \frac{V_f - V_m}{V_f}, \quad (2.36)$$

where the V_f and V_m stand for the SAW velocities on the free or metallized surface, respectively. The calculated result is shown in Fig 2.11. The 0th mode is concerned, the Electromechanical coupling coefficient reaches a maximum of 0.4% at $kh \sim 0.36$, that is, the guiding layer thickness is about 0.06 times of the wavelength. Then the coefficient keeps decreasing as kh increasing since the penetration depth is also decreasing, the strain concentrates in the guiding layer which is not piezoelectric. When kh increases to 2, the coupling coefficient descends to 0.1%.

Penetration depth

As described in equation (2.32) the penetration depth depends on the wavelength and the phase velocity. If we define the penetration depth as the depth where the displacement amplitude is 1% of the interface ($z = 0$) displacement amplitude, the penetra-

tion depth can be expressed as

$$\log(0.01) k^{-1} \left[1 - \left(\frac{c_{\text{Love}}}{c_{\text{SH, 90ST}}} \right)^2 \right]^{-\frac{1}{2}} \quad (2.37)$$



and is plot in Fig 2.12. Also the DOE is plot in Fig 2.13. We can see the penetration depth approaches 1 wavelength in this layered structure while the value of DOE/λ can be negative as the centroid of strain energy shifts into the guiding layer. Another consideration is that when the phononic crystal is present the Love wave may not keep pure-SH anymore for the complex BCs. So it is better make the Love wave slower than the quasi-SV wave to avoid energy loss. From the dispersion relation Fig 2.10, it is the interval $kh > 2$.

Finally the thickness is determined to be about one third of the wavelength (i.e., $kh \sim 2$), with our expectation of low energy loss and acceptable electromechanical coupling coefficient.

2.4 Love wave dispersion in a $\text{SiO}_2/\text{IDT}/\text{quartz}$ structure.

2.4.1 Background

In IC industry, aluminum and copper are the most common material for wire. In the MEMS field, gold and platinum are also popular material for electrodes but in the high frequency acoustic wave application, the electrodes should have good conductivity and very light weight, thus aluminum becomes the best choice not only for the price but it also has the best performance of conductivity/density ratio among all metals. Also aluminum has similar acoustic impedance to SiO_2 . (See **Table 2.4.**) So it is used in our devices as the IDT material. But however we cannot just ignore the loading effect of the electrode especially on a SH type SAW device which is very sensitive to the surface

loadings.

Since we are going to fabricate a device over 1 GHz. From the dispersion curve and the requirement $kh \sim 2$, we can conclude that the wavelength is about 3 μm . The IDT which consists of 100-nm-thick aluminum electrodes will have considerable loading effect and reduce the excited frequency. A correction formula based on the perturbation method was proposed. [50] But it assumes that the ratio of the metal thickness to the wavelength is very small ($\leq 1\%$). In our case the ratio is over 3% hence the approximation is no longer valid. We use FEM with Bloch's theorem to calculate the dispersion of the $\text{SiO}_2/\text{IDT}/\text{quartz}$ structure, and then finding the relation of the excited frequency vs. the IDT pitch, to facilitate the follow-up designs.

2.4.2 Dispersion relation

The unit cell is chosen to be 1-IDT-pitch wide, or half the wavelength as Fig 2.15. On the quartz substrate is the aluminum electrode covered by CVD SiO_2 . It is an 1-D periodic structure. Considering the wave propagating along x -axis, the dispersion relation can be calculated by FEM with Floquet's theorem mentioned before. The result is shown in Fig 2.14. We can see the Love wave opens a band gap at $k = \pi/p$ due to Bragg reflection, where p is the IDT pitch. Also the Love modes closed to the band gap becomes not propagating (group velocities vanish and show resonant phenomenon). Observing the corresponding electric field of the two modes on both sides of the band gap, we expect that the lower mode will be excited by IDT, where it has a maximum resonant amplitude at the position of the metal electrode and a node between the electrodes. Contrary, the other mode which the positions of the node and the peak of resonant are exchanged will not be excited. It is further verified by a simulation applying voltages on the infinite many pairs of IDT and calculating the admittance frequency response as Fig

2.16. As expectation the lower mode is excited and with the electromechanical coupling coefficient about 0.1% while the higher one is also excited but with extremely low coupling. The electromechanical coupling coefficient is estimated by the following formula [51]

$$K^2 \cong \frac{\pi^2}{4} \frac{f_a - f_r}{f_a}, \quad (2.38)$$

where the f_a and f_r are the resonant and anti-resonant frequency, respectively.

2.4.3 Frequency-pitch relation

And then we calculate the lower resonant mode at $k = \pi/p$ with varying the IDT pitch p (i.e., varying the unit cell geometry), we will then have the relation of the IDT resonant frequency vs. the IDT pitch. From this result we can design the IDT with precisely matching with the desired frequency. Fig 2.17 shows the excited frequency vs. the IDT pitch, with the IDT being 100-nm-thick covered by 0.9-mm-thick CVD SiO₂.

2.5 Love wave dispersion in phononic layered structures

In this section we will calculate the dispersions of Love waves in phononic SiO₂ thin film/90°-rotated ST-cut quartz structures, where the phononic SiO₂ thin film consists of machined holes arranged as square lattices in the SiO₂ thin film as Fig 2.18. We will still apply Bloch's theorem using FEM to calculate the dispersions or the band structures which are dispersions with the k vectors varying along the boundaries of the irreducible Brillouin zone. Some phenomena of Love waves propagating in such structures are read from the band structures.

2.5.1 Geometries

Fig 2.19 shows the schematic drawing of a unit cell of the PC. As we have deter-

mined the SiO₂ film thickness h to be about 0.3 times the wavelength λ , considering that we are going to apply the PC around its first Bragg's band gap of the Love wave, and with expectation that the phase velocity in the PC is not very different from the homogeneous (without PC) layered structure, from the Bragg's condition $ka = \pi$, we have $a = \lambda/2$ so the thickness is design to be 0.6 times the lattice constant a . And the machined hole radius r , behaving the strength of the modulation in the PC, is set to be $0.1a$, $0.2a$, or $0.4a$. Their band structures will be discussed in detail.

2.5.2 M-Y- Γ -X-M- Γ band structures

For the anisotropy of the substrate—90°-rotated ST-cut quartz, the complete band structure is calculated and plotted along the connecting lines between M-Y- Γ -X-M- Γ points on the boundary of the irreducible Brillouin zone.

First we shall introduce the concept of the *sound cone*. The sound cone is usually defined as the slowest bulk wave velocity of the substrate in the dispersion relation. The constant velocity surface forms a cone in the 2-D dispersion relation plot, but in the band structures that will be discussed later, the cone is sectioned as lines (the sound lines). Surface waves with dispersion relation above the sound lines are considered to be leaky for the reason that the apparent wavenumber on the surface support a certain angle such that the disturbance created by the surface wave can be transformed as the bulk wave and leaks. However if the particle motion of surface wave has very little component on that of the bulk wave, the propagation loss may be negligible. We plotted the sound lines from not only the slowest but all the three bulk wave velocities in the substrate according to the slowness curve Fig 2.8, and along M-Y- Γ -X-M- Γ . It is shown in Fig 2.20.

The band structures of the phononic crystals with $r/a = 0.1, 0.2, 0.4$ are plotted in

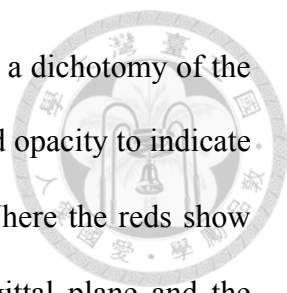


Fig 2.21 (unfiltered) and Fig 2.22 (color marked). Instead of making a dichotomy of the bulk/surface modes; Rayleigh/Love modes, we use graded colors and opacity to indicate the polarization (ROT) and energy depth (DOE/λ), respectively. Where the reds show the polarizations have larger components perpendicular to the sagittal plane and the blues have larger components in the sagittal plane. The dots with higher opacity represent the energy are concentrated near the surface. Also the three sound lines are plotted in the figures for reference. With the graded color we can observe more things from the band structures such as mode coupling phenomenon, and it is also too assertive to classify the modes in a “black or white” way especially in the PCs consist of anisotropic materials.

We shall notice that all modes near the Γ point seem to be surface modes as they have small DOE/λ . But actually it is a false appearance caused by the finite-depth model. Near the Γ point ($|\mathbf{k}| \rightarrow 0$) the wavelength approaches infinity therefore in a finite-thick plate the DOE/λ of all modes naturally approach zero. Most modes in this region behave like the plate modes and the surface modes have not developed yet. So we may ignore this region.

Some invisible lines influence the dispersion curves significantly. (See Fig 2.21.) Compared with the sound lines we found them identical. Consider the plate modes as bulk waves trapped and reflecting in the quartz plate, their phase velocities are always larger than that of the bulk waves. Thus the plate modes are always located above the corresponding sound lines. For example under the slowest shear wave (quasi-SV) sound line there is no plate modes, and between quasi-SV and quasi-SH sound lines there are plate modes with polarization *in* the sagittal plane, and above the quasi-SH sound line the plate modes with SH polarization also show. In addition, near the quasi-longitudinal

sound line, mode coupling can be observed.

Mode coupling also exist between the plate modes and the surface modes. A clear example is the quasi-Rayleigh mode and the quasi-in-plane type plate mode shown in the black circle in Fig 2.22 (c). In general with the existence of the PCs that contain complex 3-D boundary conditions, the polarization of the surface modes is unlikely to be uncoupled (i.e., have no component) with the plate modes, just with different proportion. For example the quasi-Love modes can be only slightly coupled with quasi-in-plane type plate modes. Mode coupling happens when the two modes being closed in the band structure, and *level repulsion* will be observed, which is that the two dispersion curves avoid from crossing each other, and the two modes becomes like each other. Away from the coupling region, the two modes revert to their original appearance.

Considering the fact that the dispersion curves of the plate modes depend on the substrate thickness, and the plate modes becomes more and denser in the band structure above the sound line with increasing of the substrate thickness (eigenfunctions along the thickness), we may conclude that the more and more discrete plate modes becomes continuous modes that represent bulk modes with different down-propagating angles, when the substrate's thickness approaches infinity (again the plate modes can be regarded as reflecting bulk modes). The coupling between the surface modes and the plate modes in the calculation predicts that between the surface modes and bulk modes in the real situation, that is, it indicates the leakiness of the surface modes.

It is also observed that the “folded” surface modes is also coupled with the plate modes that have not experience the folding. An example is shown in the black circle in Fig 2.22 (a). From the group velocities and mode shapes we may think the folded bands are due to the periodicity in k -space and is from another reciprocal lattice so they have wavenumbers $2\pi/a - k$, different from the unfolded bands' wavenumber k , so there

should not be coupling. But actually there is.

Assume that there are two modes propagating in a fictional homogeneous medium, which the dispersion curves are like Fig 2.23 (a). Then consider a phononic crystal with small modulation, with period a , the dispersion curves will repeat with the period equals to the reciprocal lattice, like Fig 2.23 (b). The crossing point becomes a singular point since the group velocity (propagating direction) is not defined. To fix the unusual phenomenon an anti-crossing (i.e. level repulsion) will occur here so the singularity is not exist. As the modulation of the PC increase, the level repulsion or the coupling becomes stronger, as Fig 2.23 (c). The Bragg band gap indicated by the black circle in Fig 2.23 (a) can also be explained by such interpretation, and the coupling of right and left propagating waves forms standing waves on the edges of the gap. For a strongly modulated PC, one cannot even classify a mode to a reciprocal lattice, and the waves can only be regarded as a summation of Bloch waves with different \mathbf{G} 's so the coupling will generally occur.

So we can conclude that in the PC, a surface mode become leaky as it lies above the sound lines, no matter it is a folded band or not. The degree of leakiness depends on the magnitude of the component of the surface mode on the bulk mode. The degree of leakiness of a “folded” surface modes is also depends on how strong the periodic modulation is.

As for the band gap, we found no complete (all direction) band gap for Love waves in the three PCs. But for the partial band gap, all the three PCs have, and without surprise, the gap width grows wider as the hole radius increases. For the same PC structure, it is found that the partial band gap of the Rayleigh wave is much smaller than that of the Love wave. It is due to the fact that SH-type SAWs are more sensitive to the surface loadings.

2.5.3 More on the Γ -X band structures

We plot the band structures in Γ -X direction more detailed and with wider frequency range as Fig 2.24 (unfiltered) and Fig 2.25 (color marked). The plate modes are folded but do not open a band gap for the surface modulation has little effect to them. And the invisible sound line that influence the plate modes also folded on the boundary of the irreducible Brillouin zone.

For the Love modes, they are hardly influenced by the in-plane plate modes but coupled with SH-type plate modes when the r/a is larger. The Rayleigh mode is found coupled with in-plane plate modes. Although it is predicted that the Love waves become leaky when they exceed the sound lines but they can still be found far above the sound lines. It indicates the loss is not much.

A complex band structure is calculated for the $r/a = 0.2$ case, and plotted in Fig 2.26. To know the attenuation of the evanescent waves in the first Bragg band gap, Bloch's theorem with complex wavenumbers $k_x = \pi/a - i\alpha$ is applied to calculate the dispersion relation with varying α . It is found that the attenuation of the evanescent wave at the band gap center frequency is 4.34 dB/ a . Knowing the attenuation of Love waves in the PC gives a reference for designing of devices.

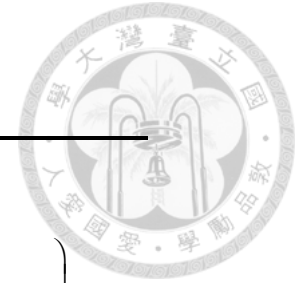


Table 2.1 Material properties of α -quartz w.r.t. crystal axes

Density (kg/m ³)	2650
Elastic stiffness tensor under a constant electric field \mathbf{c}^E in Voigt notation (Pa)	$\begin{pmatrix} 8.674 \times 10^{10} & 6.980 \times 10^9 & 1.191 \times 10^{10} & -1.791 \times 10^{10} & 0 & 0 \\ 6.980 \times 10^9 & 8.674 \times 10^{10} & 1.191 \times 10^{10} & 1.791 \times 10^{10} & 0 & 0 \\ 1.191 \times 10^{10} & 1.191 \times 10^{10} & 1.072 \times 10^{11} & 0 & 0 & 0 \\ -1.791 \times 10^{10} & 1.791 \times 10^{10} & 0 & 5.794 \times 10^{10} & 0 & 0 \\ 0 & 0 & 0 & 0 & 5.794 \times 10^{10} & -1.791 \times 10^{10} \\ 0 & 0 & 0 & 0 & -1.791 \times 10^{10} & 3.988 \times 10^{10} \end{pmatrix}$
Piezoelectric coupling tensor \mathbf{e} in Voigt notation (C/m ²)	$\begin{pmatrix} 1.710 \times 10^{-1} & -1.710 \times 10^{-1} & 0 & -4.067 \times 10^{-2} & 0 & 0 \\ 0 & 0 & 0 & 0 & 4.067 \times 10^{-2} & -1.710 \times 10^{-1} \\ 0 & 0 & 0 & 0 & 0 & 0 \end{pmatrix}$
Permittivity tensor with a constant strain $\boldsymbol{\epsilon}^S$ in matrix form (F/m)	$\begin{pmatrix} 3.9215 \times 10^{-11} & 0 & 0 \\ 0 & 3.9215 \times 10^{-11} & 0 \\ 0 & 0 & 4.1038 \times 10^{-11} \end{pmatrix}$

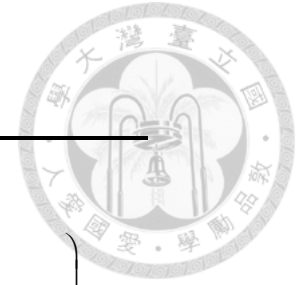


Table 2.2 Material properties of ST-cut quartz w.r.t. specimen axes

Euler angles (Φ, Θ, Ψ)	$(0^\circ, 132^\circ 45', 0^\circ)$					
Elastic stiffness tensor under a constant electric field \mathbf{c}^E in Voigt notation (Pa)	$\begin{pmatrix} 8.674 \times 10^{10} & 2.749 \times 10^{10} & -8.603 \times 10^9 & -1.052 \times 10^9 & 0 & 0 \\ 2.749 \times 10^{10} & 9.663 \times 10^{10} & -4.806 \times 10^9 & -1.344 \times 10^{10} & 0 & 0 \\ -8.603 \times 10^9 & -4.806 \times 10^9 & 1.307 \times 10^{11} & 1.838 \times 10^9 & 0 & 0 \\ -1.052 \times 10^9 & -1.344 \times 10^{10} & 1.838 \times 10^9 & 4.122 \times 10^{10} & 0 & 0 \\ 0 & 0 & 0 & 0 & 3.035 \times 10^{10} & -7.597 \times 10^9 \\ 0 & 0 & 0 & 0 & -7.597 \times 10^9 & 6.747 \times 10^{10} \end{pmatrix}$					
Piezoelectric coupling tensor \mathbf{e} in Voigt notation (C/m^2)	$\begin{pmatrix} 1.710 \times 10^{-1} & -3.832 \times 10^{-2} & -1.327 \times 10^{-1} & -8.205 \times 10^{-2} & 0 & 0 \\ 0 & 0 & 0 & 0 & -6.653 \times 10^{-2} & -9.903 \times 10^{-2} \\ 0 & 0 & 0 & 0 & -7.197 \times 10^{-2} & -1.071 \times 10^{-1} \end{pmatrix}$					
Permittivity tensor with a constant strain $\boldsymbol{\epsilon}^S$ in matrix form (F/m)	$\begin{pmatrix} 3.9215 \times 10^{-11} & 0 & 0 \\ 0 & 4.0198 \times 10^{-11} & -9.0869 \times 10^{-13} \\ 0 & -9.0869 \times 10^{-13} & 4.0055 \times 10^{-11} \end{pmatrix}$					



Table 2.3 Material Properties of 90°-rotated ST-cut quartz w.r.t. specimen axes

Euler angles (Φ, Θ, Ψ)	$(0^\circ, 132^\circ 45', 90^\circ)$
Elastic stiffness tensor under a constant electric field \mathbf{c}^E in Voigt notation (Pa)	$\begin{pmatrix} 9.663 \times 10^{10} & 2.749 \times 10^{10} & -4.806 \times 10^9 & 0 & -1.344 \times 10^{10} & 0 \\ 2.749 \times 10^{10} & 8.674 \times 10^{10} & -8.603 \times 10^9 & 0 & -1.052 \times 10^9 & 0 \\ -4.806 \times 10^9 & -8.603 \times 10^9 & 1.307 \times 10^{11} & 0 & 1.838 \times 10^9 & 0 \\ 0 & 0 & 0 & 3.035 \times 10^{10} & 0 & -7.597 \times 10^9 \\ -1.344 \times 10^{10} & -1.052 \times 10^9 & 1.838 \times 10^9 & 0 & 4.122 \times 10^{10} & 0 \\ 0 & 0 & 0 & -7.597 \times 10^9 & 0 & 6.747 \times 10^{10} \end{pmatrix}$
Piezoelectric coupling tensor \mathbf{e} in Voigt notation (C/m^2)	$\begin{pmatrix} 1.710 \times 10^{-1} & -3.832 \times 10^{-2} & -1.327 \times 10^{-1} & -8.205 \times 10^{-2} & 0 & 0 \\ 0 & 0 & 0 & 0 & -6.653 \times 10^{-2} & -9.903 \times 10^{-2} \\ 0 & 0 & 0 & 0 & -7.197 \times 10^{-2} & -1.071 \times 10^{-1} \end{pmatrix}$
Permittivity tensor with a constant strain $\boldsymbol{\epsilon}^S$ in matrix form (F/m)	$\begin{pmatrix} 4.0198 \times 10^{-11} & 0 & -9.0869 \times 10^{-13} \\ 0 & 3.9215 \times 10^{-11} & 0 \\ -9.0869 \times 10^{-13} & 0 & 4.0055 \times 10^{-11} \end{pmatrix}$



Table 2.4 Material properties of the PECVD SiO₂ and aluminum.

	PECVD SiO ₂	Aluminum
Deposition source/method	Si(OC ₂ H ₅) ₄ (TEOS), O ₂ /PECVD	99.999% aluminum/evaporation
Optical index of refractive	1.48~1.58 (See Fig. 4.34)	—
Electric conductivity (S/m)	—	3.55×10 ⁷
Density (kg/m ³)	2200	2750
Elastic stiffness	(λ, μ) = (20 GPa, 26 GPa) ^a	(E, ν) = (70 GPa, 0.35)
Shear bulk wave speed	3438 m/s	3099 m/s

^a The stiffness constants of SiO₂ are obtained from experiments while others are from the literatures

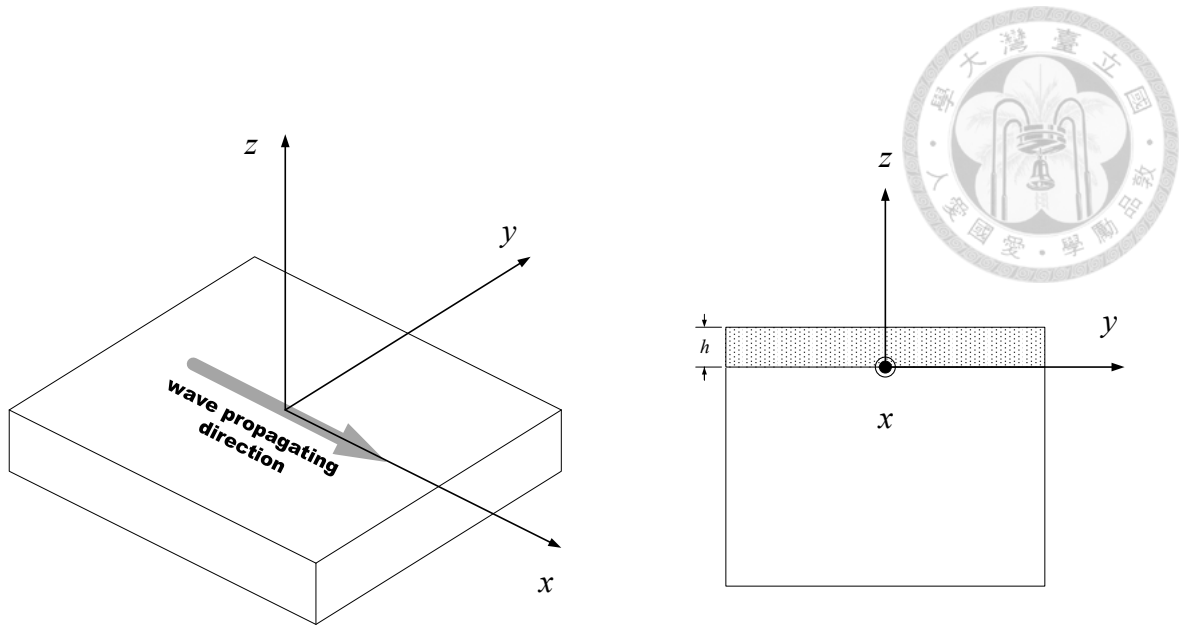


Fig. 2.1 The specimen axes.

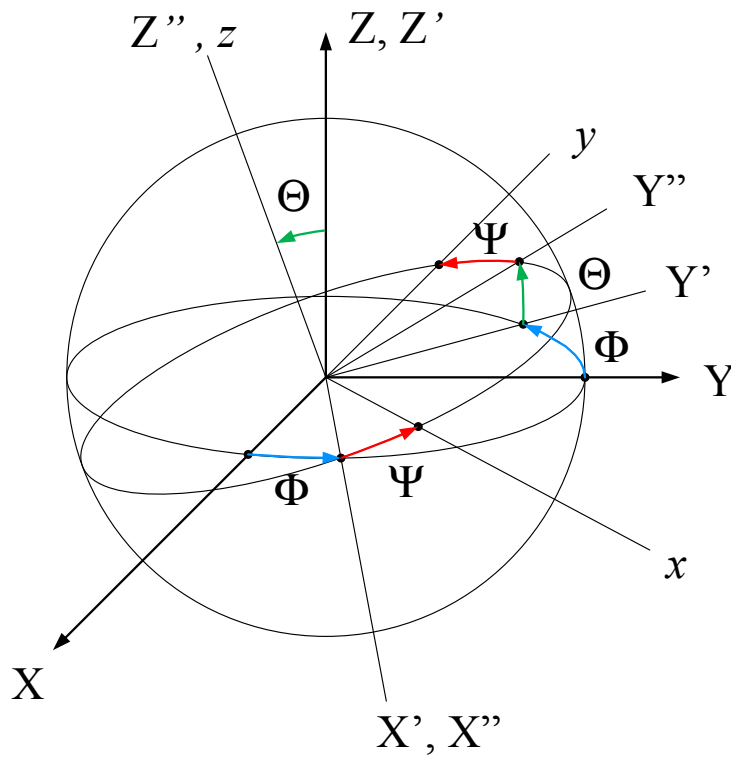


Fig. 2.2 Euler angles of the three rotations of the coordinate system, where (X, Y, Z) stand for the crystal axes while (x, y, z) stand for the specimen axes.

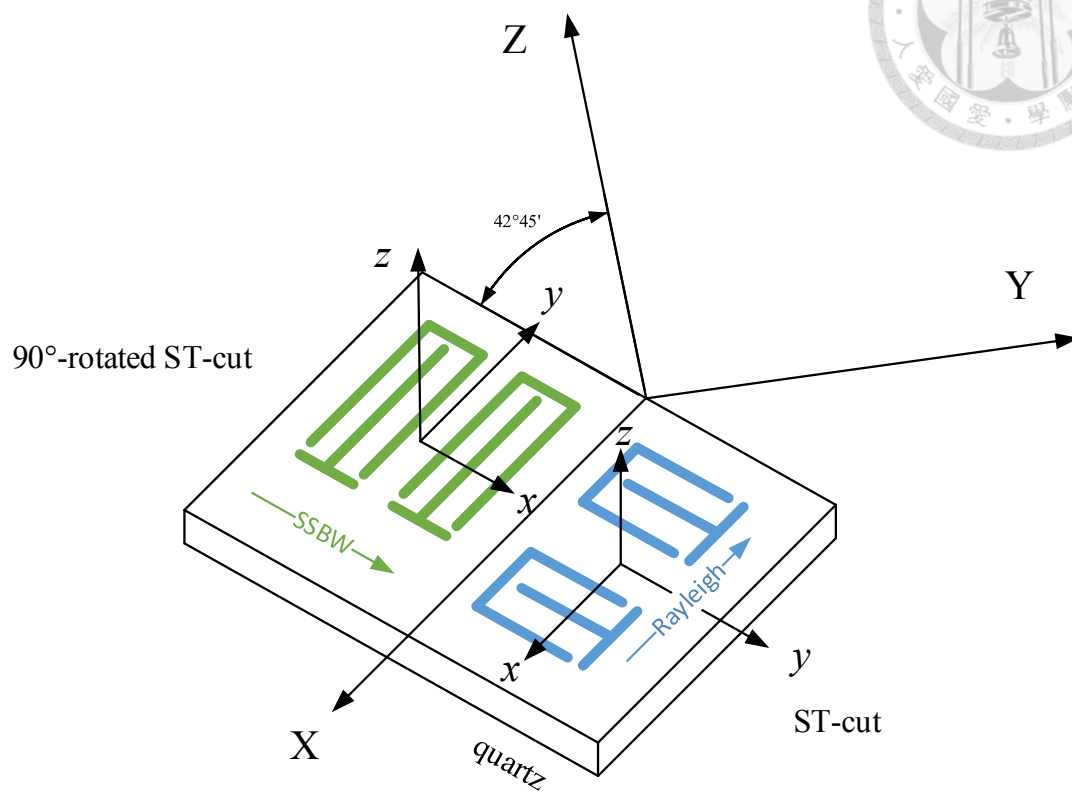


Fig. 2.3 ST-cut and 90°-z-rotated ST cut.

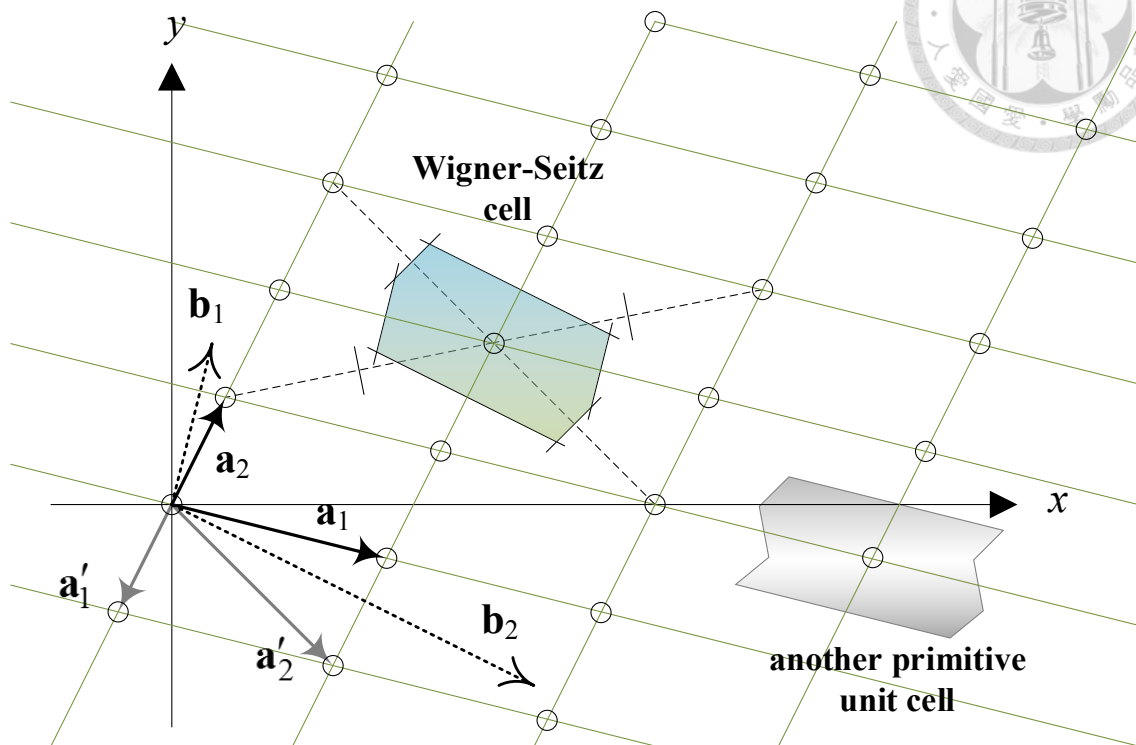


Fig 2.4 The bases of the direct and reciprocal lattices and the unit cells of a 2-D lattice.

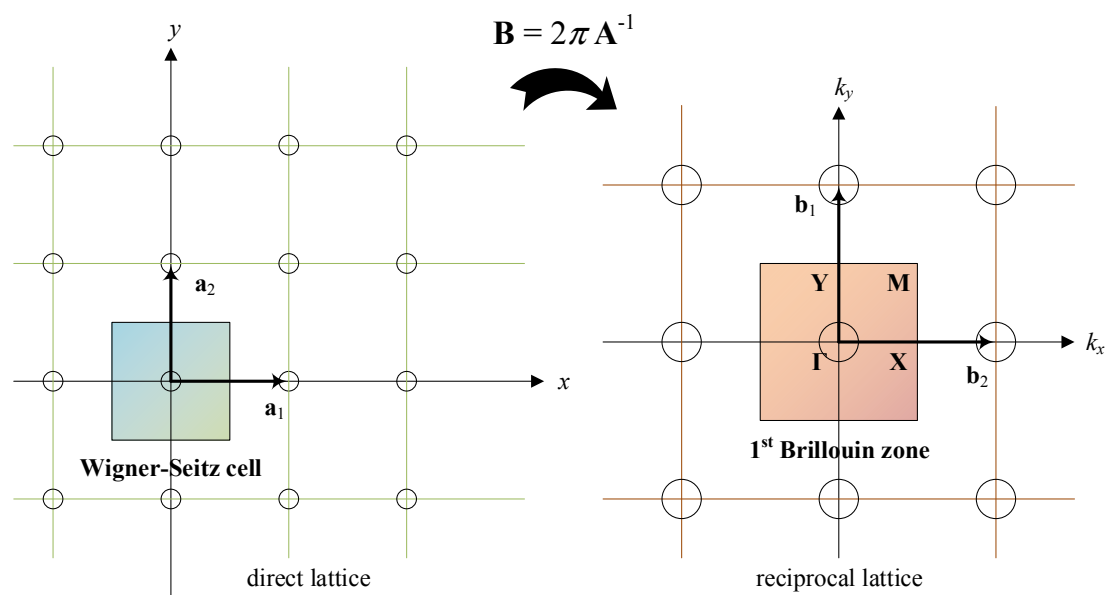


Fig 2.5 The Wigner-Seitz cell and the 1st Brillouin zone of a 2-D square lattice.

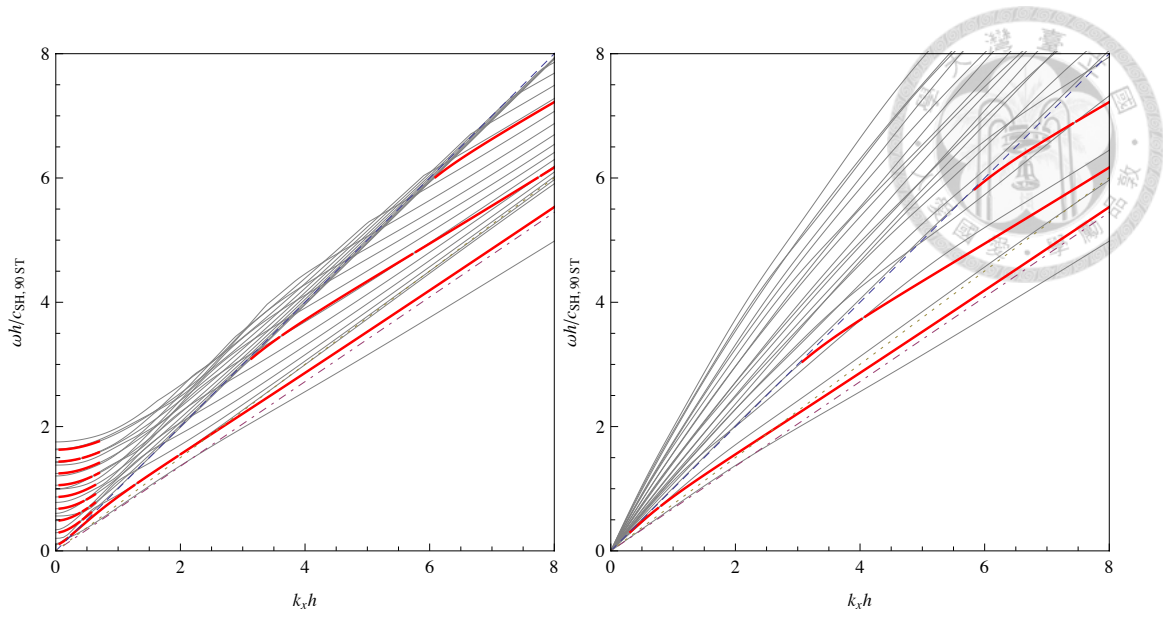


Fig 2.6 Love wave dispersion (thick red lines) obtained by a thickness-fixed ($10h$) plate model (left) and a thickness-varying (1.6λ) model (right). The blue dashed line and the purple dot-dashed line indicate the SH bulk wave of the substrate (90ST quartz) and the S wave velocity of the guiding layer (CVD SiO₂), respectively.

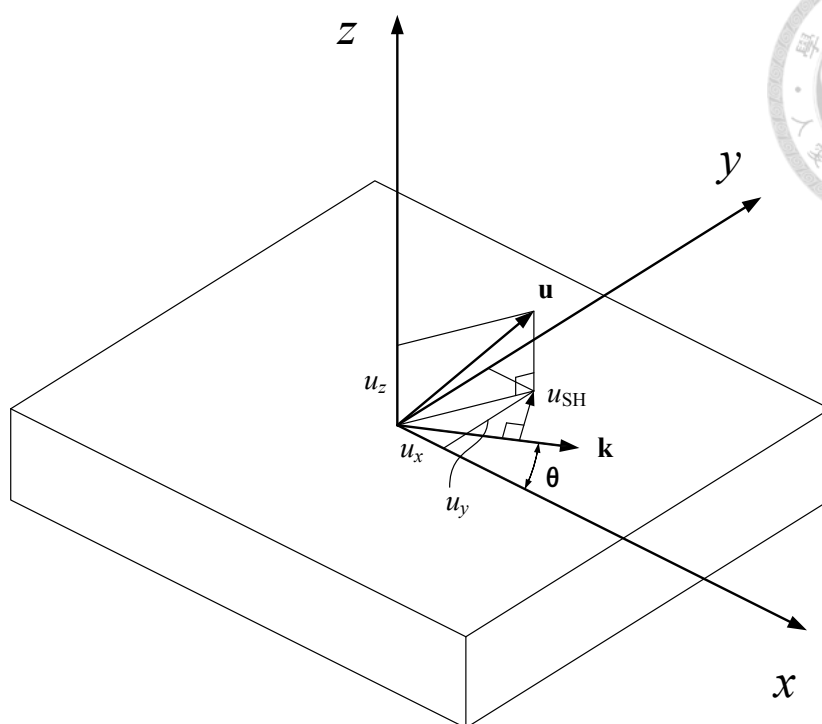


Fig 2.7 Determination of the SH component.

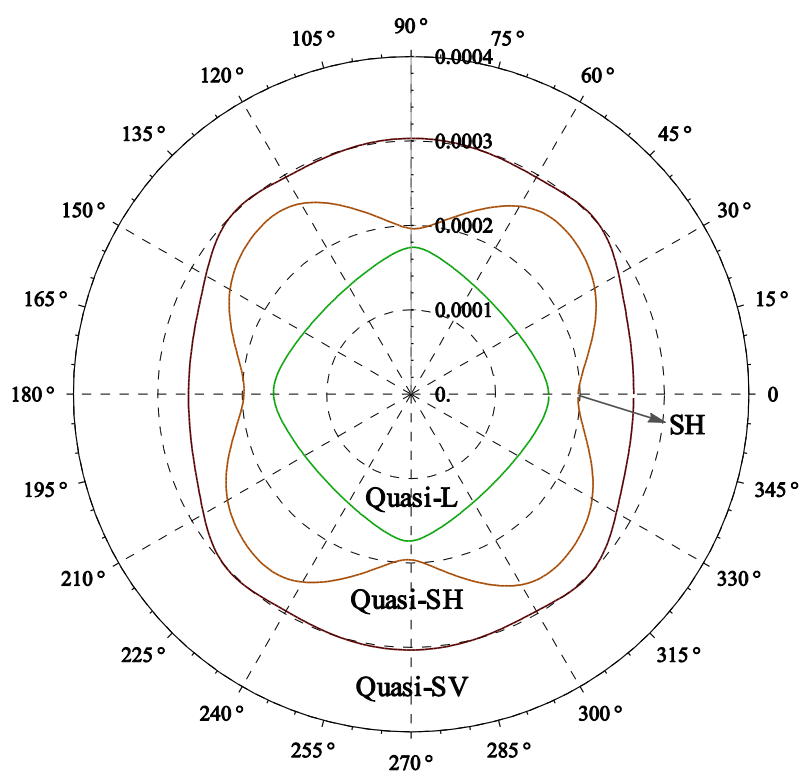


Fig 2.8 Slowness of the bulk waves in 90°-rotated ST-cut quartz along its xy -plane

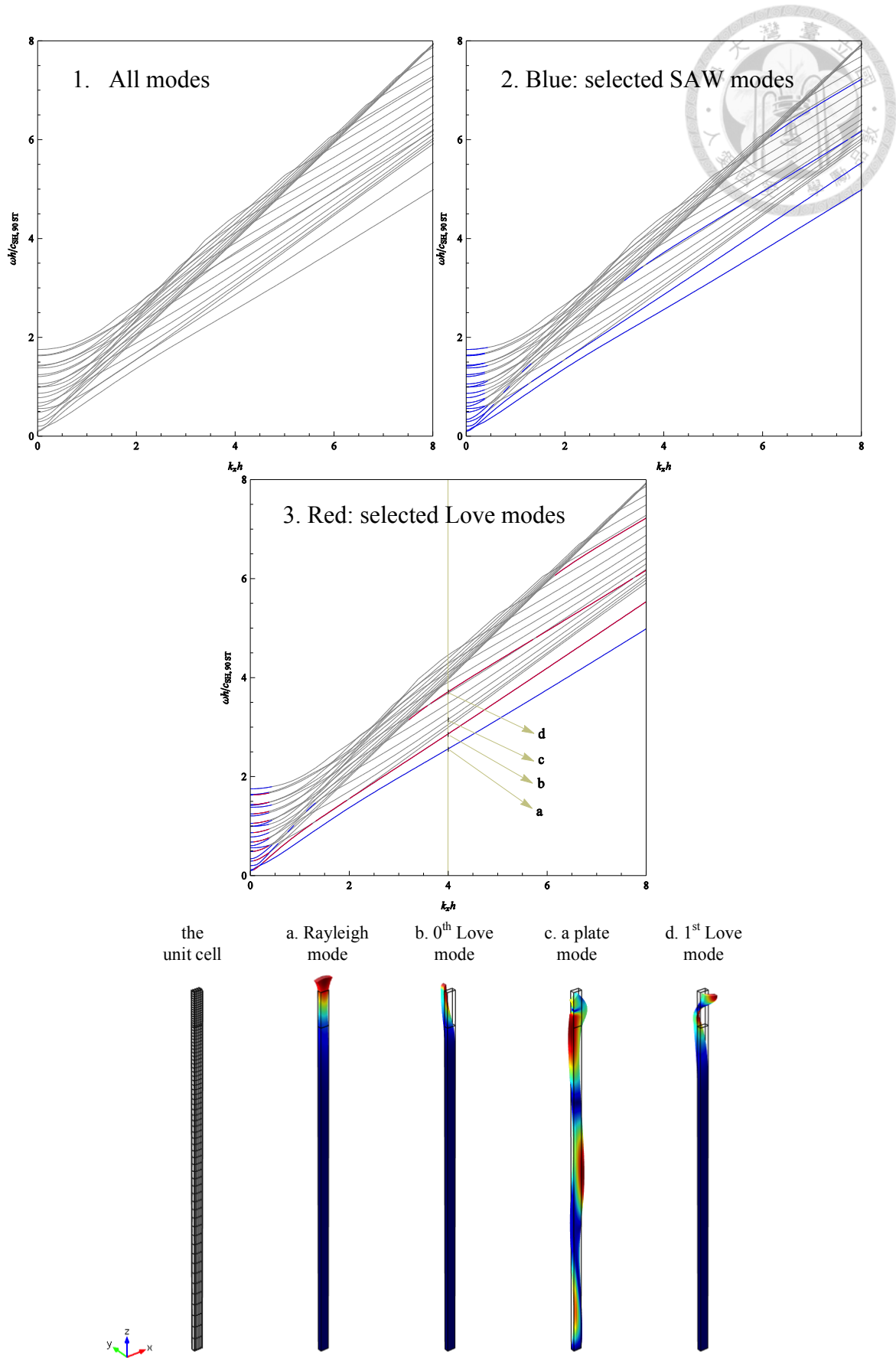


Fig 2.9 Love modes selecting

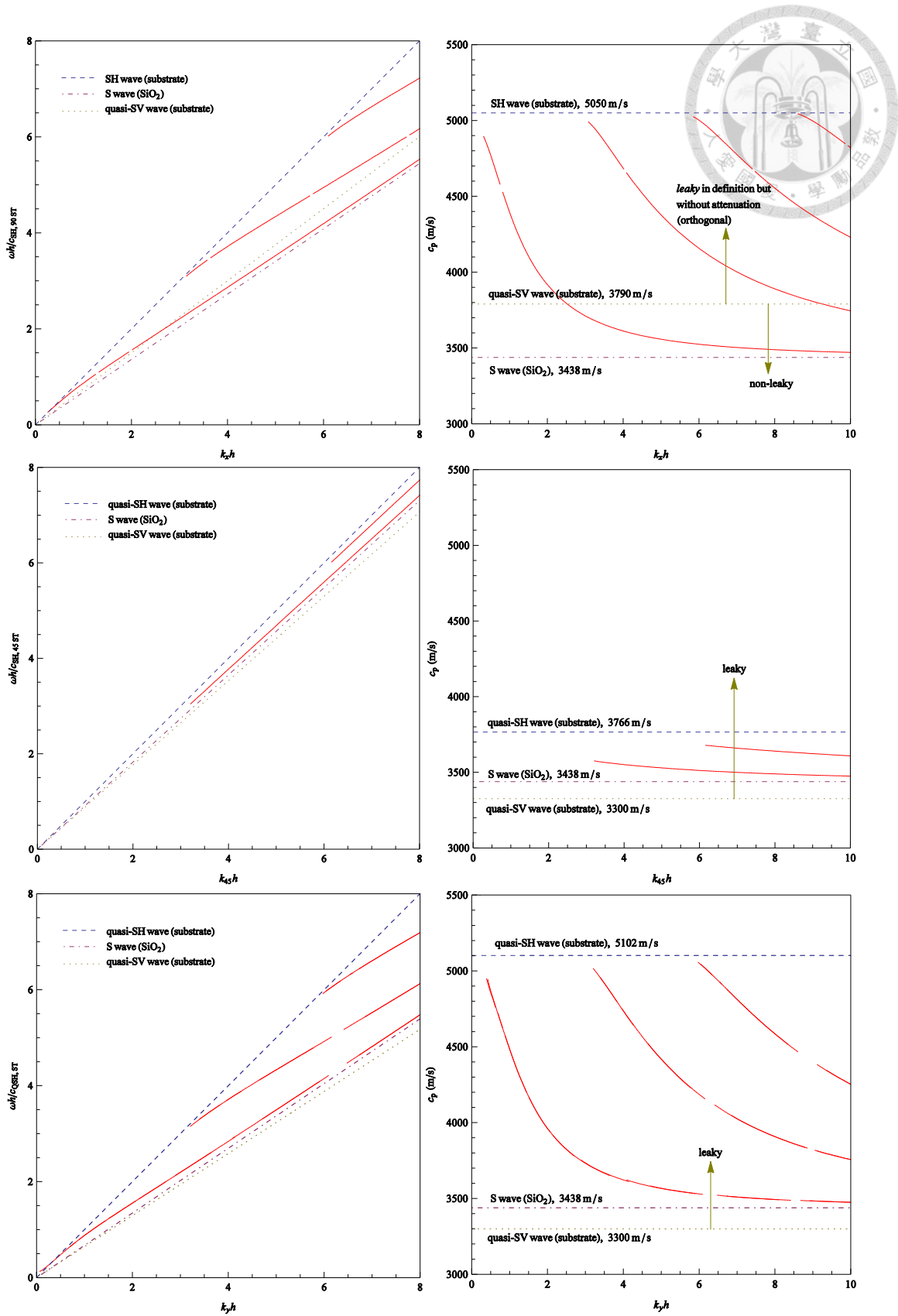


Fig 2.10 (Quasi-) Love waves' dispersions along 0° (upper), 45° (mid) and 90° (lower) off the x -axis.

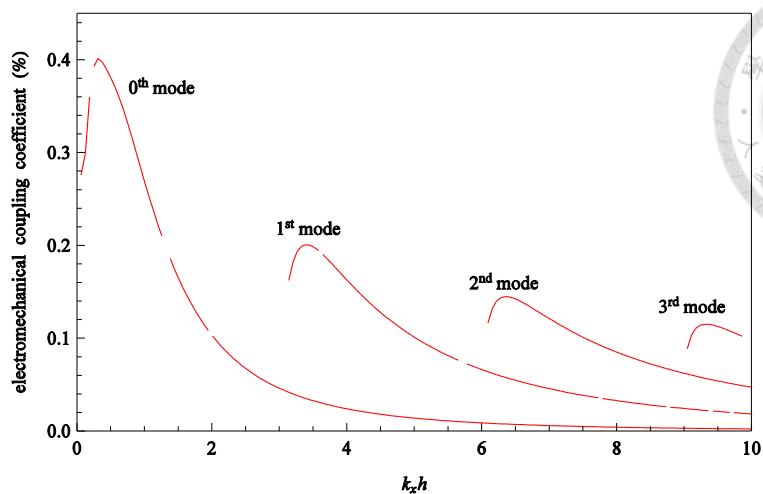


Fig 2.11 Electromechanical coupling coefficient

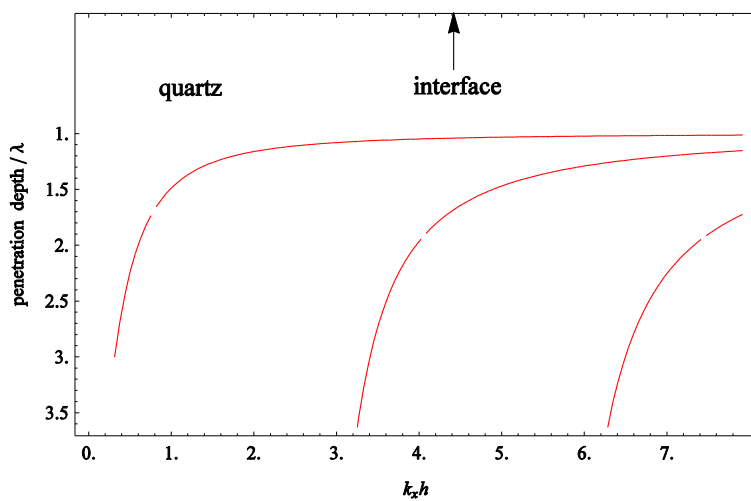


Fig 2.12 Penetration depth of the Love waves

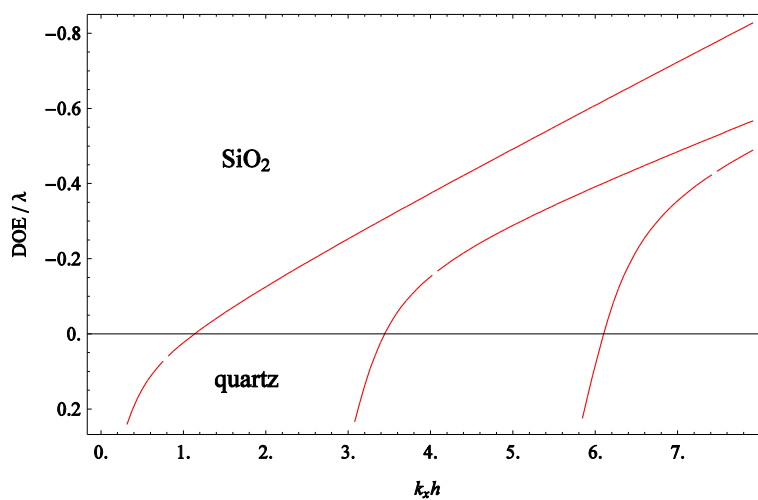


Fig 2.13 DOE of the Love waves

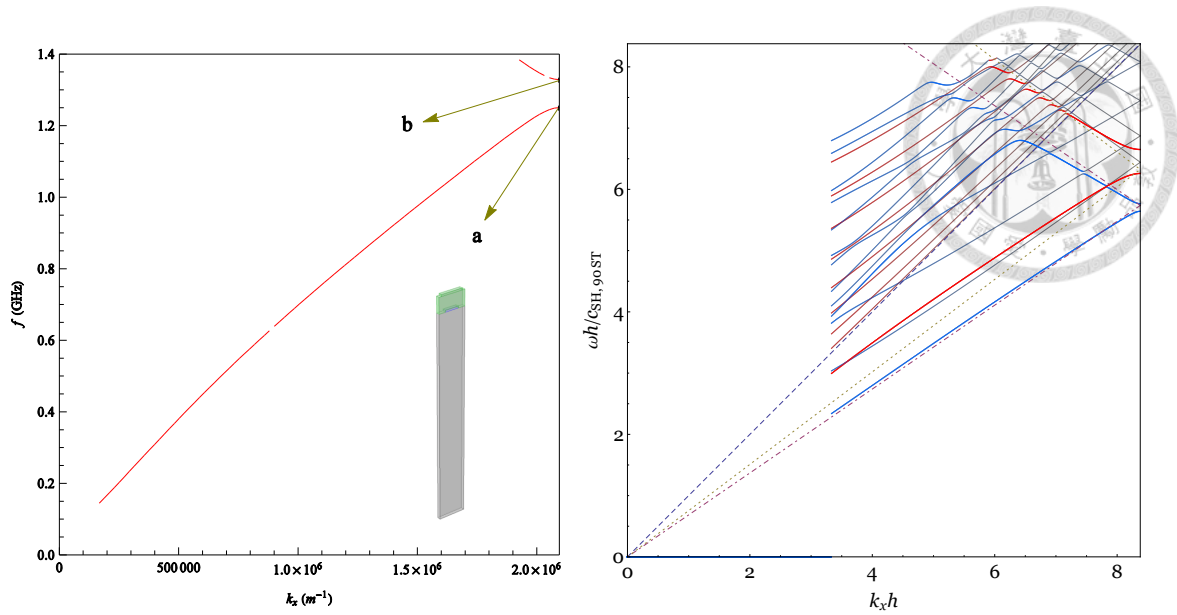


Fig 2.14 Love wave dispersion of the SiO₂/IDT/quartz structure, with SiO₂ thickness = 0.9 μm, IDT aluminum thickness = 100nm, IDT pitch = 3 μm.

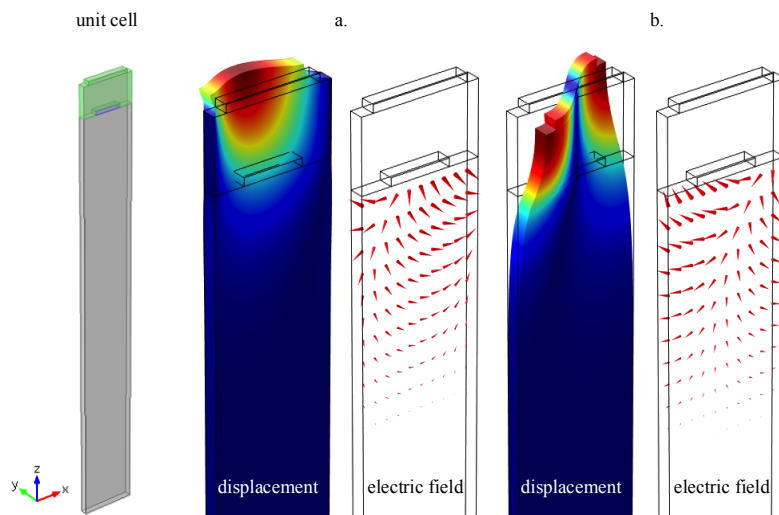


Fig 2.15 Two resonant modes on the lower (a) and the upper (b) edge of the stop band.

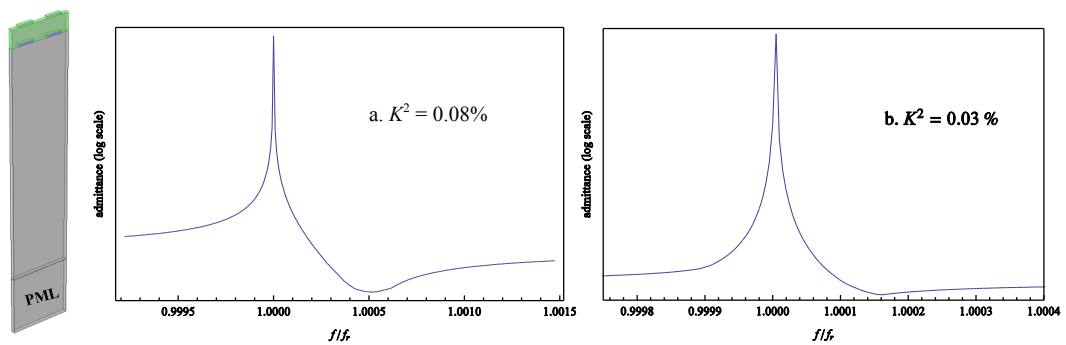


Fig 2.16 The admittance of the IDT consists of infinite pairs around the two modes.

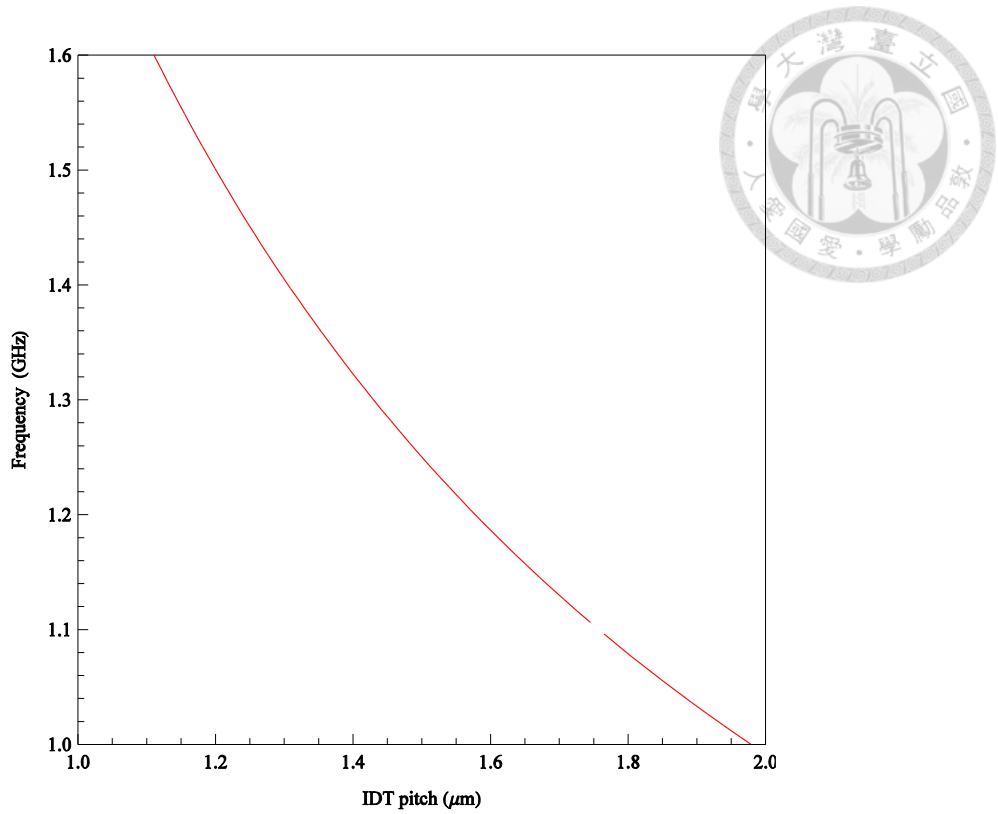


Fig 2.17 The relation of the excited frequency vs. IDT pitch of the $\text{SiO}_2/\text{IDT}/\text{quartz}$, with SiO_2 thickness = $0.9 \mu\text{m}$, IDT aluminum thickness = 100nm , IDT pitch = $3 \mu\text{m}$.

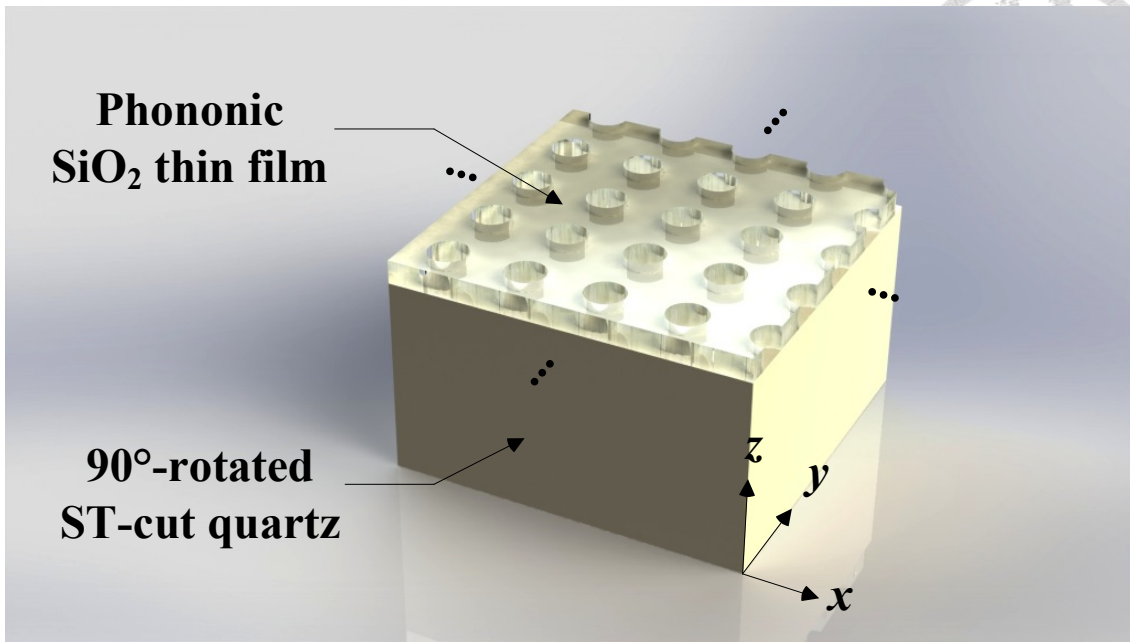


Fig 2.18 A schematic drawing of the phononic SiO₂/quartz layered structure

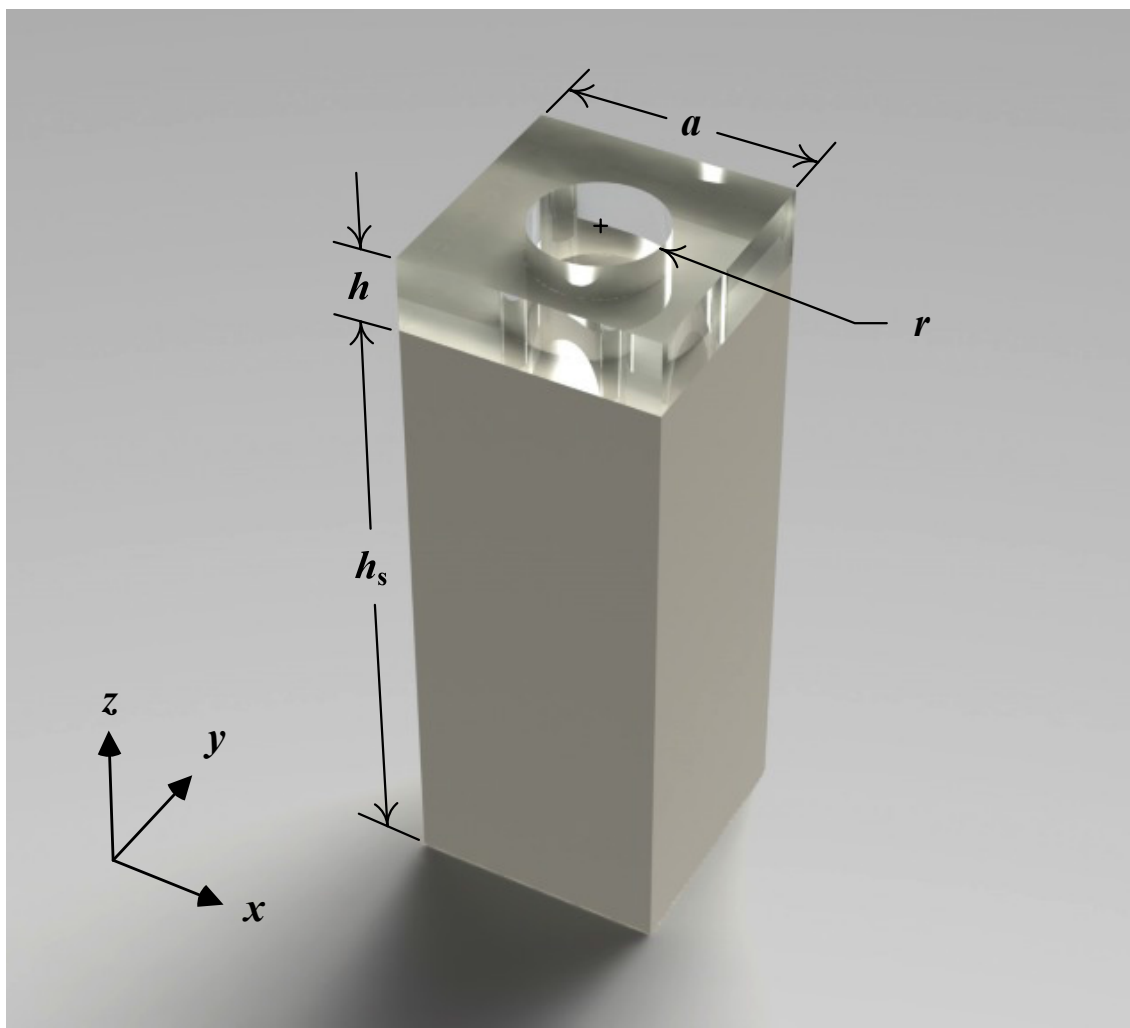


Fig 2.19 The unit cell of the phononic SiO₂/quartz layered structure

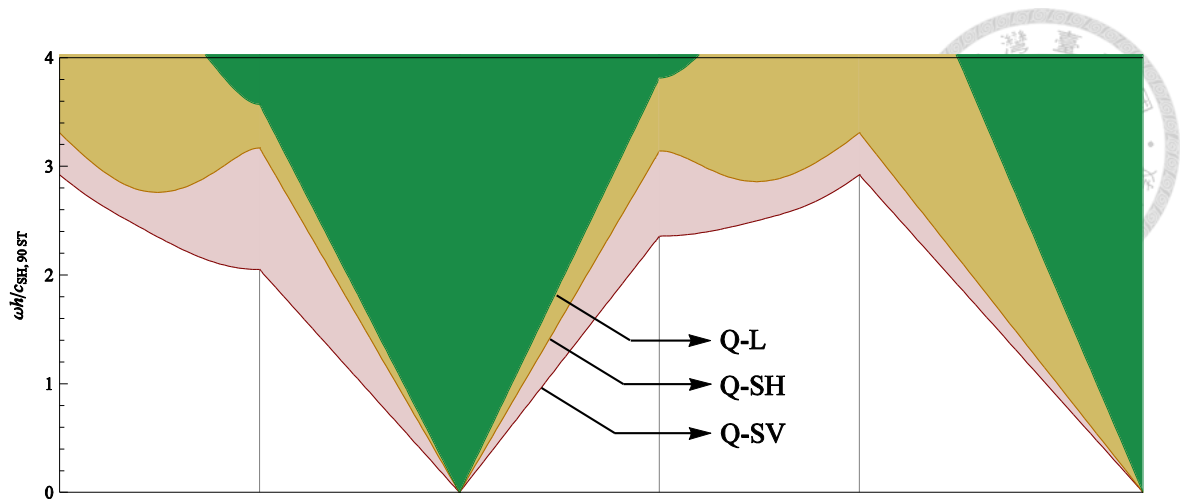


Fig 2.20 The sound lines

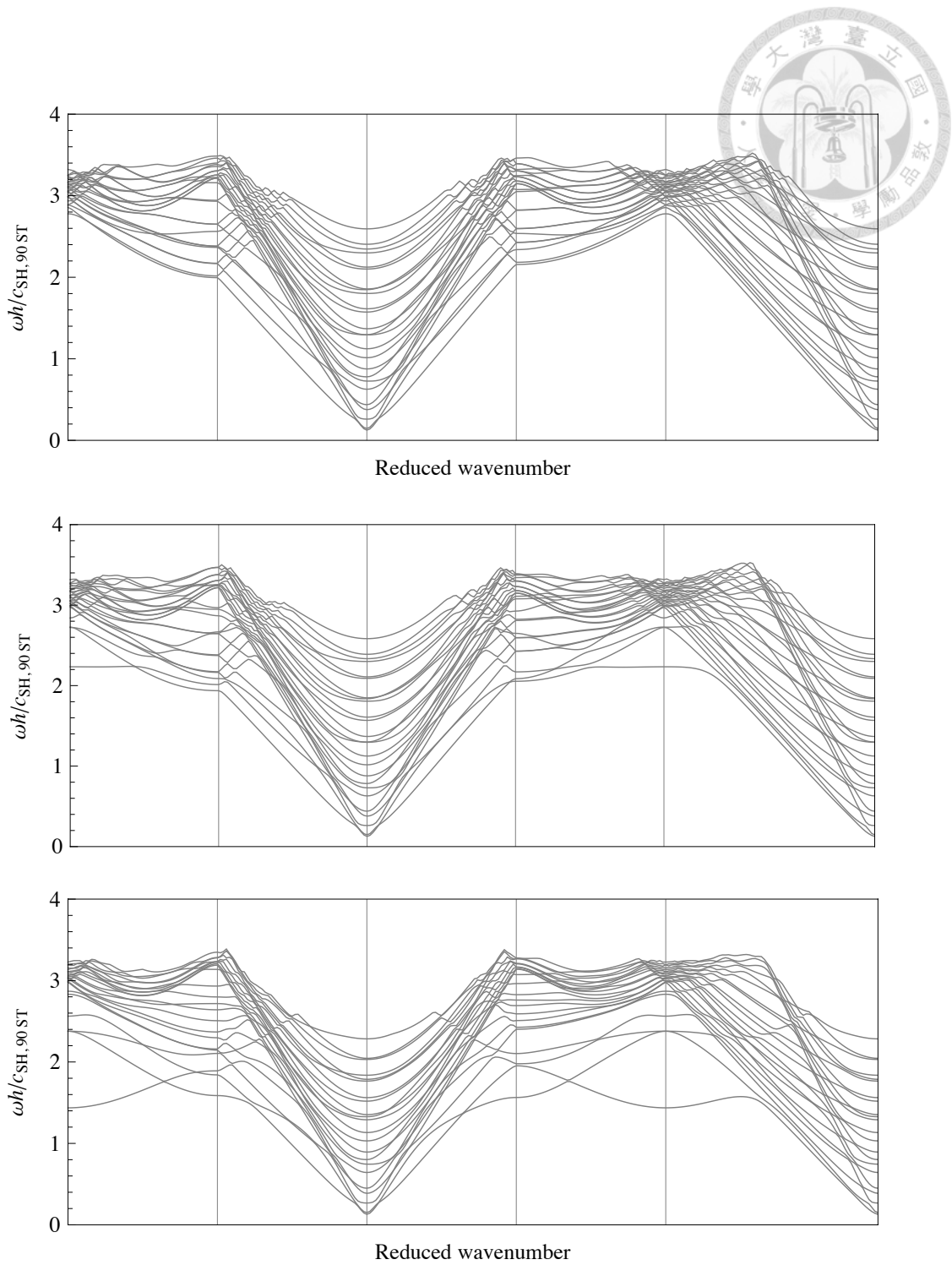


Fig 2.21 (unfiltered) calculated band structures of phononic crystals with (a) $r/a = 0.1$, (b) $r/a = 0.2$, (c) $r/a = 0.4$.

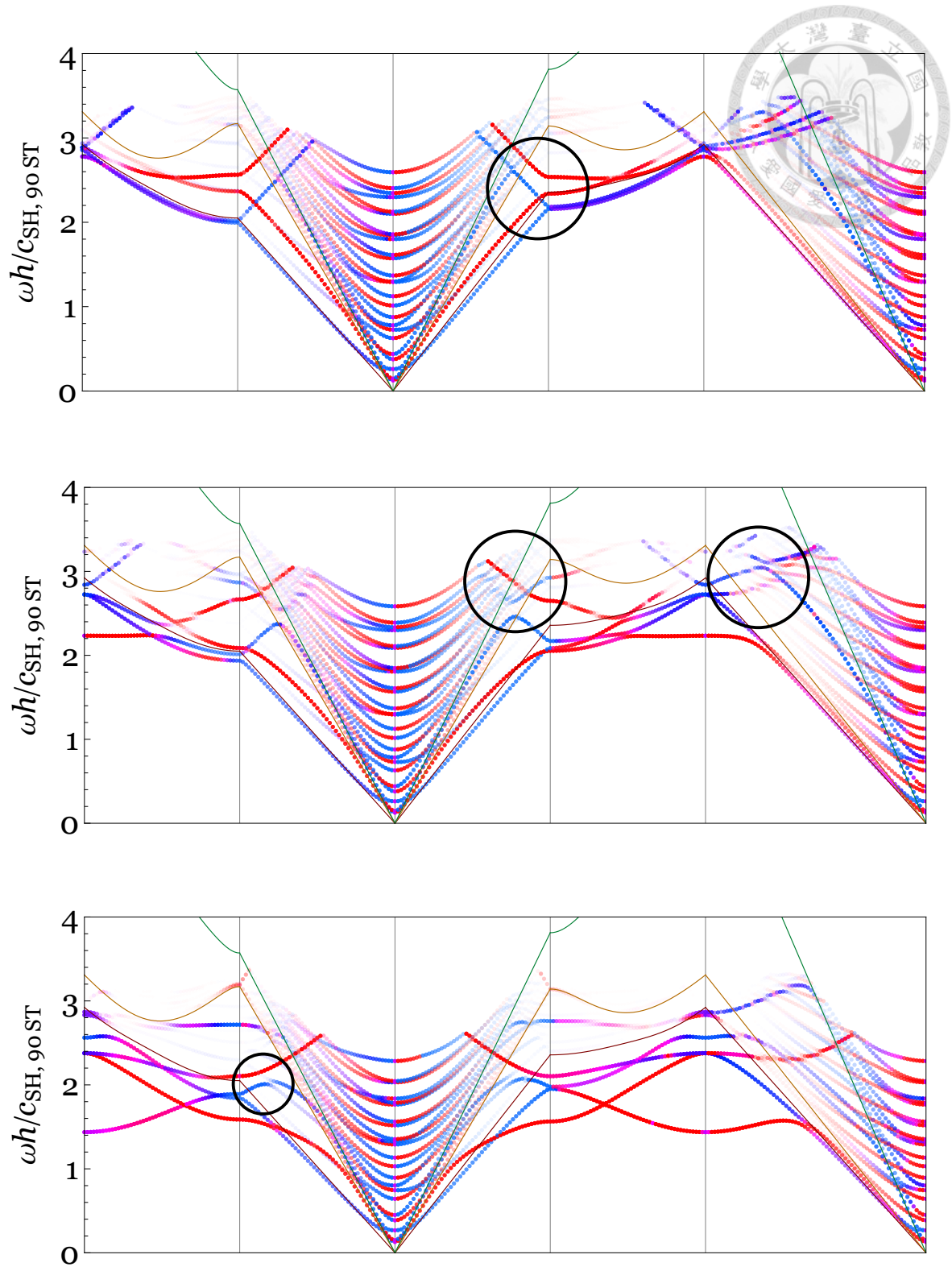


Fig 2.22 the color marked band structures of phononic crystals with (a) $r/a = 0.1$, (b) $r/a = 0.2$, (c) $r/a = 0.4$.

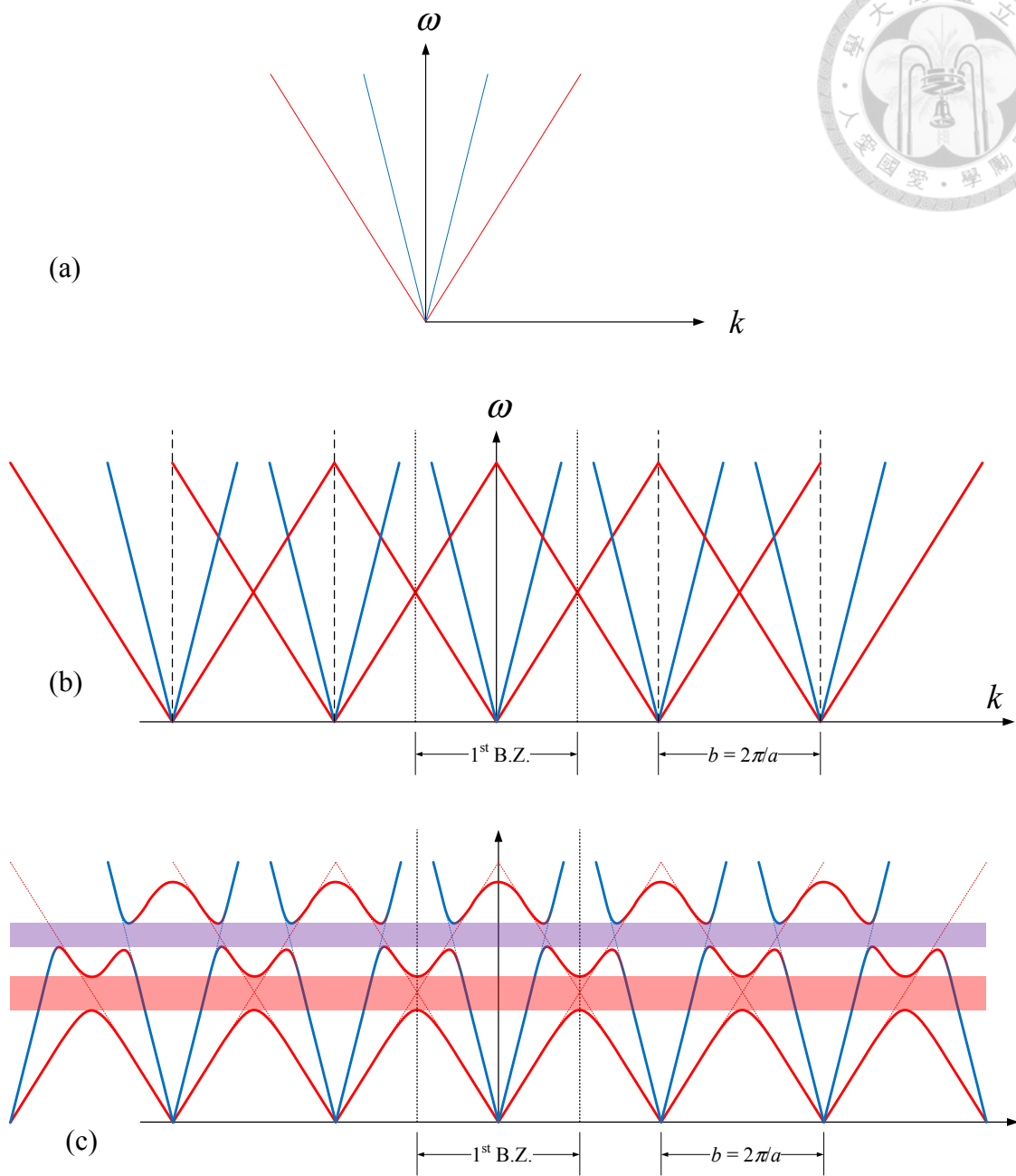


Fig 2.23 (a) Dispersion of a homogeneous medium. (b) Dispersion of a periodic structure with vanishingly small modulation (empty lattice). (c) Dispersion of a periodic structure, mode coupling happens when two modes are close and not orthogonal.

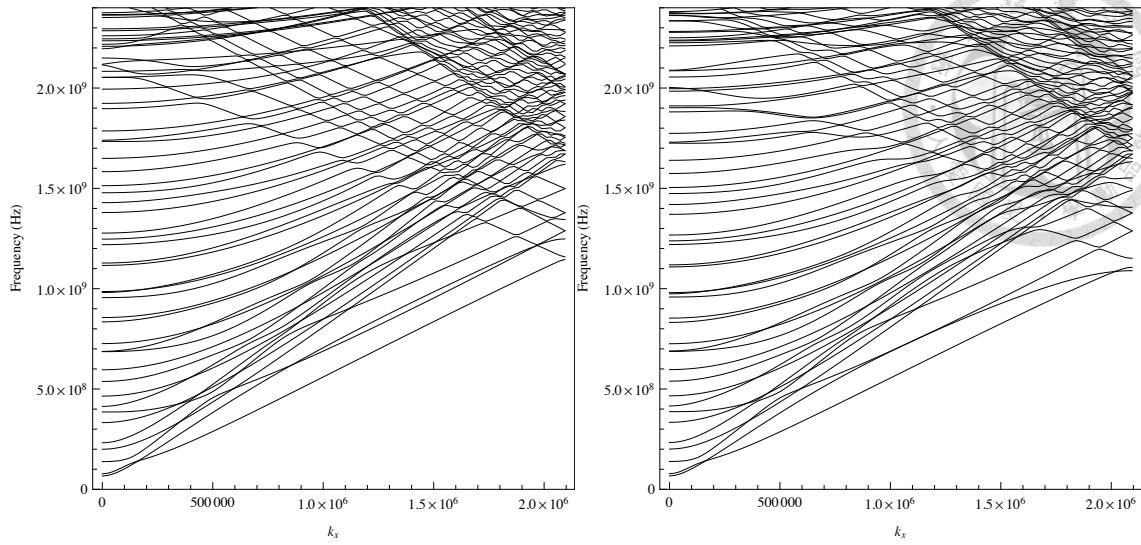


Fig 2.24 Unfiltered dispersion data of PCs with $r/a = 0.1$ (left) and 0.2 (right).

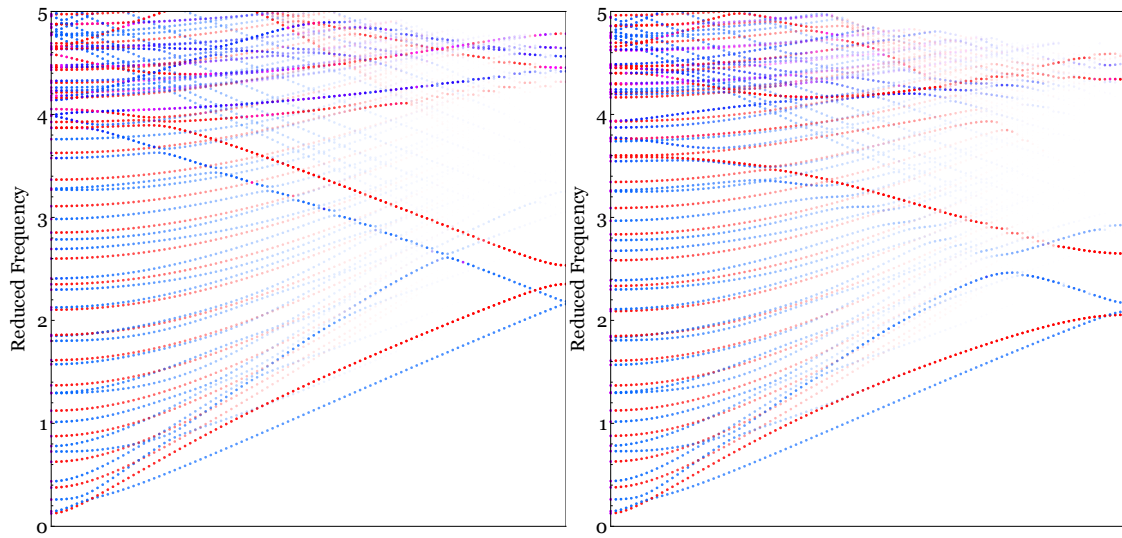


Fig 2.25 Colored dispersion data of PCs with $r/a = 0.1$ (left) and 0.2 (right).

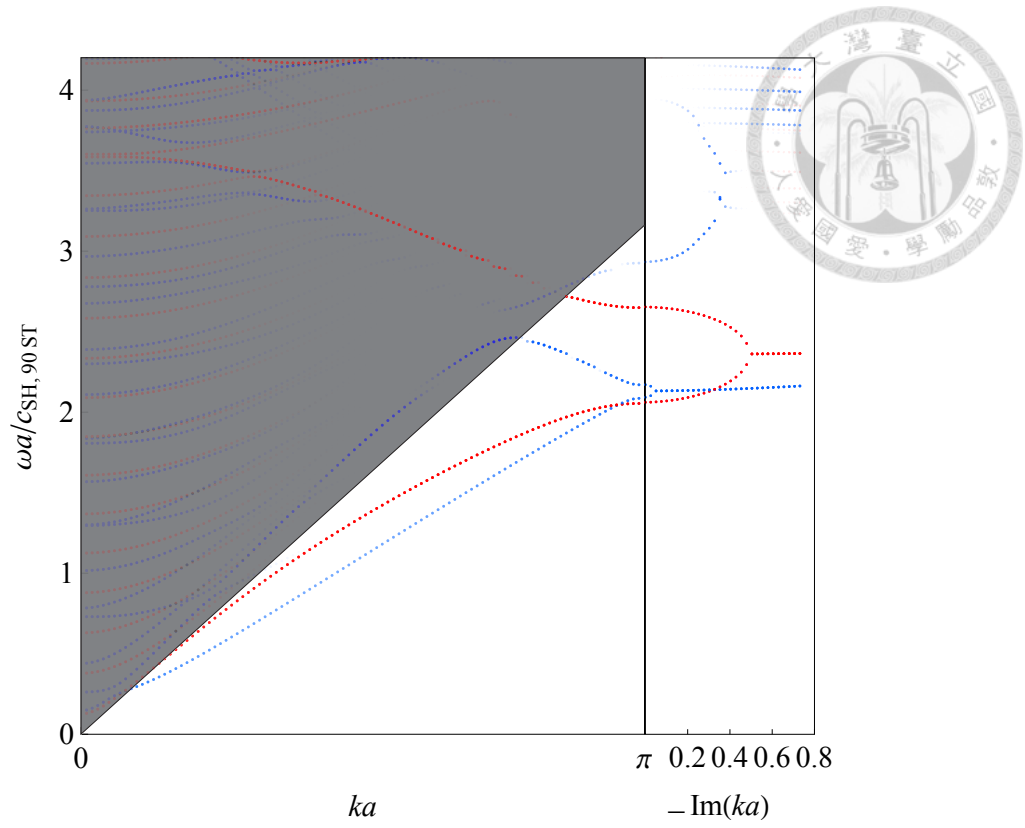


Fig 2.26 The complex band structure of the PC with $r/a = 0.2$.



Chapter 3

Design of a One-port Resonator

In this chapter we investigate the reflection performance of the proposed phononic structure and give an optimized geometry design of the one-port Love wave resonator. Also the design of the transmission experiment verifying the band gap existence is given in the text.

3.1 Design parameters of a one-port resonator

The plane structure of the 1-port resonator is shown in Fig 3.1. The two PC arrays act as the reflecting gratings and a Love wave resonant cavity forms between them. The IDT is then placed in the cavity to excite the desired resonant mode.

The number of IDT pairs (the number of wavelengths in the cavity) is usually a few dozens. Increasing the number may help on the Q factor due to the $\sin\omega/\omega$ frequency response of the IDT. If we consider the IDT as a phase array of line sources with 180° phase shift, large numbers of the IDT pairs may also reduce bulk wave loss since it has high acoustic directivity along the surface. The number also affects the electrical impedance of the device.

The aperture of the IDT can adjust the electrical impedance magnitude as well. But

it should be much larger than the wavelength to reduce the diffraction. In our resonator the aperture is set to be 100 times the wavelength. It is not but can be optimized for impedance matching with adjacent components in further applications, if needed.

The number of the PC columns is adequate for about 5~10. It shows good reflection even with only 3 columns of PCs, which is shown in the next section. Too much of the PCs increase the total size of the device only.

And the delay distance between the PCs and the IDT is a critical dimension in the resonator. There will be strong performance degeneration if there is a little bias on the delay distance. It can be optimized by the numerical method described in the upcoming sections.

3.2 Reflection on the PC border

We conducted a FEM simulation to investigate the reflection, transmission or scattering phenomenon on the PC border and find an effective reflective plane. The geometry is shown in Fig 3.2. We had 3 models with 3, 5, or 10 columns of PCs. We took only one row with periodic boundary conditions along the y -direction to reduce the calculation amount. The electric potential was applied on the interface of SiO₂ and quartz just as two pairs of IDT, as the green and the purple areas in Fig 3.2. They are away from the PC for a certain delay distance. Here the mechanical loading effect of the IDT is not considered so the pitch is determined by the Love wave velocity and the center frequency of the band gap. Then an AC power at the gap center frequency was driven, with sweeping the delay distance through a range. Perfectly matched layer (PML) was placed around the structure to reduce the unwanted reflected waves on the boundaries.

We first plot the displacement amplitude of the most left section on the interface of the model as Fig 3.3. Since the IDT generates both left and right propagating waves,

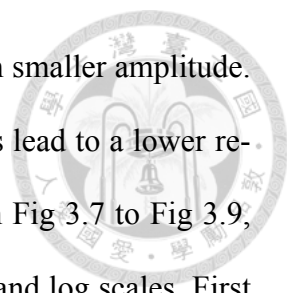
and part of the right propagating wave is reflected by the PC and interfered with the left propagating wave. From the interfered displacement amplitude the reflection coefficient could be obtain. Assume that there is an “effective reflective plane” around the border of the PC, with distance d away from the source. Part of the incident wave is reflected at this plane with reflection coefficient α , as shown in Fig 3.4. Then the interfered wave on the left is therefore

$$e^{+ikx} \left(1 + \alpha \cdot e^{ik2d} \right). \quad (3.1)$$

The absolute value of the numbers in the parentheses indicates the interference amplitude, and is plotted with different α in Fig 3.5. It is dependent on d , where the d just differs from our “delay distance” for a constant. The amplitude has a maximum $1+\alpha$ (the most constructive interference) and a minimum $1-\alpha$, the most destructive interference. So we can obtain the reflection coefficients of 3, 5, 10 rows of PCs from the maximums and minimums in Fig 3.3 by the equation

$$\alpha = \frac{\text{Max.} - \text{min.}}{\text{Max.} + \text{min.}}. \quad (3.2)$$

And they are 96.5%, 97.5% and 96.6%, respectively. It is surprising that the PC with only 3 rows has good reflection as well. We notice that in Fig 3.3 the second peak is slightly higher than the first one. This may due to that the bulk waves are also generated by the source and detected on the interface. The bulk waves have amplitude inversely proportional to the distance from the source. Since the estimated reflection coefficient is affected by the presence of bulk waves, the true reflection coefficient of PC for Love waves should be larger than the values mentioned above. We also plotted the interfered displacement amplitude at positions 0.5 and 1 times the wavelength beneath the interface to detect the skimming bulk wave, as shown in Fig 3.6. We can see the amplitude is much smaller and with lower reflection coefficients. The wavenumber of the skim-

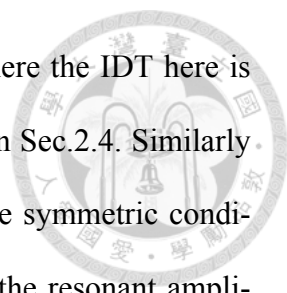


ming bulk wave is not matched with the IDT pitch, so it shows much smaller amplitude. And the skimming bulk wave is not reflected by the surface PC thus lead to a lower reflection coefficient. A series of plots of the simulation are shown in Fig 3.7 to Fig 3.9, where the color indicates the displacement amplitude in both linear and log scales. First the constructive and destructive interferences are obvious. And focusing on the log scale plots, for example Fig 3.7 (c), we see a yellow beam toward the left with shallow skimming and this is obviously the SH-type bulk wave. And in Fig 3.7 (d) the yellow part looks like a sector, it is the color of both the Love wave and the bulk wave. Although it looks like leakiness but we know that the Love wave is NOT leaky as its phase velocity is slower than that of the SH bulk wave. And if we look at Fig 3.9 (d), we see the skimming bulk wave can propagate beneath the PC. The bulk wave can be reduced by increasing the number of IDT pairs, since their wavelength are not matched and the Love wave is non-leaky.

Back to the reflection/transmission problem. The incident wave amplitude can be obtained as $(\text{Max.} + \text{min.})/2$, thus the transmission coefficient can be found by the ratio of the amplitude on the right of PC to the incident amplitude. And the scattered amount into the bulk is obtained by $1 - \text{reflection coefficient} - \text{transmission coefficient}$.

3.3 Optimization for the delay distance

In the previous section, a delay distance can be found such that a most constructive interference is achieved. However with the mechanical loading effect of the IDT, the interference amplitude becomes complex as Fig 3.11. This may be due to the internal reflection of the metal gratings. Instead of finding the delay distance for the strongest interference, we directly made a resonator model as Fig 3.12, and optimize the delay distance such that a greatest resonance is in the cavity. In this model we have 10.5 pairs

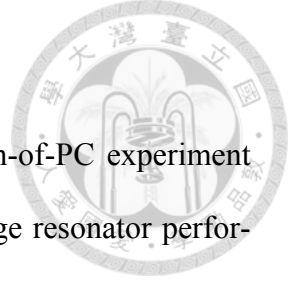


of IDT in the resonator and 10 columns of PCs as the reflector, where the IDT here is with full consideration of the mechanical loading effect, as we did in Sec.2.4. Similarly we take only one row with periodic conditions. We also applied the symmetric condition to reduce the degree of freedom in FEM calculation. We plot the resonant amplitude vs. the delay distance in Fig 3.13. The optimized delay distance is where the resonant amplitude achieves a maximum. We found maximums show repeatedly with spacing about half the wavelength, but not exactly. Also the response rapidly deteriorates as the delay distance slightly deviate from the optimized value.

3.4 Resonator evaluation

The frequency response of the optimized resonator is calculated, and the electrical admittance $Y = G + iB$ is plotted in Fig 3.14. The Q factor of the resonator is about 1400 estimated by the fraction of the resonant frequency over the half-conductance bandwidth. And the resonant displacement amplitude is plotted in Fig 3.15. To find out where the energy leaks, we plotted the mechanical power flux $P_i = T_{ij}\dot{u}_j$ as Fig 3.16 and the out flux component on the model boundary as Fig 3.17. In Fig 3.17 we see green color on the right boundary of the guiding layer. It means no energy loss from here for the PC reflects almost all Love wave. But a little lower we see a red region. It is the skimming bulk wave traveling under the PC and the energy leaves the resonator, it can be reduced with large number of IDT pairs. On the bottom boundary we see red and blue colors. The energy loss here may due to the finite-depth model with PML, which is different from the real situation.

In the simulation the material damping and the ohmic loss have not been included which may make the Q factor decrease more or less.



3.5 Experiment setup

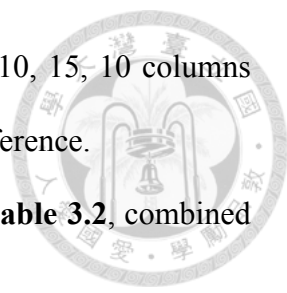
There are two sub-experiments in the thesis: The transmission-of-PC experiment that verifies the existence of the partial band gap, and the GHz range resonator performance experiment. The setups are described below.

Fabrication ability should be considered when designing the dimensions. We chose the resonant frequency of the resonator (i.e., center frequency of the band gap) to be 1.25 GHz, thus the geometry dimensions are determined from the dimensionless band structure (Fig 2.22) as follows: lattice constant $a = 1.5 \mu\text{m}$; PC hole radius $r = 300 \text{ nm}$; CVD SiO_2 film thickness $h = 900 \text{ nm}$. It seems comfortable with the NEMS process containing electron beam lithography.

In the transmission-of-PC experiment we use slanted finger IDTs (SFITs) to generate and receive broad band Love waves by electrical signals, and the PC array is placed between the 2 SFITs thus the transmission of Love waves through the PC can be measured from the insertion loss of the two ports. Since the calculated partial band gap is located from 1.09 ~ 1.40 GHz, the excited frequency of the SFIT is set from 0.95 ~ 1.56 GHz, which the bandwidth is twice the gap width. From the frequency-pitch relation plot (Fig 2.17) we found the SFIT pitch should be from 1.15 ~ 2.12 μm . The corresponding minimum line width is 570 nm. It is reported that asymmetric arrangement in the number of SFIT pairs helps reject the side lobe responses, so the numbers of SFIT pairs are set to be 32/40 pairs or 24/30 pairs. The aperture is set to be 100 times the maximum wavelength (423 μm) to reduce the diffraction effect. The maximum tilt angle (40 pairs SFIT) is 5° . And the propagation distance is designed long enough such that the triple transit echo is not mixed with the direct signal in time domain in order to apply the time gating technique when analyzing the measured signals. The SFIT geom-

etry parameters are listed in **Table 3.1**. Transmission of PCs with 10, 15, 10 columns were measured. Also SFIT signal without PCs were measured for reference.

As for the resonator we have 10.5, 30.5, 60.5 pairs of IDT as **Table 3.2**, combined with 10, 15, 20 columns of PC reflector, totally 9 versions.



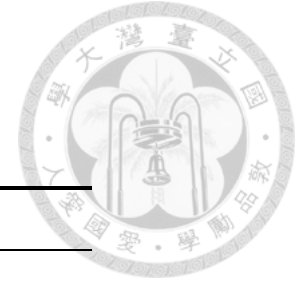


Table 3.1 SFIT parameters.

	#1	#2
# of Pairs	32.5/40.5	24.5/30.5
Pitch	1.15 ~ 2.12 μm	1.15 ~ 2.12 μm
Aperture	423 μm	423 μm
Maximum tilt angle	4°/5°	3°/4°
Propagation length ^a	332 μm	251 μm
Aluminum thickness	100 nm	100 nm

^a The propagation length is measured from center to center of the SFITs.

Table 3.2 IDTs for resonators.

# of Pairs	10.5, 30.5, 60.5
Pitch	1.50 μm
Aperture	300 μm
Aluminum thickness	100 nm

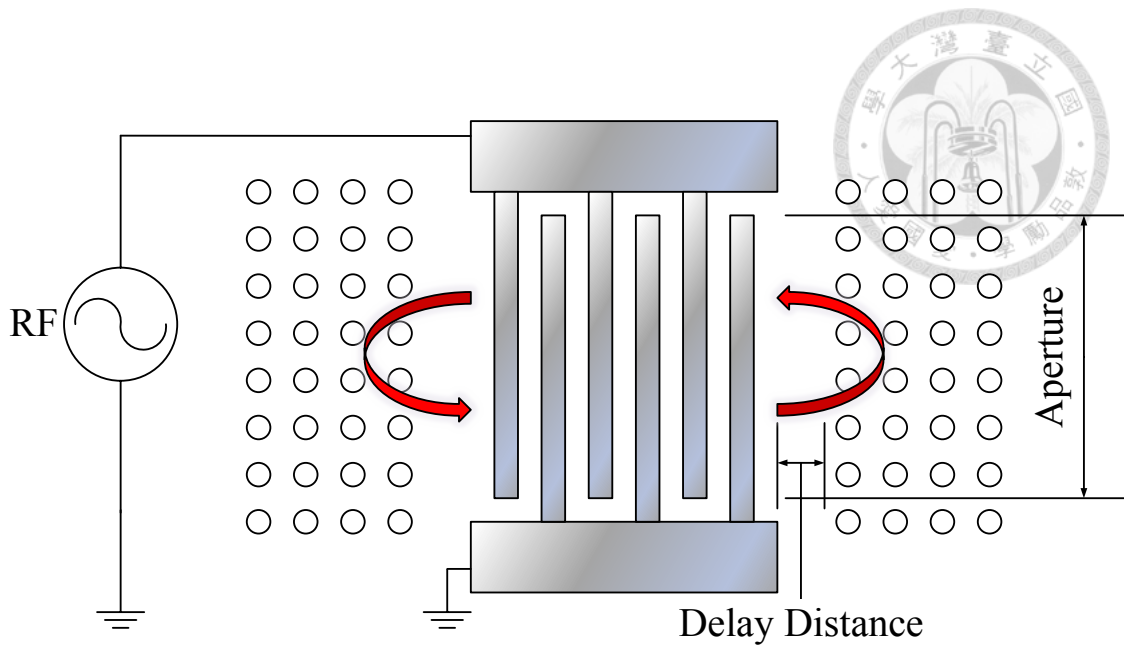


Fig 3.1 A schematic drawing of the layout of the one-port resonator

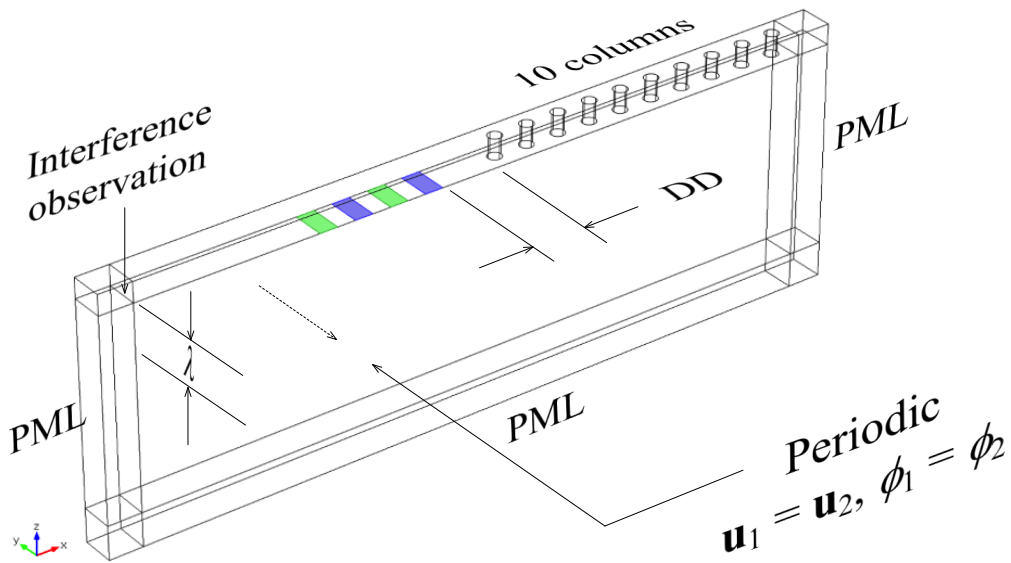


Fig 3.2 Geometry of the FEM simulation investigating PC reflection

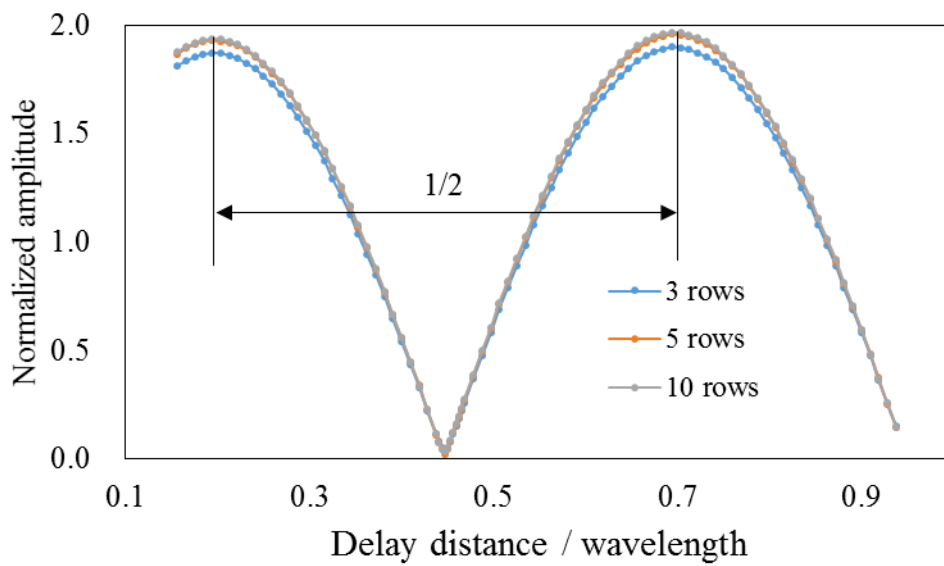


Fig 3.3 interfered displacement amplitude

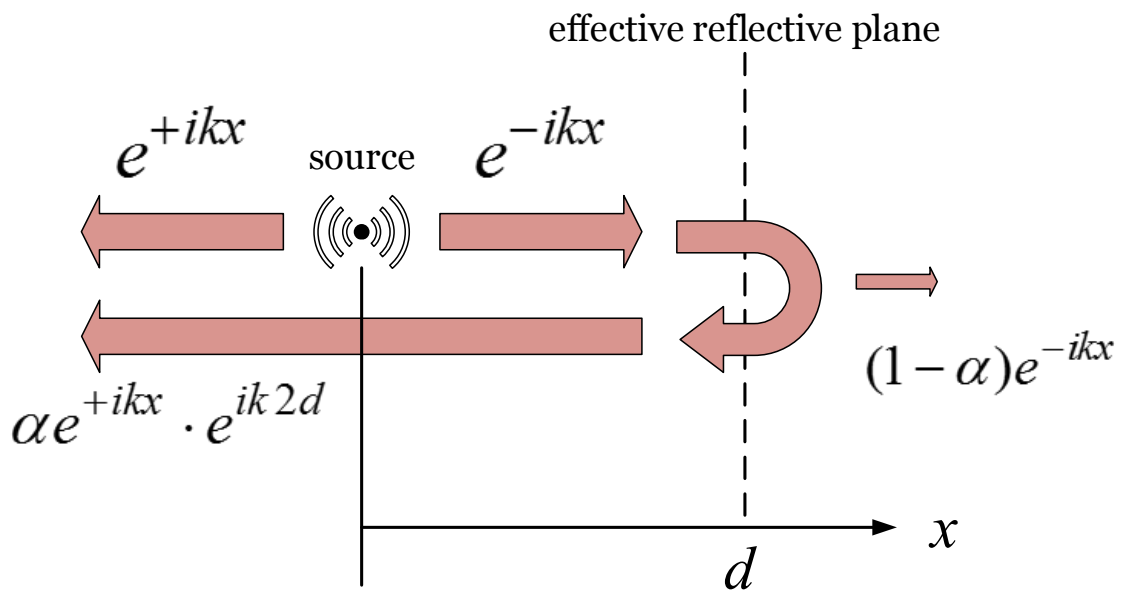


Fig 3.4 A schematic drawing shows the reflection at the effective plane

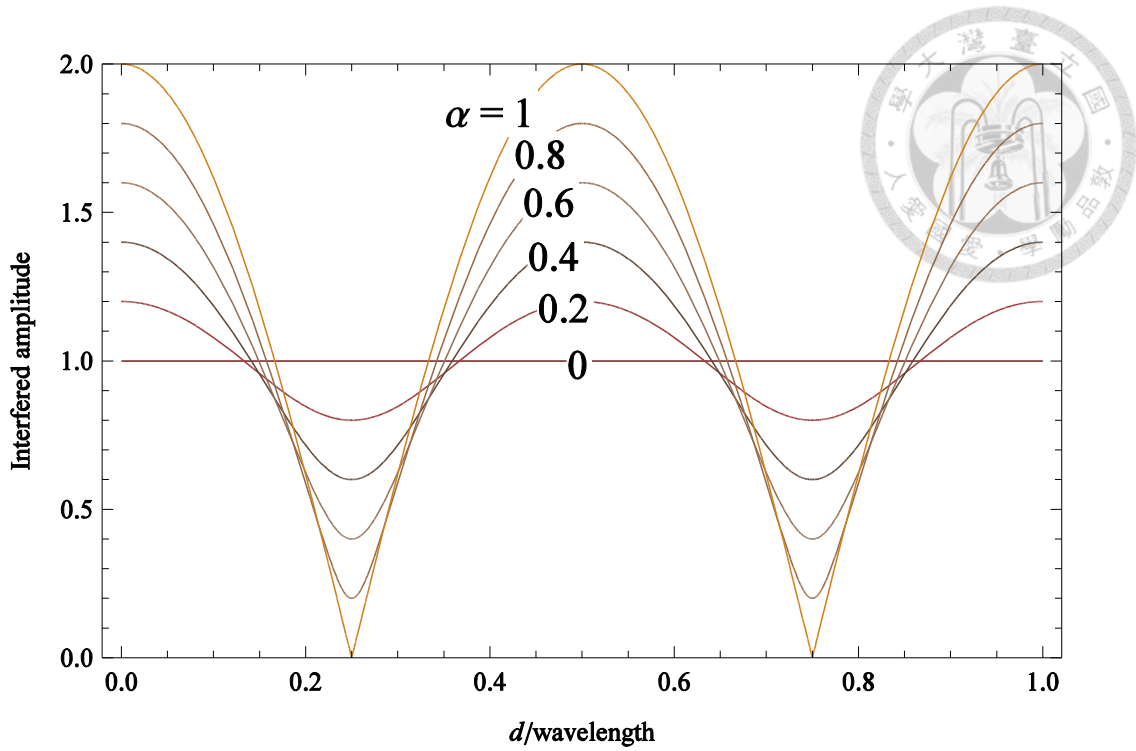


Fig 3.5 Interfered amplitude vs. $d/\text{wavelength}$ with different α .

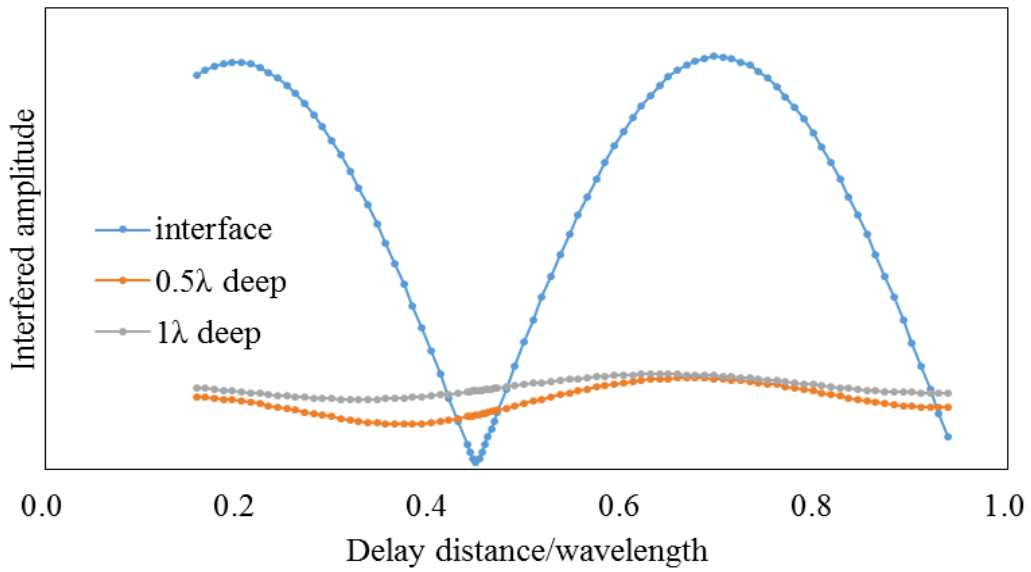


Fig 3.6 interfered displacement amplitude at different depth

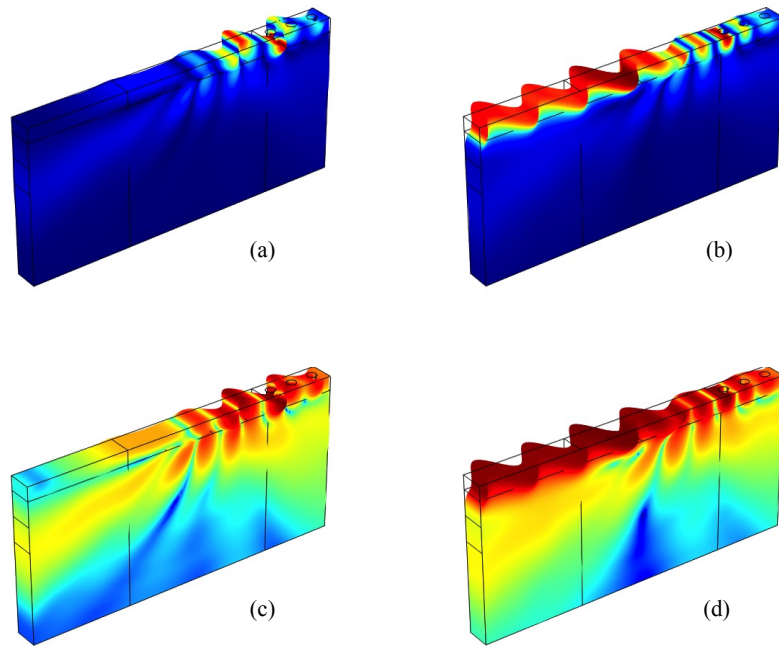
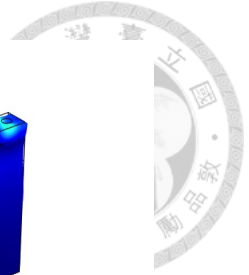


Fig 3.7 Reflection simulation on 3 rows of PC. (a), (c): destructive interference. (b), (d): constructive interference. (a), (b): colors indicate the y -displacement in linear scale. (c), (d): colors indicate the y -displacement in log scale.

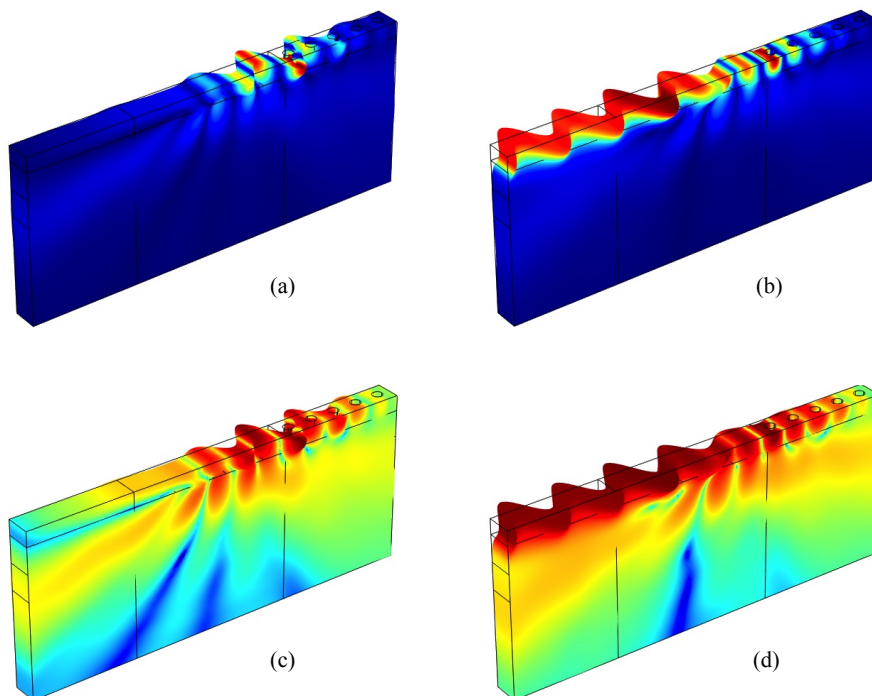


Fig 3.8 Reflection simulation on 5 rows of PC. (a), (c): destructive interference. (b), (d): constructive interference. (a), (b): colors indicate the y -displacement in linear scale. (c), (d): colors indicate the y -displacement in log scale.

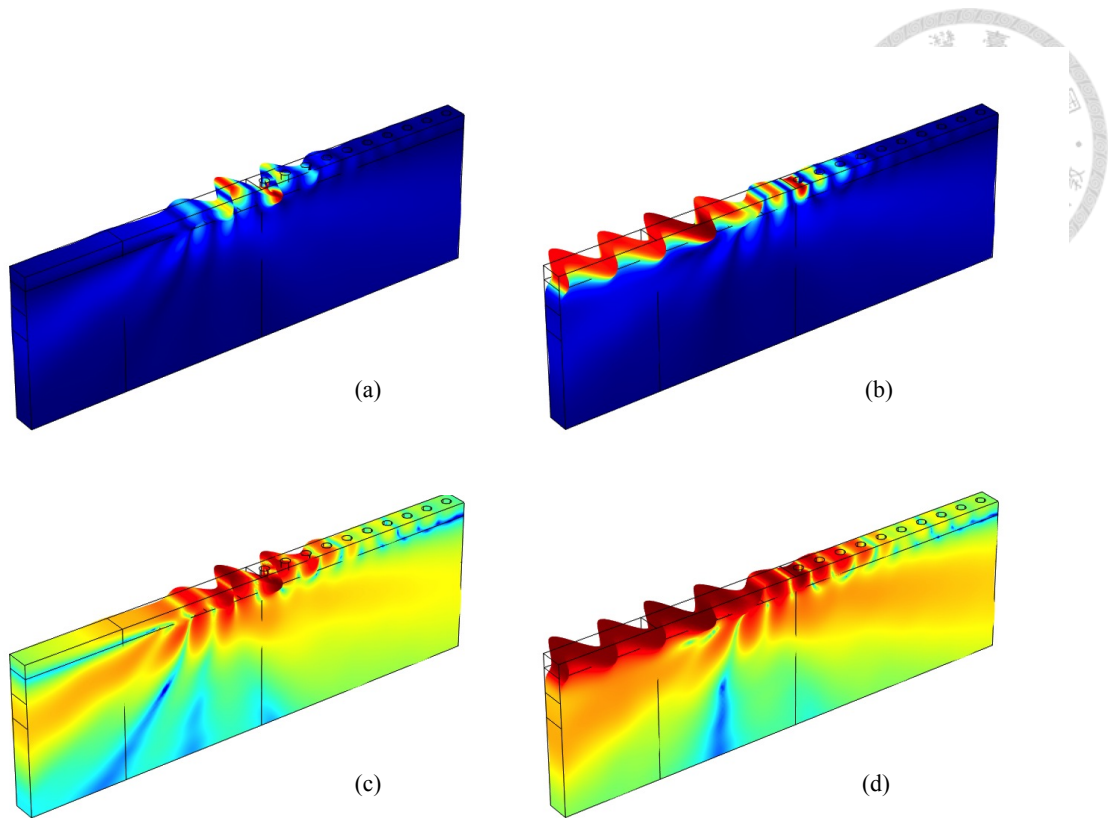


Fig 3.9 Reflection simulation on 5 rows of PC. (a), (c): destructive interference. (b), (d): constructive interference. (a), (b): colors indicate the y -displacement in linear scale. (c), (d): colors indicate the y -displacement in log scale.

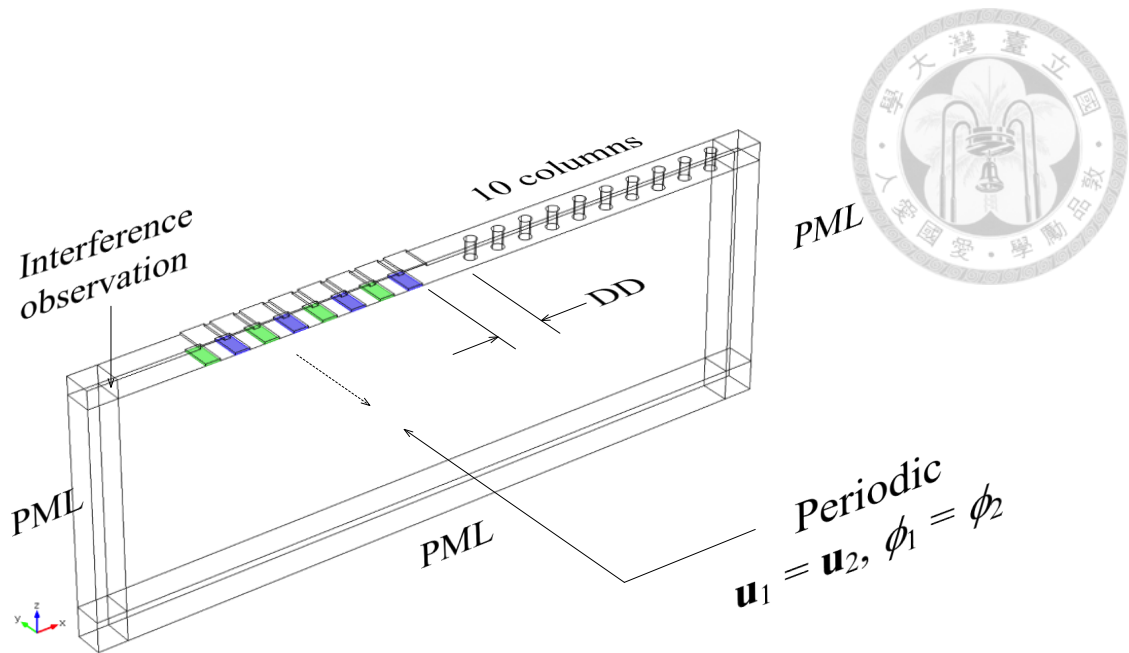


Fig 3.10 Geometry of the FEM simulation

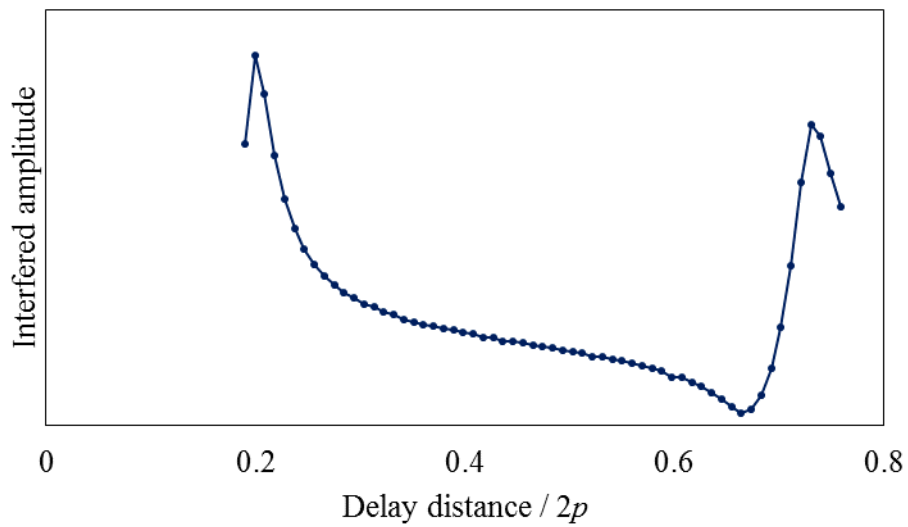


Fig 3.11 interfered displacement amplitude (with mechanical loading effect of IDT)

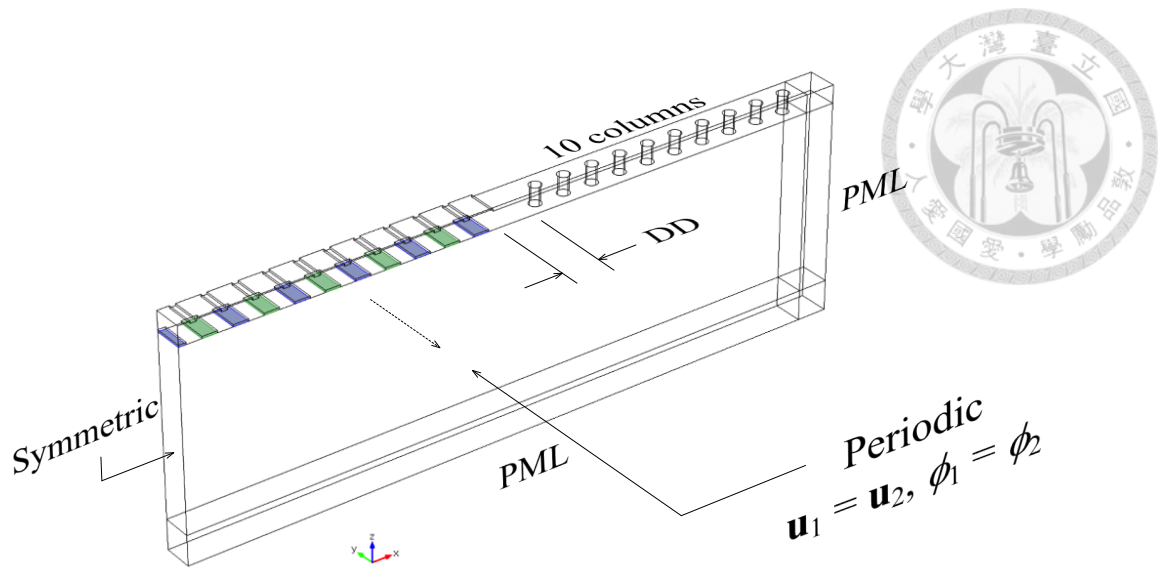


Fig 3.12 Geometry of the FEM simulation (resonator)

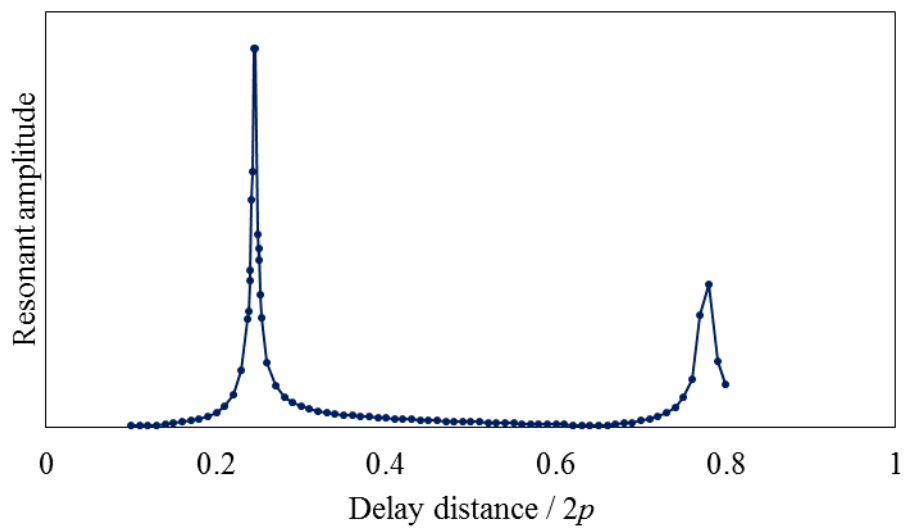


Fig 3.13 Resonant displacement amplitude (with mechanical loading effect of IDT)

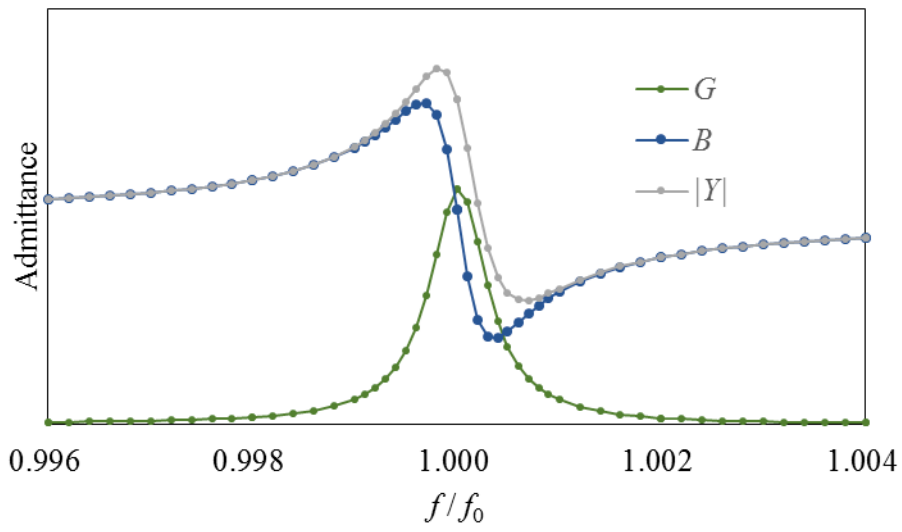


Fig 3.14 Simulated admittance of the resonator

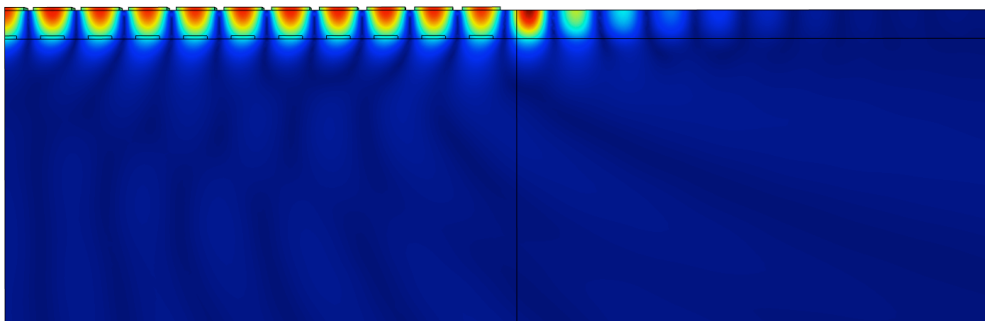


Fig 3.15 Transverse displacement amplitude at resonance

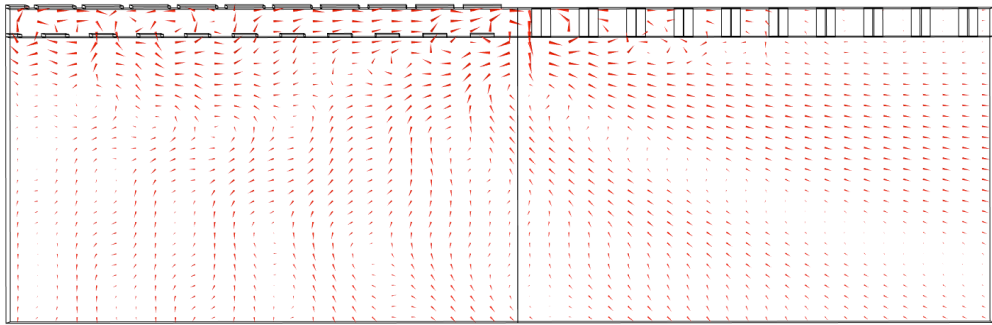


Fig 3.16 Mechanical power flux at resonance

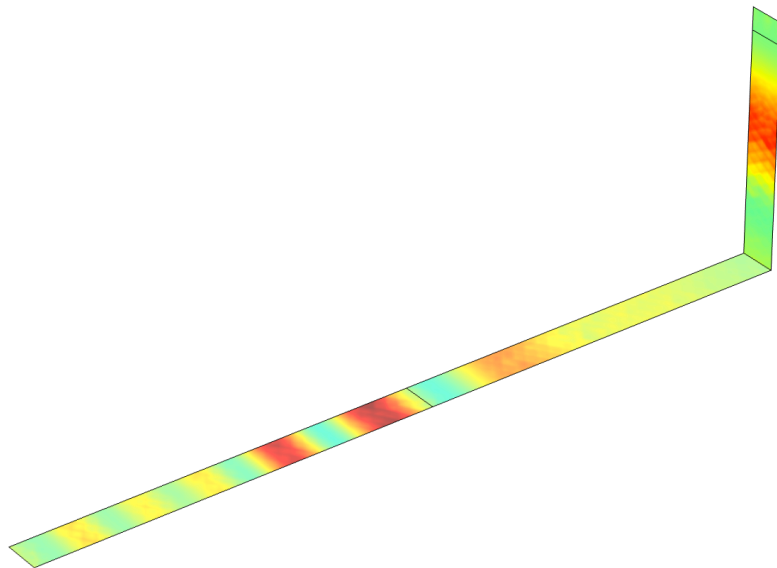


Fig 3.17 Mechanical power flux on the model boundary at resonance

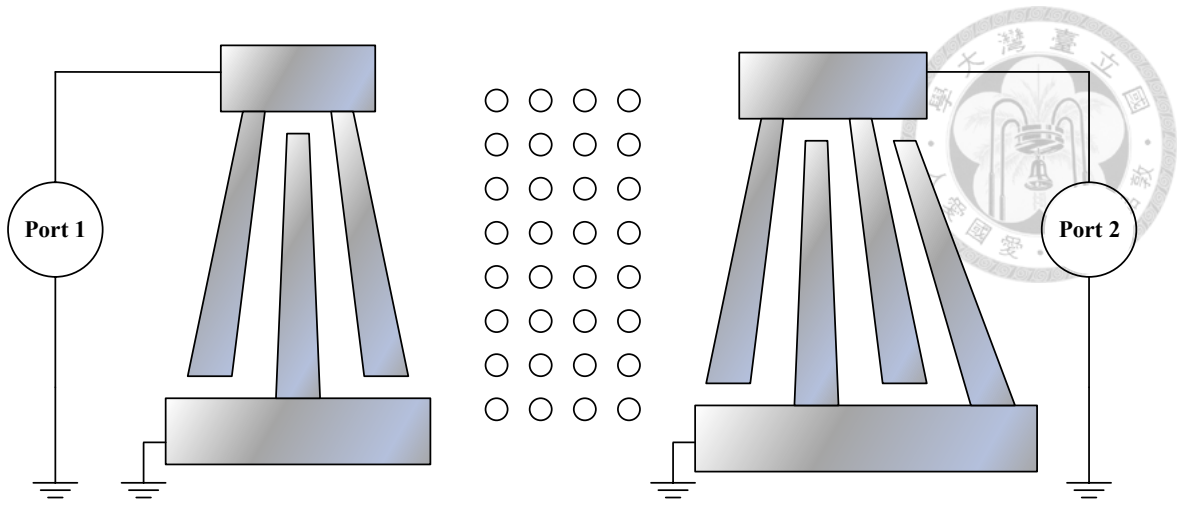


Fig 3.18 Experiment setup of PC transmission experiment.



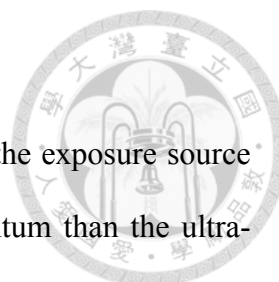
Chapter 4

Fabrications

In this chapter, the fabrication process is demonstrated in detail. Fig. 4.1 shows a schematic picture and Fig. 4.2 shows a section view of the device – a phononic SiO₂/IDT/quartz structure. Electron beam (EB) lithography was utilized to generate sub-micrometer patterns for IDTs and PCs. The patterns of aluminum wire and the contact pad window on SiO₂ film were defined by photolithography. All metal depositions were done through the evaporation method for good smoothness and ease for lift-off. SiO₂ film was deposited by a plasma-enhanced chemical vapor deposition (PECVD) method for the high deposition rate and the low residual stress. And the two SiO₂ etching step were accomplished through the reactive ion etching (RIE) process instead of wet etching method to reach vertical side walls. Full process charts are shown from Fig. 4.4 to Fig. 4.10.

4.1 Brief of EB lithography

In the fabrication process, three times of EB lithography were carried out. Some basic concepts of EB lithography and the methodology the author implemented will be briefed in this section.



4.1.1 Why EB lithography

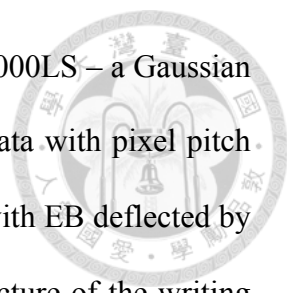
The resolution of lithography is limited by the wavelength of the exposure source and the resist thickness. Since the EB have a much higher momentum than the ultraviolet (UV) light used in photolithography, the wavelength of EB is much smaller deduced from the famous de Broglie relation $\lambda = h / p$, where λ , h , and p represent the wavelength, Plank's constant and the momentum, respectively. Therefore EB lithography can achieve much better resolution than photolithography does. In practical, patterns with size 10 nm can be generated by EB lithography. [55]

4.1.2 Anti-charging

However, some difficulties were to be dealt with. The first was the electron charging effect. Since the substrate of our device was an insulating material (quartz), the emitted electrons from the electron gun accumulated near the top surface of the substrate, formed a negative charge, and made the exposure EB deflected, finally resulted in pattern distortion and field stitching error. A schematic picture of the charging effect is shown in Fig. 4.11. A commercial anti-charging chemical ESpacer 300Z was coated on the top of EB resist to solve this problem. With a spin rate of 2000 rpm, one can obtain a thin conductive layer of thickness about 200 Å which does not affect the exposure mechanism. Since the chemical is very expensive (\$3000 for 100 ml), it was taken by a micropipette. After exposure, ESpacer was removed by water rinsing before development. Fig. 4.15 shows the microscope picture of the developed patterns without and with coating of ESpacer.

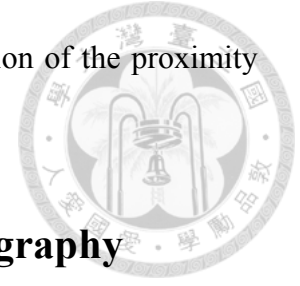
4.1.3 Dose determination and the proximity effect

The second was determination of the appropriate dose value and correction of the



proximity effect. The EB lithography system used was JEOL JBX-5000LS – a Gaussian vector scan system. The CAD pattern was transformed into pixel data with pixel pitch set to be 0.00125 μm . The pattern was then exposed pixel by pixel with EB deflected by electrostatic and magnetic "lenses." Fig. 4.12 shows a schematic picture of the writing strategy. [56] With back scattering of electrons on the substrate, the region near the desired exposed area also received dose more or less as shown in a schematic drawing Fig. 4.13. In fact every exposed pixel could be considered generating a 2-D Gaussian distribution of dose on the substrate. The standard deviation of the Gaussian function (i.e. the spot radius) was related to the substrate material, exposure current, acceleration voltage, calibration condition, focus of the EB, etc. With this phenomenon, the appropriate dose value was also dependent on pattern size; larger or denser patterns received more dose than smaller or sparser patterns did even when the exposure time were the same. **Table 4.1** shows the trends how these factors affected the required doses. Also the shape of the developed pattern was affected by this back-scattering effect, especially near the border of a dense pattern, or a small pattern close to a large pattern, the patterns after development were usually not as the desired pattern drawn in the CAD file. Fig. 4.16 is a photo of a developed PC pattern. We observed that the circles around the corner were smaller than the interior ones which they were the same in the computer drawing. This was called the proximity effect. An efficient way was proposed to simulate and correct the proximity effect: the exposed dose could be determined by calculating the convolution of the CAD pattern with a 2-D Gaussian function, and the developed shape could be found by making it binary with a grayscale threshold, as shown in Fig. 4.14, where the Gaussian radius and the threshold could be determined from the experiment. Thus the proximity effect can be addressed by altering the original CAD pattern and doing simulation iteratively.

After determination of the appropriate dose value and correction of the proximity effect, a desired developed pattern was obtained.



4.2 Making the alignment marks for EB lithography

4.2.1 Background

As mentioned before, the delay distance between PCs and IDTs is a critical factor to the performance of the resonator, thus the alignment of the two times of EB lithography (i.e. IDT and PC) should be executed precisely. Our substrate was a 20 mm × 20 mm × 0.5 mm quartz wafer. As shown in Fig. 4.3, 4 copies of the same layout were on it. Each of them contained 4 different layouts; each of them will be called a “chip” in the following. So we had 16 chips on a single wafer, which the chip had a size 2.5 mm × 2.5 mm. As reported [56], with alignment to a set of global wafer marks, the alignment tolerance is about 0.5 μm. However the tolerance was required to be less than order of 10^{-1} of the wavelength, or, less than 0.3 μm, and the less the better. Also knowing that the best tolerance (< 0.1 μm) can be achieved when the alignment marks are within several hundred micrometers of the critical region [56], thus alignments should be carried out for every single chip writing, with alignment marks around each chip.

Unlike the optical alignment for photolithography, there were requests for alignment marks used in EB lithography. Since the instrument detected the mark position by emitting EB and receiving scattered electrons, the marks should be made by materials with high atomic numbers such as tungsten, platinum, or gold, or, made by deeply etched patterns [56]. Unfortunately, the IDT layer which made by 100nm thick of aluminum was inadequate for alignment marks, so a “0th layer” with alignment marks only should be fabricated before any actual device structure was made. The mark material

was chosen to be 150-nm-thick gold, which provided a strong reflection signal when being scanning.

The wafer marks were large crosses of width 3 μm and length 1000 μm , placed at the top, bottom, left, and right sides of the wafer. They were used to correct overall position shift, rotation, and gain of the wafer, and helped finding the smaller chip marks, while the chip marks corrected shift, rotation, and gain for individual chip exposure.

We found that the alignment marks scanned in IDT layer alignments became unusable after deposition of SiO_2 . The reason was that the EB resist on scanned region was exposed (by scanning EB), aluminum remains after lift-off, and after high temperature SiO_2 CVD process, aluminum and gold formed intermetallic compounds, so the marks could not be used anymore as shown in Fig. 4.17, Fig. 4.18 . To address this, 3 sets of chip marks were made. One for IDT alignment, one for PC alignment, and a backup, as Fig. 4.18.

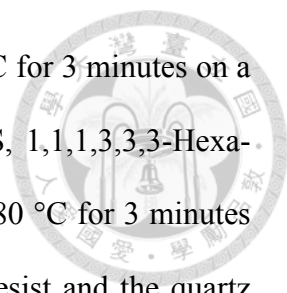
4.2.2 Process and parameters

The alignment marks was made by lift-off technique with EB lithography. The reason of lift-off but not etching method was that a much shorter EB writing time was required. The procedure is detailed as below, and the process chart is shown in Fig. 4.4.

1. Cleaning

The quartz wafer received from the supplier was first cleaned by 1:1 mixture of sulfuric acid (H_2SO_4) and hydrogen peroxide (H_2O_2) solution, left to stand for several hours, then rinsed by de-ionized water (DI water) for several times. After that, the wafer is spin-dried and baked in a 145 $^\circ\text{C}$ oven for more than 20 minutes to remove the water.

2. Spin coating of OAP, EB resist, and ESpacer



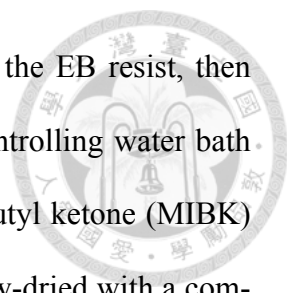
Before coating of the chemicals, a dehydration baking at 180 °C for 3 minutes on a hot plate was applied. After cooling, OAP (also known as HMDS, 1,1,1,3,3,3-Hexamethyldisilazane) was spin-coated at 3000 rpm and then baked at 180 °C for 3 minutes on a hot plate. It acted as an adhesion promoter between the EB resist and the quartz substrate. After cooling, EB resist ZEP520A was coated at 3000 rpm, and pre-baked at 180 °C for 3 minutes to remove the solvent from the resist. ZEP520A is a high resolution positive EB resist with high dry etching resistance. But here it was used for a lift-off purpose. After cooling down, the anti-charging layer ESpacer 300Z was coated at 2000 rpm, and then baked on a 70 °C hot plate for 3 minutes.

3. EB writing

The coated wafer was then sent into the chamber of EB lithography. Before entering the clean room, a job deck file, a schedule file, and the CAD file in GDSII format were already prepared, where the job deck file and the schedule file contained the EB writing parameters such as the arrangement of the patterns, the dose time, the mark information, the cyclic calibration setup, and the electron optical system type, while the CAD file contained the writing patterns. After the file conversion and a rigorous calibration of the instrument including adjusting the beam current, correction of focus and astigmatism, etc., the patterns were written on the substrate with the EB. The exposure current was set to be 100 pA, and the acceleration voltage was 50 kV. The best dose value determined to write this pattern under this conditions is 71.2 $\mu\text{C}/\text{cm}^2$, or, in words of actual writing parameters, pixels with a pitch 0.00125 μm and a skip number 4 are exposed by the EB for 178 ns. The total writing took about 2.5 hours.

4. Development

After exposure, the sample was rinsed by DI water in a beaker 30 seconds for 3



times (with clean DI water every time) to remove the ESpacer on the EB resist, then developed in the developer ZED-N50 at 23 °C in a temperature controlling water bath for 2 minutes shown in Fig. 4.25. It was then rinsed in methyl isobutyl ketone (MIBK) for 1 minute to purge it from the developer. After, the sample is blow-dried with a compressed N₂ gun and baked on a 110 °C hot plate for 3 minutes. The Scanning electron microscope (SEM) pictures of a developed pattern are shown in Fig. 4.19.

5. Deposition of Au/Ti

Before the metal deposition, 30 seconds of O₂ plasma ashing (operation pressure: 200 Pa, RF power: 130 W) was applied to ensure no residual resist on the developed area. After, the sample was put into the deposition chamber; a cryopump vacuumed the chamber to a high vacuum (less than 8×10^{-6} Torr). Then the metal was deposited by EB evaporation method – which has bad ability of stage coverage compared with sputtering method, but it becomes an advantage in lift-off purpose. A calibrated AT-quartz vibration thickness gage was used to monitor the deposited metal thickness. 100 Å of titanium was first deposited on the chip as an adhesion layer; 1500Å of gold is then deposited. The acceleration voltage of the EB is controlled from 2.5 kV to 3 kV, and the current ranges from 20 mA to 100 mA to adjust the deposition rate. Photographs of the EB evaporator are shown in Fig. 4.26.

6. Lift-off

The sample was immersed in Microposit Remover 1165 (contains 95% of *N*-Methylpyrrolidinone (NMP)) at room temperature for more than 12 hours (or heated to 70 °C, with agitation, shorten to 1~2 hours) for lift-off. ZEP520A was dissolved and therefore the metal on the resist is removed. Then the sample was cleaned by isopropyl alcohol (IPA) with ultrasonic vibration. Before it dries, it was cleaned by IPA and water

jet spray to prevent metal particles from reattaching to the wafer.



4.3 Fabrication of the aluminum IDT

The fabrication of IDT was also accomplished via the metal lift-off technique with EB lithography and the process chart is shown in Fig. 4.5.

1. EB lithography

The EB lithography of IDTs was similar to that of the alignment marks, but with alignment to the marks during EB writing. The typical scanning signals of the alignment marks are shown in Fig. 4.27. The required dose rose to $74.4 \mu\text{C}/\text{cm}^2$ (exposed time: 186 ns) as the patterns being finer. The total writing took about 7 hours. SEM pictures of developed patterns are shown in Fig. 4.20.

2. Deposition of aluminum

The aluminum was also deposited by EB evaporation method. Since there is good adhesion between aluminum and SiO_2 , no additional adhesion layer was needed here. 1000 Å of aluminum was deposited on the sample.

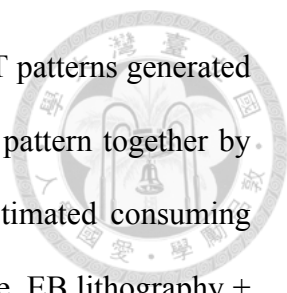
3. Lift-off

The lift-off process was the same as the previous section. The microscope photographs of fabricated IDTs are shown in Fig. 4.21.

4.4 Fabrication of the aluminum wire

4.4.1 Background

In the case of IDT with micrometers of line width, photolithography is suitable to generate the IDT pattern, IDT and wire are usually drawn in the same mask, and they



are fabricated together with the same material. But in the case of IDT patterns generated by EB lithography, it is impractical to generate both IDT and wire pattern together by EB lithography, since the writing area would be too large; the estimated consuming time would be days or even weeks! So a combinative lithography (i.e. EB lithography + photolithography) is needed. In other words our wire pattern was generated by photolithography, with parts of it overlaying on the IDT bus bar to make connection.

On the other hand, these structures was later covered by a CVD SiO₂ film, and the film would be etched through in the upcoming process. Thus the wire material was expected to be strongly resistive to the SiO₂ etching process to avoid damage. In the original plan, wet etching process with hydrogen fluoride (HF) based etchant was applied to open the contact pad window, so the wire material was chosen to be gold for its chemical inertia and good conductivity. However a false step was made. During 350°C SiO₂ CVD process, gold and aluminum on the overlay part formed gold–aluminum intermetallic compounds such as Au₅Al₂, AuAl₂, Au₂Al, ... Although predicted by the Al-Au phase diagram, none of these intermetallic compounds would form until the temperature reached 524 °C, since the metal films were thin, atomic interdiffusion took place at a lower annealing temperature, actually any possible compounds could form. [57] Some of these compounds were brittle or with low electric conductivity, sometimes even made the circuit open, as Fig. 4.22, so this process was confirmed unworkable. Another idea was to replace gold by platinum/aluminum double layer for platinum can protect aluminum from etching of HF but it has a relative higher electrical resistance and is hard to deposited to a enough thickness (through EB evaporation), while aluminum is well conductive. But similar things happened. Although the Al-Pt alloy film showed an acceptable conductivity but it couldn't stand the etching of HF, as Fig. 4.23. Finally the wire material was decided to be 3000 Å thick aluminum. Such thick aluminum still

could be dissolved in buffered HF solution in a short time, but shows a good resistance to fluorine based RIE. Consequently, RIE became the choice to reveal the contact pad under the oxide film.



4.4.2 Process and parameters

The wire material was chosen to be 3000 Å thick aluminum. It was also fabricated using lift-off technique for the IDT pattern would be etched if an etching method were applied instead. A special photoresist (PR) intended for lift-off technique was used. The process chart is shown in Fig. 4.6 and Fig. 4.7.

1. Photolithography

An image reversal PR AZ 5214E was employed in this photolithography. It was a positive resist, but with a special reversal mechanism, a negative wall profile was obtained which was appropriate for lift-off technique. The conditions are detailed in the following.

First the sample was cleaned by acetone, methanol, and DI water in sequence with ultrasonic vibration, then spin-dried, baked in a 145 °C oven for 15 minutes. After cooling, PR AZ 5214E was spin-coated on the sample at 2000 rpm; about 2 μm thick PR film was coated. It was then baked on a 110 °C hot plate for 1 minute to evaporate the solvent in the PR. Next, the sample was exposed under the mask with dose 50 mJ/cm². It was expected that the exposed region has an edge profile with positive slope about 80°, which was a common result for a positive PR due to the light being attenuated when penetrating through the PR. And next, the reversal baking, which made the exposed area from soluble to insoluble: The sample was baked on a 120 °C hot plate for 2 minutes. There was a special cross-linking agent in the PR, which became active at temperatures above 110 °C (and only in the exposed area), hence the exposed area was

cross-linked and becomes insoluble in developer. Afterwards a flood exposure without a mask with 500 mJ/cm^2 dose was applied on the sample, thus the rest area was exposed and became soluble. After development, patterns with desired negative wall profile are obtained. Here a special additive from InterVia Company and surfactant was added into the developer (2.38 wt% Tetramethylammonium hydroxide, (TMAH) water solution) to prevent the developer from etching the aluminum pattern of IDT.

2. Deposition of aluminum

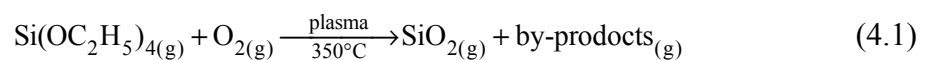
The aluminum was also deposited by EB evaporation method. A 3000 \AA aluminum film was deposited on the sample.

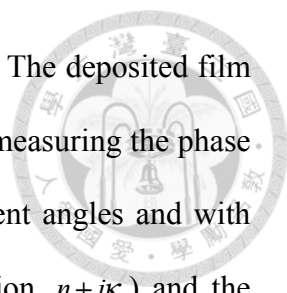
3. Lift-off

Aluminum on AZ 5214E was removed by acetone with ultrasonic vibration and a help of a cotton swab. Then methanol and DI water cleaning were applied in sequence.

4.5 Deposition of SiO_2 film

Silicon dioxide can be deposited by several methods including evaporation, sputtering, atmospheric pressure CVD (APCVD), low pressure CVD (LPCVD), and PECVD. Under consideration of the required thickness, the deposition rate, residual stress and the film quality, PECVD was the optimal process for us. Thus the film was deposited by a PECVD method from tetraethoxysilane (TEOS) and oxygen mixtures, which is sometimes called the P-TEOS CVD process. The instrument used was a SAMCO CVD system shows in Fig. 4.28, with the conditions described below: substrate temperature: $350 \text{ }^\circ\text{C}$; O_2 flow rate: 100 sccm; TEOS flow rate: 12.2 sccm; operation pressure: 0.6 Torr; RF power: 250 W. The plasma reaction may be expressed as





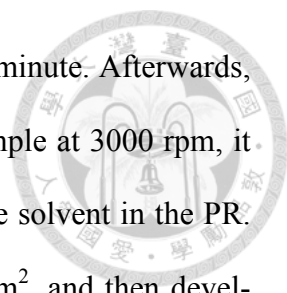
A 9000 Å thick oxide film was deposited with a rate 2700 Å/s. The deposited film was evaluated via an ellipsometry system shown in Fig. 4.29. With measuring the phase shifts and attenuations of polarized UV lights from different incident angles and with different wavelengths, optical constants (complex index of refraction $n + ik$) and the thickness of the film can be obtained simultaneously. The methodology is briefed below: If the optical constants are known, thickness can be found by starting from an initial thickness guess and iterational comparing the measured data and correcting the estimated thickness. Inversely if the thickness is known, the optical constants can be found in a similar way. If both thickness and the optical constants are unknown, they can still be found by starting from initial guess of both, and iterational correction of each other until achieving a good match with the measured data. Fig. 4.34 shows the calculated optical constants of the PECVD oxide.

4.6 Revealing of the contact pad

After deposition of silicon dioxide, the contact pad was then covered with an insulating layer. It had to be revealed so that the probe could have an electrical contact on it when characterization of the device. Attempts on wet etching and dry etching were made. Although the wet etching was simpler in procedure, many problems occurred including the metal wire problem discussed in previous section, and also side etching problem (due to lack of adhesion between PR and substrate) and alignment marks being lifted off (due to Ti or quartz substrate etched by HF) shown in Fig. 4.24. Finally RIE with PR mask was applied to remove the oxide on the contact pad.

1. Photolithography

The sample was cleaned by acetone, methanol, and DI water in sequence with ultrasonic vibration, then spin-dried, baked in a 145 °C oven for 15 minutes. After cooling,



OAP was coated at 3000 rpm, and then baked in a 90 °C oven for 1 minute. Afterwards, the PR OFPR-800LB (viscosity 200 cP) was spin-coated on the sample at 3000 rpm, it was then baked on a 110 °C hot plate for 3 minutes to evaporate the solvent in the PR. Next, the sample was exposed under the mask with dose 340 mJ/cm², and then developed in 2.38% TMAH solution, rinsed by DI water, baked in a 90 °C oven for 15 minutes. Thus the PR mask for RIE is made.

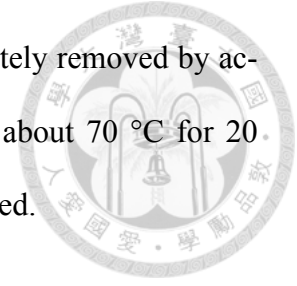
2. RIE

The instrument used was an ANELVA RIE system shown in Fig. 4.30. The commonly used gases for SiO₂ etching are CF₄ and CHF₃, since free fluorine can be liberated in the plasma. Higher etching rate can be achieved with CF₄ compared with CHF₃, for more free fluorine can be released. However better etching selectivity of SiO₂ over PR is achieved with CHF₃ gas due to increased formation of polymer in the presence of hydrogen, which the polymer is the by-product of the etching process, and it protects the PR from etching. But the etching profile becomes tapered also due to increasing of polymer (on the side wall). After all we chose CHF₃. We found that the polymer also remains on the etched area after etching, i.e., on the aluminum contact pad, increases the contact resistance. So argon (Ar) was also added with our expectation to reduce the polymer remained, and to increase the etching anisotropy (wall verticality) because the argon ion played the physical etching just like sputtering. But with adding of argon, the etching selectivity became lower with expectation.

The etching conditions are described below: CHF₃ flow rate: 20 sccm; Ar flow rate: 10 sccm; operation pressure 5 Pa; RF power 120W; etching time: 4 minutes + 4 minutes with a 10-minute cooling break to prevent PR from being scorched.

3. Resist stripping

After a high temperature RIE process, PR could not be completely removed by acetone but was stripped by EKC 265 post-etch residue remover at about 70 °C for 20 minutes. The sample was then rinsed by IPA and water, and then dried.



4.7 Fabrication of the PC structure

The PC structures which are arrays of holes, are made by RIE with EB resist ZEP 520A as the etching mask. Fig. 4.10 shows the process chart.

1. EB lithography

The EB lithography is similar to the IDT fabrication, but now with PC patterns, different dose $77 \mu\text{C}/\text{cm}^2$, and it aligns to another set of chip marks. One thing to note is that since the GDSII format accepts patterns in polygons only, the circles of PC is transform to decagons under consideration of conversion time and file size. After development, one cannot tell the difference from them to circles. Fig. 4.31 shows a photograph of the monitor of the EB lithography system when the PC pattern is being written.

2. RIE

The etching mask is 3000~4000 Å-thick ZEP 520A, which is not quite thick for etching a 9000 Å SiO_2 layer. Considering the etching selectivity and the etched wall profile which are discussed in last section, a compromise is made by etching the SiO_2 by two steps: the first step with CHF_3 only and the second with both CHF_3 and argon gas. The conditions are detailed as the following. Step 1, CHF_3 flow rate: 20 sccm; pressure 5 Pa; RF power 120 W; etching for 4 minutes; 10-minute break for cooling. Step 2, CHF_3 flow rate: 20 sccm; Ar flow rate: 10 sccm; pressure 5 Pa; RF power 120 W; etching for 4 minutes.

3. Resist stripping

The post-etch resist is stripped by EKC 265 and then rinsed by IPA and water. After that, the device is finally completely made. Some SEM images of the PC structure are shown in Fig. 4.32 and Fig. 4.33.

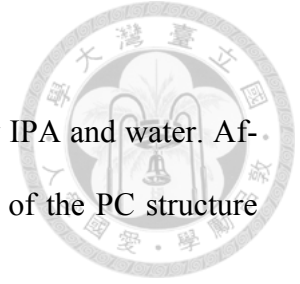




Table 4.1 Dependence of required dose on some factors

	Changing on the factor	Required dose
Pattern size	↑	↓
Pattern density	↑	↓
Resist thickness	↑	↑
Acceleration voltage	↑	↑
Substrate atomic number	↑	↓

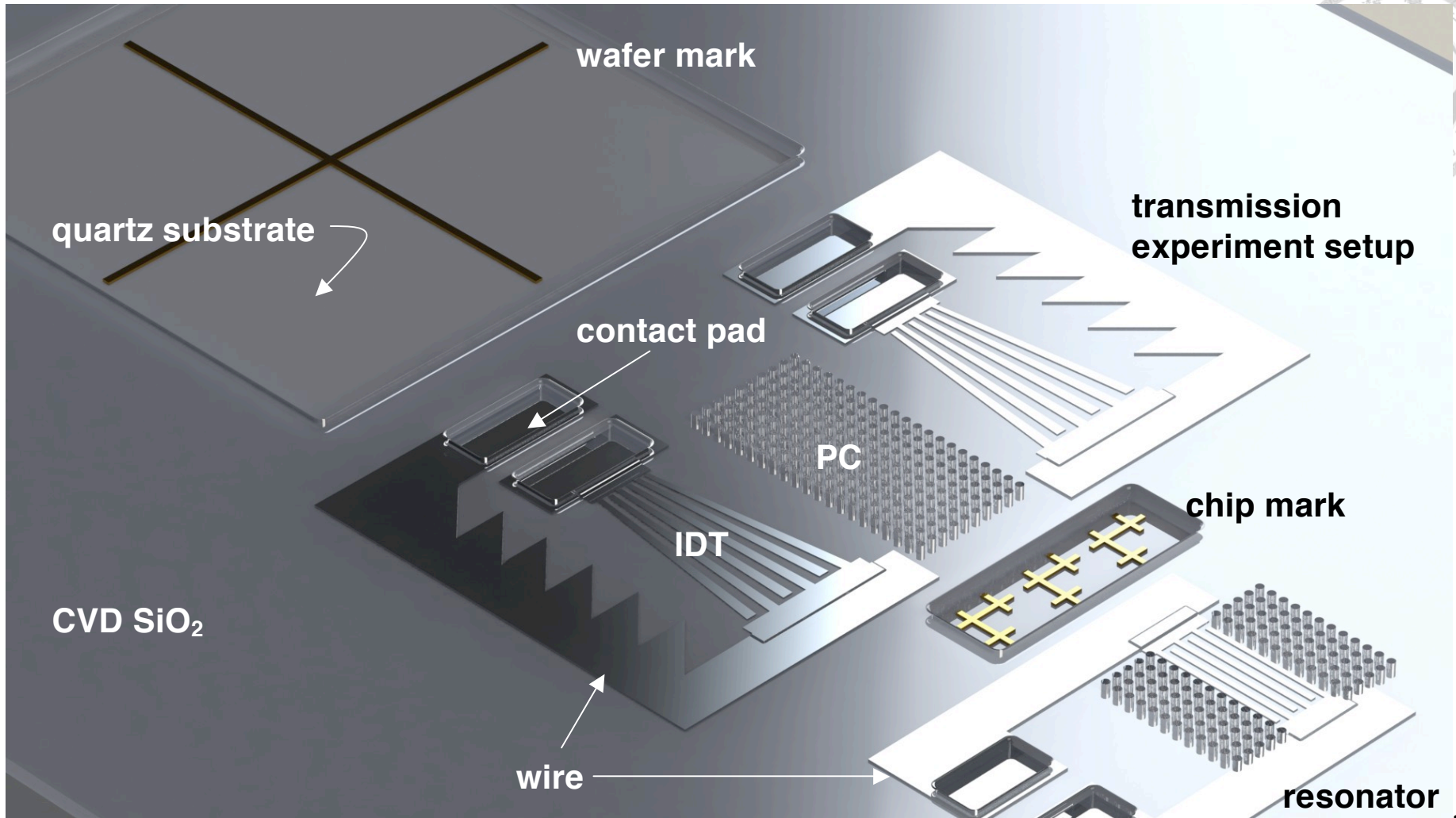
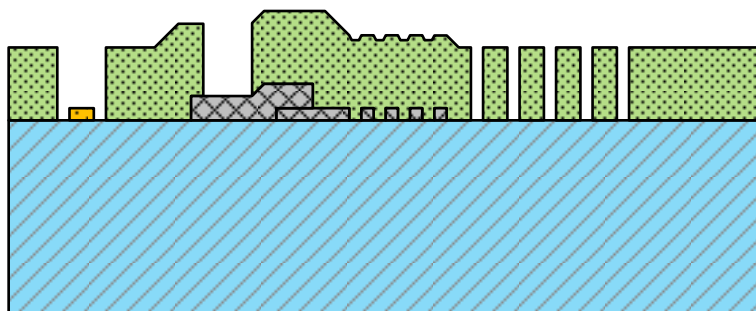
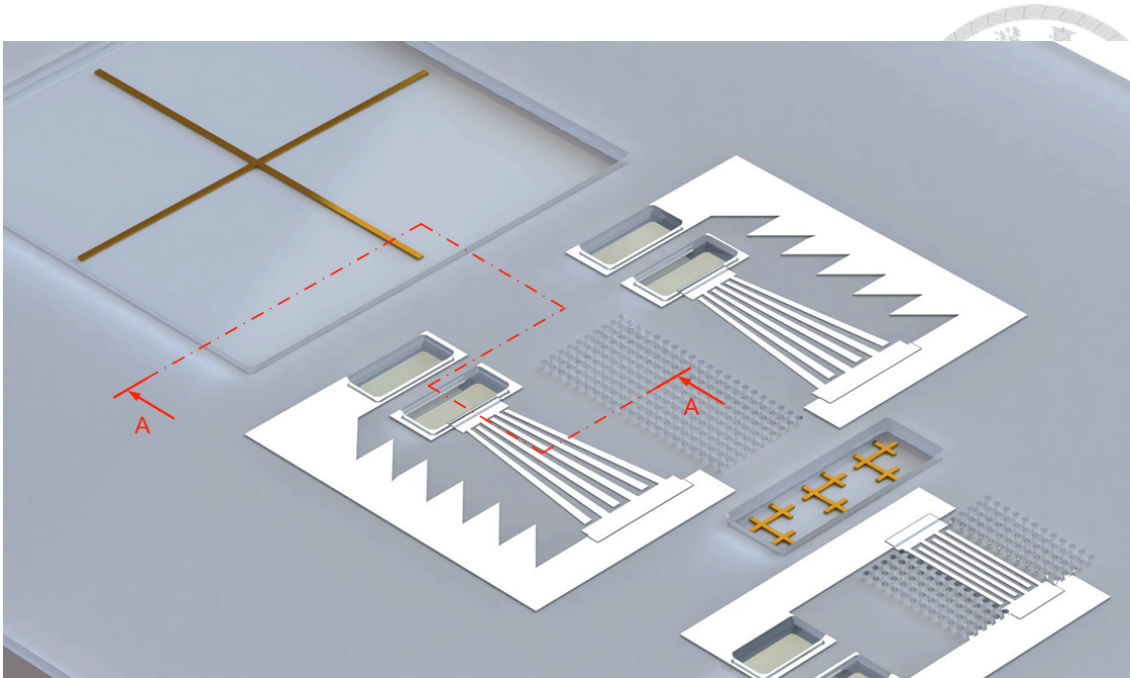


Fig. 4.1 A schematic picture of the device (not to scale)







- | | | | |
|---|----------------------|---|----------|
|  | CVD SiO ₂ |  | Gold |
|  | ST-cut quartz |  | Aluminum |

Fig. 4.2 A section view of the device (not to scale)

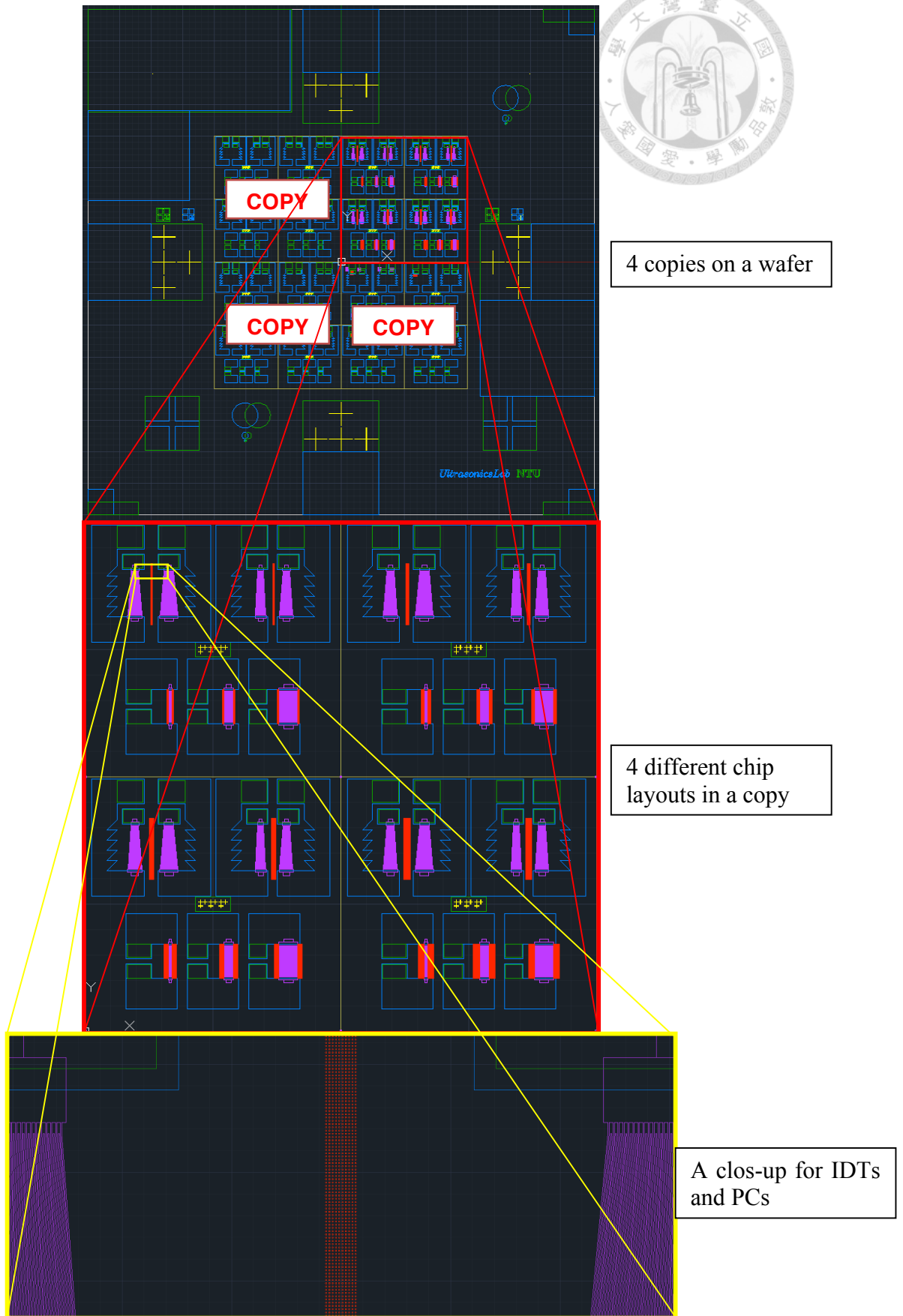
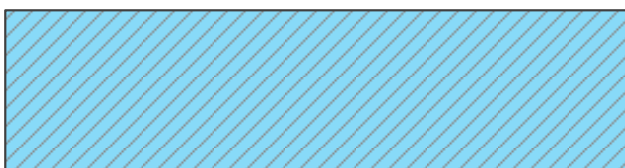
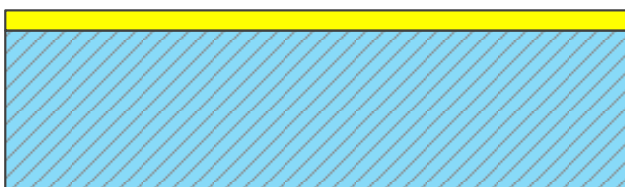


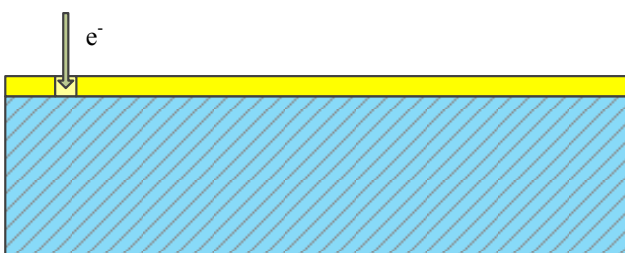
Fig. 4.3 The layout design



Wafer cleaning by
 $H_2SO_4 : H_2O_2 = 1:1$ solution,
 D.I. water rinsing.



Dehydration baking @ $180^\circ C \times 3$ minutes,
 coating of OAP @ 3000rpm,
 baking @ $180^\circ C \times 3$ minutes,
 coating of ZEP520A @ 3000rpm (4000Å),
 baking @ $180^\circ C \times 3$ minutes,
 coating of ESpacer™ 300Z @ 2000rpm,
 baking @ $70^\circ C \times 3$ minutes.



Electron beam writing, with
 exposure dose: $71 \mu C/cm^2$,
 exposure current: 100pA,
 acceleration voltage: 50kV.



Development:
 ESpacer™ removal by D.I. water
 rinsing 30 seconds $\times 3$ times,
 dipping in developer ZED-N50 @
 $23^\circ C$ for 2 minutes,
 rinsing in MIBK @ $23^\circ C$ for 1 minute,
 baking @ $110^\circ C \times 3$ minutes.



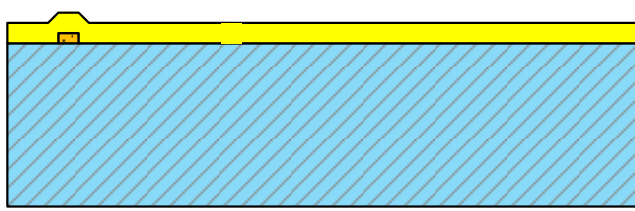
Deposition of Au/Ti by EB
 evaporator,
 acceleration voltage: 2.5~3.0kV,
 current: 20mA~100mA
 thickness of Au/Ti = $1500\text{Å}/100\text{Å}$



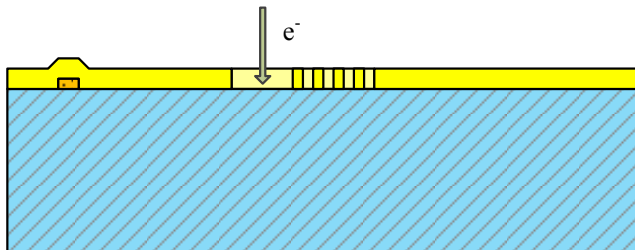
Lift-off by REMOVER 1165 @ R.T.
 for 12 hours (or heated, shorter)
 IPA ultrasonic cleaning,
 IPA & water jet spray cleaning



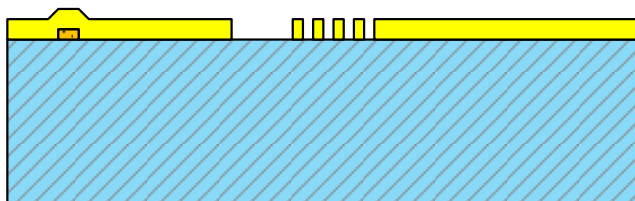
Fig. 4.4 Fabrications of the alignment mark



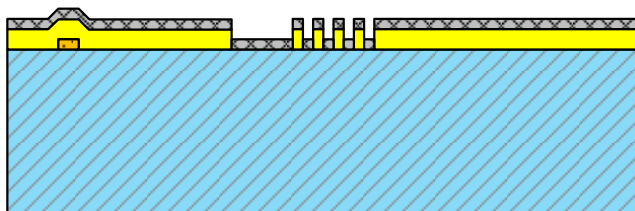
Dehydration baking @ 180°C × 3 minutes,
 coating of OAP @ 3000rpm,
 baking @ 180°C × 3 minutes,
 coating of ZEP520A @ 3000rpm (4000Å),
 baking @ 180°C × 3 minutes,
 coating of ESpacer™ 300 @ 2000rpm,
 baking @ 70°C × 3 minutes.



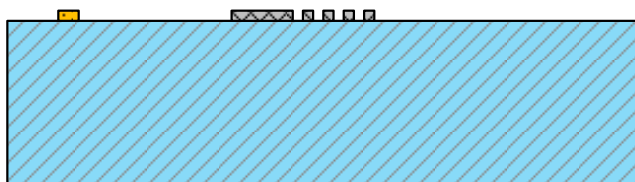
Electron beam writing, with
 exposure dose: 74C/cm²,
 exposure current: 100pA,
 acceleration voltage: 50kV.



Development:
 ESpacer™ removal by D.I. water
 rinsing 30 seconds × 3 times,
 dipping in developer ZED-N50 @
 23°C for 2 minutes,
 rinsing in MIBK @ 23°C for 1 minute,
 baking @ 110°C × 3 minutes.



Deposition of Al by EB evaporator,
 acceleration voltage: 2.5~3.0kV,
 current: 20mA~100mA
 thickness of Al = 1000Å



Lift-off by REMOVER 1165 @ R.T.
 for 12 hours (or heated, shorter)
 IPA ultrasonic cleaning,
 IPA & water jet spray cleaning

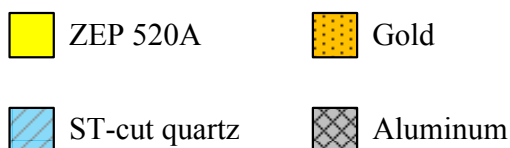
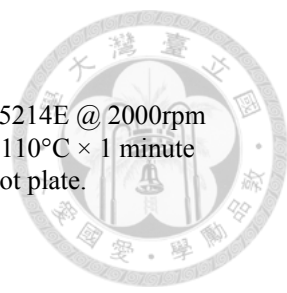
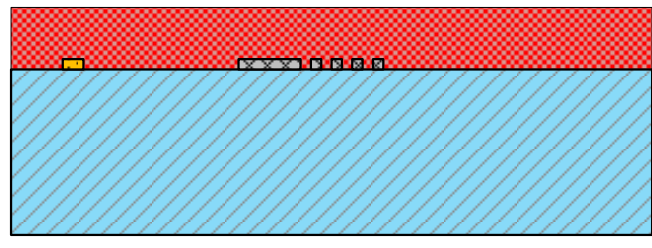


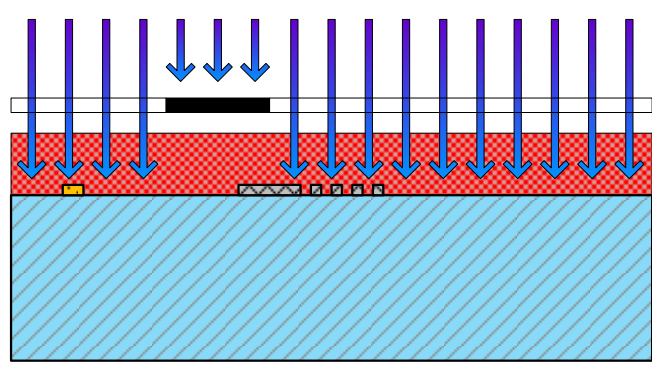
Fig. 4.5 Fabrications of the IDT



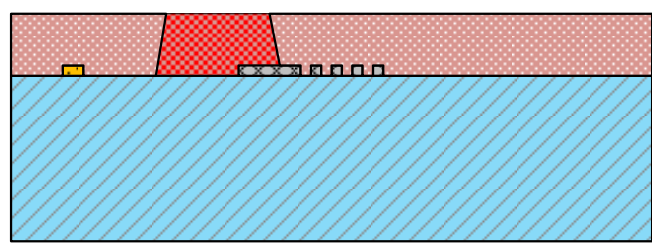
Coating of AZ 5214E @ 2000rpm
pre-baking @ 110°C × 1 minute
by hot plate.



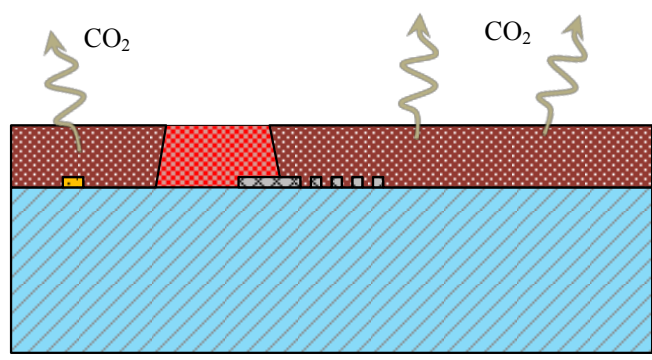
First exposure (with mask), with dose
50mJ/cm².



The exposed region becomes developer-
soluble.



Reverse baking @ 120°C × 2 minutes,
The exposed region is cross-linked and
becomes inert, while the unexposed
region remains photo-active.






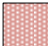


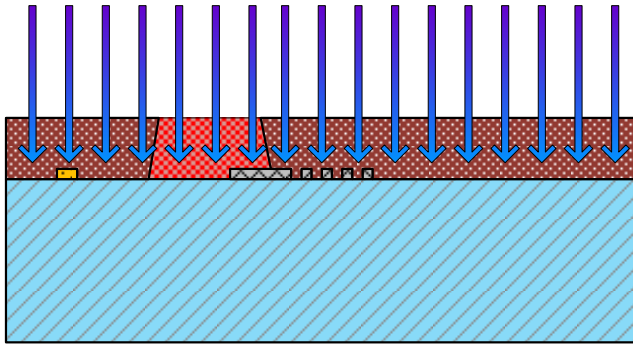
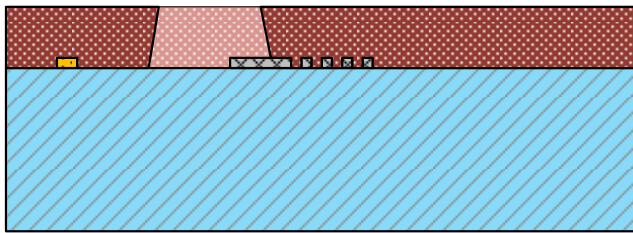
- | | | | |
|---|---------------|---|-------------------------------|
|  | Gold |  | AZ 5214E (photo-active) |
|  | Aluminum |  | Exposed AZ 5214E (soluble) |
|  | ST-cut quartz |  | Cross-linked AZ 5214E (inert) |

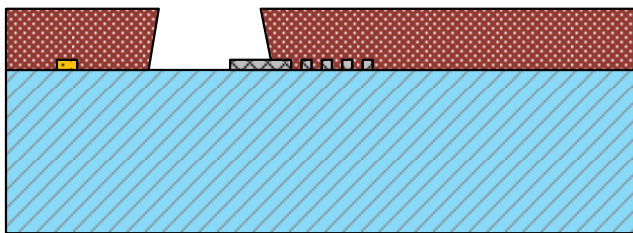
Fig. 4.6 Fabrications of the wire (i)



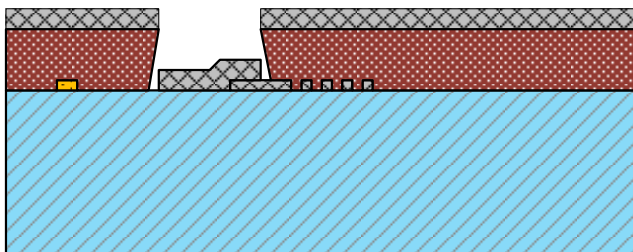
Flood exposure (without mask), with dose $500\text{mJ}/\text{cm}^2$.



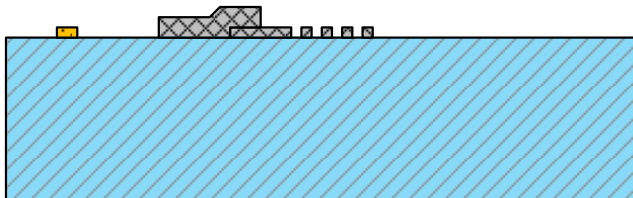
The region not exposed at the first time is exposed and becomes developer-soluble



Developing using 1:9 mixture of InterVia™ additive and 2.38% TMAH, about 40 seconds



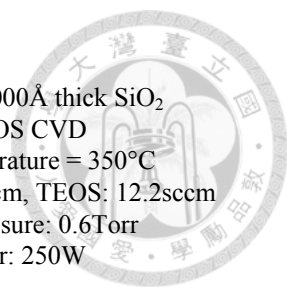
Deposition of Al by EB evaporator, acceleration voltage: 2.5~3.0kV, current: 20mA~100mA, thickness of Al = 3000\AA



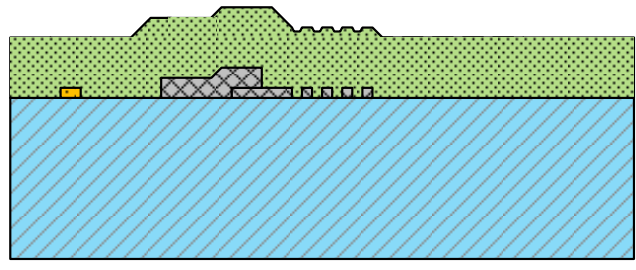
Lift-off by acetone + ultrasonic cleaning.

- | | |
|---|---|
|  Gold |  AZ 5214E (photo-active) |
|  Aluminum |  Exposed AZ 5214E (soluble) |
|  ST-cut quartz |  Cross-linked AZ 5214E (inert) |

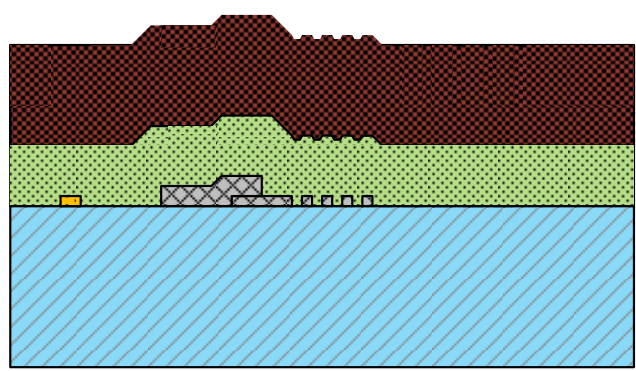
Fig. 4.7 Fabrications of the wire (ii)



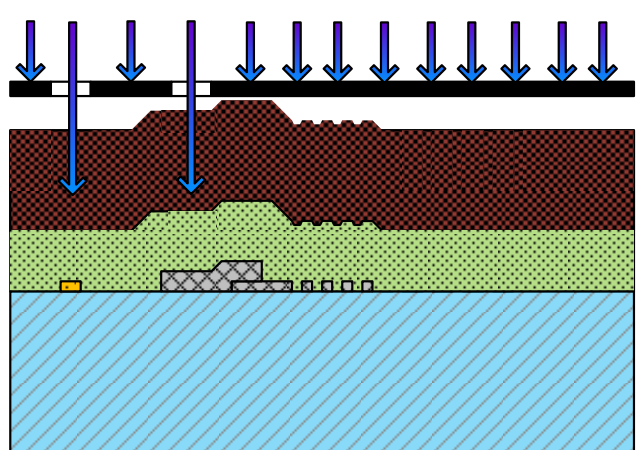
Deposition of 9000Å thick SiO₂
 by P-TEOS CVD
 substrate temperature = 350°C
 Flow rate: O₂: 100sccm, TEOS: 12.2sccm
 operation pressure: 0.6Torr
 RF power: 250W



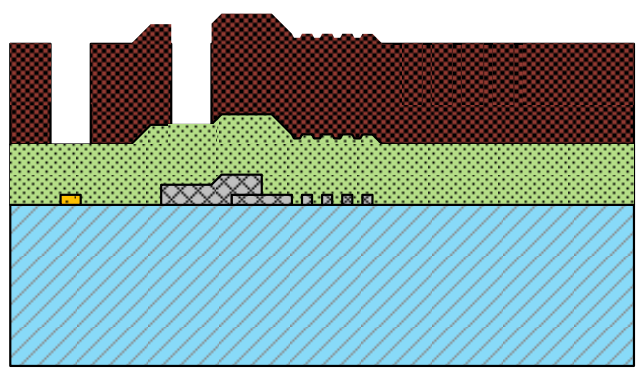
Coating of OAP @ 3000rpm
 baking @ 90°C × 1 minute (oven)
 Coating of OFPR-800 (200cP) @
 3000rpm (3.3mm)
 pre-baking @ 110°C × 3 minute (hot
 plate).



Exposure,
 dose = 340mJ/cm²

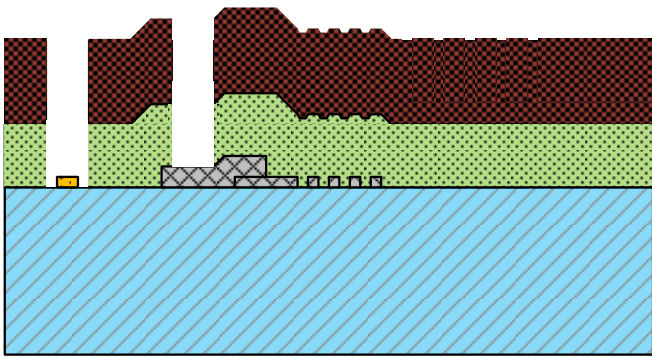


Developing in 2.38% TMAH,
 DI water rinsing,
 post-baking @ 90°C × 15 minutes
 (oven)

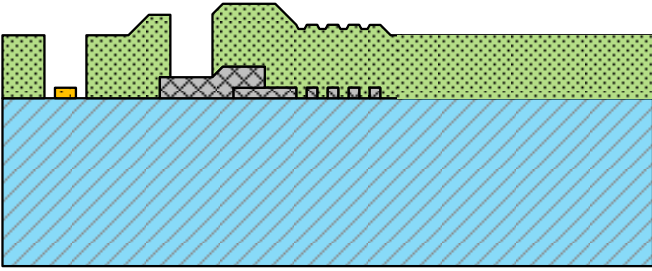


- OFPR-800
- Gold
- CVD SiO₂
- ST-cut quartz
- Aluminum

Fig. 4.8 Fabrications of the contact pad window (i)



SiO₂ RIE
CHF₃: 20sccm, Ar: 10sccm, pressure
5Pa, RF power 120W× (4+4) minutes
(with 10 minutes cooling break).



Resist stripping by
EKCTM 265 post-etch residue remover






-  OFPR-800
-  Gold
-  CVD SiO₂
-  ST-cut quartz
-  Aluminum

Fig. 4.9 Fabrications of the contact pad window (ii)

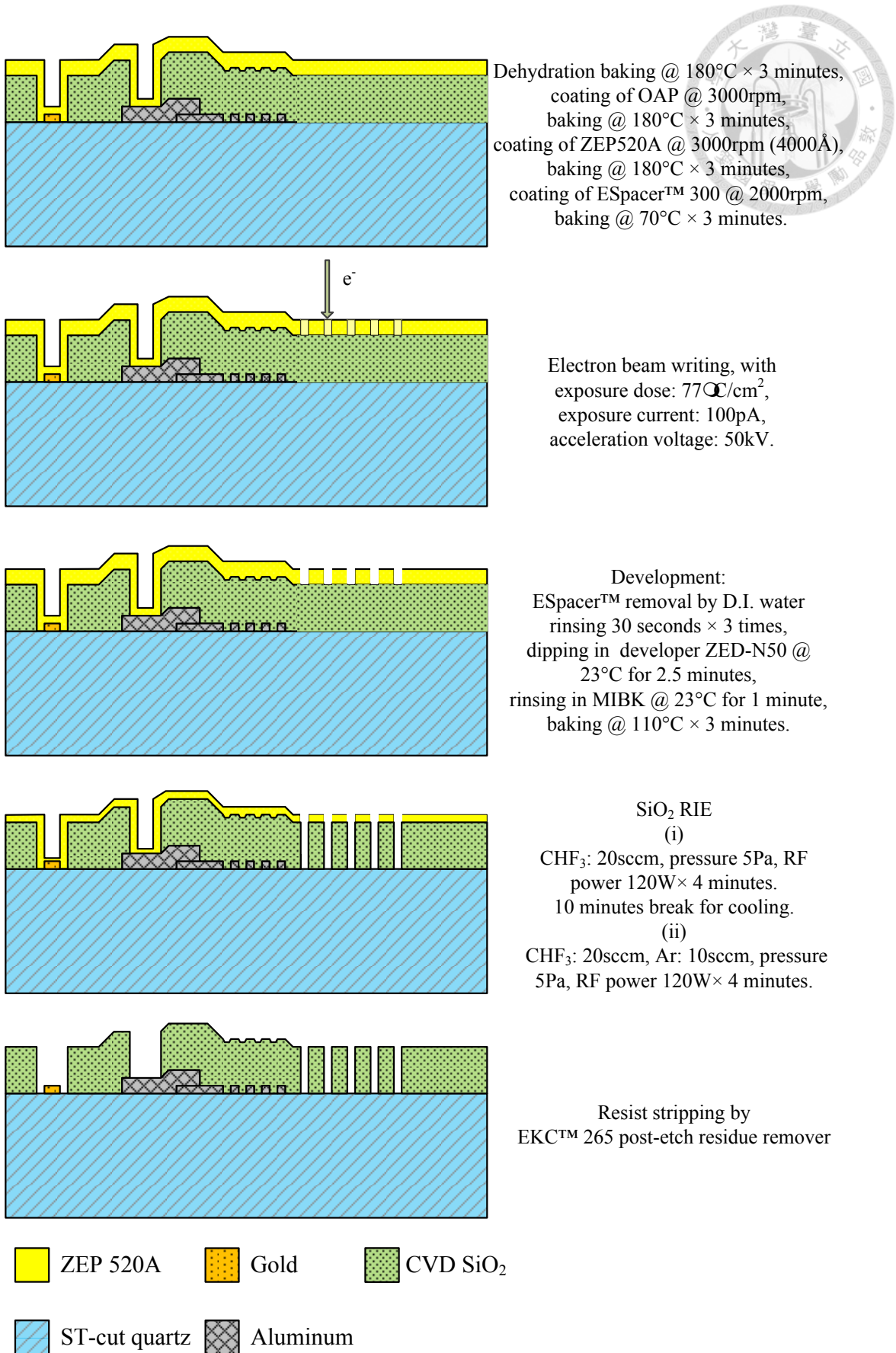


Fig. 4.10 Fabrications of the PC structure

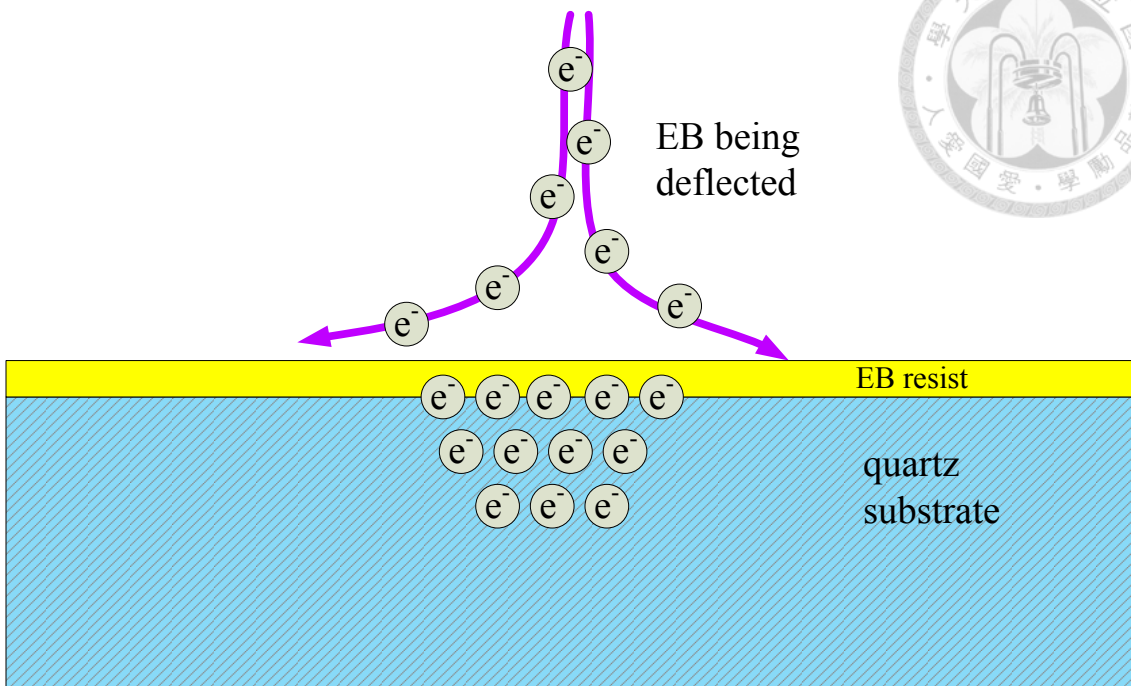


Fig. 4.11 A schematic drawing of the electron charging effect

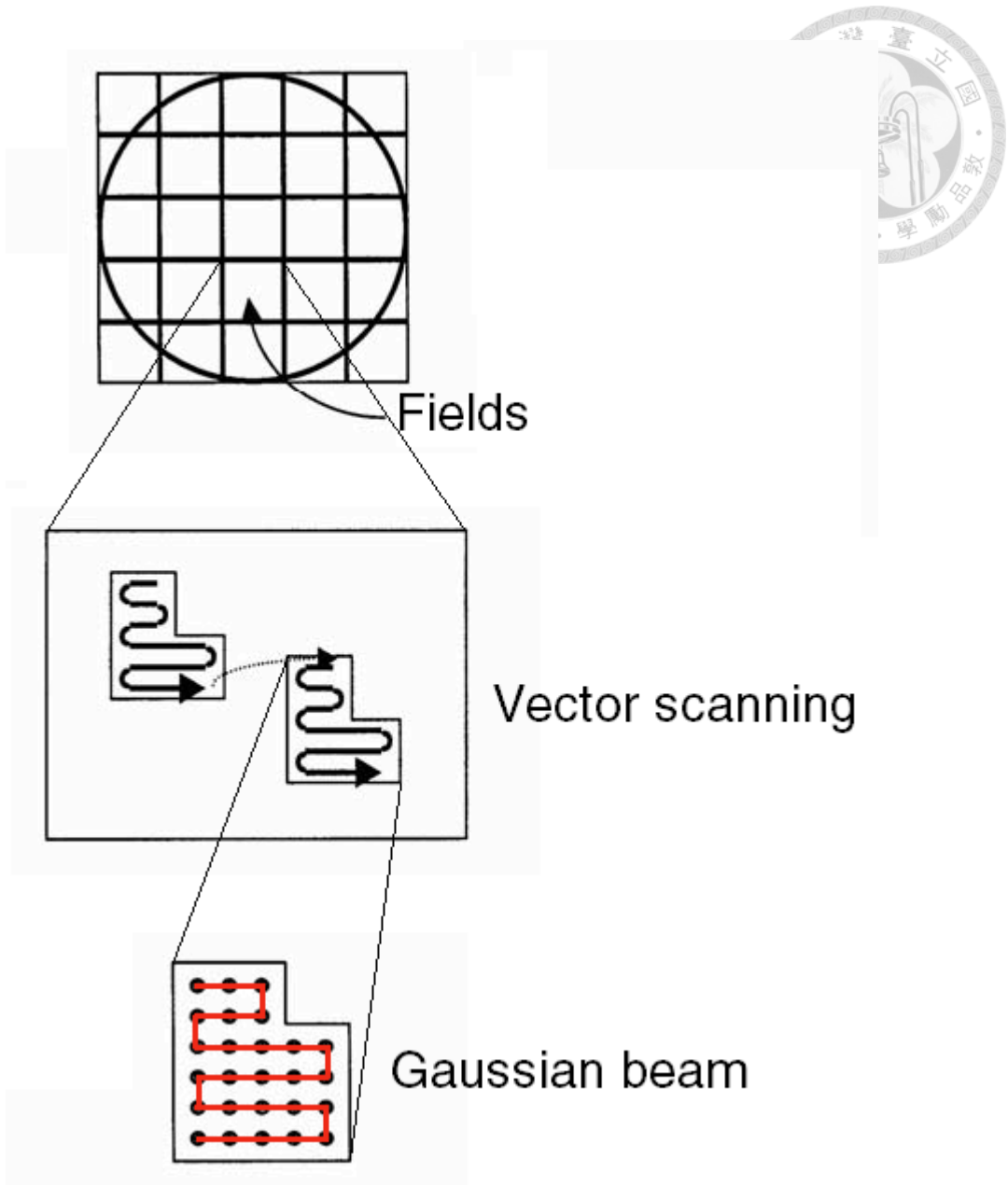


Fig. 4.12 The writing strategy of a Gaussian vector scan lithography system [56]

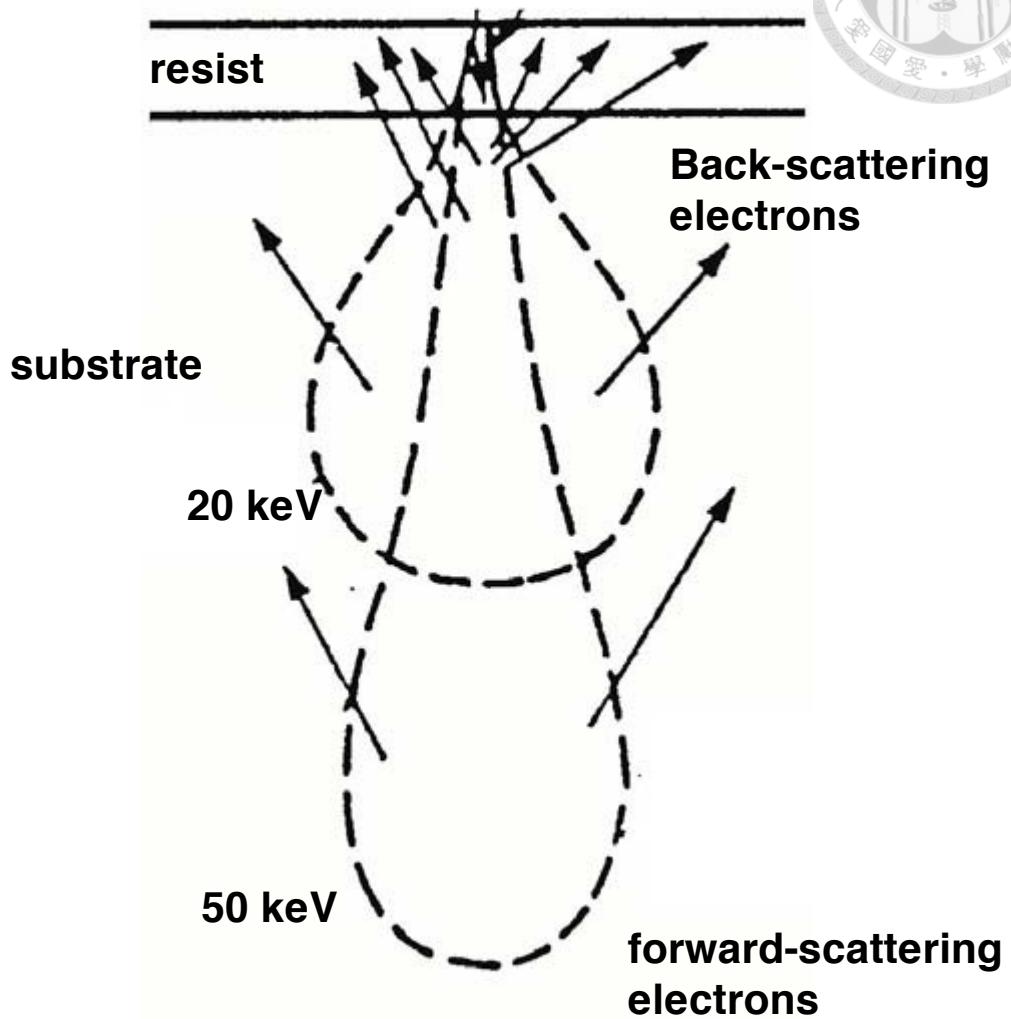
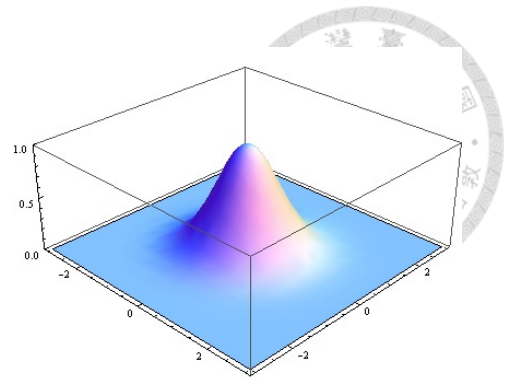


Fig. 4.13 Back-scattering electrons expose the resist as well. [56]

PROXIMITY



CAD pattern



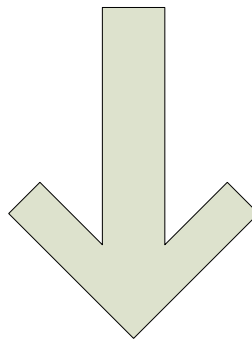
Dose distribution



PROXIMITY



Exposed dose



PROXIMITY



Developed pattern

Fig. 4.14 Simulation of the proximity effect

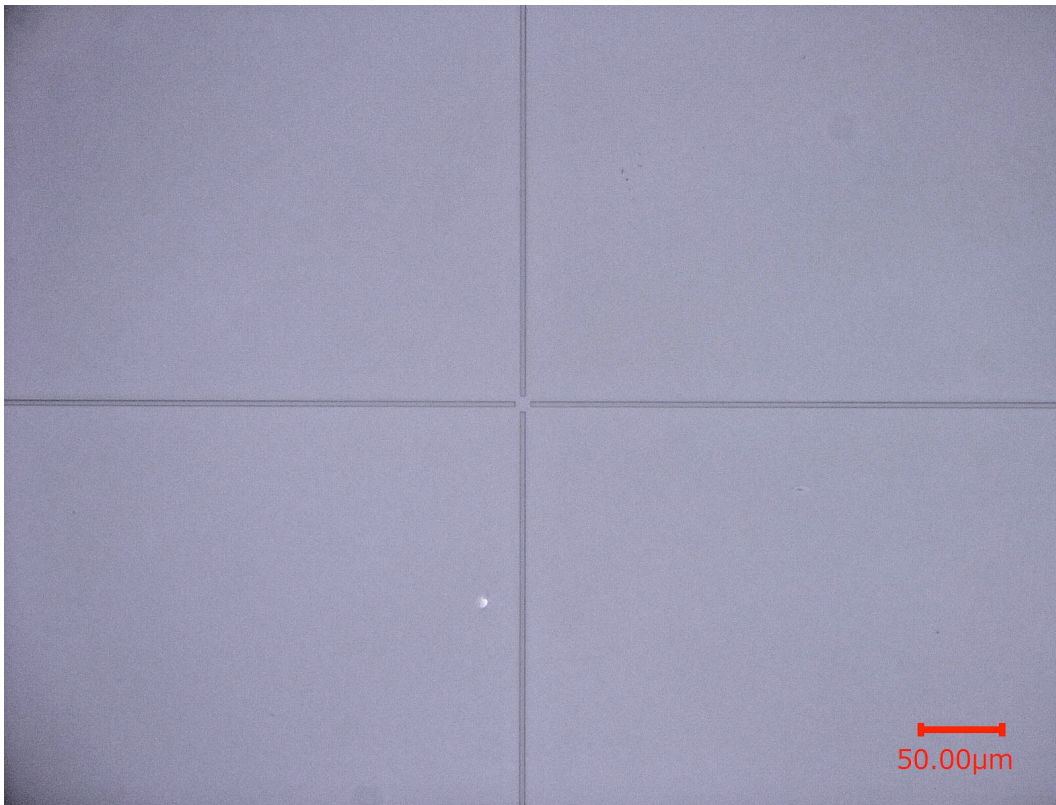
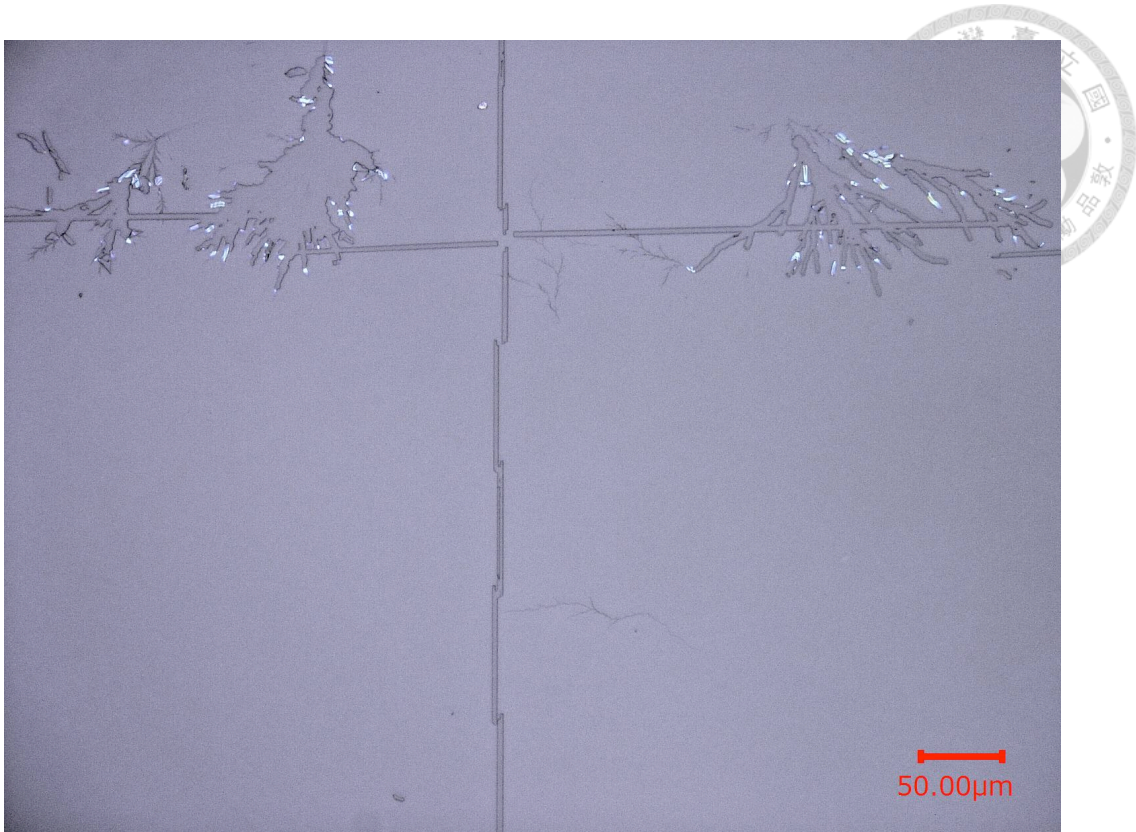


Fig. 4.15 Developed patterns without (upper) and with (lower) coating of ES spacer

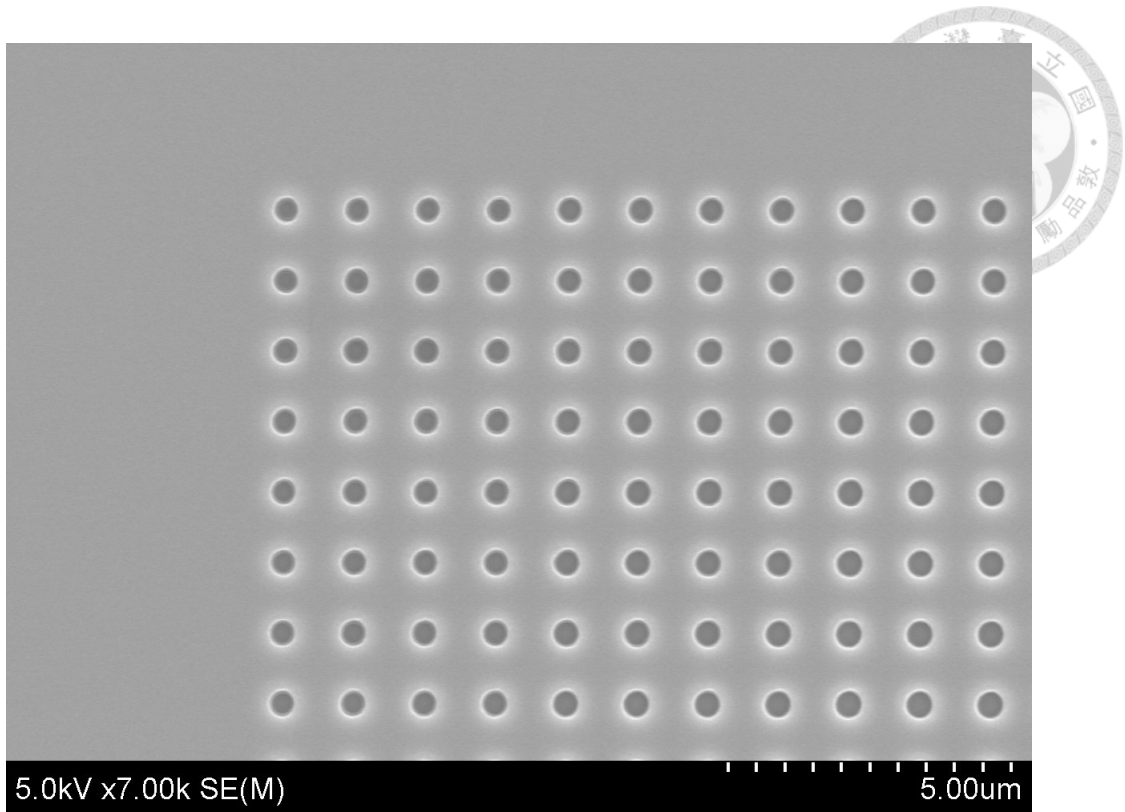


Fig. 4.16 Circle size changing due to proximity effect.

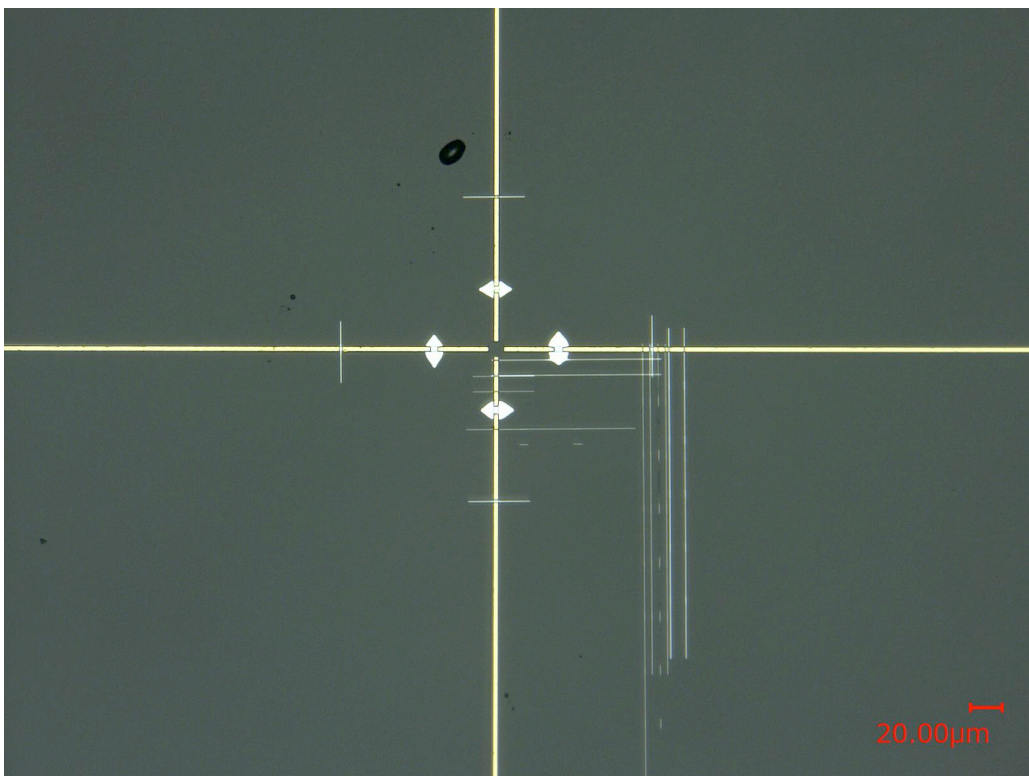


Fig. 4.17 A wafer mark after fabrication of IDT (Al remains on scanned area)

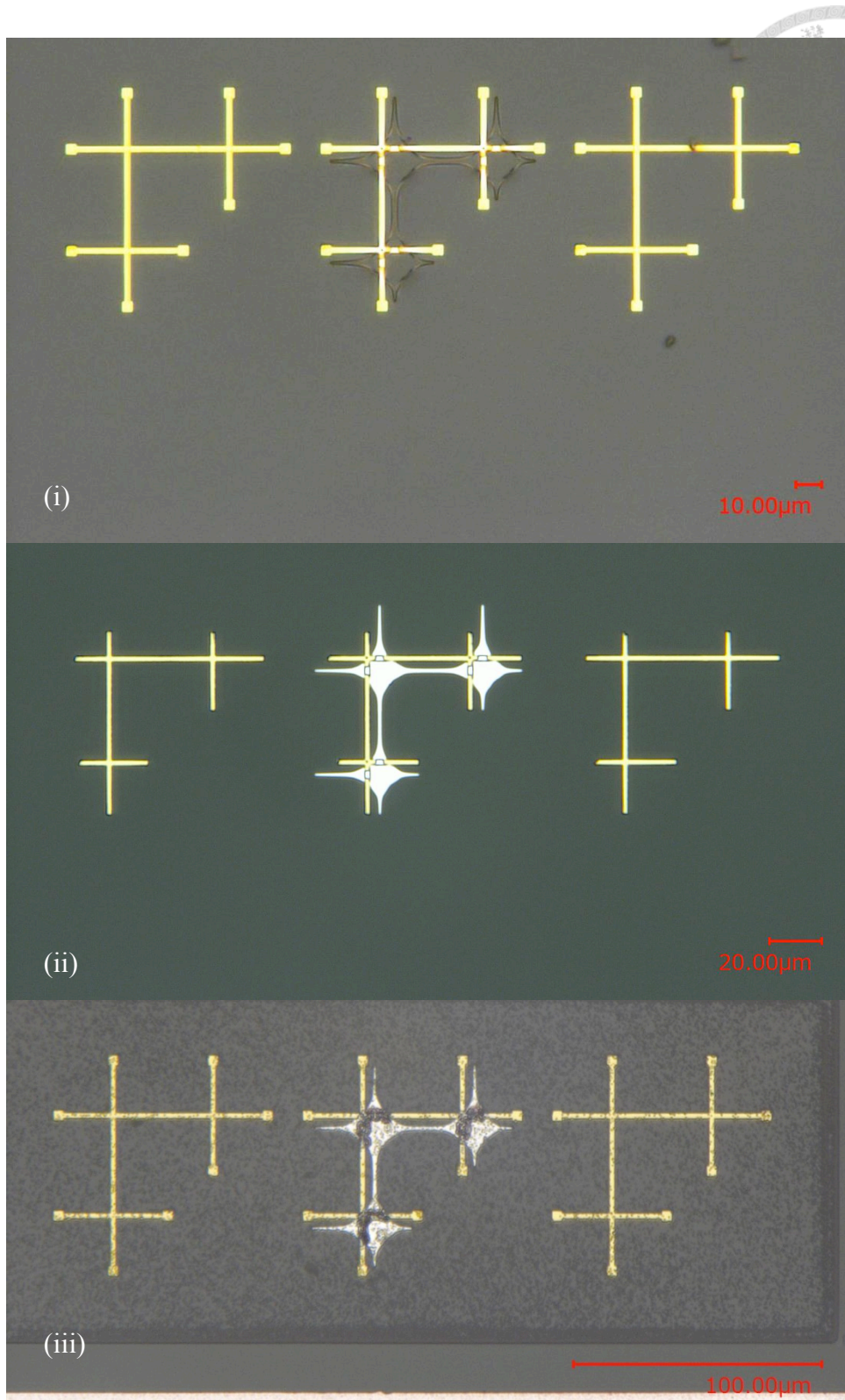


Fig. 4.18 The chip mark becomes unusable.

- (i) Resist on scanned area is exposed and removed.
- (ii) Al remains on it after lift-off.
- (iii) Formation of Au-Al intermetallic. This photo is taken after contact pad revealing.

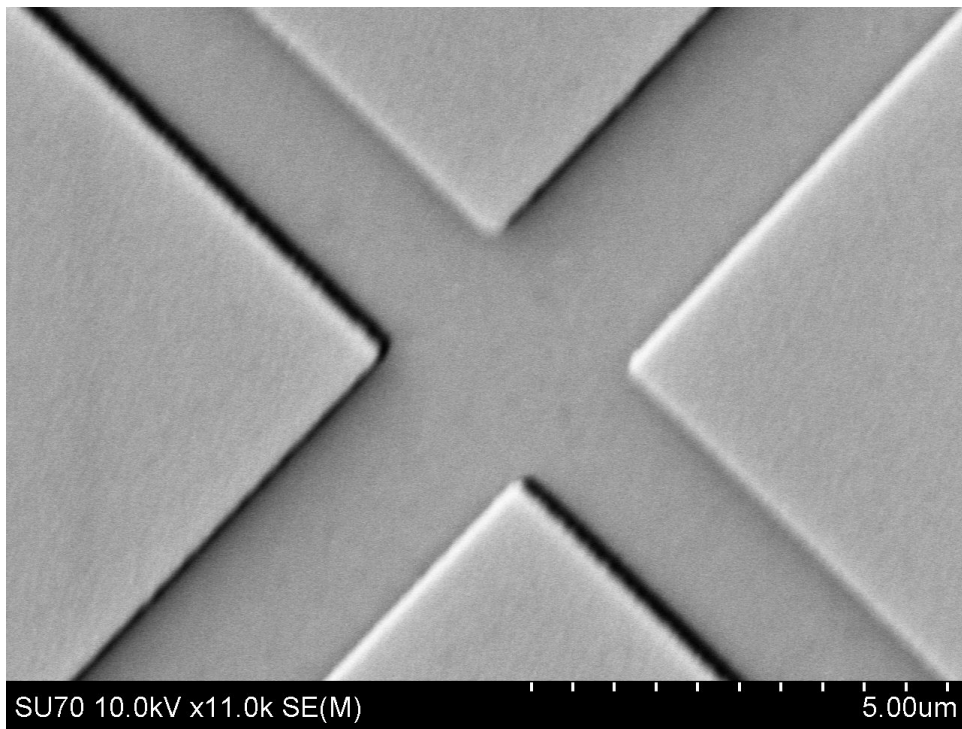
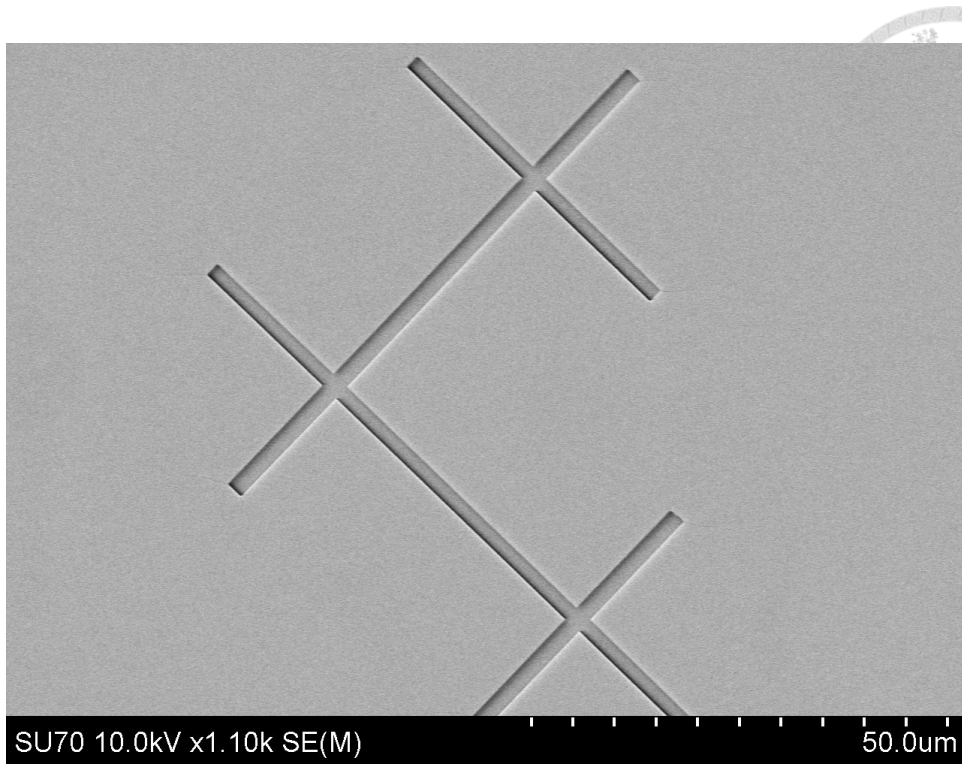


Fig. 4.19 SEM images of a developed alignment mark pattern

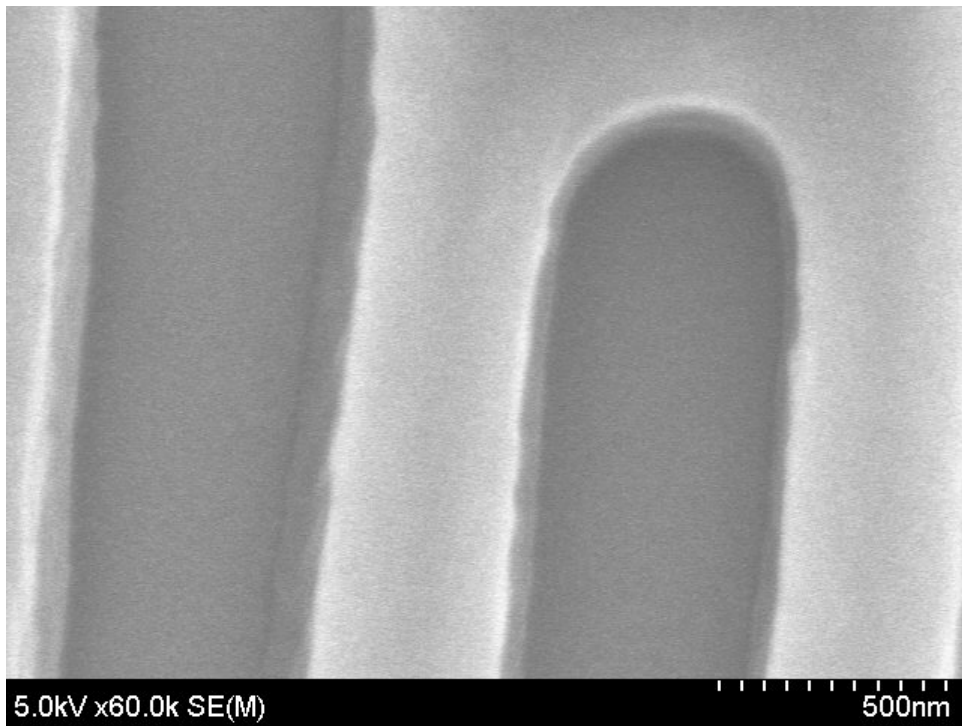
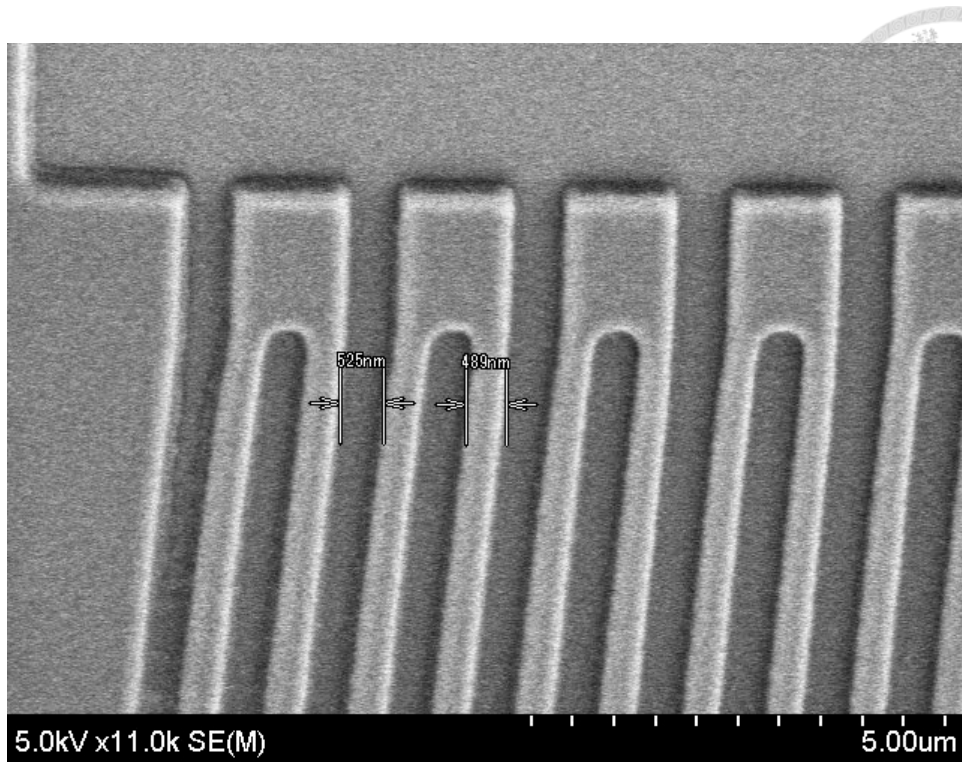


Fig. 4.20 SEM images of a developed IDT pattern

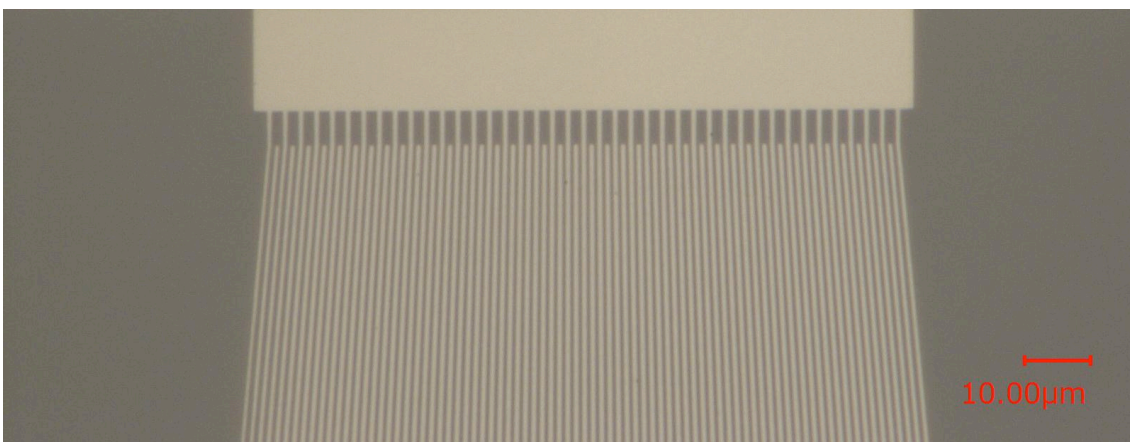


Fig. 4.21 Microscope pictures of fabricated IDTs

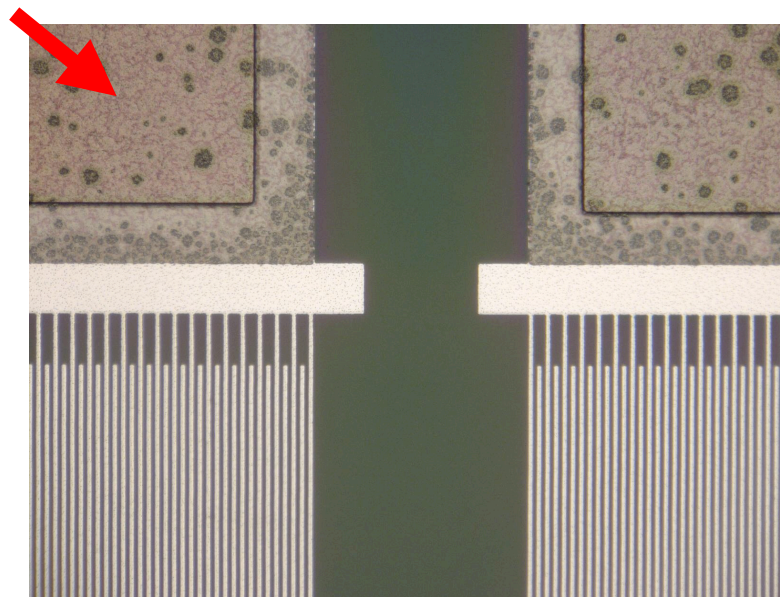
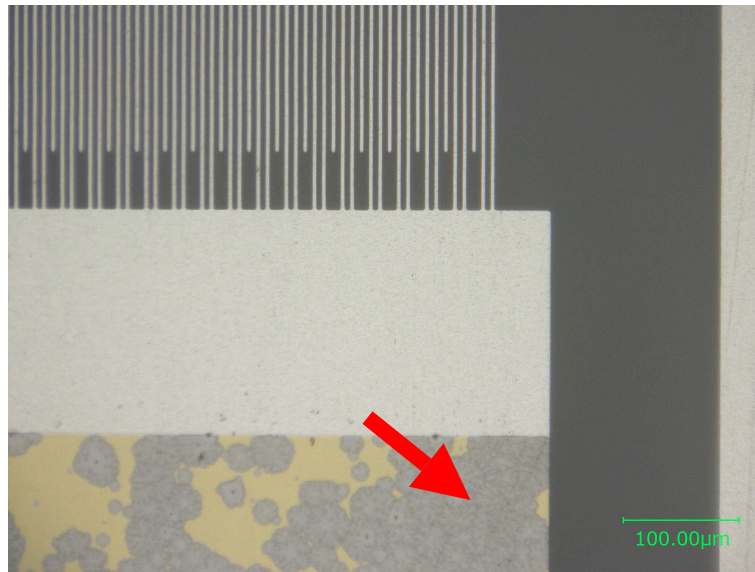


Fig. 4.22 A variety of Au-Al intermetallic

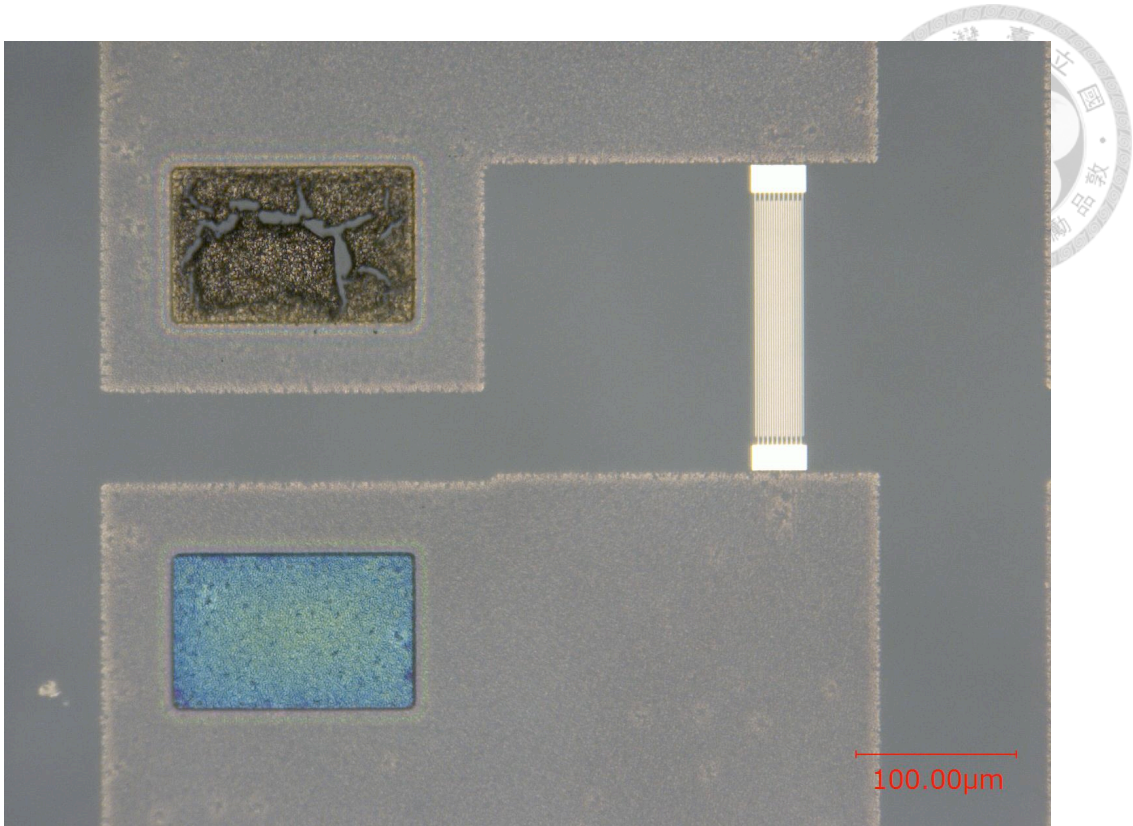


Fig. 4.23 A Pt/Al contact pad was damaged during buffered HF wet etching

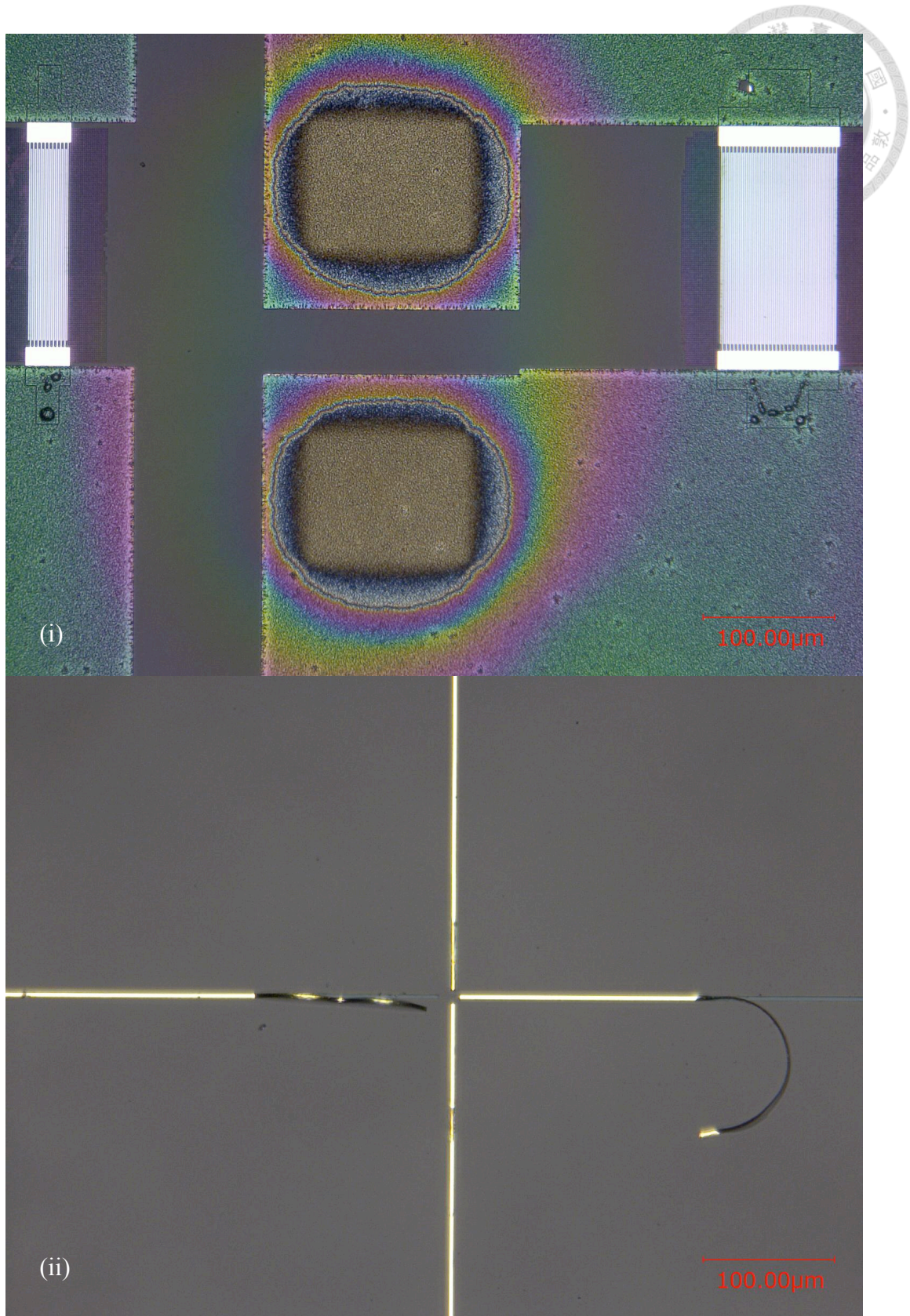


Fig. 4.24 Problems in wet etching

(i) side etching, (ii) lift-off of the alignment mark (Au/Ti)

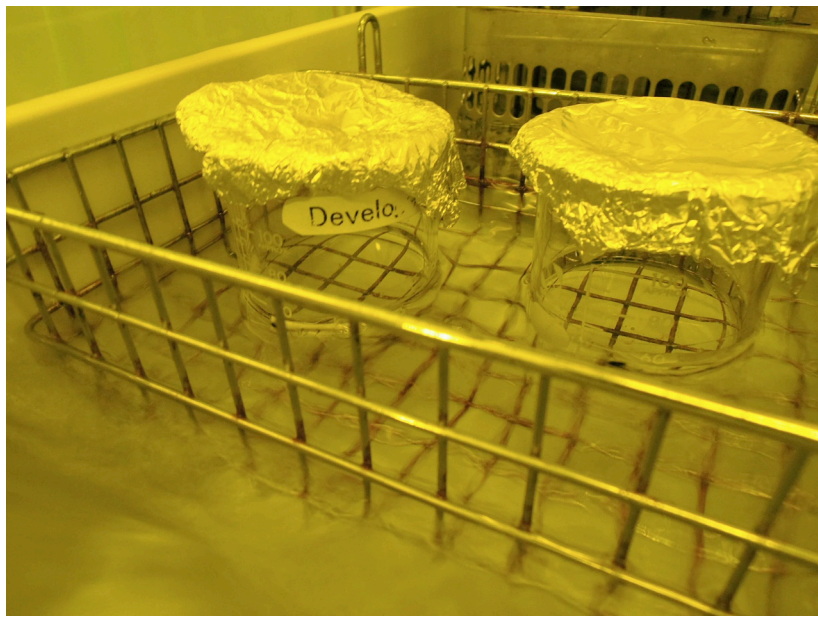
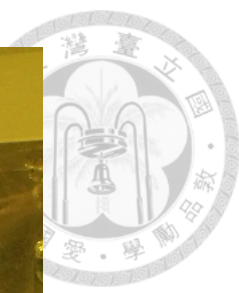


Fig. 4.25 Development is carried out in a 23°C water bath.

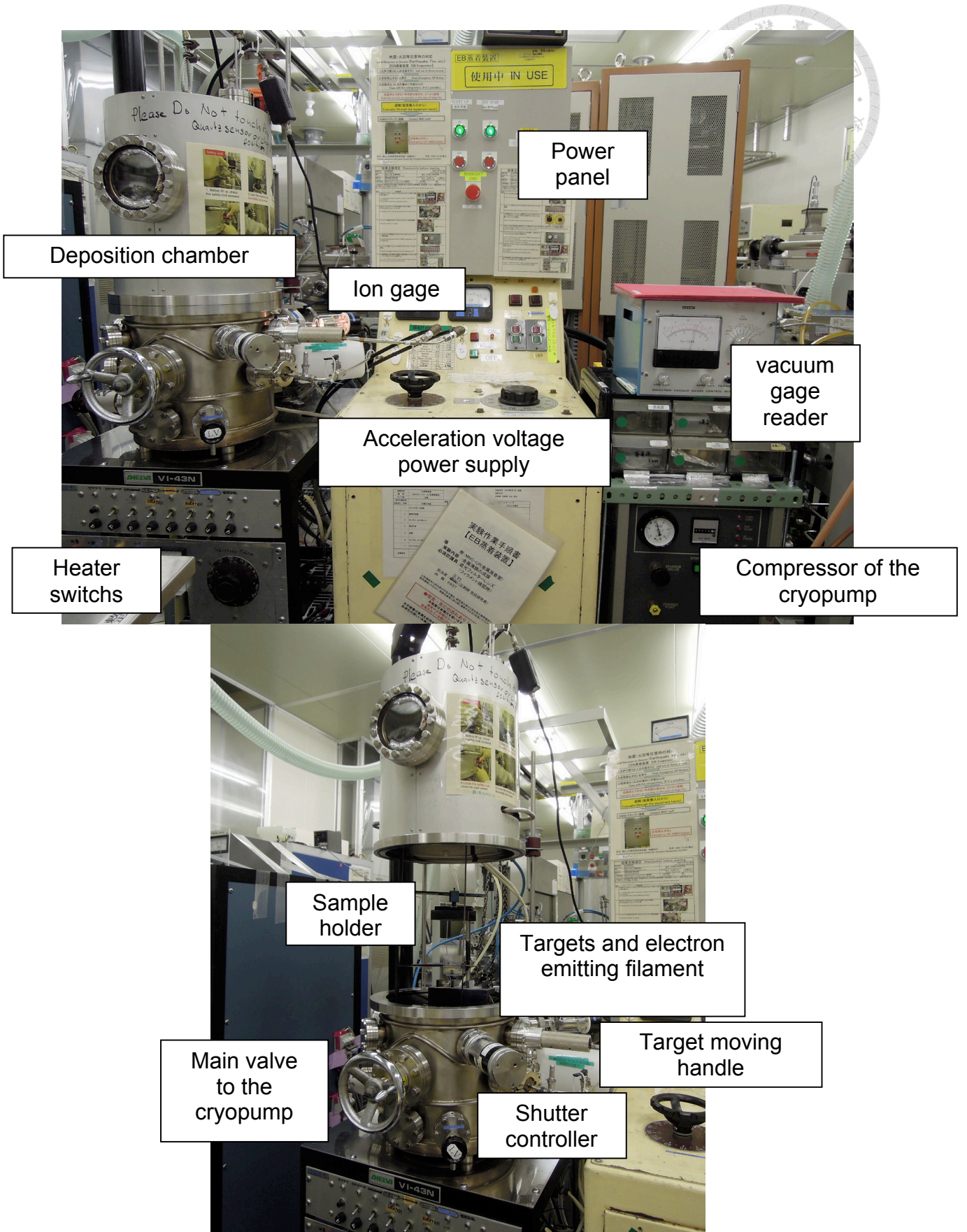


Fig. 4.26 The EB evaporator

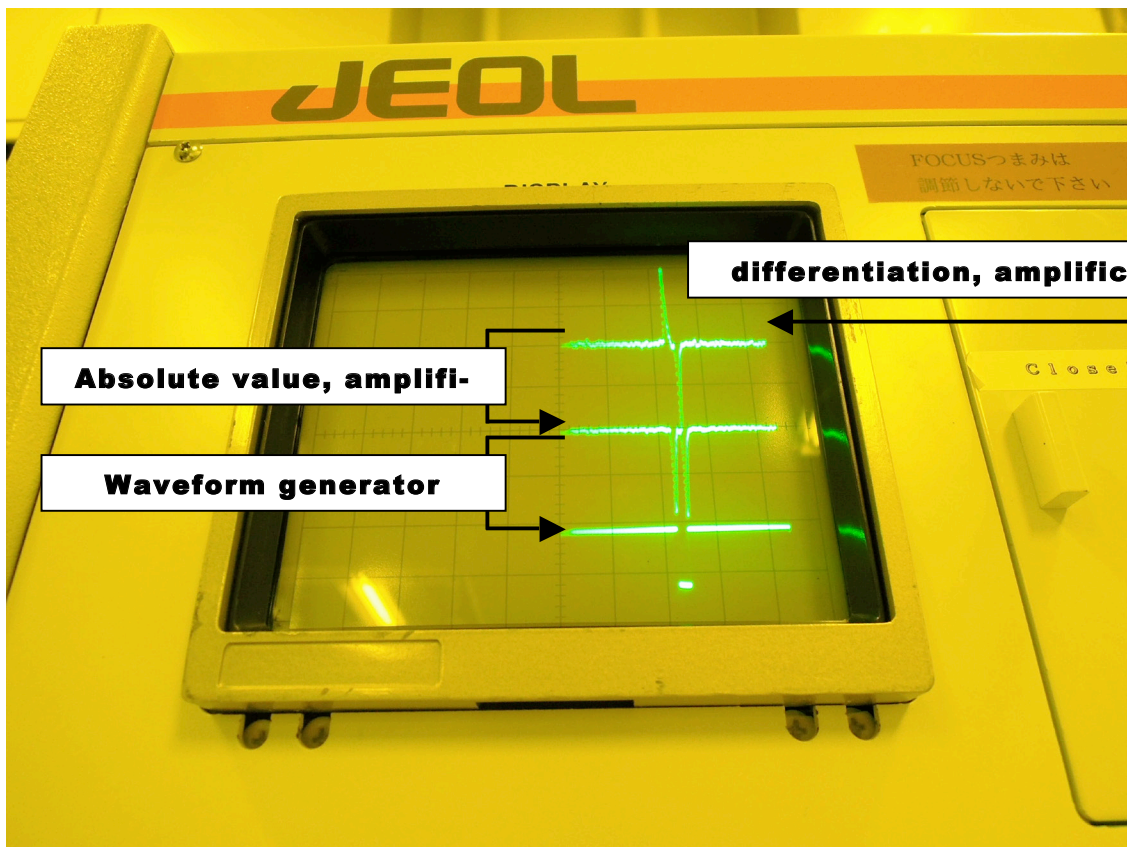
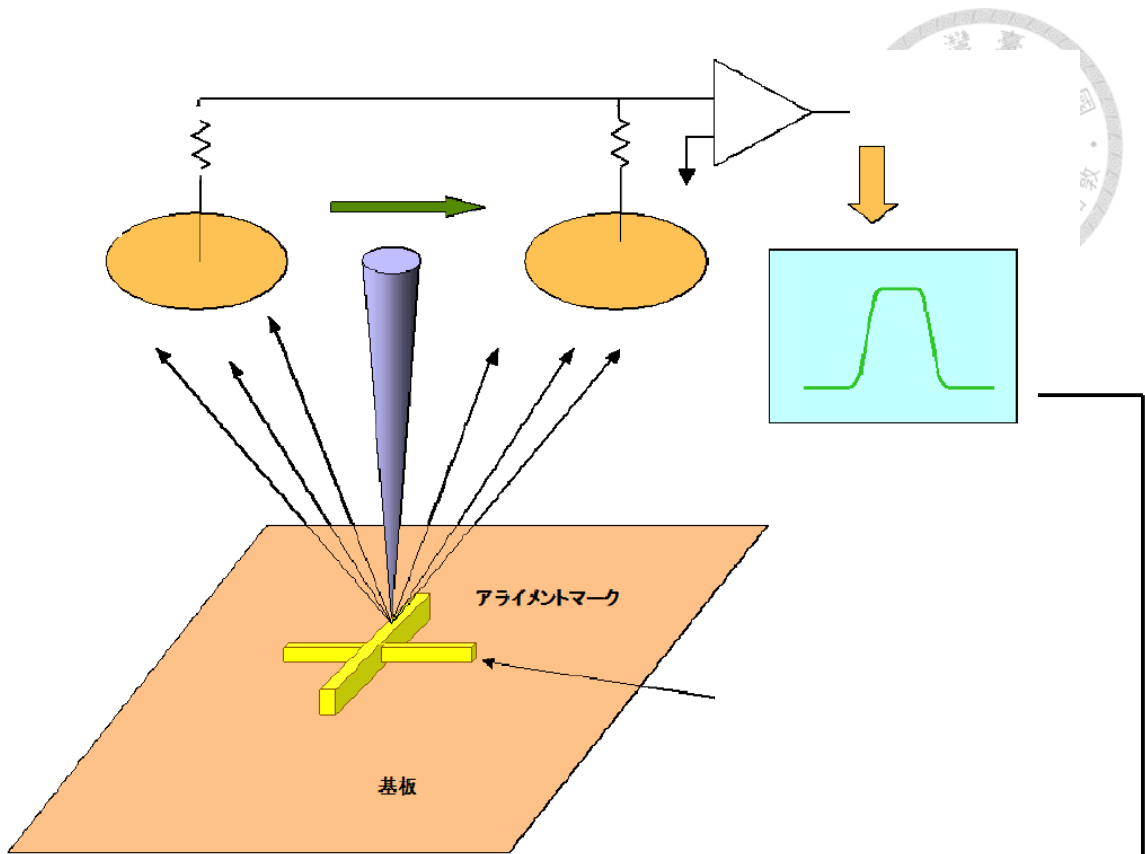


Fig. 4.27 The strategy of scanning a mark (upper) and the detected signals (lower)



Fig. 4.28 The P-TEOS CVD system

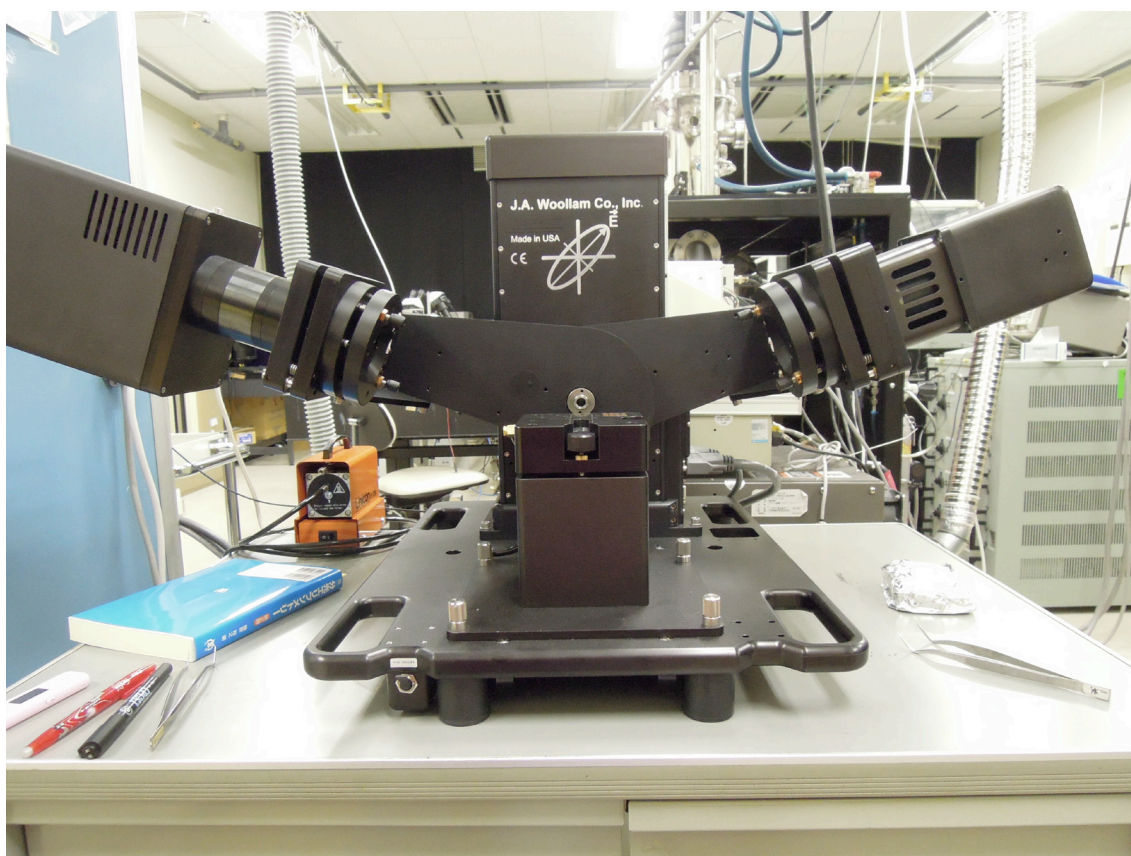


Fig. 4.29 The ellipsometer

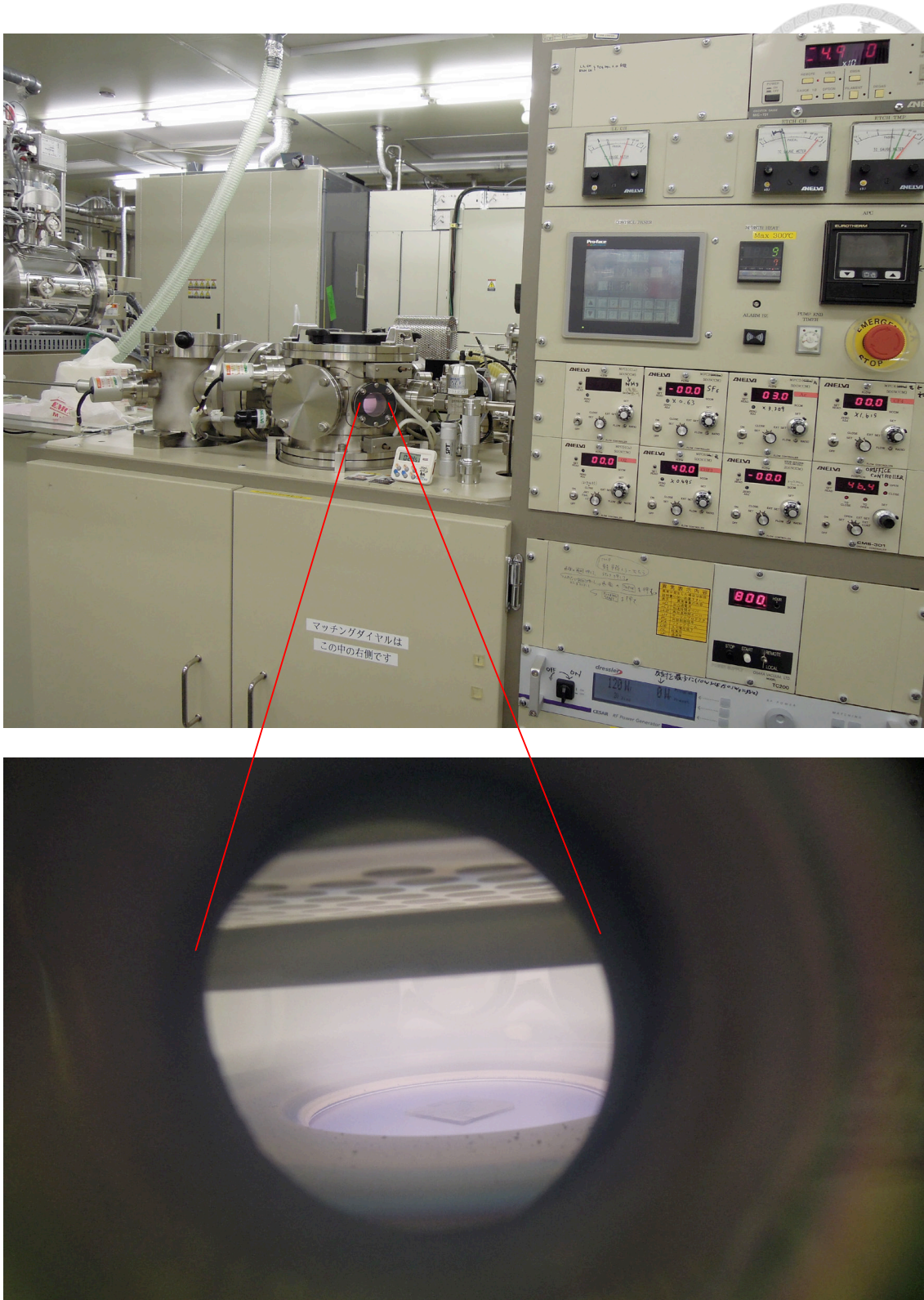


Fig. 4.30 The RIE system

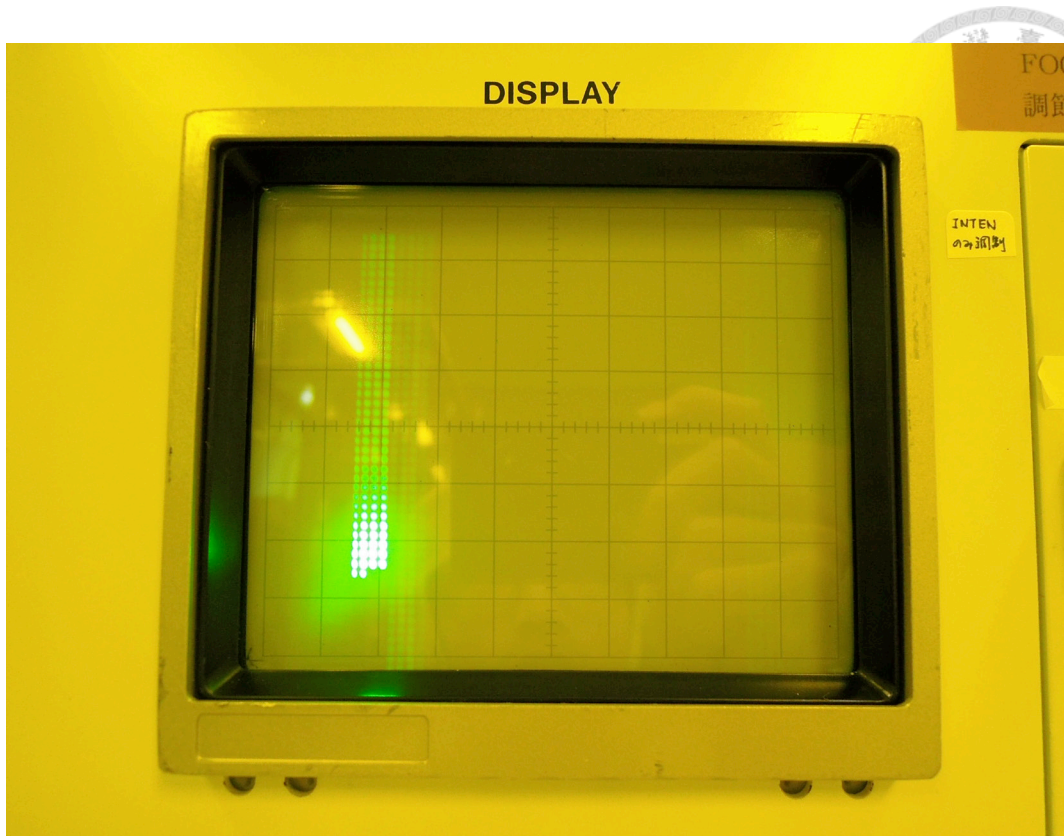


Fig. 4.31 PC patterns being written by the EB lithography system

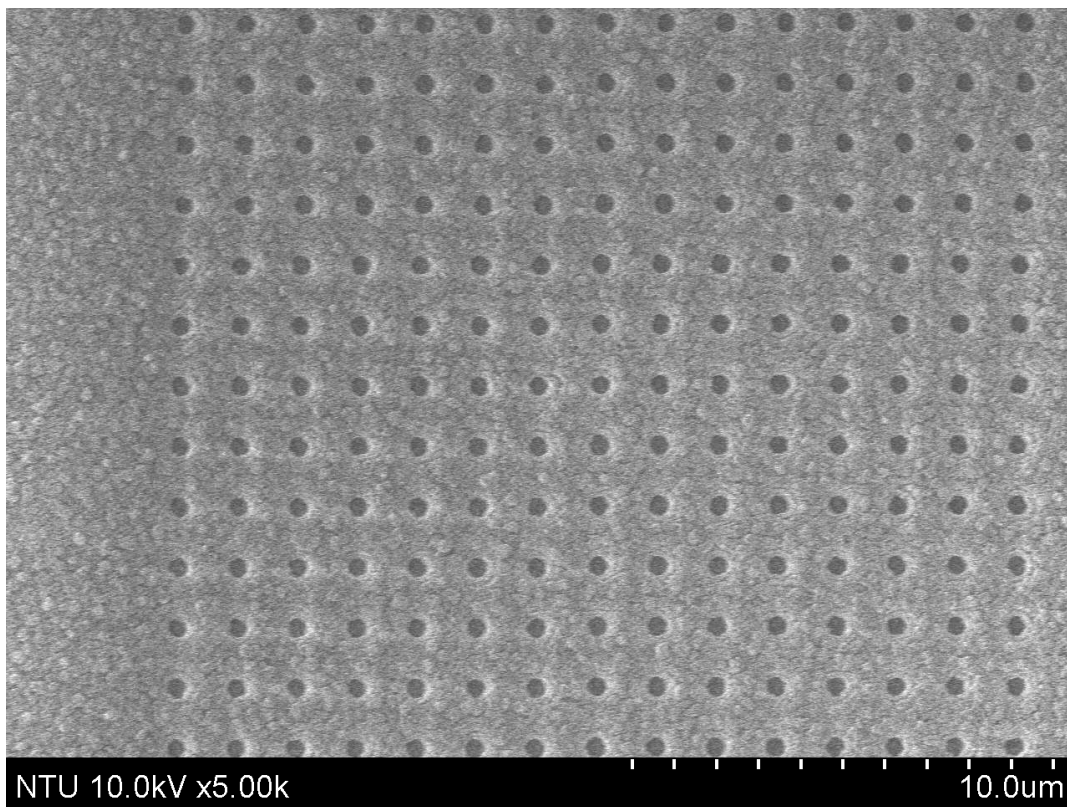


Fig. 4.32 a SEM image of the PC structure

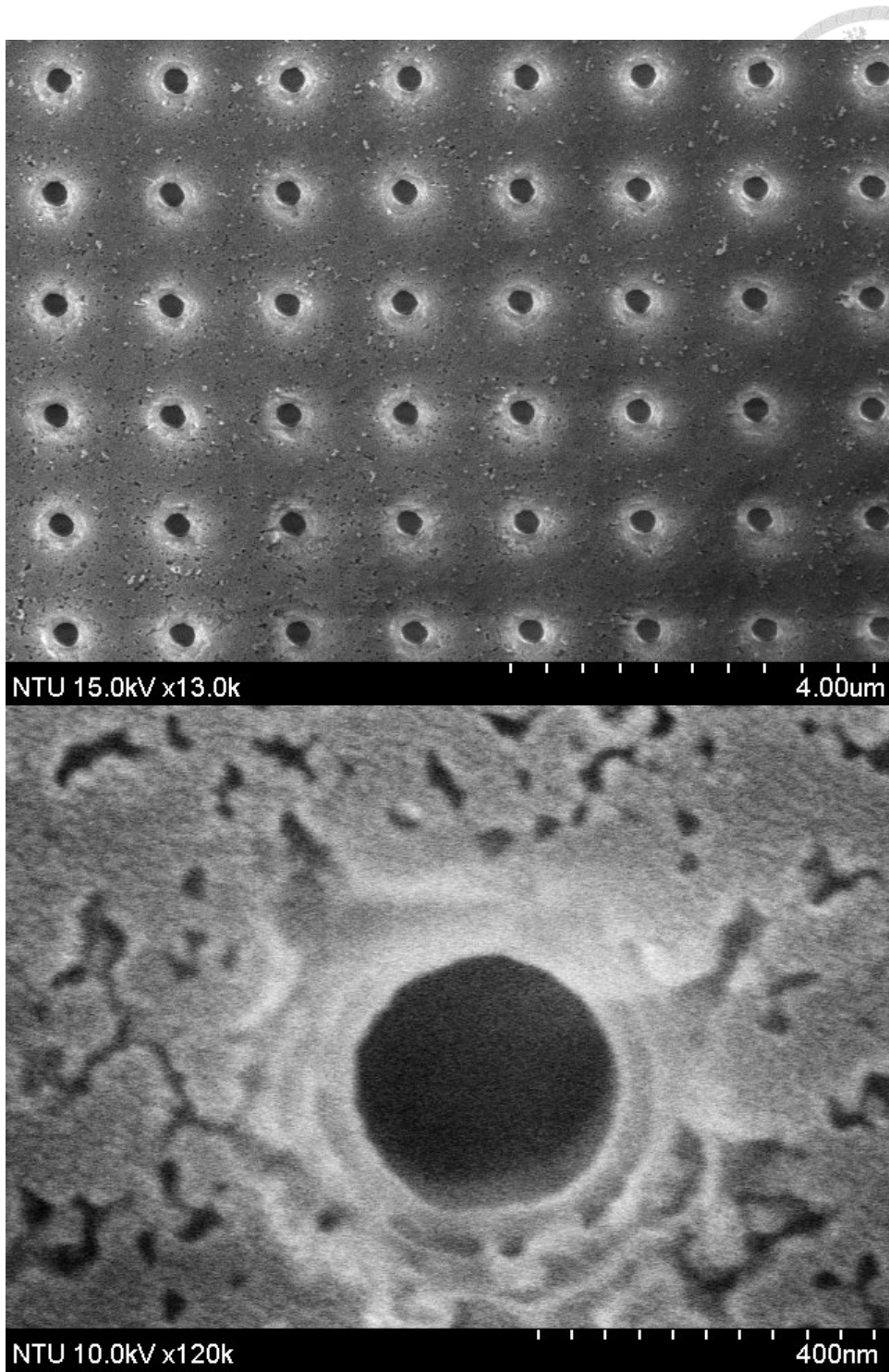


Fig. 4.33 more SEM images of the PC structure

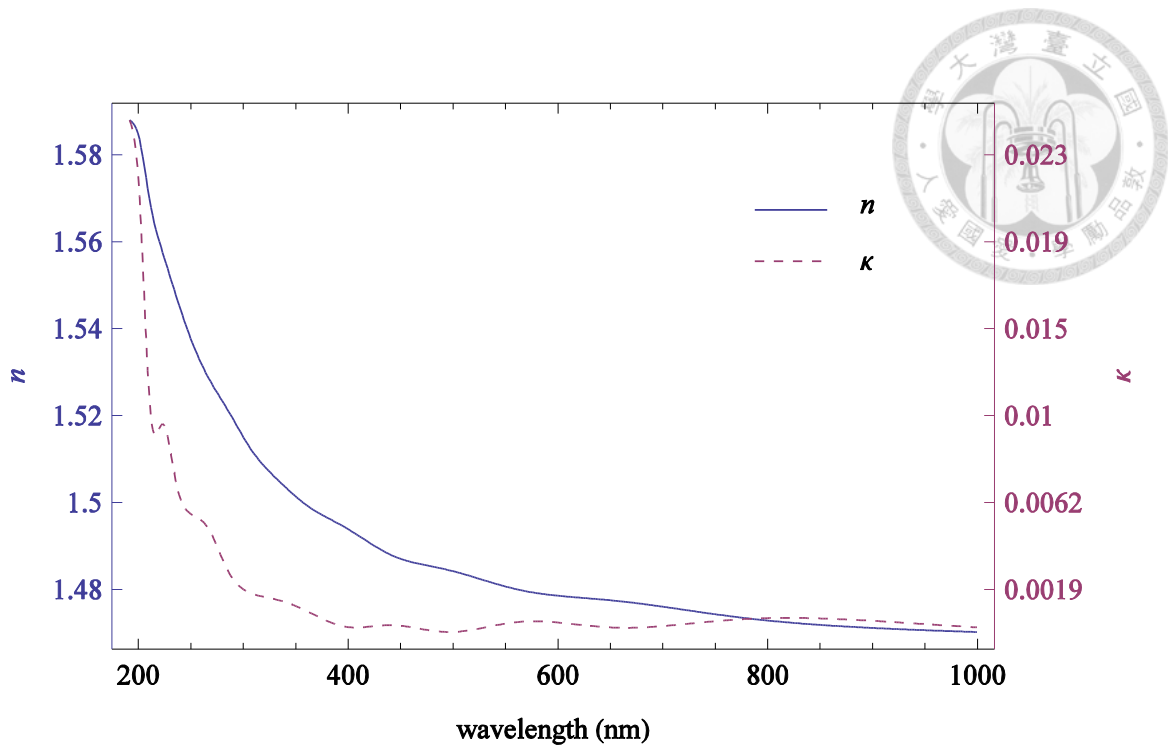


Fig. 4.34 Complex index of refraction ($n + i\kappa$) of P-TEOS SiO₂ vs. wavelength



Chapter 5

Experiment Results

We used the vector network analyzer (VNA) Agilent E5071C (Fig 5.1) with Cascade Microtech's ACP40-GS/SG-250 microprobes (Fig 5.2) to characterize the devices. Before measurement the VNA were calibrated via an impedance standard substrate such that the ports (including the cables and the probes) were matched with $(50 + j0) \Omega$.

5.1 Transmission of PCs

We measured the S_{21} signals and compared with the cases with and without PC, we obtained the transmission of the PC.

5.1.1 SFIT without PC —verification of SFIT designs

The measured signals contained electromagnetic (EM) feed through and triple transit echo (TTE) signals that were unwanted and disturbed us seriously. Therefore we use the time-gating technique to filter them out.

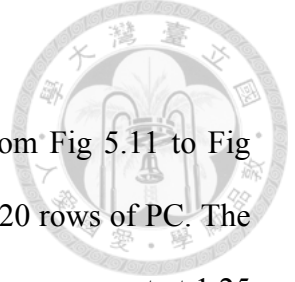
The original measured signals were in frequency domain, where the direct signal, electromagnetic feed through and TTE signals were mixed together. But after we applied the inverse Fourier transform (FT), they are separated in time domain (the impulse response). Then we captured the interval that contains the direct signal only, filled other

intervals with zeros, and do FT, we then got the desired frequency spectrum of the direct signal.

Here is an example of the signals of SFIT set #2 (See **Table 3.1.**) on non-rotated ST-cut quartz (Rayleigh wave signal). Fig 5.3 is the time domain signal. The most left was the EM feed through signal since it had the speed of light. Two small wave packets followed. They are LSAWs that are faster than the Rayleigh wave. And the direct Rayleigh wave arrived at about 0.08 μs . The sinc function envelope was clear. The TTE of the Rayleigh wave signal came at triple of the direct Rayleigh wave arrival time. Fig 5.4 shows the frequency spectrum of the original and gated signal. The original signal has only ripples around the frequency range while the gated signal shows a square tableland. The frequency range was matched with the Rayleigh wave velocity on ST-cut quartz (3158 m/s).

Fig 5.5 and Fig 5.6 shows the signals of SFIT set #2 on 90°-rotated ST-cut quartz (LSAW). We found the direct response smaller, and oblique in frequency response. This may be due to stronger internal reflection in the IDT (usually higher for SH-type SAWs), and the effect is even stronger at higher frequency since the ratio of metal strip thickness to the wavelength is larger.

{Fig 5.7, Fig 5.8} and {Fig 5.9, Fig 5.10} are Love wave signals of SFIT #1 and #2, respectively. The signals were even weaker for the electromechanical coupling was smaller. The EM feed through signal looked like a decaying function of time, but still remained a considerable value compared with the Love wave signal when Love wave arrived. This may be the reason why the background noise in frequency domain could not be suppressed. On the other hand the range 0.95 ~ 1.65 GHz was coincident with expectation.



5.1.2 SFIT with PC

Here are the signals with PCs lying in between the SFITs. From Fig 5.11 to Fig 5.22 are the signals of six combinations of SFIT #1, #2 with 10, 15, 20 rows of PC. The rejection in the band gap is obvious. From the complex band structure we expect at 1.25 GHz, the tunneling signals should have attenuation about 43 dB, 65 dB, 80 dB for 10, 15, 20 rows of PC, respectively. But since there were background noise, we could not observe such attenuation difference. However at the edges of the stop band the response of 10 rows PC is relative rounded while that of 20 rows PC is steeper.

Comparing SFIT #1 and #2, we found the signal of #2 is better substantially, which the #2 had less pairs of electrodes.

5.2 One-port resonator

We evaluate the resonators by their electrical admittances. And the admittance is calculated from the measured S_{11} signal of the resonator as follows.

The admittance is the reciprocal of the impedance,

$$\mathbf{Y} = \frac{1}{\mathbf{Z}}. \quad (5.1)$$

Where \mathbf{Y} and \mathbf{Z} represent the admittance and the impedance of the device, and the bold face means they are complex since the potential and the current can be not in phase. And the S_{11} can be treated as the reflection coefficient from port 1 to the device, we have

$$\begin{aligned} S_{11} &= \frac{\mathbf{Z}_1 - \mathbf{Z}}{\mathbf{Z}_1 + \mathbf{Z}} \\ &= \frac{50\Omega - \mathbf{Z}}{50\Omega + \mathbf{Z}}, \end{aligned} \quad (5.2)$$

for the impedance of port 1 is calibrated as $(50 + j0) \Omega$. Therefore

$$\mathbf{Z} = 50\Omega \frac{1 - \mathbf{S}_{11}}{1 + \mathbf{S}_{11}}, \quad (5.3)$$

and

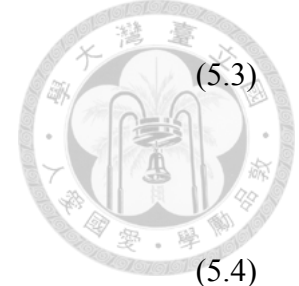
$$\mathbf{Y} = (50\Omega)^{-1} \frac{1 + \mathbf{S}_{11}}{1 - \mathbf{S}_{11}}. \quad (5.4)$$

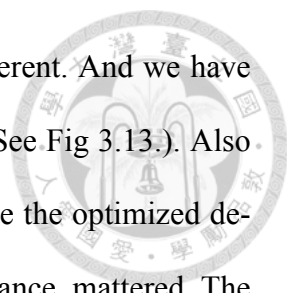
The admittance has unit Ω^{-1} , or Siemens (S). And the real part of the admittance is called the conductance (G) while the imaginary part is called the susceptance (B), or,

$$\mathbf{Y} = G + jB. \quad (5.5)$$

Dozens of resonators were made, and the admittances of some of them are plotted from Fig 5.23 to Fig 5.25. The susceptance has a background slope which represents the static capacity of the IDT. The slope is significant relative to the resonance shows it had low electromechanical coupling. It is also found the susceptance is approximately proportional to the number of IDT pairs. The conductance has this trend also, but the peak of conductance is highly depends on the resonant performance and is with more uncertainty.

One of the most important factor to evaluate the performance of a resonator is its Q factor. Originally it is defined as the ratio of the stored energy to the dissipated energy in a half cycle. It can be estimated by the inverse of the fractional width between frequencies where the conductance becomes the half height of its peak [58]. The best Q factor obtained among these resonators is about 400, which is smaller than the simulated result (1400). We found resonators with 20 rows of PC reflectors was not necessarily better than resonators with 15 or 10 rows PC since the reflection are all strong enough. Instead a much more critical factor was the fabrication precision. The PC pattern with correction of the proximity effect (holes dimension near PC border were closer to the design) had much better response then that without the correction, although both of the





PCs reflected waves well, the optimized delay distance became different. And we have shown the delay distance influences the performance significantly (See Fig 3.13.). Also bias on the CVD SiO₂ or aluminum electrodes thickness may change the optimized delay distance. And the alignment errors, directly altered the delay distance, mattered. The most serious fabrication error was the size of the PC structure. From the SEM images of the PC holes Fig. 4.33 we found the fabricated holes had radii about 160 nm however they were designed to be 300 nm.

The material damping loss might decrease the Q. The damping of SiO₂ was unknown but was sure larger than single crystals that usually used, especially in ultra-high frequency range.

And the ohmic loss existed because we observed that the conductance had a background value, with a slope. Away from resonant the static capacity dominated which current existed in the IDT and ohmic loss showed for the resist of the metal. Of course at resonance the ohmic loss was even larger.

We also found that some resonators had split peaks on their conductance response which shows multiple resonances. Consider the resonator with Fabry-Perot model, there are infinite many resonant modes in the resonator cavity which their resonant frequency is proportional to the number of half wavelengths in the cavity (assuming non-dispersion). Although the modes are orthogonal to each other they may be non-orthogonal to the same excitation, thus they can be excited simultaneously. Especially for a resonator designed with large number of half wavelengths inside its cavity, the neighboring modes are close in frequency and can be excited if there is some alignment error.

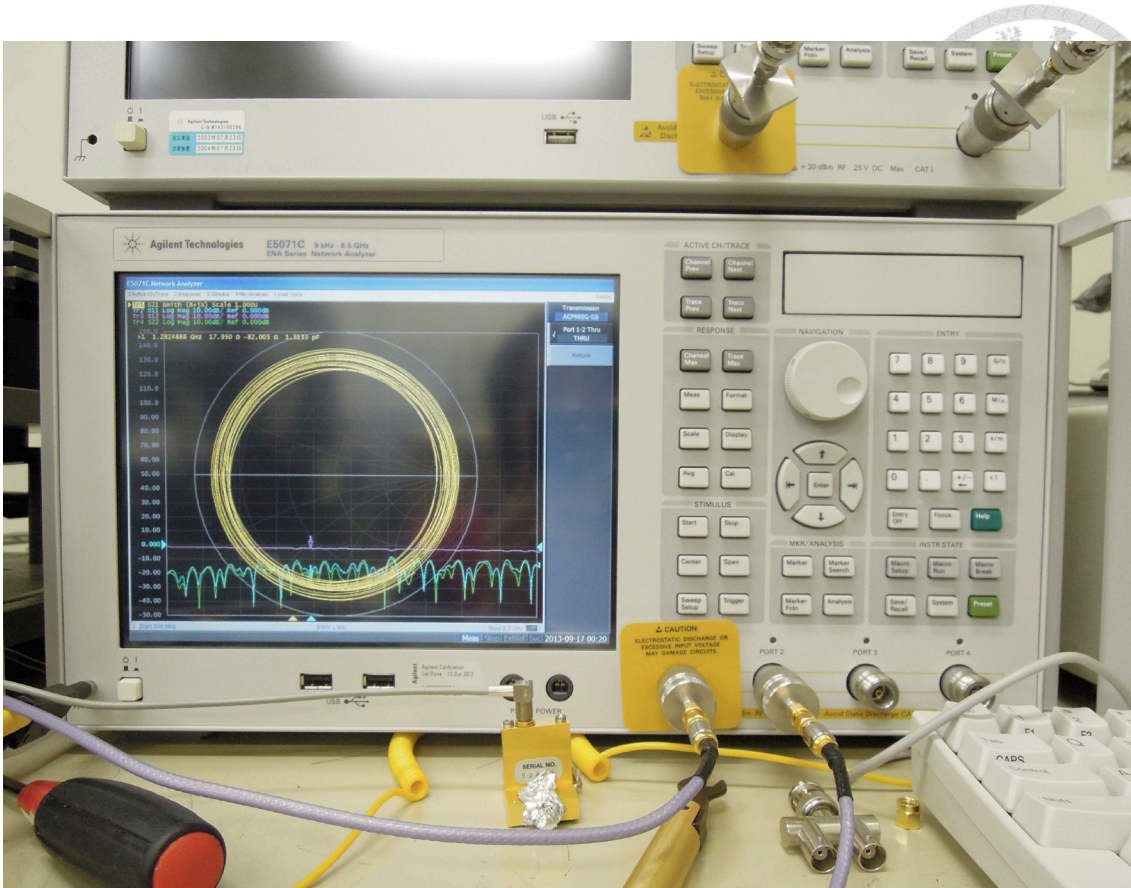


Fig 5.1 VNA Agilent E5071C

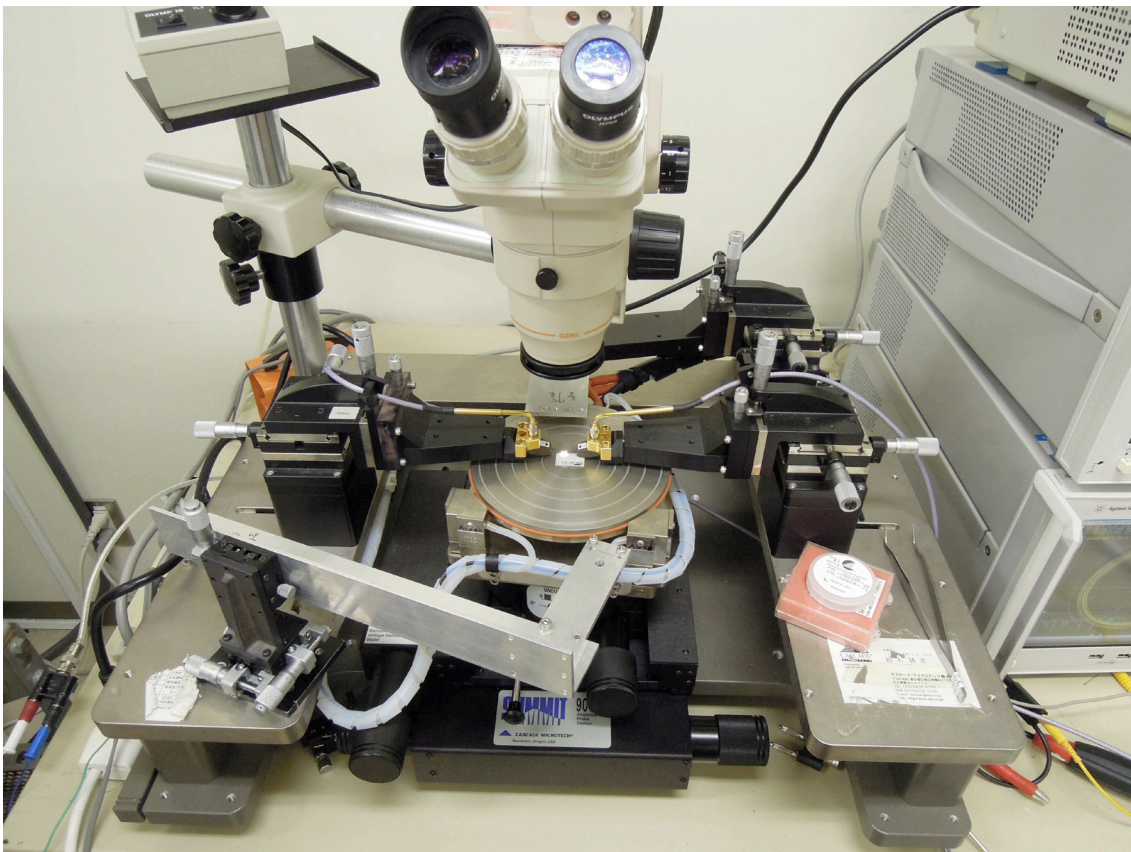


Fig 5.2 Cascade Microtech probes with the platform

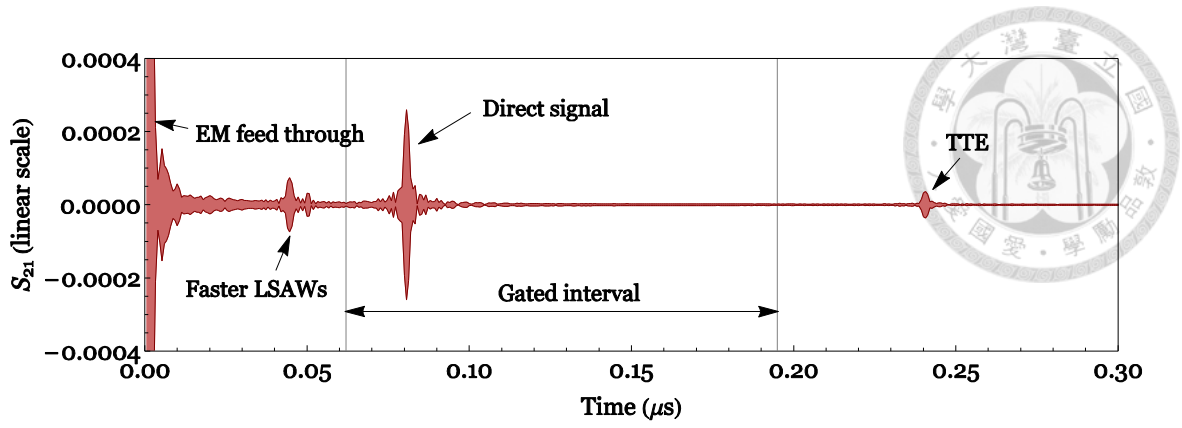


Fig 5.3 Impulse response of SFIT #2 on ST-cut quartz.

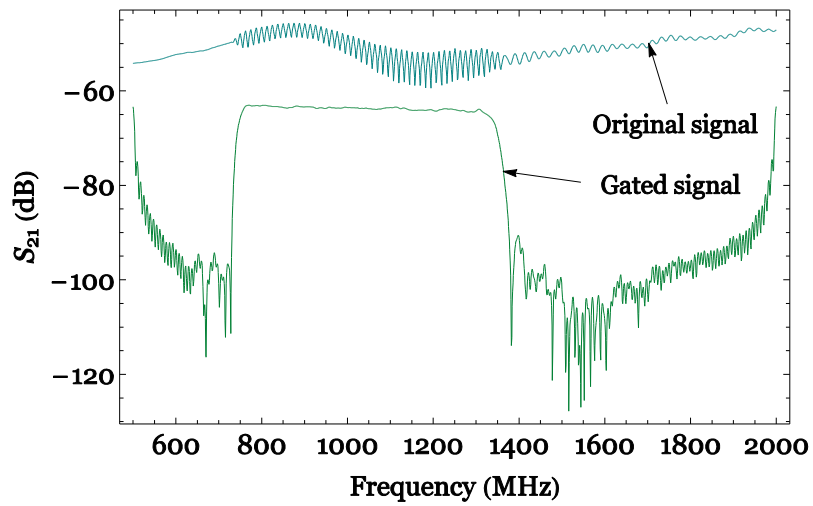


Fig 5.4 Original and gated signal in frequency domain.

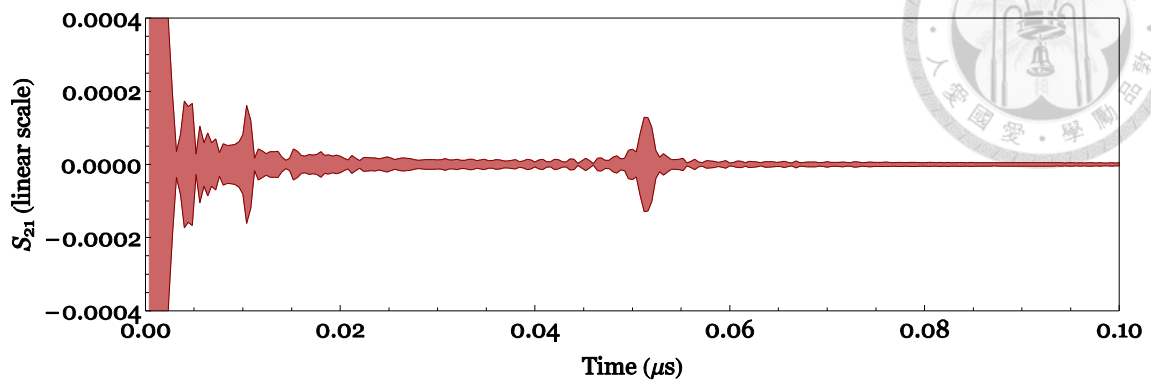


Fig 5.5 Impulse response of SFIT #2 on 90°-rotated ST-cut quartz.

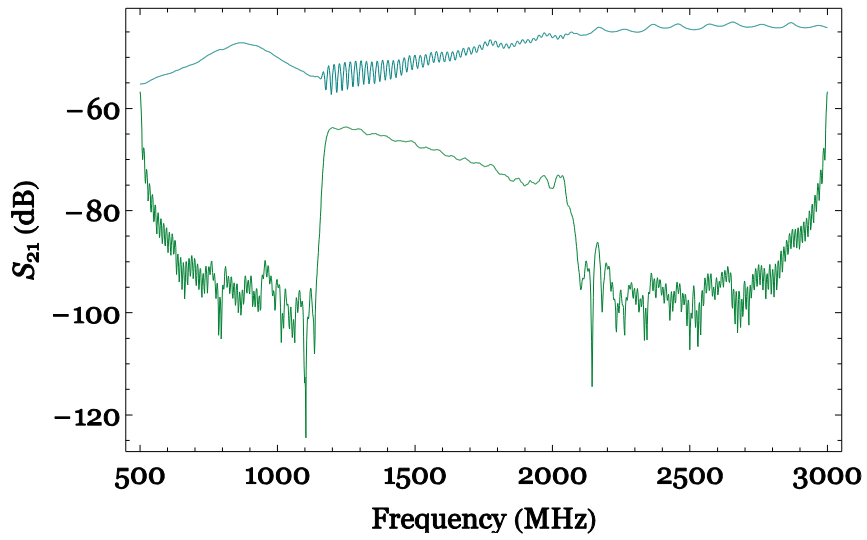


Fig 5.6 Original and gated signal of SFIT/90°-rotated ST-cut quartz in frequency domain.

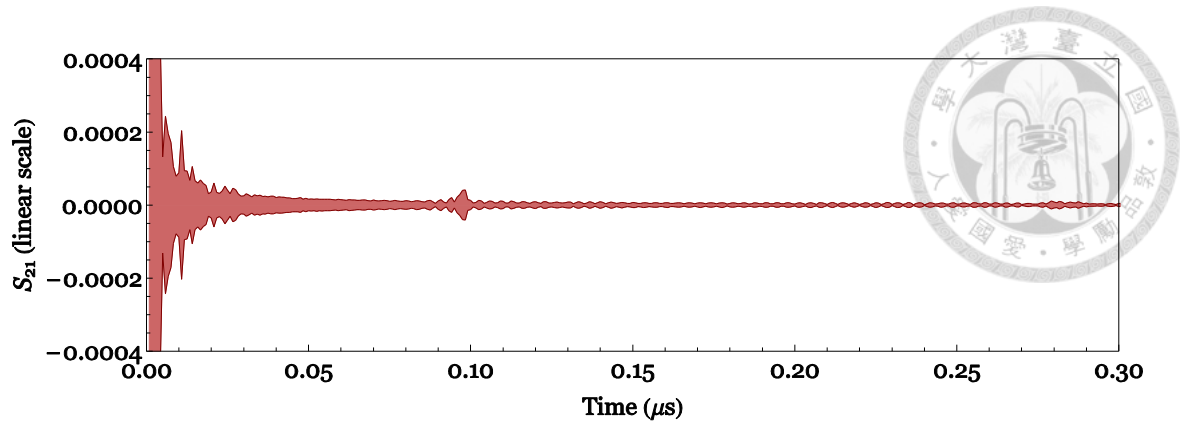


Fig 5.7 Impulse response of SiO₂/SFIT #1/90°-rotated ST-cut quartz

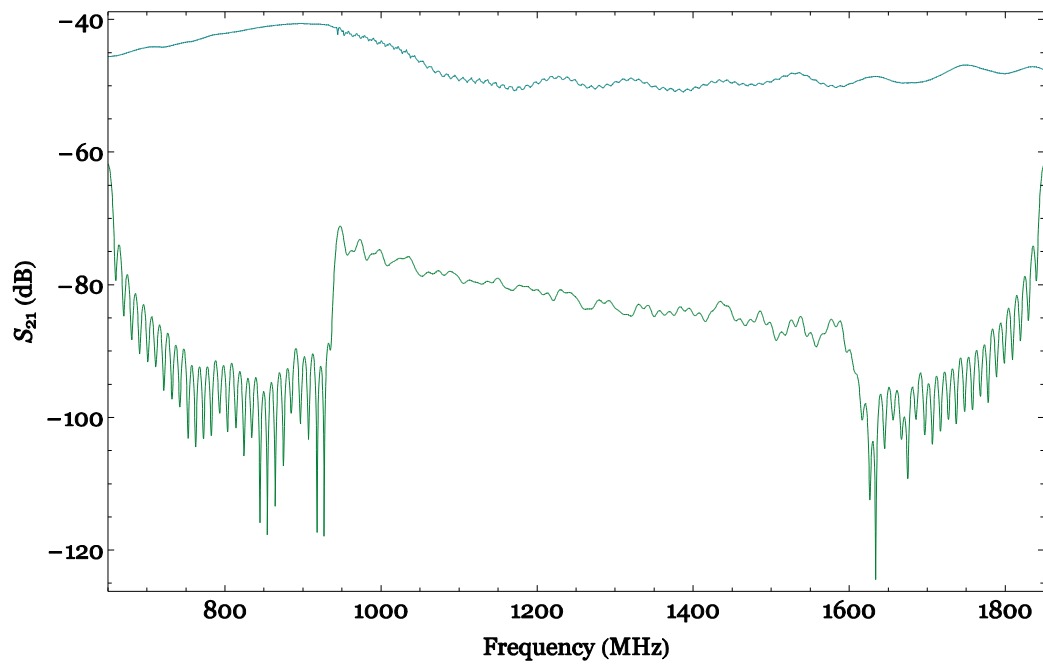


Fig 5.8 Original and gated signal of SiO₂/SFIT #1/90°-rotated ST-cut quartz in frequency domain.

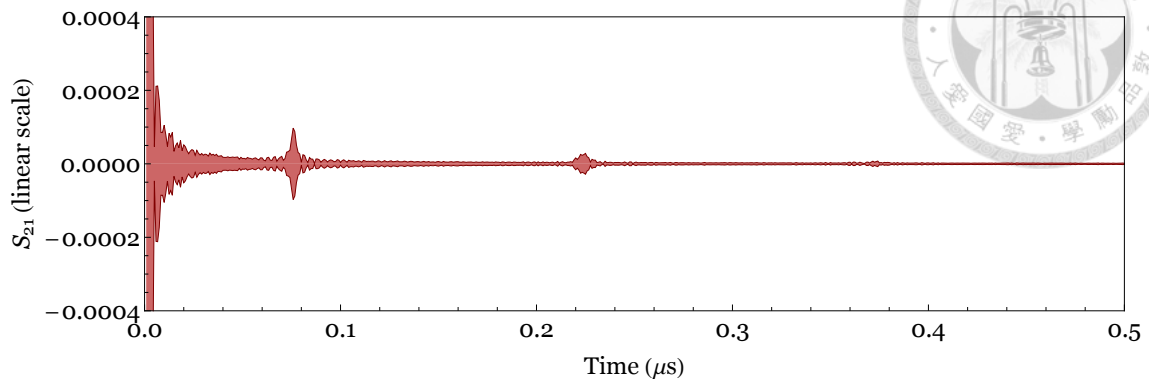


Fig 5.9 Impulse response of SiO₂/SFIT #2/90°-rotated ST-cut quartz

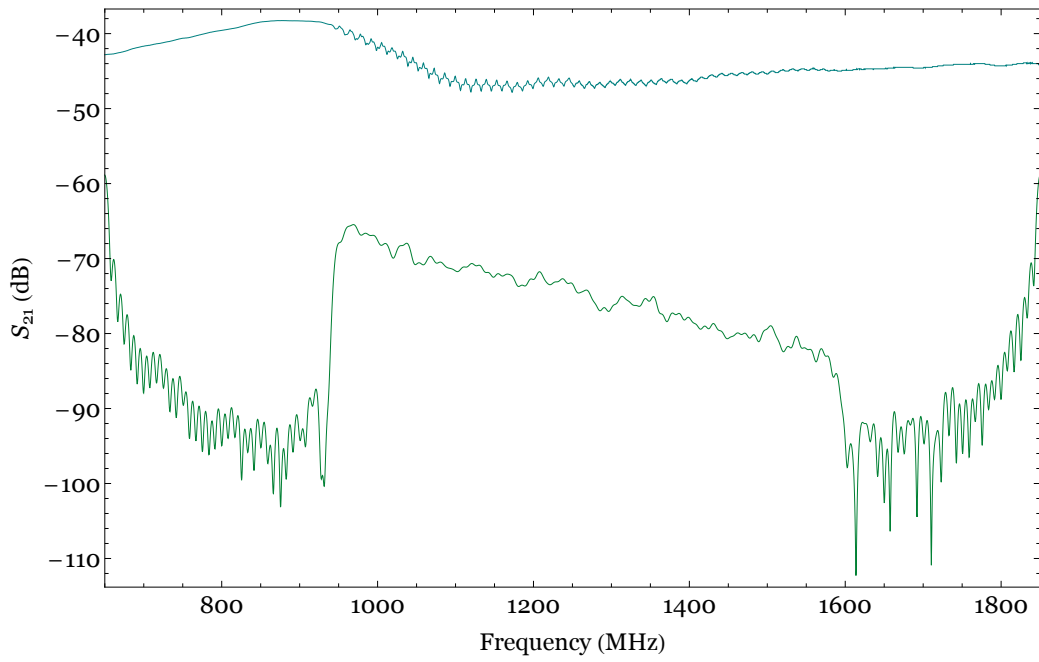


Fig 5.10 Original and gated signal of SiO₂/SFIT #2/90°-rotated ST-cut quartz in frequency domain.

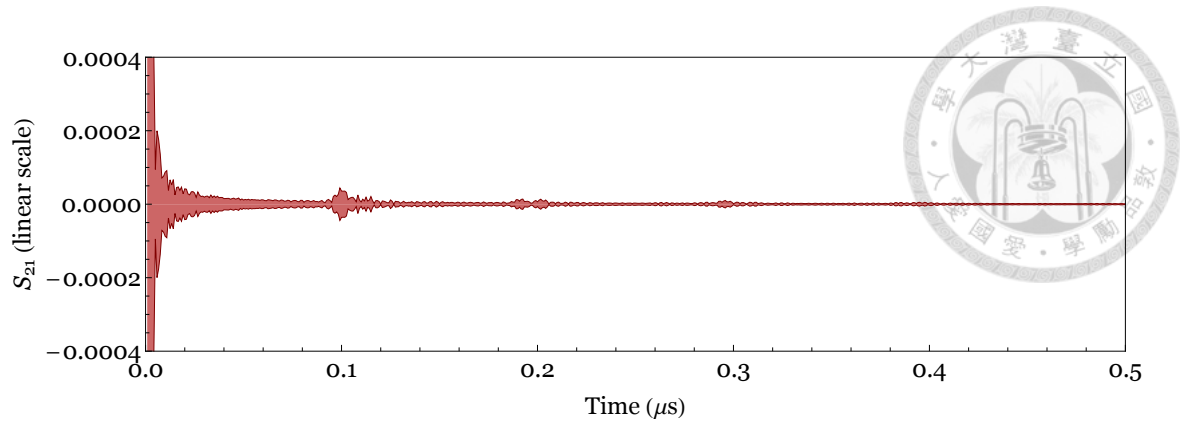


Fig 5.11 Impulse response of SFIT #1 with 10 rows of PC

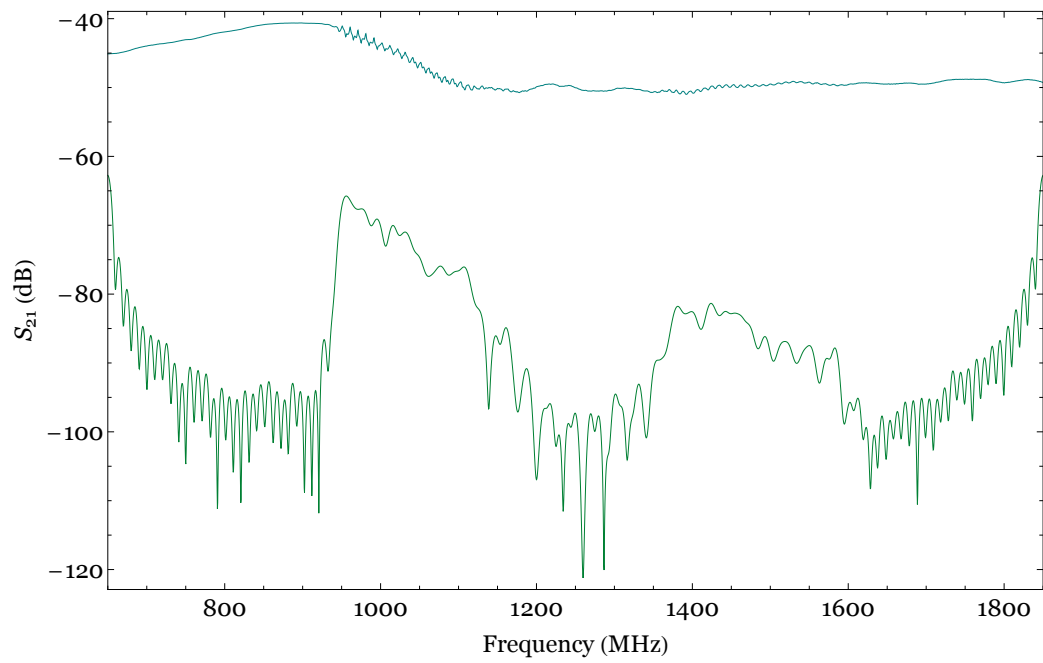


Fig 5.12 Frequency response of SFIT #1 with 10 rows of PC

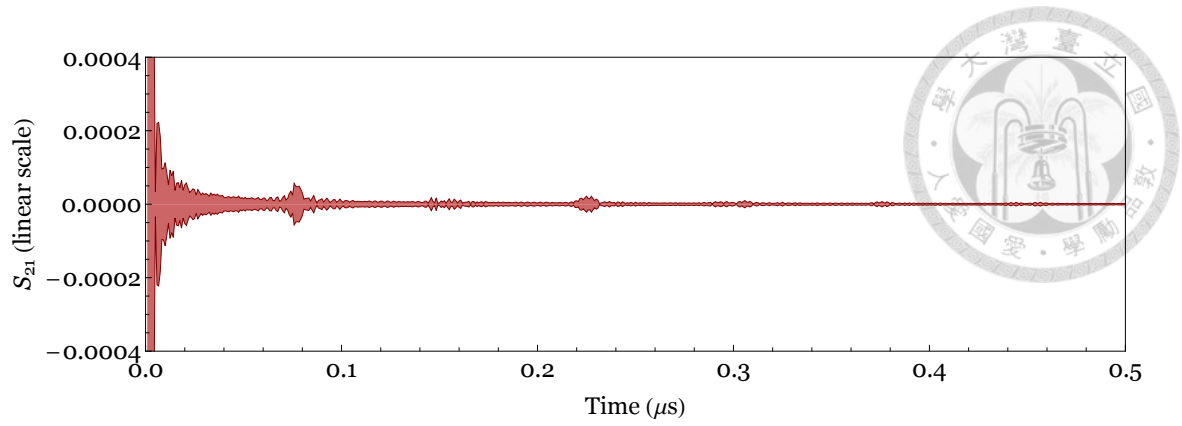


Fig 5.13 Impulse response of SFIT #2 with 10 rows of PC

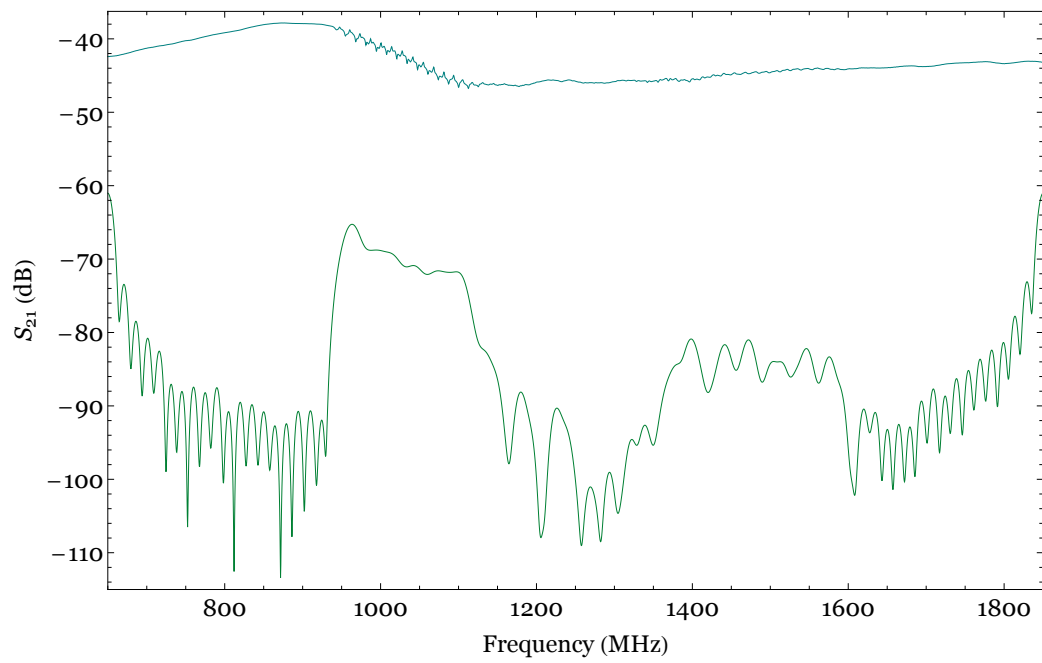


Fig 5.14 Frequency response of SFIT #2 with 10 rows of PC

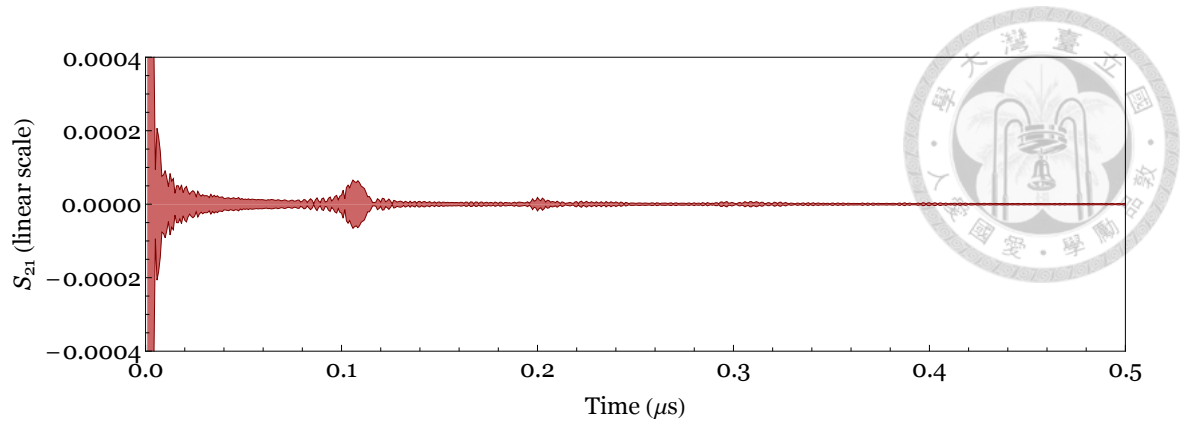


Fig 5.15 Impulse response of SFIT #1 with 15 rows of PC

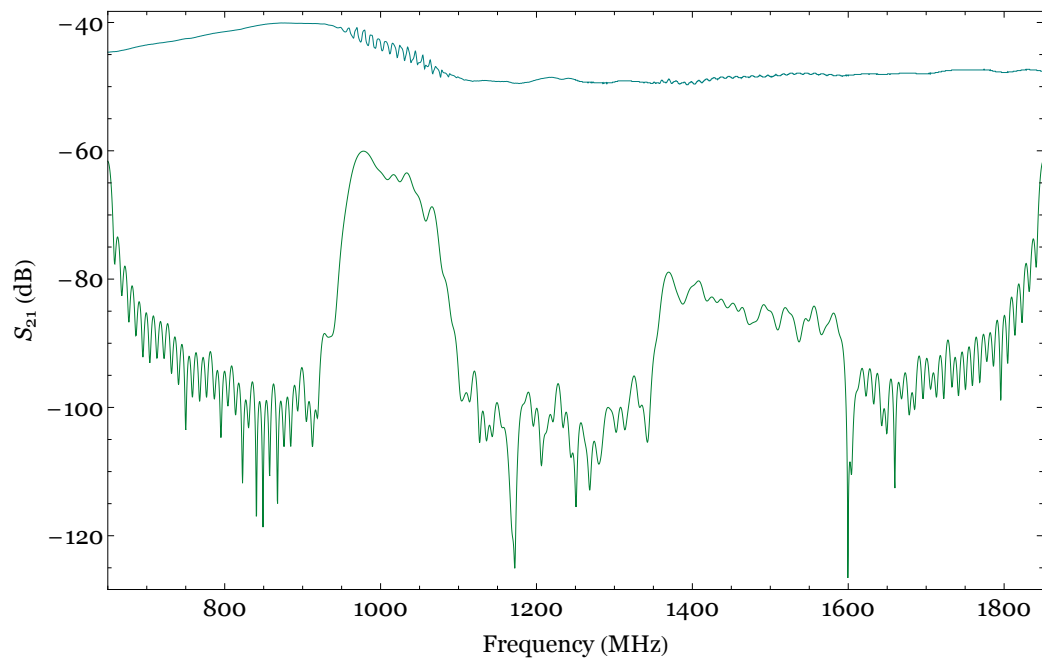


Fig 5.16 Frequency response of SFIT #1 with 15 rows of PC

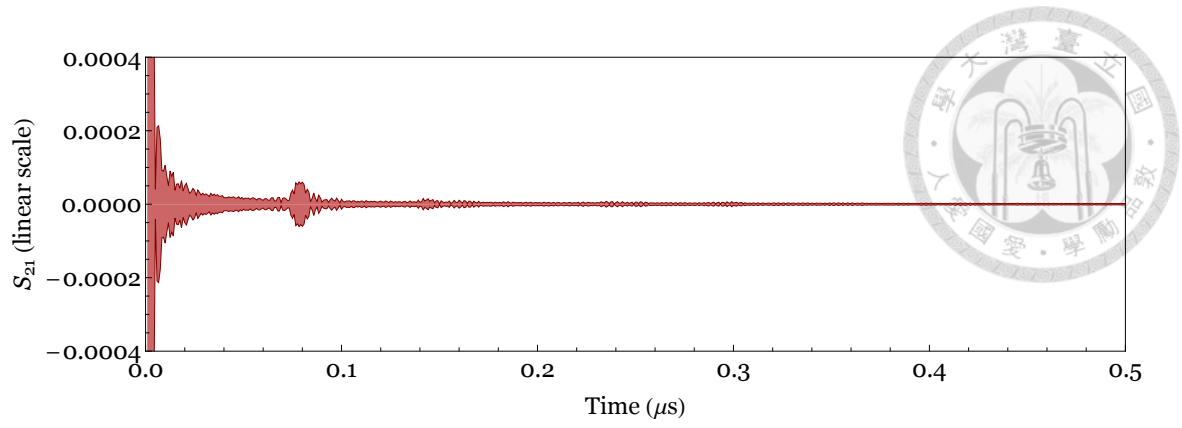


Fig 5.17 Impulse response of SFIT #2 with 15 rows of PC

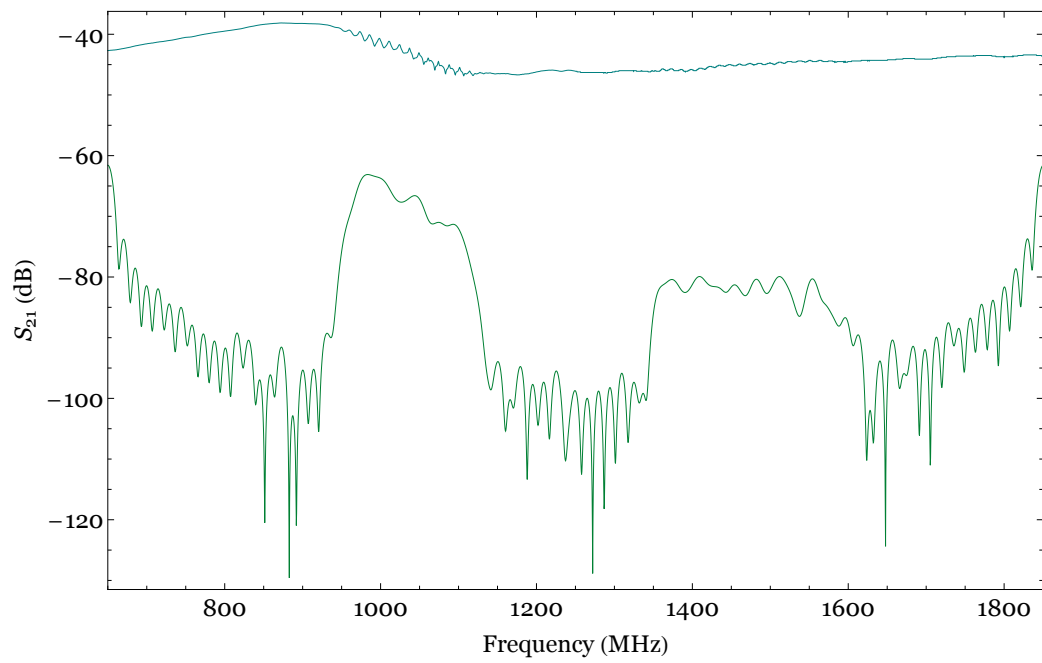


Fig 5.18 Frequency response of SFIT #2 with 15 rows of PC

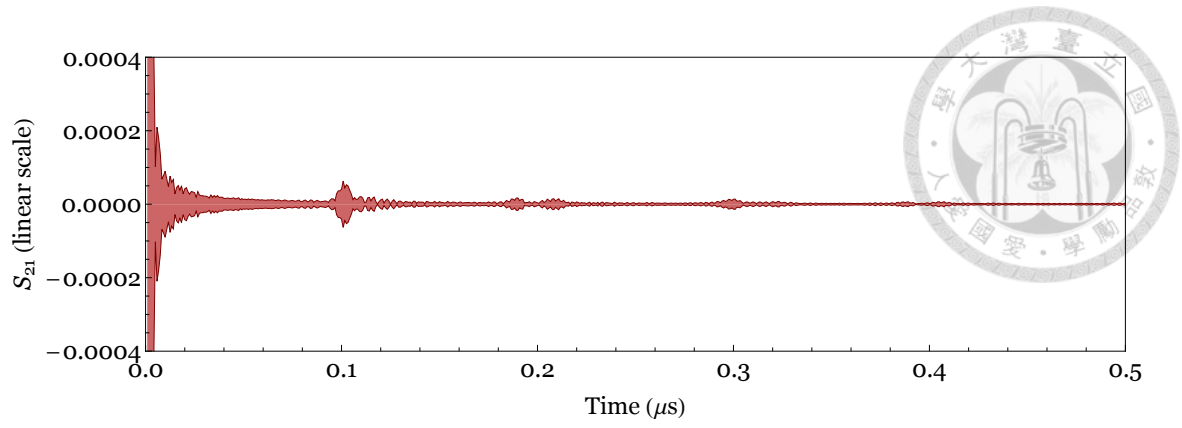


Fig 5.19 Impulse response of SFIT #1 with 20 rows of PC

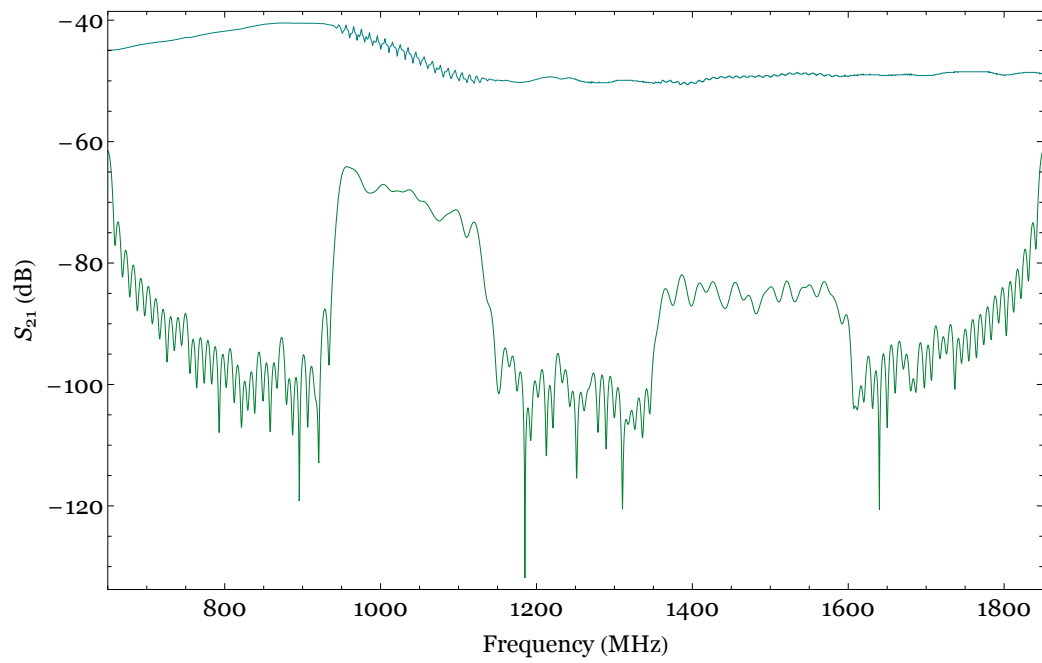


Fig 5.20 Frequency response of SFIT #1 with 20 rows of PC

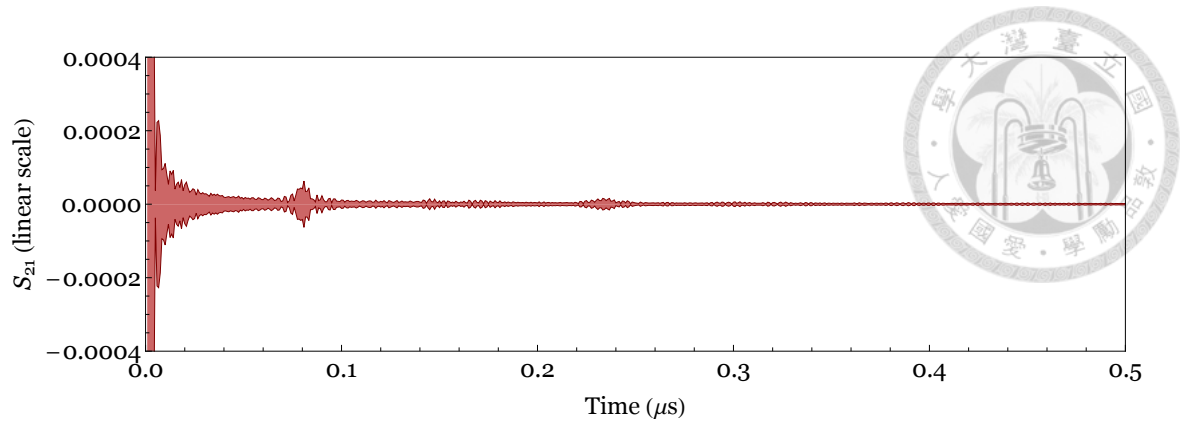


Fig 5.21 Impulse response of SFIT #2 with 20 rows of PC

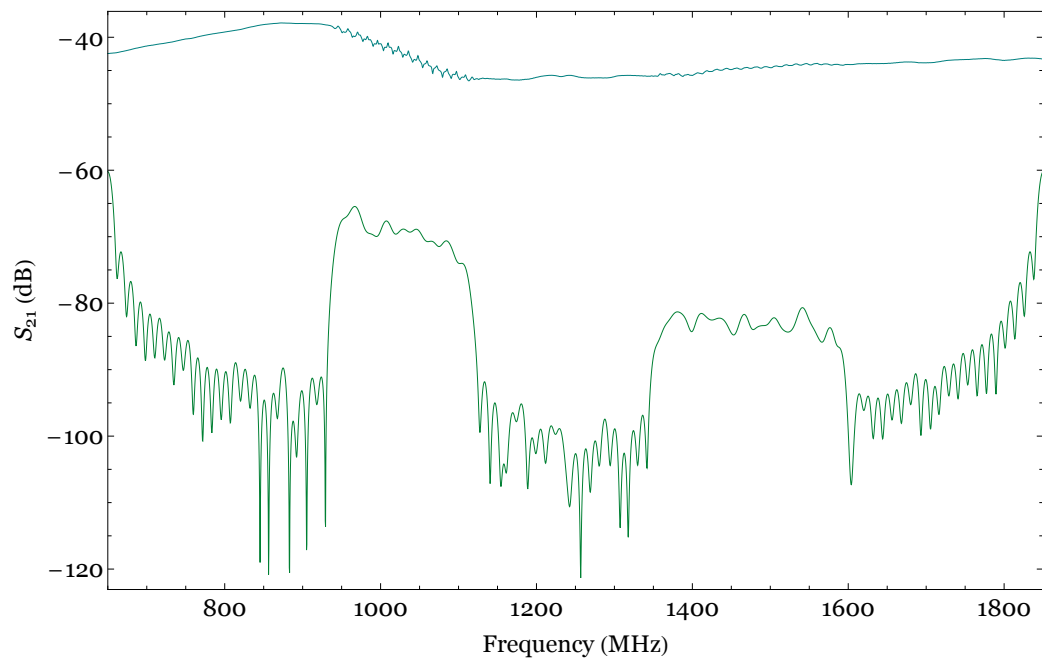


Fig 5.22 Frequency response of SFIT #2 with 20 rows of PC

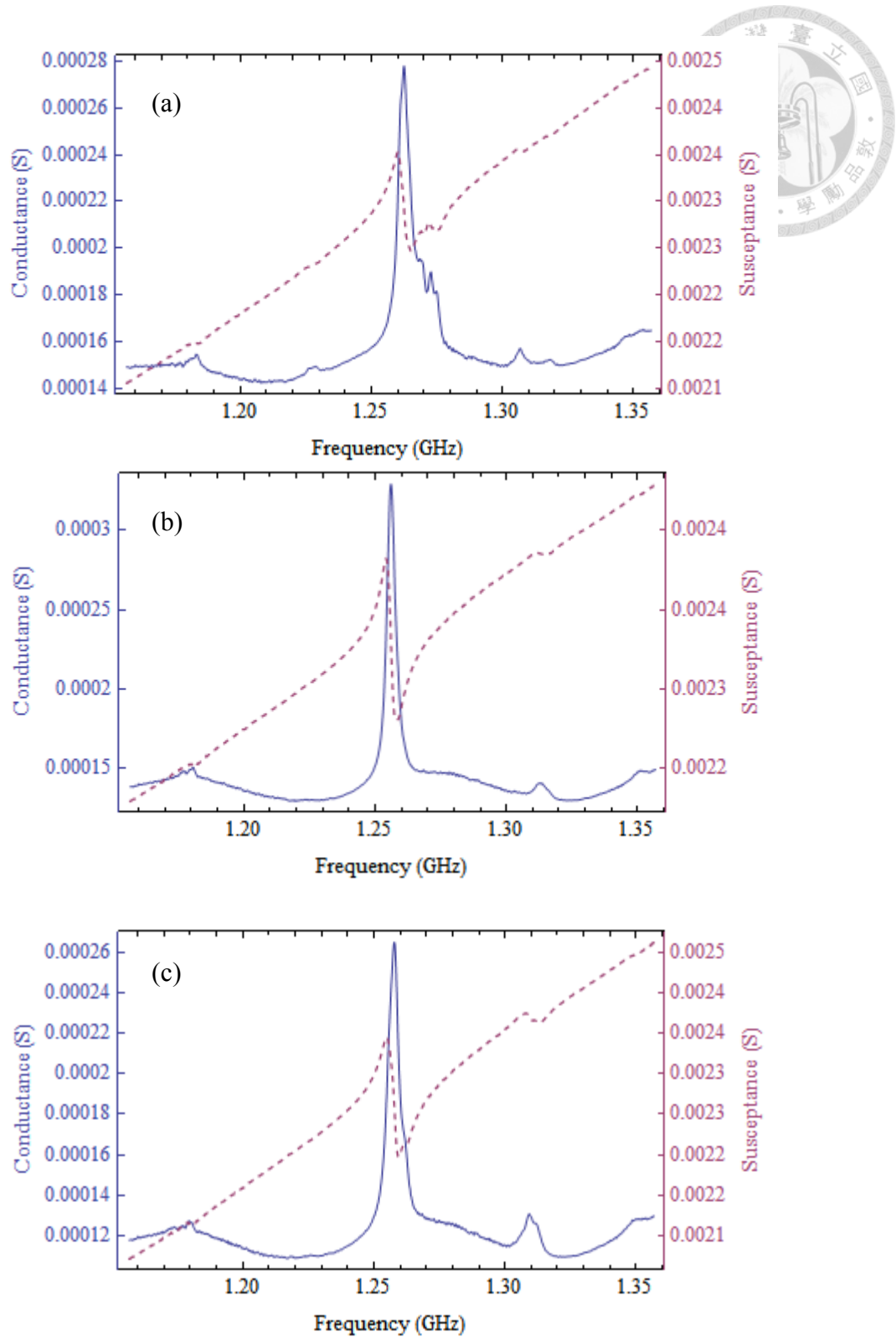


Fig 5.23 Admittance signals of resonators containing 10.5 IDT pairs with (a) 10, (b) 15, (c) 20 rows PC as reflectors

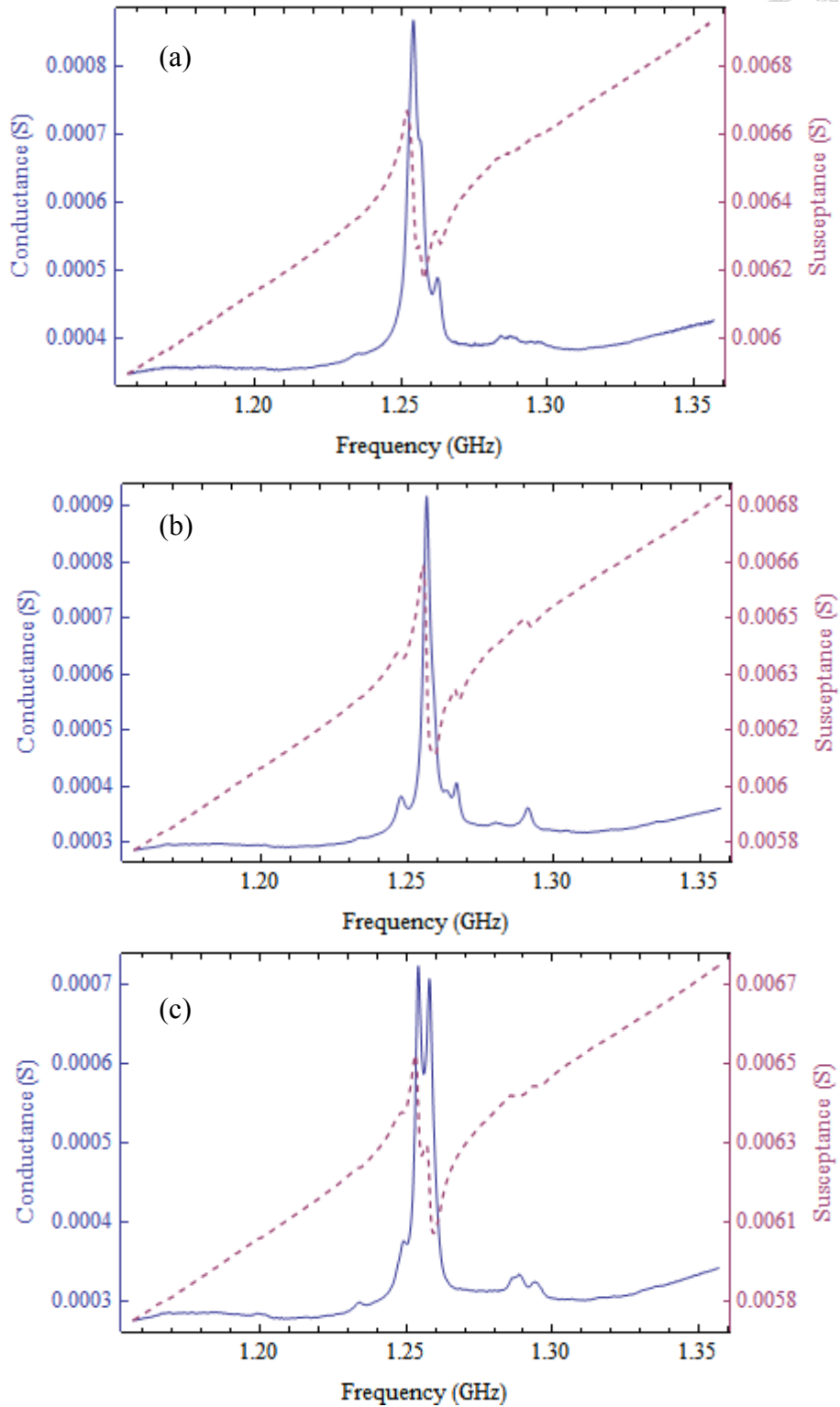


Fig 5.24 Admittance signals of resonators containing 30.5 IDT pairs with (a) 10, (b) 15, (c) 20 rows PC as reflectors

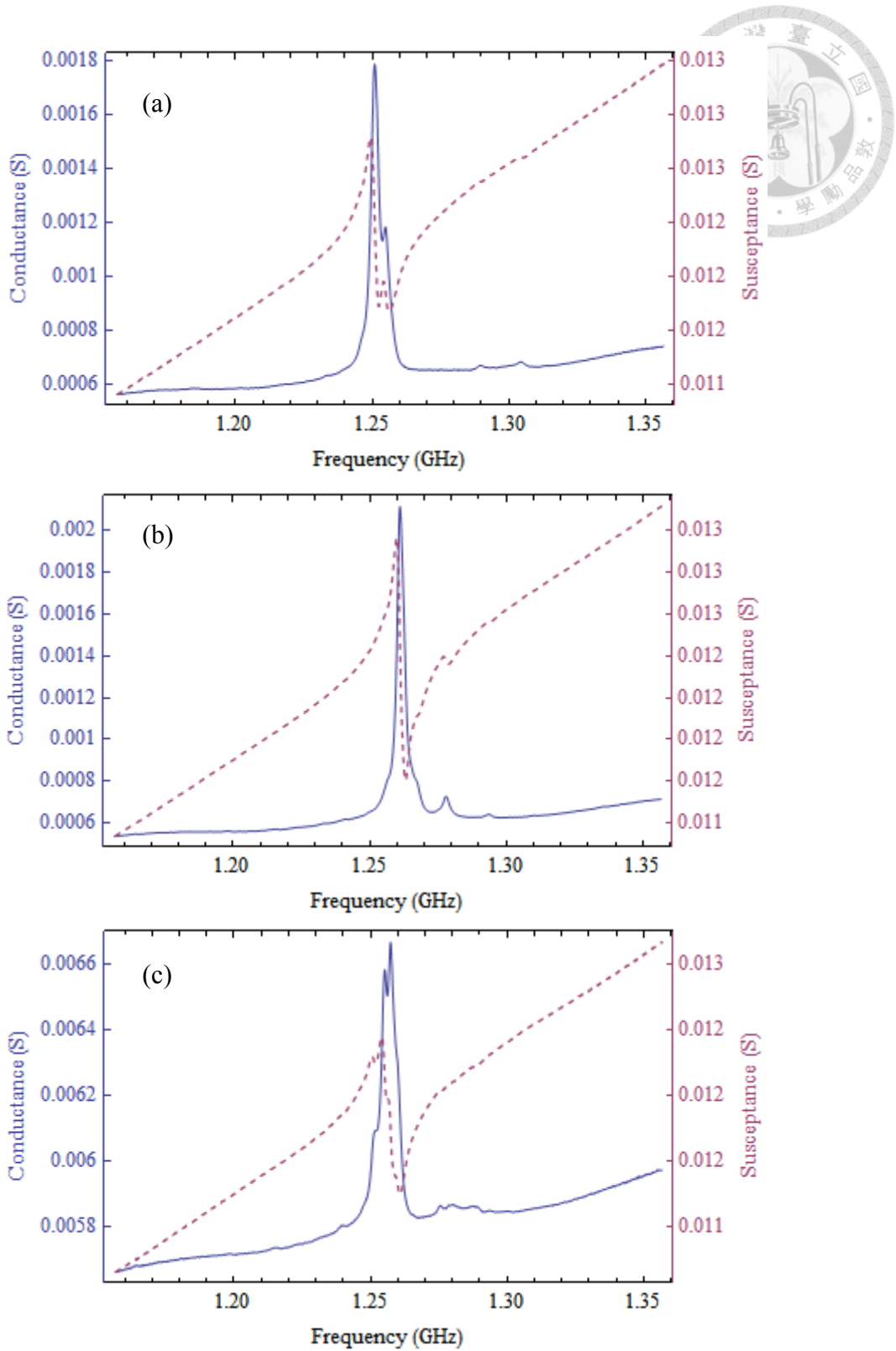


Fig 5.25 Admittance signals of resonators containing 30.5 IDT pairs with (a) 10, (b) 15, (c) 20 rows PC as reflectors



Chapter 6

Conclusions and Future Works

6.1 Conclusions

In this thesis we present the methods analyzing acoustic waves in 2-dimensional phononic crystals. We investigate surface waves especially the Love wave propagating in the surface PC that has periodic structure modulations only near the free surface, strictly a quasi-2-D structure. And the anisotropy of the material are considered to calculate the complete band structure. We used a finite-depth model to calculate the propagating eigenmodes, and proposed an explanation for the level repulsion between surface modes and plate modes. Also the region above the sound line used to be not discussed in the literatures, were discussed. Degree of leakiness of the surface waves in the PC is therefore learned.

We analyzed a phononic SiO₂ thin film/90°-rotated quartz substrate structure and expected a partial band gap for Love waves. The gap was later verified through the experiment. The reflection/transmission phenomenon of Love waves incident into the PC at the stop band frequency was investigated. Such phononic structure has excellent reflection coefficient with little periods. A 1-port Love wave resonator base on the PC re-

flecting was designed and made. The method of designing the resonator is detailed in the thesis.

In the experiments we applied the advanced NEMS fabrication technology to fulfill the acoustic devices that operates in the GHz range. The experiments agreed with the theory.

6.2 Future works

In the finite-depth model, we claimed that the degree of leakiness of a surface mode can be deduced by strength of coupling with the plate modes, however a quantitative estimation is lacking. This can be a next subject.

Resonator with stronger electromechanical coupling has more advantages in the applications, therefore quartz may be replaced by other piezoelectric materials such as lithium niobate or lithium tantalate. The possible applications of the Love wave resonators are filters in communications or sensors, especially for bio-sensors. SH-type SAWs are sensitive to the surface loadings and less leaky in liquids. And with the IDT protected by chemical resistive and temperature stable material SiO_2 it is suitable to operate in various sensing occasions. And with ultra-high operation frequency the sensitivity for mass loading is even higher.

Appendix Determination of the Elastic Stiffness of the PECVD SiO₂



A.1 Background

As reported in the literatures [59]-[64], mechanical properties of SiO₂ vary from different deposition methods such as CVD [59]-[61] or sputtering [62]-[64]. Even more, the properties of SiO₂ films can also be altered via the deposition conditions. To have good matching between simulations and experiments, the mechanical properties of SiO₂ film deposited by the certain machine with the conditions identical to the fabrications were measured before the devices were designed.

A.2 Methods

A method based on SAW propagation is proposed to estimate the two Lamé constants via the experiment data. By measuring the phase velocities of the Rayleigh wave and Love wave on the SiO₂/quartz layered half space with a certain kh number, the two Lamé constants can be found.

First the SiO₂ film is assumed to be homogeneous and isotropic, and has a density of 2200 kg/m³, for the density seems not affected by different deposition methods reported in the literatures. And then the SiO₂ film is deposited on the ST-cut quartz, with IDT on the interface between SiO₂ and quartz to generate SAWs. Given a wavelength defined by the pitch of the IDT, one can obtain the phase velocities of the excited SAWs by the frequency response of the IDT with the relation.

$$c_p = f \lambda, \quad (\text{A.1})$$

where c_p is the phase velocity, f is the responded frequency, and λ is the wavelength. In this experiment we used relatively thick SiO₂ film ($\sim 4 \mu\text{m}$; actually fabricated thickness: $3.72 \sim 4.00 \mu\text{m}$) and long wavelength ($15 \mu\text{m}$ and $25 \mu\text{m}$), therefore the loading effect of the 100-nm-thick aluminum electrodes was ignored. Theoretically, the result of one experiment setup is enough to find the Lamé constants. But 2 sets with different kh number was done to confirm the correctness of these constants.

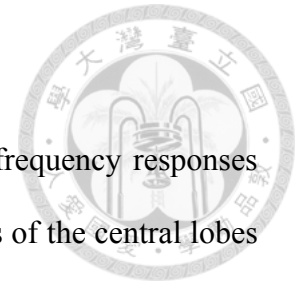
Some two-port, filter-like devices with two identical IDTs were made to find the responded frequency f , as shown in Fig. A1. With long enough delay lines between the IDTs, one can separate the triple transit echo (TTE) in the time domain impulse response. The IDT parameters are listed in **Table A1**.

As discussed in Section 2.3, a pure-SH Love wave can be generated on SiO₂/90°-rotated ST-cut quartz. Since only shear strain exists in the SiO₂ film, the Love wave properties depends on only the second Lamé constant μ (shear modulus), and are independent of the first Lamé constant λ . We made a plot of Love wave phase velocity vs. shear modulus with kh around 1.7, 1.0, by FEM simulation, comparing with the experiment result we obtained the shear modulus $\mu = 26 \text{ GPa}$ (see Fig. A2, uppers).

The only unknown left to be determined is the first Lamé constant λ . It can be found by measuring the Rayleigh wave velocity. Since the IDT is decoupled with the Rayleigh wave on 90ST quartz direction, we made another set of IDT that is perpendicular to the previous one, i.e., on the ordinary ST-cut quartz. Then similarly a plot of Rayleigh wave phase velocity vs. the first Lamé constant λ was made by FEM simulation with kh around 1.7, 1.0 (knowing $\mu = 26 \text{ GPa}$), comparing with the experiment result we obtained the first Lamé constant $\lambda = 20 \text{ GPa}$ (see Fig. A2, lowers).

A.3 Experiment Results

The impulse response (by inverse FT) and time-gated/original frequency responses of the IDT filters are shown in Fig. A3 ~ A8. We can see the shapes of the central lobes were not symmetric, and the envelopes time domain impulse responses were not perfectly diamond-shaped. These were caused by the internal reflection in the IDTs. And it made the peak frequencies slightly shifted. However the edges of the central lobe (the notch frequencies) were not altered.¹ So instead of taking the peak frequency, we took the average of the lobe edge frequencies as the responded frequency to calculate the phase velocity. It can also be found in the responses of split-finger 2121 type IDTs, the effect of internal reflection and the TTE were much smaller than the original IDTs for the period of the mechanical loading was orthogonal to the excited wave.



¹ K. Hashimoto, Surface Acoustic Wave Devices in Telecommunications Modeling and Simulation, Berlin: Springer, 2000, pp. 206-209.



Table A1 IDT parameters for SiO₂ stiffness measurement

	# 1	# 2	# 3	# 4
Orientation	ST-cut & 90°-rotated ST-cut quartz			
Pitch	7.5 μm	7.5 μm	12.5 μm	12.5 μm
# of pairs	40.5	60.5	40.5	40.5
aperture	1500 μm	1500 μm	2500 μm	2500 μm
type	normal	normal	normal	“2121”

All the IDTs are made of 100-nm-thick aluminum and are covered with ~4-μm-thick PECVD SiO₂

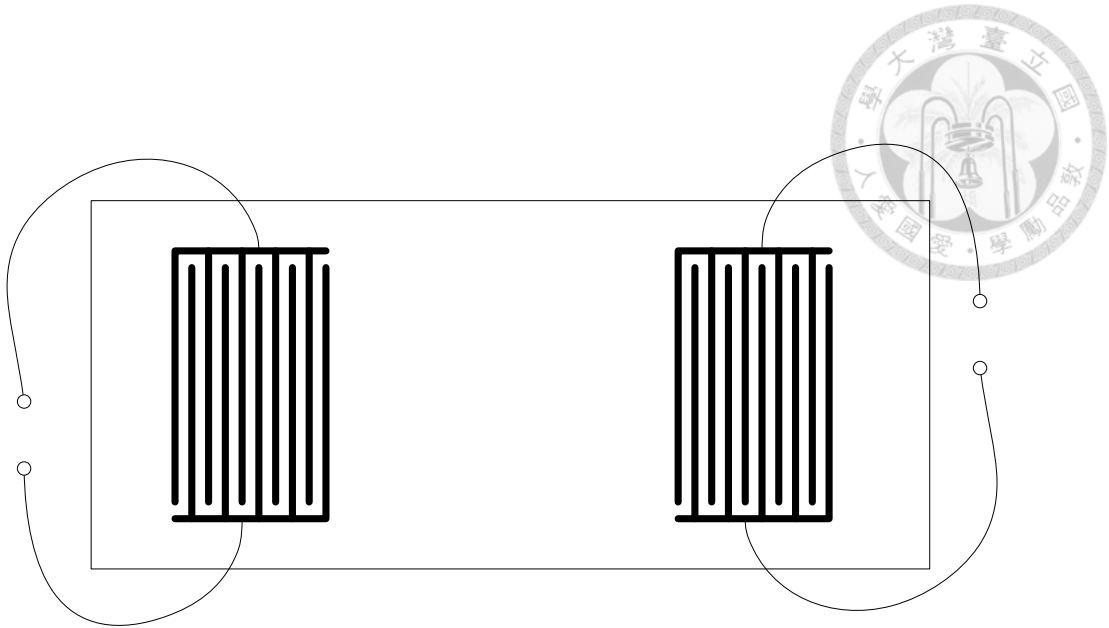


Fig. A1 A schematic drawing of the devices measuring SiO₂ stiffness.

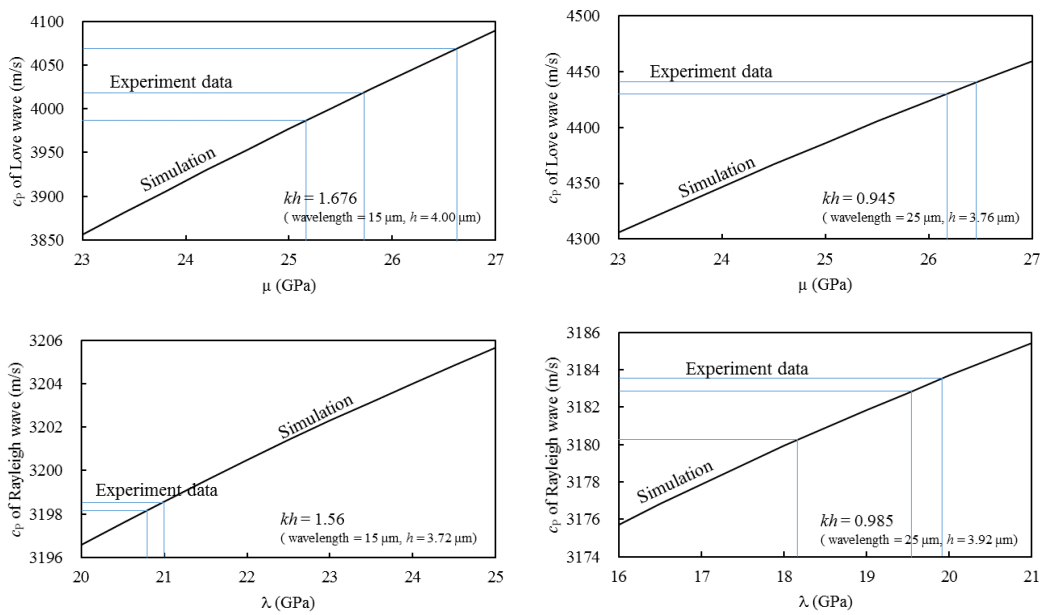


Fig. A2 Measured and simulated phase velocities of Love waves and Rayleigh waves vs. Lamé constants. In the lower two figures, the second Lamé constant μ was fixed 26 GPa

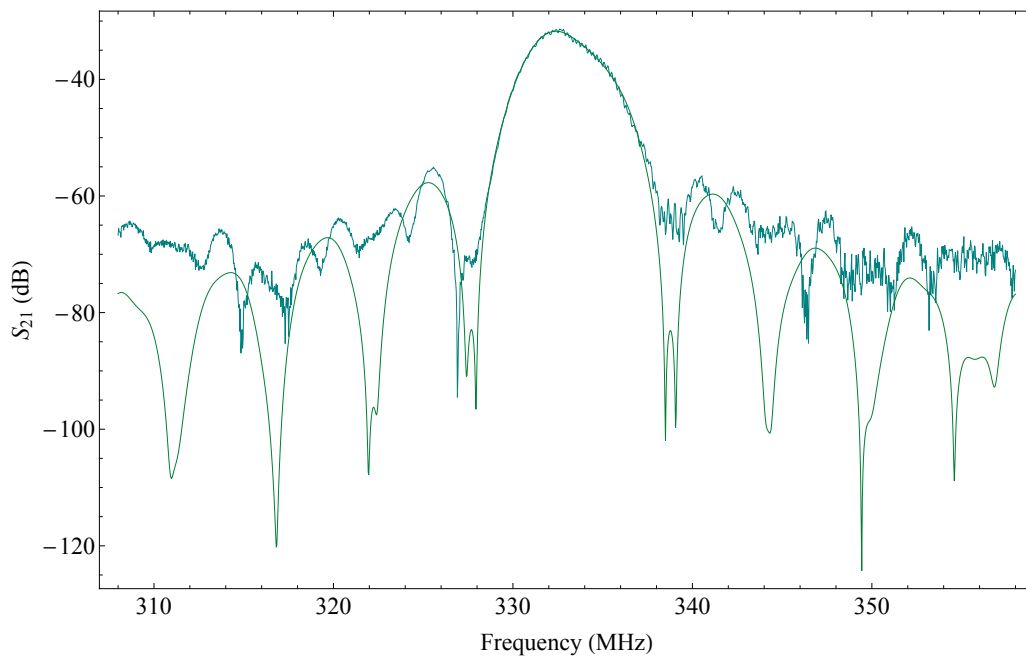
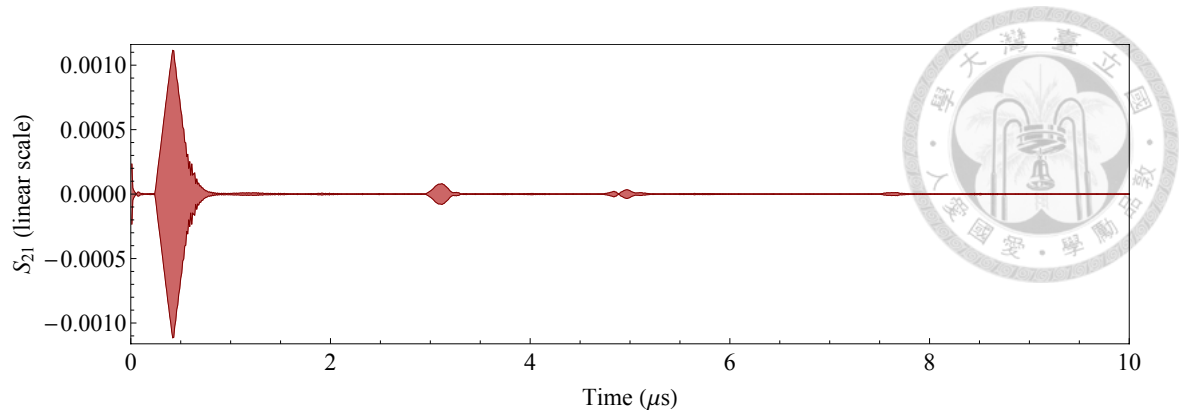


Fig. A3 The response of the filter consisted of 2 IDTs of 60 pairs on 90ST quartz,
wavelength = 15 μ m.

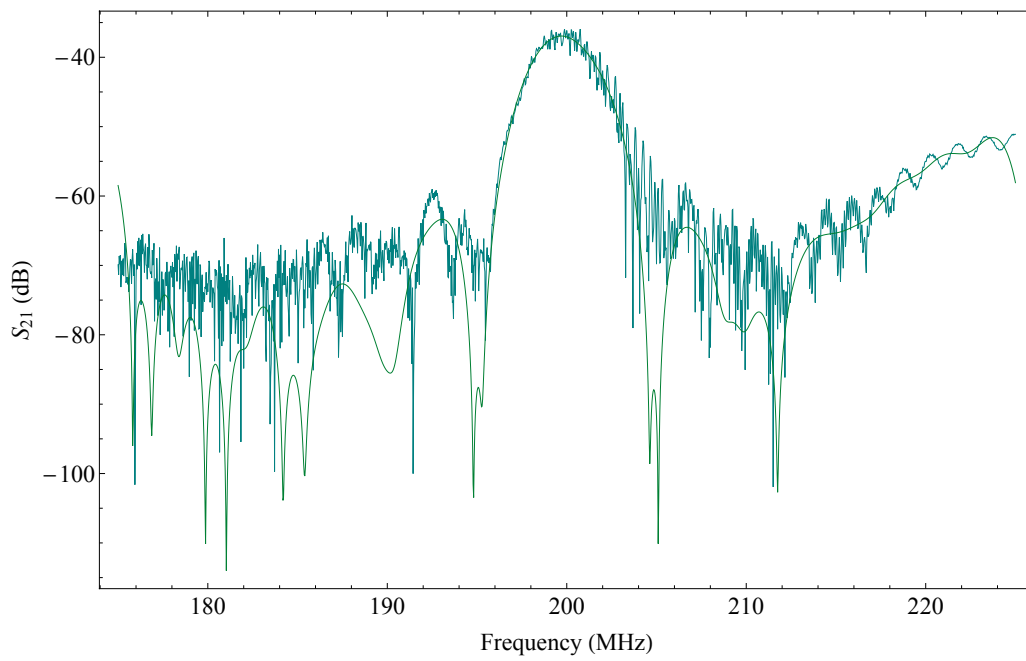
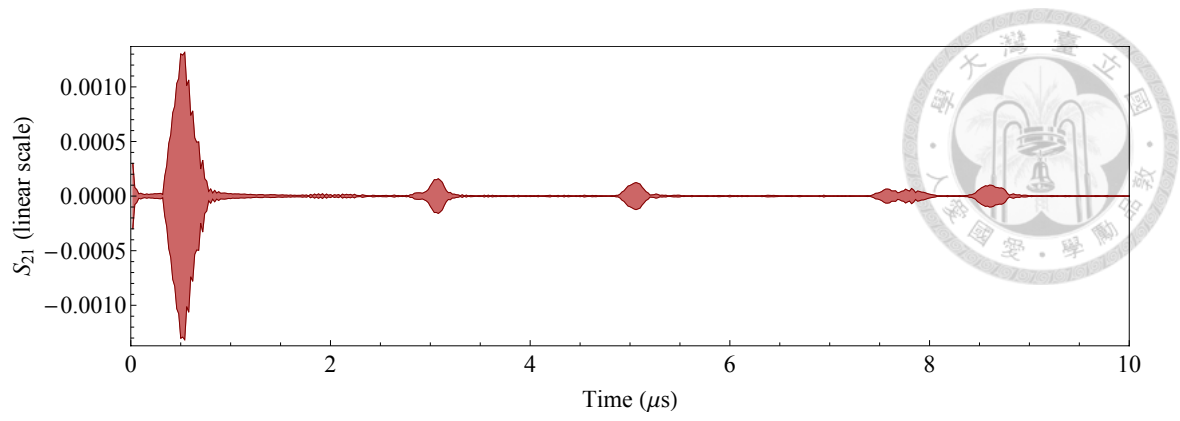


Fig. A4 The response of the filter consisted of 2 IDTs of 40 pairs on 90ST quartz,
wavelength = 25 μ m.

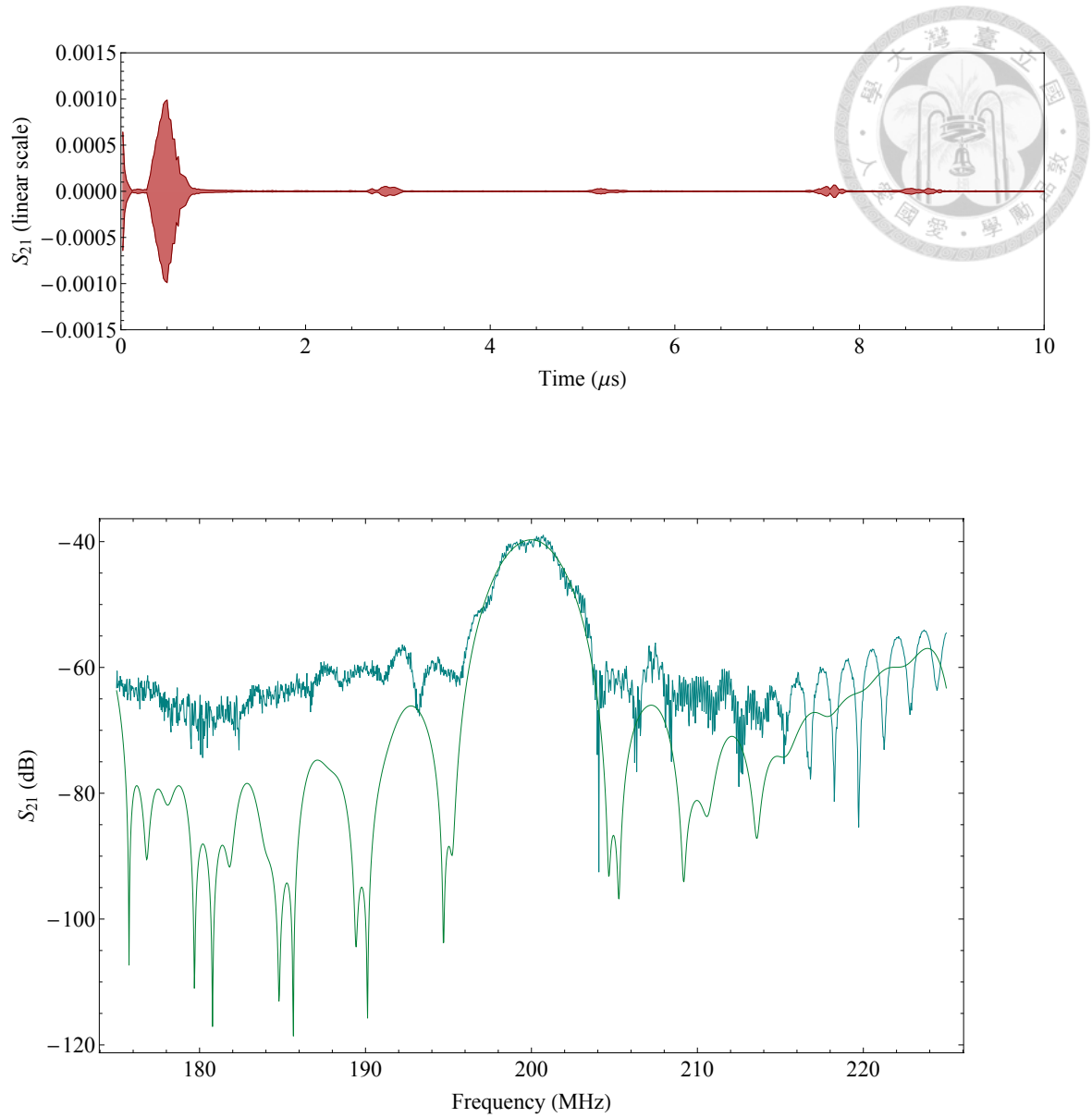


Fig. A5 The response of the filter consisted of 2 “2121” type IDTs of 40 pairs on 90ST quartz, wavelength = 25 μm .

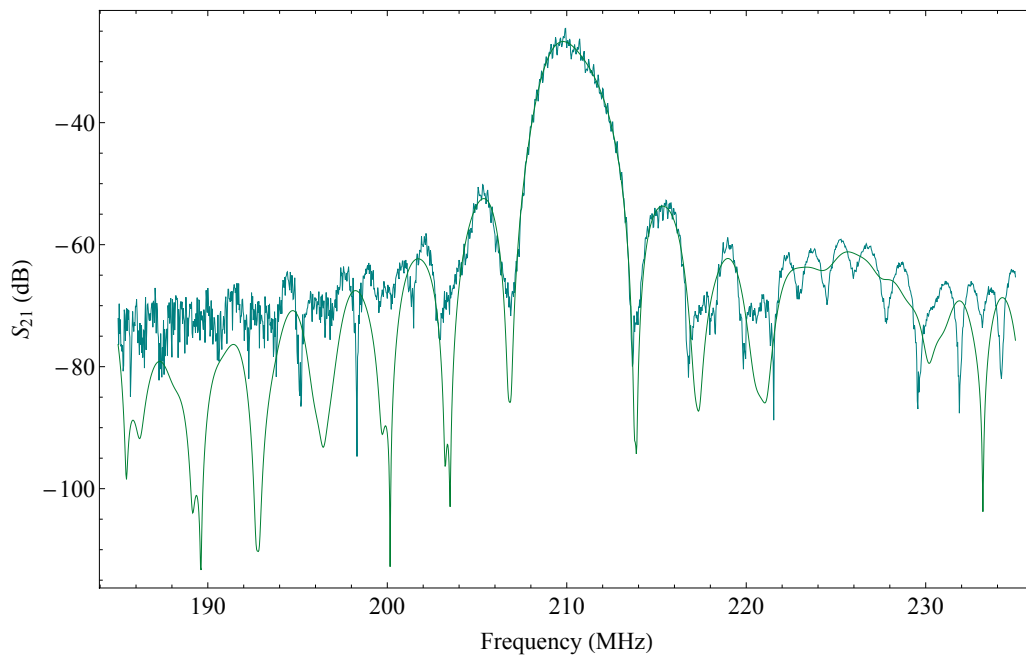
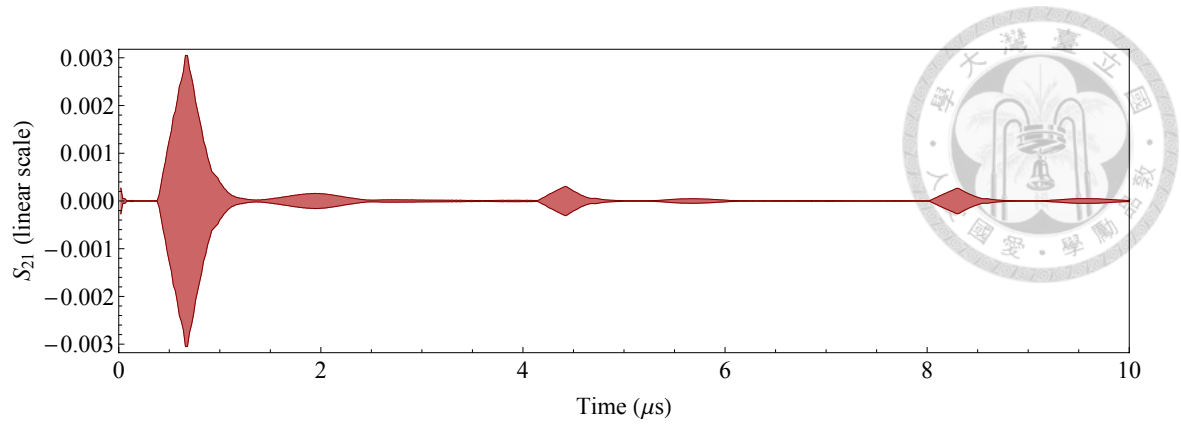


Fig. A6 The response of the filter consisted of 2 IDTs of 60 pairs on ST cut quartz,
wavelength = 15 μ m.

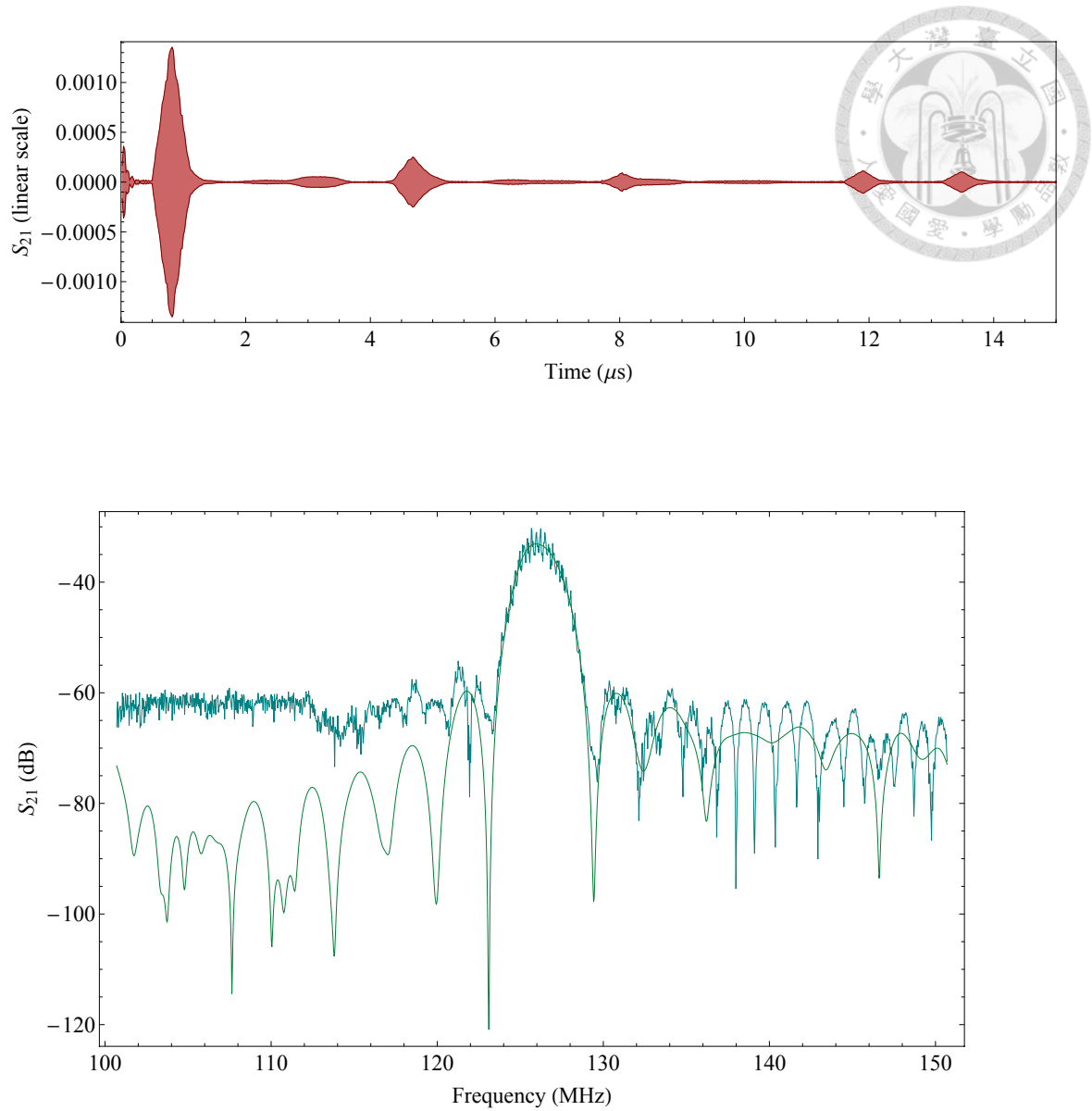


Fig. A7 The response of the filter consisted of 2 IDTs of 40 pairs on ST cut quartz,
wavelength = 25 μm .

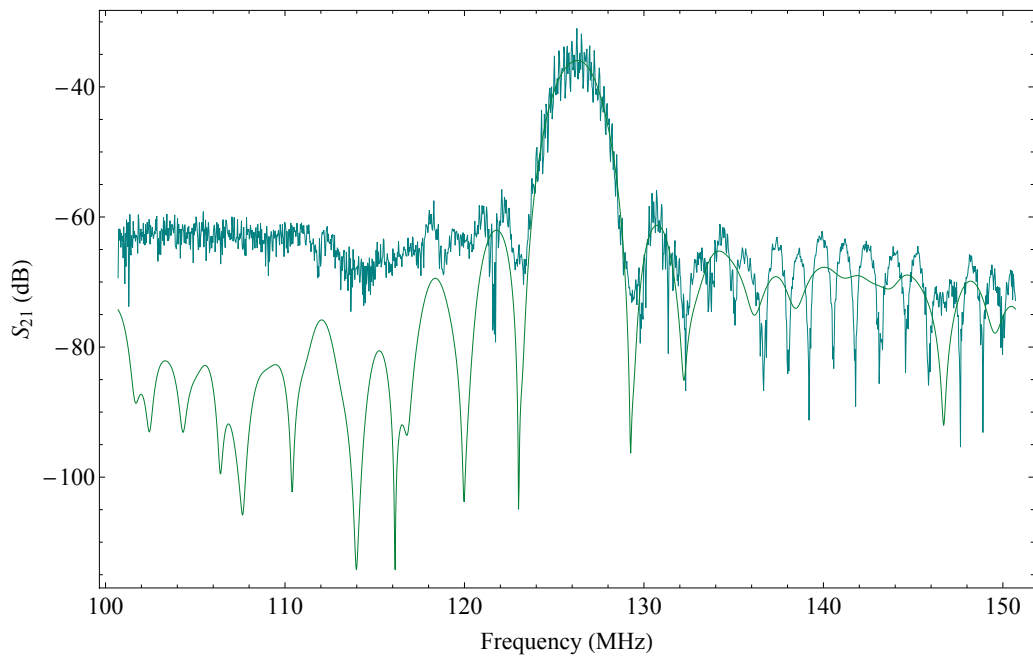
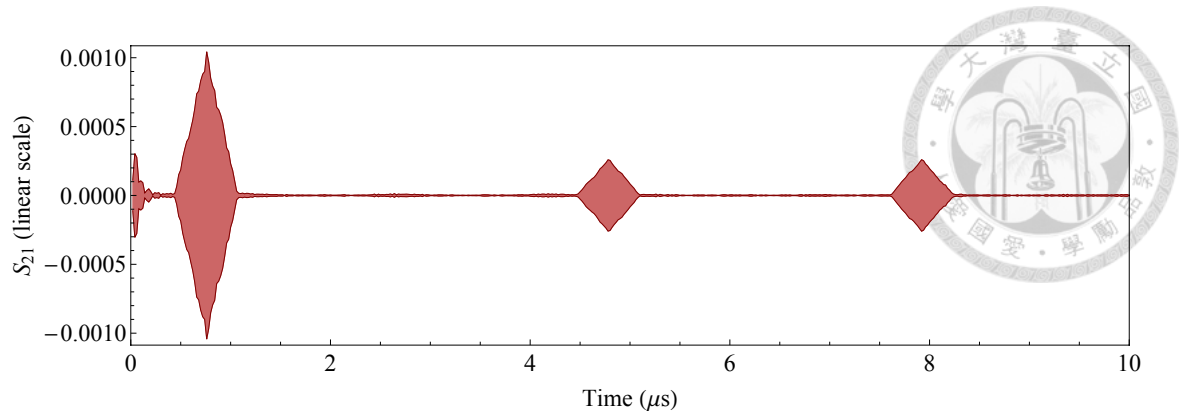
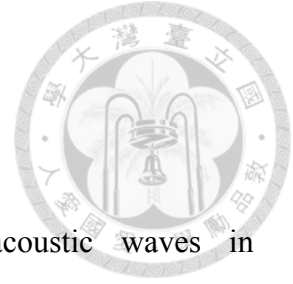



Fig. A8 The response of the filter consisted of 2 “2121” type IDTs of 40 pairs on ST cut quartz, wavelength = 25 μm .

REFERENCE



- [1] X. D. Zhang, Z. Y. Liu, “Negative refraction of acoustic waves in two-dimensional phononic crystals,” *Appl. Phys. Lett.* **85**, 341-343, 2004.
- [2] S. X. Yang, J. H. Page, Z. Y. Liu, M. L. Cowan, C. T. Chan, and P. Sheng, “Focusing of sound in a 3D phononic crystal,” *Phys. Rev. Lett.* **93**, 024301, 2004.
- [3] K. Imamura and S. Tamura, “Negative refraction of phonons and acoustic lensing effect of a crystalline slab,” *Phys. Rev. B* **70**, 174308, 2004.
- [4] L. Feng, X. P Liu, M. H Lu, Y. B Chen, Y. F Chen, Y. W Mao, J. Zi, Y. Y Zhu, S. N Zhu, and N. B Ming, “Acoustic Backward-Wave Negative Refractions in the Second Band of a Sonic Crystal,” *Phys. Rev. Lett.* **96**, 014301, 2006.
- [5] M. H. Lu, C. Zhang, L. Feng, J. Zhao, Y. F. Chen, Y. W. Mao, J. Zi, Y. Y. Zhu, S. N. Zhu, and N. B. Ming, “Negative birefracton of acoustic waves in a sonic crystal,” *Nature materials* **6**, 744-748, 2007.
- [6] J. C. Hsu and T. T. Wu, “Lamb waves in binary locally resonant phononic plates with two-dimensional lattices,” *Appl. Phys. Lett.* **90**, 201904, 2007.
- [7] T. T. Wu, W. S Wang, J. H Sun, J. C Hsu, and Y. Y Chen, “Utilization of phononic-crystal reflective gratings in a layered surface acoustic wave device,” *Appl. Phys. Lett.* **94**, 101913, 2009.
- [8] J. H Sun and T. T Wu, “A Lamb wave source based on the resonant cavity of phononic-crystal plates,” *IEEE Trans. Ultrason. Ferroelectr. Freq. Control* **56**, 121-128, 2009.
- [9] S. Mohammadi, A. A. Eftekhari, W. D. Hunt, and A. Adibi, “High-Q micromechanical resonators in a two-dimensional phononic crystal slab,” *Appl. Phys. Lett.*

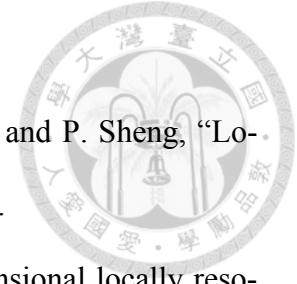
94,051906, 2009.

- 
- [10] C. Y. Huang, J. H. Sun, and T. T. Wu, “A two-port ZnO/silicon Lamb wave resonator using phononic crystals,” *Appl. Phys. Lett.* **97**, 031913, 2010.
- [11] S. Benchabane, A. Khelif, J.-Y. Rauch, L. Robert, and V. Laude, “Evidence for complete surface wave band gap in a piezoelectric phononic crystal,” *Physical Review E* **73**, 065601, 2006
- [12] Saeed Mohammadi, *et al.* “High-Q micromechanical resonators in a two-dimensional phononic crystal slab,” *Applied Physics Letters* **94** (5), pp. 051906-051906, 2009.

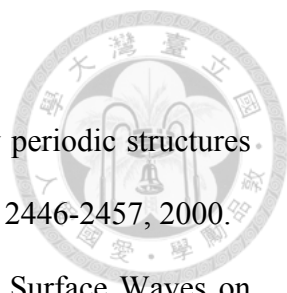
1.2

- [13] A. E. H. Love, *Some Problems of Geodynamics*, Chapter XI, London: Cambridge University Press, 1911, pp. 144-178.
- [14] Jeffrey L. Bleustein, “A new surface wave in piezoelectric materials,” *Applied Physics Letters*, Vol.13, No. 12, 1968, pp. 412-413.
- [15] Y. V. Gulyaev, “Electroacoustic Surface Waves in Solids,” *JETP Letters*, Vol.9, 1969, p. 37.
- [16] Kiyoshi Nakamura, “Shear-horizontal piezoelectric surface acoustic waves,” *Japanese Journal of Applied Physics*, Vol.46, No. 7B, 2007, pp. 4421-4427.
- [17] M. F. Lewis, “Surface Skimming Bulk Waves, SSBW”, in *Proceedings of IEEE Ultrasonic Symposium*, 1977, pp. 744-752.
- [18] M. S. Kushwaha, P. Halevi, L. Dobrzynski, and B. Djafari-Rouhani, “Acoustic Band Structure of Periodic Elastic Composites,” *Physical Review Letters* Vol. 71, No. 13, pp. 2022-2025, 1993
- [19] T. T. Wu, Z. G. Huang, and S. Lin, “Surface and bulk acoustic waves in two-dimensional phononic crystal consisting of materials with general anisotro-

- py,” *Phys. Rev. B* **69**, 094301, 2004.
- [20] Z. Liu, X. Zhang, Y. Mao, Y. Y. Zhu, Z. Yang, C. T. Chan, and P. Sheng, “Locally resonant sonic materials,” *Science* **289**, 1734-1736, 2000.
- [21] G. Wang, X. Wen, J. Wen, L. Shao, and Y. Liu, “Two-dimensional locally resonant phononic crystals with binary structures,” *Phys. Rev. Lett.* **93**, 154302, 2004.
- [22] Y. Tanaka and S. Tamura, “Surface acoustic waves in two-dimensional periodic elastic structures,” *Phys. Rev. B* **58**, 7958-7965, 1998.
- [23] T. T. Wu, Z. C. Hsu, and Z. G. Huang, “Band gaps and the electromechanical coupling coefficient of a surface acoustic wave in a two-dimensional piezoelectric phononic crystal,” *Phys. Rev. B* **71**, 064303, 2005.
- [24] S. Benchabane, A. Khelif, J.-Y. Rauch, L. Robert, and V. Laude, “Evidence for complete surface wave band gap in a piezoelectric phononic crystal,” *Phys. Rev. E* **73**, 065601, 2006.
- [25] J. H. Sun and T. T. Wu, “Propagation of surface acoustic waves through sharply bent two-dimensional phononic crystal waveguides using a finite-difference time-domain method,” *Phys. Rev. B* **74**, 174305, 2006.
- [26] J. C. Hsu and T. T. Wu, “Efficient formulation for band-structure calculations of two-dimensional phononic-crystal plates,” *Phys. Rev. B* **74**, 144303, 2006.
- [27] A. Khelif, B. Aoubiza, S. Mohammadi, A. Adibi, and V. Laude, ” Complete band gaps in two-dimensional phononic crystal slabs,” *Phys. Rev. E* **74**, 046610, 2006.
- [28] J. H. Sun and T. T. Wu, “Propagation of acoustic waves in phononic-crystal plates and waveguides using a finite-difference time-domain method,” *Phys. Rev. B* **76**, 104304, 2007.
- [29] S. Mohammadi, A. A. Eftekhar, A. Khelif, W. D. Hunt, and A. Adibi, “Evidence of large high frequency complete phononic band gaps in silicon phononic crystal



plates,” *Appl. Phys. Lett.* **92**, 221905, 2008.

- 
- [30] Z. Liu, C. T. Chan, and P. Sheng, “Elastic wave scattering by periodic structures of spherical objects: Theory and experiment,” *Phys. Rev. B* **62**, 2446-2457, 2000.
- [31] B. A. Auld, J. J. Gagnepain, and M. Tan, “Horizontal Shear Surface Waves on Corrugated Surfaces,” *Electron. Lett.*, **12**, 650, 1976
- [32] Daniel F. Thompson and B. A. Auld, “Surface Wave Propagation under Metal Strip Gratings,” in *Proceedings of IEEE Ultrasonic Symposium*, 1986, pp. 261-266.
- [33] K. Hashimoto, Hiroki Asano, Tatsuya Omori and Masatsune Yamaguchi, “Ultra Wideband Love Wave Devices Employing Cu-Grating/Rotated YX LiNbO₃ Substrate Structure,” in *Proceedings of IEEE Ultrasonic Symposium*, 2004, pp. 917-920.
- [34] A. Isobe, M. Hitaka, K. Asai, and A. Sumioka, “Grating-Mode-Type Wide-Band SAW Resonators for VCOs,” in *Proceedings of IEEE Ultrasonic Symposium*, 1998, pp. 111-114
- [35] M. Kadota, et al., “SAW substrate for Duplexer with Excellent Temperature Characteristics and Large Reflection Coefficient realized by using Flattened SiO₂ Film and Thick Heavy Metal Film,” In *Microwave Symposium Digest, 2006, IEEE MTT-S International*. IEEE, 2006. pp. 382-385.
- [36] Toshiki Yasue, Tomoya Komatsu, Nobuyuki Nakamura, Ken-ya Hashimoto, Hideki Hirano, Masayoshi Esashi, Shuji Tanaka, “Wideband Tunable Love Wave Filter Using Electrostatically Actuated MEMS Variable Capacitors Integrated on Lithium Niobate, ” *Sensors and Actuators A*, Vol. 188, Amsterdam: Elsevier, 2012, pp. 456-462.
- [37] Waldemar Soluch, “STW In-Line Acoustically Coupled Resonator Filter on

Quartz,” *IEEE Transactions on Ultrasonics, Ferroelectrics, and Frequency Control*, Vol. 55, No. 4, 2008, pp. 879-882.



[38] A. E. H. Love, *Some Problems of Geodynamics*, Chapter XI, London: Cambridge University Press, 1911, pp. 144-178.

[39] Standards Committee of the IEEE Ultrasonics, Ferroelectrics, and Frequency Control Society, *IEEE Standard on Piezoelectricity*, ANSI/IEEE Std 176-1987, Sep. 7, 1987

[40] J. D. Achenbach, *Wave Propagation in Elastic Solids*, Amsterdam: North-Holland, 1973, pp. 218-220.

[41] Daniel Royer, Eugène Dieulesaint, and D.P. Morgan (Translator), *Elastic Waves in Solid*, Vol. I, Berlin: Springer, 2000, pp. 305-308.

[42] C. K. Campbell, *Surface Acoustic Wave Devices for Mobile and Wireless Communications*, San Diego: Academic Press, 1996, pp. 45, 50.

[43] R. Bechmann, A. D. Ballato, and T. J. Lukaszek, “Higher Order Temperature Coefficients of the Elastic Stiffness and Compliances of Alpha-Quartz,” United States Army Electronics Research and Development Laboratory, Fort Monmouth, New Jersey, USAELRDL Tech. Rep. Nr. 2261, Sep. 1963.

[44] Léon Brillouin, *Wave Propagation in Periodic Structures*, 2nd ed., New York: Dover Publications, 1953, pp. 156, 131.

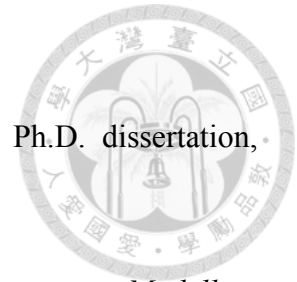
[45] Gaston Floquet, “Sur les équations différentielles linéaires à coefficients périodiques,” *Annales scientifiques de l’École Normale Supérieure*, Sér. 2, 12, 1883, pp. 47-88.

[46] Felix Bloch, “Über die Quantenmechanik der Elektronen in Kristallgittern,” *Zeitschrift für Physik*, Vol. 52, Issue 7-8, Berlin: Springer, 1929, pp. 555-600.

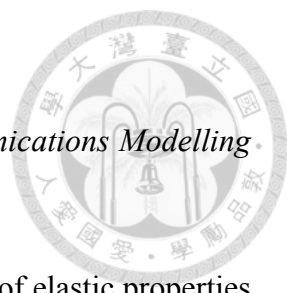
[47] J. D. Achenbach, *Wave Propagation in Elastic Solids*, Amsterdam: North-Holland,

1973, pp. 228-229.

- [48] Y.-Y. Chen, “層狀表面聲波元件之理論、實驗及其應用,” Ph.D. dissertation, National Taiwan University, Taipei, Taiwan, 1992.
- [49] K. Hashimoto, *Surface Acoustic Wave Devices in Telecommunications Modelling and Simulation*, Berlin: Springer, 2000.
- [50] T. Thorvaldsson and B. P. Abbot, “Low Loss SAW Filters Utilizing the Natural Phase Unidirectional Transducer (NSPUDT),” in *Proceedings of IEEE Ultrasonic Symposium*, 1990, pp. 43-48
- [51] Daniel Royer, Eugène Dieulesaint, and D.P. Morgan (Translator), *Elastic Waves in Solid*, Vol. II, Berlin: Springer, 2000, p. 27.
- [52] PECVD thin-film TEOS glass on gallium arsenide using SAW techniques.” in *Proceedings of IEEE Ultrasonic Symposium*, 1994, pp.381-384.
- [53] Z. Wang and J. D. N. Cheeke, and C. K. Jen. “Sensitivity analysis for Love mode acoustic gravimetric sensors,” *Applied physics letters* Vol. 64, No. 22, New York: AIP Publishing, 1994, pp. 2940-2942.
- [54] Kovacs, G., et al. “Love waves for (bio)-chemical sensing in liquids,” in *Proceedings of IEEE Ultrasonic Symposium*, 1992, pp. 281-285.
- [55] T. Nishida, M. Notomi, R. Iga, and T. Tamamura, “Quantum Wire Fabrication by E-Beam Elithography Using High-Resolution and High-Sensitivity E-Beam Resist ZEP-520, *Japanese Journal of Applied Physics*, Vol. 31, 1992, pp. 4508-4514
- [56] M. A. McCord, M. J. Rooks, *Handbook of Microlithography, Micromachining and Microfabrication, Vol. 1: Microlithography*, Bellingham: SPIE Press, 1997, pp. 139-250
- [57] J.L. Murray, H. Okamoto and T. B. Massalski, “The Aluminum-Gold System,” *Phase Diagrams of Binary Gold Alloys*, Russell Township: ASM Intl., 1987, pp.



20-30.

- 
- [58] K. Hashimoto, *Surface Acoustic Wave Devices in Telecommunications Modelling and Simulation*, Berlin: Springer, 2000, pp. 123-125.
- [59] T.-T. Wu, Y.-Y. Chen, G.-T. Huang, P.-Z. Chang, "Evaluation of elastic properties of submicrometer thin films using slanted finger interdigital transducers," *Journal of applied physics*, Vol. 97, No. 7, New York: AIP Publishing, 2005, pp. 073510-073510-5
- [60] G. Carlotti, L. Doucet, and M. Dupeux. "Elastic properties of silicon dioxide films deposited by chemical vapour deposition from tetraethylorthosilicate," *Thin Solid Films*, Vol. 296, No.1, Amsterdam: Elsevier, 1997, pp. 102-105.
- [61] F. S. Kickernell, T. S. Hickernell, and H. M. Liaw. "The characterization of PECVD thin-film TEOS glass on gallium arsenide using SAW techniques." in *Proceedings of IEEE Ultrasonic Symposium*, 1994, pp.381-384.
- [62] Z. Wang and J. D. N. Cheeke, and C. K. Jen. "Sensitivity analysis for Love mode acoustic gravimetric sensors," *Applied physics letters* Vol. 64, No. 22, New York: AIP Publishing, 1994, pp. 2940-2942.
- [63] Kovacs, G., et al. "Love waves for (bio)-chemical sensing in liquids," in *Proceedings of IEEE Ultrasonic Symposium*, 1992, pp. 281-285.
- [64] Kalantar-Zadeh, K., Wlodarski, W., Galatsis, K., & Holland, A., "Study of novel Love mode surface acoustic wave filters." In *IEEE Frequency Control Symposium and PDA Exhibition*, 2002, pp. 74-77.

This document is edited by Word 2011 on a Macbook.